The Variability of M Dwarfs

By

Niall Thomas Goulding

A thesis submitted to the University of Hertfordshire
in partial fulfilment of the requirements of the degree of
Doctor of Philosophy.
School of Physics, Astronomy and Mathematics

September 2013

Typeset in LaTeX 2_ε.

Acknowledgements

This thesis is dedicated to my parents, Debbie, who was always there for me, and to Martin, who couldn't be.

The person I would firstly like to thank, to whom I am most grateful, is my supervisor John Barnes, for his support, insight, advice and knowledge shared throughout my time at the University of Hertfordshire. His supervision was entirely invaluable. In addition I would like to thank my other supervisors, David Pinfield, especially for his guidance and for enabling this work to take place, and to Silvia Catalan. An extra thanks to John for his tireless grappling with some of the coding vital to this work, and for tolerating my relentless inability to properly proof read! Additionally, I would like to thank Hugh Jones, who also provided substantial advice thoughout my PhD. It has been a pleasure working with each of you.

I would like thank the many friends I have found at UH for being there along the way. To Chris, Sam L., Phil, Liz, Gemma, Jose, Mahesh, Sam H., and James F., thank you for the uncountably many tea and lunch breaks we shared together, that I will very much miss. There are no doubt many laughs and conversations had I will remember for years to come. In particular to Chris, who provided something resembling sanity during the folie à deux we likely shared during the final stages of our time at UH! And of course, for the past years of friendship. Thank you too, to the many friends with whom I have had the pleasure of sharing offices. James, Joanna, Brigitta, Andy, ZengHua, David, Mark, Federico, Lientjie, Beatriz, Leigh, Alessandro and Jeremy, it was truly a happy time working alongside you all. About UH, my friends have said in

jest 'no one ever leaves', but it is because of them I hope this proves true.

I am thankful to colleagues from the RoPACS network who contributed to the published work pertaining to this thesis, and for their formative discussions and comments along the way, in particular to Jayne Birkby and Simon Hodgkin. And thank you to my examiners, Chris Watson and Antonio Chrysostomou, for your final comments that shaped this thesis. On one page in a draft of this thesis, marked up with corrections, Chris had written the word "beautiful!", in reference to a result shown on that page. If that result continues to stand as valid, as I think it should, then I can consider this thesis worthy of all my efforts. For I have therefore found at least one new thing in the Universe, of which my appreciation was shared with at least one other person.

And finally, thank you to Adam. You provided the one constant throughout the last four years, and I cannot conceive of having done this without you.

Abstract

M dwarfs have been the subject of renewed interest as potential habitable planet hosts and have increasingly become the targets of planet detection surveys. Currently, however, the number of detections of transiting M dwarf planets remain low. The characterisation of M dwarf activity is an important consideration for such surveys, and provides constraints on the modelling of magnetically active low mass stars. Currently the spottedness of M dwarfs is not well understood owing to their intrinsic faintness and the lack of diagnostics for assessing starspot morphologies and distributions.

The WFCAM Transit Survey (WTS) contains long term observations of M dwarfs in the near infra-red and presents an opportunity to study the long term variability of M dwarfs. The M dwarfs in the WTS are identified by use of colour-spectral type relations, and the periodically variable M dwarfs in the sample are detected using a Lomb-Scargle periodogram analysis. A total of 72 periodically variable M dwarfs are found with periods ranging from 0.16 to 90.33 days. The relations between the spectral subtypes, amplitudes and periods are studied and comparisons to earlier works studying M dwarf rotation are made. A number of examples of significant spot evolution are found, which exhibit complex light curve morphologies that vary in form and amplitude over periods of months to years. This provides an indication as to the nature of the spottedness of these stars.

Simulations are performed to probe the connection between spot coverage, temperature and light curve amplitude. Using the results from these simulations, the spot

coverage fractions of the WTS M dwarfs are estimated and they are found to be heavily spotted. Dynamic models with spots evolving at various average rates are used to explore how spot evolution can drive increased dispersion in the light curves, and to what extent this affects the detectability of periodicity by the method used. It is found that spot evolution can invoke significant noise in an M dwarf light curve, and in combination with photon noise, can in some instances inhibit the detection of a period. In reflection of the results, the relation between the light curve dispersion and spot coverage of the WTS M dwarfs is considered and it is found that more heavily spotted M dwarfs have intrinsically noisier light curves. The morphologies of the light curves produced by the simulations, and the manner in which they evolve, are qualitatively similar to the real M dwarfs in the WTS sample and indicate how models extrapolated from sunspot distributions can explain behaviour seen in active M dwarf light curves.

Contents

1

Introduction

The M dwarfs constitute the coolest, lowest mass, and most plentiful members of the main-sequence. Main-sequence M dwarf (MV) stars span the mass range of approximately 0.075–0.6$M_\odot$ but are defined by the presence of TiO absorption bands in their spectra, being cool enough for such metal oxides to be stable in their atmospheres. M dwarfs straddle the peak of the initial mass function (and thereby, for low-mass stars, the present day mass function) at 0.1$M_\odot$ and are the most common class of star in the galaxy. The 100 closest known stellar systems to the Sun include 99 M dwarfs as either single stars or binary companions[1]. Indeed, the closest known star to the Sun, Proxima Centauri, is an M5 dwarf.

During an era in which the number of exoplanetary discoveries per year is growing

[1]Research Consortium of Nearby Stars, `http://www.chara.gsu.edu/RECONS/TOP100.posted.htm`, see Henry et al. (2006)

exponentially[2], the interest in low-mass, main-sequence stars has been augmented for manifold reasons from both the perspective of photometric and spectroscopic observations. A combination of the drive to understand planet formation in lower mass regimes and the prospect of detecting habitable planets orbiting low mass dwarfs, enabled by improvement of near-infra-red detector technology, has hugely increased the rate of publications concerned with M dwarfs in recent years.

There is a real possibility that the first approximately Earth-size (0.5-2 $R_\oplus$) planet in a habitable zone (HZ) to be detected will be orbiting an M dwarf given the tentative frequency of such planets predicted from Kepler observations (Borucki et al., 2011; Kopparapu, 2013). Estimates for $\eta_\oplus$, the frequency of HZ Earth-size planets (0.5-2 $R_\oplus$), range from $0.15^{+0.13}_{-0.06}$ (Dressing & Charbonneau, 2013) to $0.51^{+0.10}_{-0.20}$ Kopparapu (2013) for M dwarfs implying there could be significant numbers of such planets, and even >10 within 10pc of the Sun. Assessing the variability of stars is vital for the proper characterisation of any orbiting planets by means of both radial velocity and transit detection. Even on relatively inactive G type stars, variations in magnitude have been shown to be an important consideration for the prospect of detecting transiting planets during preparations for now-fruitful missions such as Kepler (Carpano et al., 2003) where such noise could not simply be assumed to be white, while Ballerini et al. (2012) show how incomplete consideration for the effects of stellar spots warrant revisions of transiting planet parameterisation.

Naïvely, the prospects of detecting a transiting Earth analogue around an M dwarf seem favourable. Firstly, the ratio of the sky-projected area between the planetary disc and that of the the star is ten-fold greater than for a solar analogue, secondly, M dwarfs are plentiful in the local population of stars, and thirdly, the period of such a planet orbiting in the HZ is necessarily short. As of mid 2013, however, only 9 planets transiting M dwarfs have been detected, none of which orbit within the habitable zone (although three Kepler Objects of Interest [KOIs] do, as of July 2013, if they are confirmed as planets). NASA's planned Transiting Exoplanet Survey Satellite (TESS) will search for planets transiting nearby M dwarfs at near infra-red wavelengths

[2]See `exoplanet.eu`

(Ricker et al., 2010). While the activity of solar-like stars is well constrained, this cannot be said for M dwarfs, and the effects M dwarf activity has on planetary transit detections remain an open inquiry.

The question of M dwarf activity is also important in answering some more tentative questions pertaining to astrobiology. Intense flaring on M dwarfs (e.g. Tofflemire et al., 2012) could also have implications for biochemistry and macroscopic life on orbiting planets, and luminosity variations in the relatively inactive Sun are under contemporary scrutiny for their contribution to climate variation on Earth. While understanding the fundamentals of M dwarf magnetism and activity are concerns for contemporary astronomers, future questions of how the more active M dwarfs could affect the ability of an M dwarf planet to sustain life will be informed by current endeavours.

1.1 The stellar dynamo

While a full discussion and investigation of stellar dynamos and magnetic phenomena are beyond the scope of this work, it is important to discuss them to give some context to the observations of M dwarf activity and the extent of our knowledge concerning it.

1.1.1 Partially radiative

The MV spectral type traverses the range of low-mass stars amidst which the radiative envelope surrounding the core disappears and the switch over to being fully convective occurs. This occurs at $m \approx 0.3\mathrm{M}_{\odot}$, corresponding to stars where $\mathrm{T}_{\mathrm{eff}} \approx 3250 - 4100\mathrm{K}$ (Chabrier & Baraffe, 2000). For stars above this mass, including the Sun, there exists a boundary between the convective and radiative zone called the tachocline (Spiegel & Zahn, 1992). It is here that there is a strong shear caused by the solid-body like rotation of the radiative core and the differential rotation of the convective zone. This form of dynamo, found in partially radiative main-sequence stars, is known as the $\alpha\Omega$ dynamo. The Ω refers to the stretching of the meridional magnetic field by differential rotation such that it develops a strong azimuthal and ultimate toroidal component, while α refers to the twisting of this toroidal field into smaller loops, as

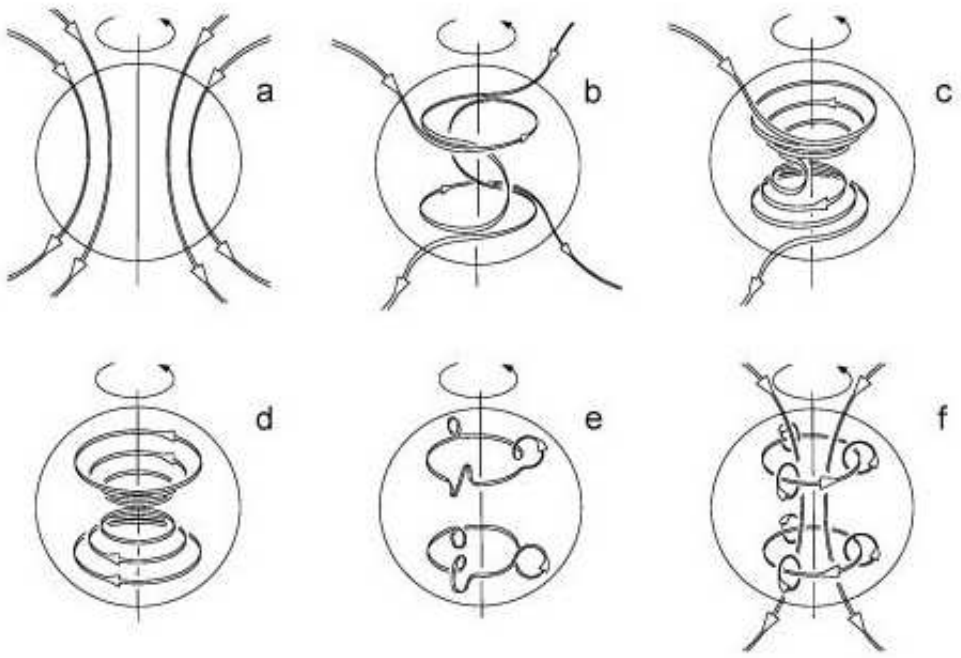

FIGURE 1.1: An illustration of the stellar $\alpha\Omega$ dynamo from **?**. In a to d the differential rotation acting on the poloidal magnetic field results in the toroidal component (the Ω effect) while in e to f the convective turbulence twists toroidal fields regenerating the poloidal component (the α effect).

shown in Figure 1.1.

Magnetic flux tubes are stored as rings at the base of the convection zone in the convective overshoot region, where convection overshoots into the radiative zone. Instabilities in the rings cause them to be driven poleward out of the equatorial plane and towards the surface under magnetic buoyancy (e.g. Parker, 1955; Moreno-Insertis et al., 1992). Driven by discoveries of high-latitude spots on stars other than the sun (as discussed in Section 1.2.2), Schüssler et al. (1996) modelled the trajectories of flux tubes through the convective zone in order to understand how the rotation rate of a star determines the range at which flux tubes emerge and form spots on stars including the Sun. Magnetic buoyancy, through the stratified plasma of the convection zone, causes the part of the wreath like toroidal flux tube formed by the Ω component to rise through the plasma, while the Coriolis force causes the rising flux tube to be deflected polewards until emerging from the photosphere. The exact emergent latitude is determined by the balance of the magnetic buoyancy, the field line curvature, and the rotationally

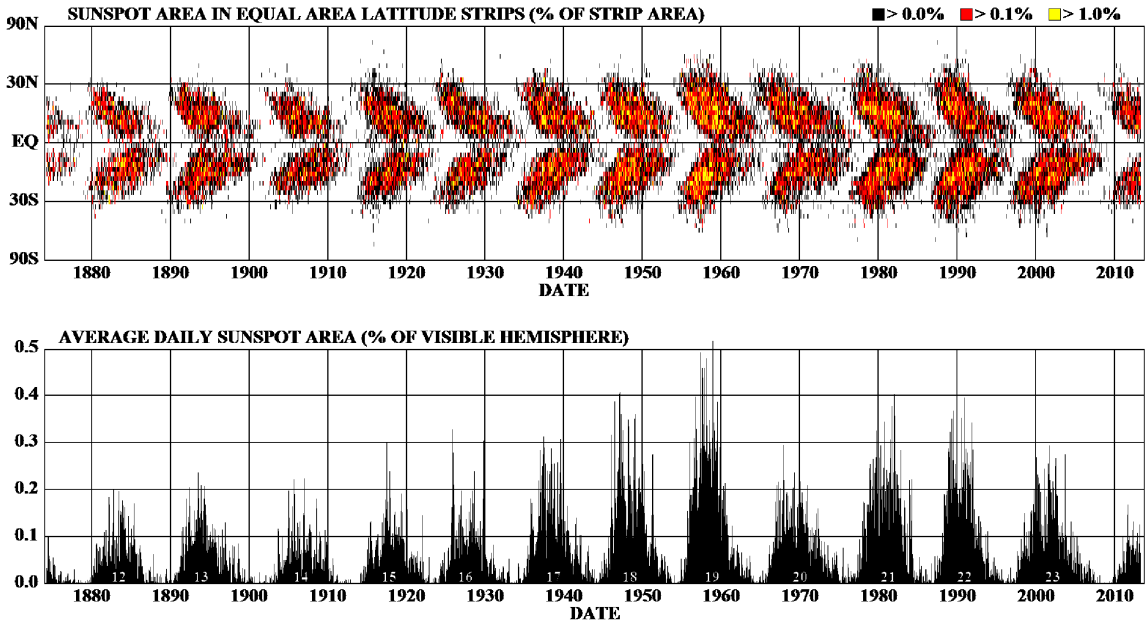

Figure 1.2: The 'Butterfly Diagram' for The Sun from **?**, updated with new data up until June 2013. The diagram shows the latitude dependant emergence of spots over time illustrating the solar cycle.

induced forces. For this reason there is an expectation that rapidly rotating partially radiative main sequence stars should exhibit high latitude spots. Sunspots emerge in two regions that girdle the Sun, the average latitude of which migrates from $\pm 27°$to $\pm 8°$over the course of a solar cycle (Parker, 1955; Ossendrijver, 2003); the distribution of sunspot locations on the Sun are well portrayed by the famous 'Butterfly Diagram' that charts the latitudes of sunspots with time, as shown in Figure 1.2.

1.1.2 Fully convective

For an M dwarf with $m \lessapprox 0.3 M_{\odot}$ there is no radiative zone and thus no tachocline can exist. Furthermore, differential rotation occurs at a lesser, possibly negligible, rate for low-mass dwarfs (Petit et al., 2004; Barnes et al., 2005). A naïve expectation would be that there is a sharp decrease in magnetic activity as the means of dynamo generation ceases to occur. However, the converse of this is true, and there is in fact a gradual transition to a more active regime. It is known that turbulence in the convective zone can also generate a dynamo (Durney et al., 1993) and that this could therefore

generate small scale, turbulent magnetic fields in fully convective M dwarfs. This form of dynamo, thought to operate in fully convective stars and Brown dwarfs, is the α^2 dynamo Durney et al. (1993); Chabrier & Küker (2006).

Observations of the magnetic fields of fully convective M dwarfs paint a somewhat contrary picture. Donati (2011) presents Zeeman Doppler Image (ZDI) observations of late-F to late-M dwarfs and reveal a variety of different magnetic field topologies for the fully convective dwarfs in fields, as predicted from magnetohydrodynamic (MHD) simulations of rapidly rotating fully convective M dwarfs (Browning, 2008), that resemble those of stars with a dynamo largely generated by a tachocline. This is somewhat surprising given the expectation of a dynamo generated by turbulence in the convective zone. In stark contrast to this are others that show a more distributed, non-axisymmetric toroidal topology; a dichotomy Donati (2011) suggests may result from a bistable behaviour of dynamo processes. The various dynamo configurations are shown in Figure 1.3. Morin et al. (2008a) find in ZDI observations of the M4V star V374 Peg, as do Phan-Bao et al. (2009) for the young M4V star G 164-31, that the magnetic energy is mainly stored in a combination of the global axisymmetric, poloidal field as well as small scale fields.

A number of attempts to model the dynamo of fully convective stars, both on the large and small scale, have been made. Dobler et al. (2006) perform MHD simulations to find the large scale magnetic field of a fully convective rotating sphere heated like a star and find a symmetrical quadrupolar topology with a dipolar component for the global field. Browning (2008) model $0.3\mathrm{M}_{\odot}$ fully convective stars and find that near the core energy transfer is still a primarily radiative process. The results of these simulations agrees with those of Dobler et al. (2006) in that at some rotation rates a symmetric field with a dipolar component can be produced, in addition to those occurring on small scales, and a strong toroidal component that can persist for years. Studies by Dorch & Ludwig (2002) into the small scale magnetic fields in fully convective M dwarfs indicate that such fields are qualitatively similar to the small scale fields of the Sun and grow on a time scale of a few minutes.

A full understanding of the how the dynamo of wholly convective stars operates,

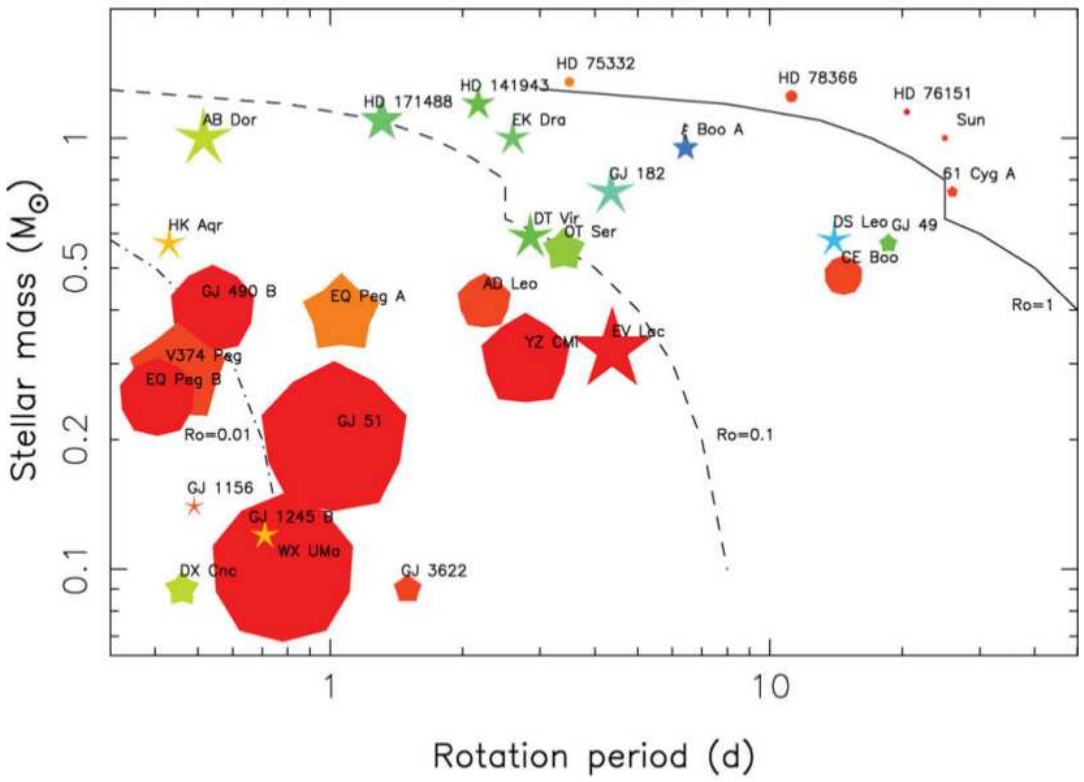

Figure 1.3: The properties of the magnetic topologies of main-sequence stars from Donati (2011, Figure 1). Symbol size indicates the relative magnetic energy density, colour denotes field configurations (blue for purely toroidal to red for purely poloidal fields) and shape depicts the degree of axisymmetry of the poloidal component (decagons for purely axisymmetric and stars for purely non-axisymmetric poloidal fields respectively). The dotted, dashed and solid lines represent Rossby numbers (1, 0.1 and 0.01 respectively) that is essentially the ratio of the Coriolis force to the inertia from the angular momentum of the star. The diagram shows the diverse nature of the magnetic fields for both the fully convective and partially radiative M dwarfs.

and how this forms the magnetic field topologies seen in the limited observations of those of M dwarfs, and indeed, to what extent these dictate the formation of spots, is lacking due to current observational constraints. Therefore, it remains unclear what the expectations of spot coverage should be and how much we can infer a spot pattern from the magnetic topology, and vice versa (Dobler et al., 2006; Reiners, 2012). At least in the case of the Sun, the latitudinal distribution of sunspots does not reflect the full topology of the solar magnetic field (Ossendrijver, 2003); as discussed in Section 1.1.1, it is the toroidal component of the solar magnetic field that ultimately gives rise to sunspots. Chabrier & Küker (2006) predicts that a turbulent dynamo such as that

found in fully convective stars would produce small, low contrast spots, but refers to the need for Doppler Images (see 1.2.2) of fully convective stars to verify this. Thus, questions remain: in M dwarfs, does a distributed dynamo mean a more distributed spot coverage, does a toroidal field mean a latitude dependent spot coverage, and does the duration of magnetic structures in stars dictate the life time of spots? It is beyond the scope of this work to consider fully answering such questions, although they remain important considerations in the context of building a fuller picture of the activity of M dwarfs.

1.1.3 Rotation and activity

As a protostellar core collapses under gravity, the conservation of angular momement causes an increase in the rotation rate with decreasing radius. Angular momentum is, however, lost through various processes that slow the rotation rate; while bipolar flows can moderate the angular momentum gained from material accreted on to the forming star, it is transfered away from the star through instabilities in the its associated disk, and through magnetic braking (**?**). The latter occurs when the inner stellar wind is connected magnetically to the star such that it is corotating, and angular momentum is thus lost with the material composing the wind as it departs the star. This process continues once the star enters the main sequence with some initial rotation period, and the star continues to lose angular momentum due to magnetically driven stellar winds (Kawaler, 1988).

Much of the knowledge of M dwarf activity is the result of observing chromospheric emission lines as activity tracers, such as Hα and Ca II. Some studies of Hα emission of M dwarfs show that Hα is saturated across rotation periods. Mohanty & Basri (2003) suggest that this is either because the dynamo of M dwarfs is so strongly dependent on rotation that it saturates even at low rotation rates, or that a turbulent M dwarf dynamo is efficient enough to saturate Hα emission independently of rotation period. With a larger sample, Reiners & Basri (2008) find that for stars rotating slower than their detection limit there is instead a larger scatter of Hα luminosities, perhaps indicating some dependency at sufficiently slow rotation. In a Ca II H and K line survey

of M dwarfs Browning et al. (2010) find that $v\sin i > 2.5\mathrm{kms}^{-1}$ (the minimum they measure) is sufficient but not necessary to cause activity. Reiners et al. (2012a) obtain a similar threshold of $v\sin i > 3\mathrm{kms}^{-1}$ from Hα emission. They also find that, following the trends in rotation, there is an onset of more scattered activity moving to fully convective stars. They find that for earlier M dwarfs the fraction of active stars is very low, rising greatly for spectral types of around M3 and later. While the fraction of active M dwarfs as traced by Hα emission increases with later spectral type (Mohanty & Basri, 2003; Lee et al., 2010), Reiners & Basri (2008) and Bell et al. (2012) also find that Hα luminosity decreases with later spectral types. Lee et al. (2010) examine short term Hα light curves and find that amplitude increases with later spectral types, although this is potentially because the overall luminosity for later spectral types is lower. From Hα observations the emerging picture is, therefore, of the fraction of M dwarfs showing activity increasing for later spectral types, so too the variability in activity, while the magnitude of the activity decreases.

M dwarf $v\sin i$ measurements have shown a correlation between rotation and spectral type. In a compilation of new and literature sources of M dwarf $v\sin i$, Jenkins et al. (2009, and references therein) show that there is an increase in the dispersion of $v\sin i$ for later spectral types, and that M dwarfs form two significantly distinct populations dependent on whether they are partially radiative or fully convective. This is thought to be an aspect of the increased spin down time for later M dwarfs (e.g. Mohanty & Basri, 2003). The reason for this, as suggested by Mohanty & Basri (2003), is that the increasingly neutral atmosphere of mid- to late-M dwarfs decouples from the magnetic field resulting in less efficient magnetically driven angular momentum loss, in addition to the aforementioned decrease in Hα emission. Reiners et al. (2012a) find the increase in $v\sin i$ dispersion holds for early- to mid-M dwarfs also, however. Irwin et al. (2011) find periodically variable M dwarfs in the MEarth survey light curves of period between 0.28 and 154 days. They similarly find the onset of more rapid rotation for fully convective M dwarfs, confirming the results of $v\sin i$ surveys. Age estimates for fully convective M dwarfs in the MEarth sample show that all the young (<2Gyr) stars rotate with periods of a few days or less, whereas the old (>8Gyr) stars hold a range of

periods from <1d to >100d. It is supposed by the authors that the magnetic topology is the cause for this: the dynamo of fully convective stars is expected to be turbulent and less effective at causing angular momentum loss via stellar wind. Contrary to the earlier models invoking the change in magnetic topology, or its interaction with the stellar atmosphere, as the cause for the increase in shorter rotation periods (and thus high $v\sin i$ and activity for later M dwarfs), Reiners & Mohanty (2012b) show it is in fact purely the magnetic field strength, ultimately dependent on the radius, that is responsible for this relation.

1.2 Starspots

1.2.1 The Solar Case

While the study of photospheric spots on stars in general is by no means a fully matured field of research, the study of stellar spots in one specific case, the Sun, has been an active area of the scientific research since the 19^{th} century. Systematic observations of the Sun throughout the 20^{th} century have allowed for the long term behaviour and trends in the nature of sunspots to be determined.

A sunspot is a cool, dark, depressed area on the Sun's photosphere. Sunspots are formed at the intersection of emerging magnetic flux tubes with the photosphere, generated at the base of the convection zone as described by Parker (1955), girdling the axis of the Sun. Although Cowling (1946) first proposed that part of the tube was convected towards the surface, it is now thought that parts of the flux tube rise due to magnetic buoyancy in a plasma stratified by gravity (Parker, 1955). Although a flux tube emerges as an Ω shaped loop from the photosphere, it does not necessarily form two similar spots at both photospheric footprints; the leading polarity tends to form larger spots whereas the trailing polarity forms more dispersed and fragmented spots (Fan et al., 1993).

Once fully formed, sunspots are comprised of small, central regions called umbrae and larger, surrounding penumbrae. The penumbra of a spot is hotter and brighter than

the umbra, and is approximately four times the size of the umbra. A table of literature sources as summarised by Solanki (2003) in a review of sunspots of the ratio between total and umbral sunspots area (r_A) can be found in Table 1.1. Regions of a sunspot can be as cool as 2000K cooler than the surrounding photosphere (Sütterlin & Wiehr, 1998).

r_A	Source
5.2–6.3 (solar max to min)	Jensen et al. (1955)
5.9 ± 1	Tandberg-Hanssen (1956)
5.9 ± 1	Gokhale & Zwaan (1972)
4.9 ± 0.6	Rodríguez Medina (1983)
4 ± 1	Osherovich & Garcia (1989)
4.6	Steinegger et al. (1990)
4.1–5.2 (large to small spots)	Brandt et al. (1990)
5.7	Antalová (1991)
5	Beck & Chapman (1993)

TABLE 1.1: A collection of values for $r_\mathrm{A} = A_\mathrm{total}/A_\mathrm{u}$, the ratio of umbral to total sunspot area, compiled by Solanki (2003). Jensen et al. (1955) find a $\sim$1 difference in values due to time in the solar cycle and Brandt et al. (1990) find a dependence of r_A on spot size. In the simulation carried out in Section 4.3, a value of 5 is assumed for the r_A following Solanki & Unruh (2004).

The distribution of sunspot sizes is now well known to be of log-normal form, as first found by Bogdan et al. (1988) using data obtained from the Mount Wilson plates collected between 1917 and 1982, and subsequently confirmed with other observations (e.g. Baumann & Solanki, 2005; Penn & MacDonald, 2007). The form of the solar spot size distribution, as described by Bogdan et al. (1988), is as follows:

$$\ln\left(\frac{\mathrm{d}N}{\mathrm{d}A}\right) = -\frac{(\ln A - \ln\langle A\rangle)^2}{2\ln\sigma_A} + \ln\left(\frac{\mathrm{d}N}{\mathrm{d}A}\right)_\mathrm{max}, \tag{1.1}$$

and is commonly rearranged in the exponential form:

$$\frac{\mathrm{d}N}{\mathrm{d}A} = \left(\frac{\mathrm{d}N}{\mathrm{d}A}\right)_\mathrm{max} \exp\left[\frac{(\ln A - \ln\langle A\rangle)^2}{2\ln\sigma_A}\right], \tag{1.2}$$

where N is the number of spots, A is the area of a spot, $(dN/DA)_{\max}$ is the maximum height of the distribution, σ_A determines the width of the distribution, and $\langle A \rangle$ represents the mean spot size. These latter three parameters are deterministically linked to the spot coverage fraction of the photosphere, such that given any particular values of σ_A and $\langle A \rangle$ the height of the distribution will determine the coverage fraction, and so on. The implication of this distribution is that most of the area of the spotted photosphere is accounted for in smaller spots while small amounts of the spottedness of the photosphere contribute to the largest of spots.

This log normal distribution is ubiquitous in the description of sunspot sizes. Baumann & Solanki (2005) used the Greenwich Photoheliographic Results (the longest and most complete record of sunspots spanning 98 years of observations) to investigate both the distribution of sunspot sizes at their maximum development, and the instantaneous distribution. They found that, in both cases, the distribution is well described by the form found by Bogdan et al. (1988). Furthermore, they found that the distribution holds regardless of whether the entire spot areas, inclusive of the penumbrae, or just the umbrae, are considered, or whether single spots or sunspot groups are considered. The distribution can therefore be considered temporally and scalingly robust.

Sunspot growth is reasonably rapid, occuring on a timescale of hours, and driven primarily by growth in the penumbra. Schlichenmaier et al. (2010b) perform observations in the G band and Ca II K line and find that once the umbra has formed its size remains nearly constant. The evolution in the spot size is largely the result of changes in the penumbral size, a result largely corroborated by Gafeira et al. (2012), and is driven by small-scale magnetic flux emergence (Schlichenmaier et al., 2010a). Sunspots grow more rapidly than they decay, with the extremes of the decay rate distribution reaching orders of $10^4\,\%\,\mathrm{day}^{-1}$ (Howard, 1992; Lustig & Wohl, 1995). Using combined data from the Greenwich Observatory and the Solar Optical Observatories Network from 1874 to 2009, Javaraiah (2011) finds that the growth rate of spots averaged over the period of 1874 to 2009 is $\sim$70% greater than the similarly averaged decay rate. The growth rates themselves are found to be heavily dependent on the solar cycle, with the annual averages ranging from an a minimum of 52% day^{-1} and a

maximum of 183% day^{-1}. (Howard, 1992) finds from the Mount Wilson sunspot data spanning 1917 to 1985 that the average growth rate is 502% day^{-1}.

Sunspot decay, being a more gradual process, has been subject to a greater degree of characterisation than growth. It has long been established that sunspots begin to decay as soon as they have reached their maximum area (Cowling, 1946). The lifetime of a sunspot from its emergence to is decay is described by the Genvyshev-Walder relation Waldmeier (1955), and takes the form:

$$A_0 = WT, \tag{1.3}$$

where A_0 is the maximum area the spot reaches, T is the lifetime of the spot, and W is the decay rate, determined to be $10.89 \pm 0.18\,\mathrm{MSH\,day^{-1}}$ (micro solar hemisphere, *i.e.* $5 \times 10^7 \mathrm{A}_\odot$, Petrovay & van Driel-Gesztelyi, 1997). It follows that if the lognormal distribution of areas is linearly related to the lifetime of spots, the spot lifetimes must also be lognormally distributed, although it does not determine the rates at which spots grow and decay overall.

While there is a linear relation between maximum spot size and lifetime, a population of sunspots decays with a lognormal distribution of decay rates. This is not a contradiction but is in fact necessitated if larger spots decay with a smaller percentage change than small spots yet have larger absolute decay rates. The result of this is that the decay rates are lognormally distributed in such a way that there remains a linearity between the maximum spot area and the spot lifetime as dictated by the relation. The distribution of sunspot decays rates was first determined, much like the distribution of spot sizes, to be described by a log normal distribution by (Martinez Pillet et al., 1993). Simulations by Baumann & Solanki (2005) find that scenarios invoking such log normally distributed decay rates better match observations of sunspot size distributions both taken instantaneously and considering the maximum areas of fully developed sunspots.

There is some degree of controversy surrounding the decay law that describes how a spot decreases in size with regards to its decay rate and time. Although early work considered exponential decay laws (Bumba, 1963), the focus of recent papers

studying the decay laws of sunspots concerns the validity of either a parabolic or linear decay law (Martinez Pillet et al., 1993; Petrovay & van Driel-Gesztelyi, 1997; Baumann & Solanki, 2005). The aforementioned simulations by Baumann & Solanki (2005) and observations by Martinez Pillet et al. (1993) are unable to distinguish between the two laws, whereas Petrovay & van Driel-Gesztelyi (1997) conclude, from their fitting to observed decay rates, firmly in favour of a parabolic decay law.

1.2.2 The spots of other stars

While predictions of spot patterns from observations of the magnetic fields and modelling of their dynamos are currently unable to fully inform us of expected spot distributions on all M dwarfs, the spot coverage itself can be directly parameterised. This is commonly addressed through three means: spectroscopic observations, photometric observations, and model based predictions.

The are multiple ways through which spectroscopy can be used to measure spot coverage in many main-sequence stars. O'Neal et al. (2004) used titanium oxide (TiO) bands as a measure of the filling factors and spot temperatures of G and K dwarfs. They determine the visible surface spot coverage at different phases by means of measuring the varying strength of the TiO bands that become stronger at lower temperature. Filling factors between 0.22 and 0.45 are found for the active stars they observed. This technique is of no use for M dwarfs as low-mass stars are cool enough for the entire photosphere to show strong TiO bands (O'Neal et al., 2005) which are thus a defining feature of M type spectra; indeed, M dwarf spectra are used a proxy for spot spectra by O'Neal et al. (2004). O'Neal et al. (2005) also attempted to use vanadium oxide (VO) lines as a diagnostic of spot coverage in M dwarfs, but with little success. A lack of an analogous diagnostic for M dwarfs remains a challenge to the proper measurement of their spot coverages, although the use of the FeH band at 9900Å remains a future possibility (O'Neal et al., 2005).

Another technique reliant on spectroscopy is Doppler imaging (DI). As pioneered by Vogt & Penrod (1983) and Vogt et al. (1987) for the use of mapping the RS CVn star HD 1099, it exploits the Doppler effect to measure the changes in a line profile as

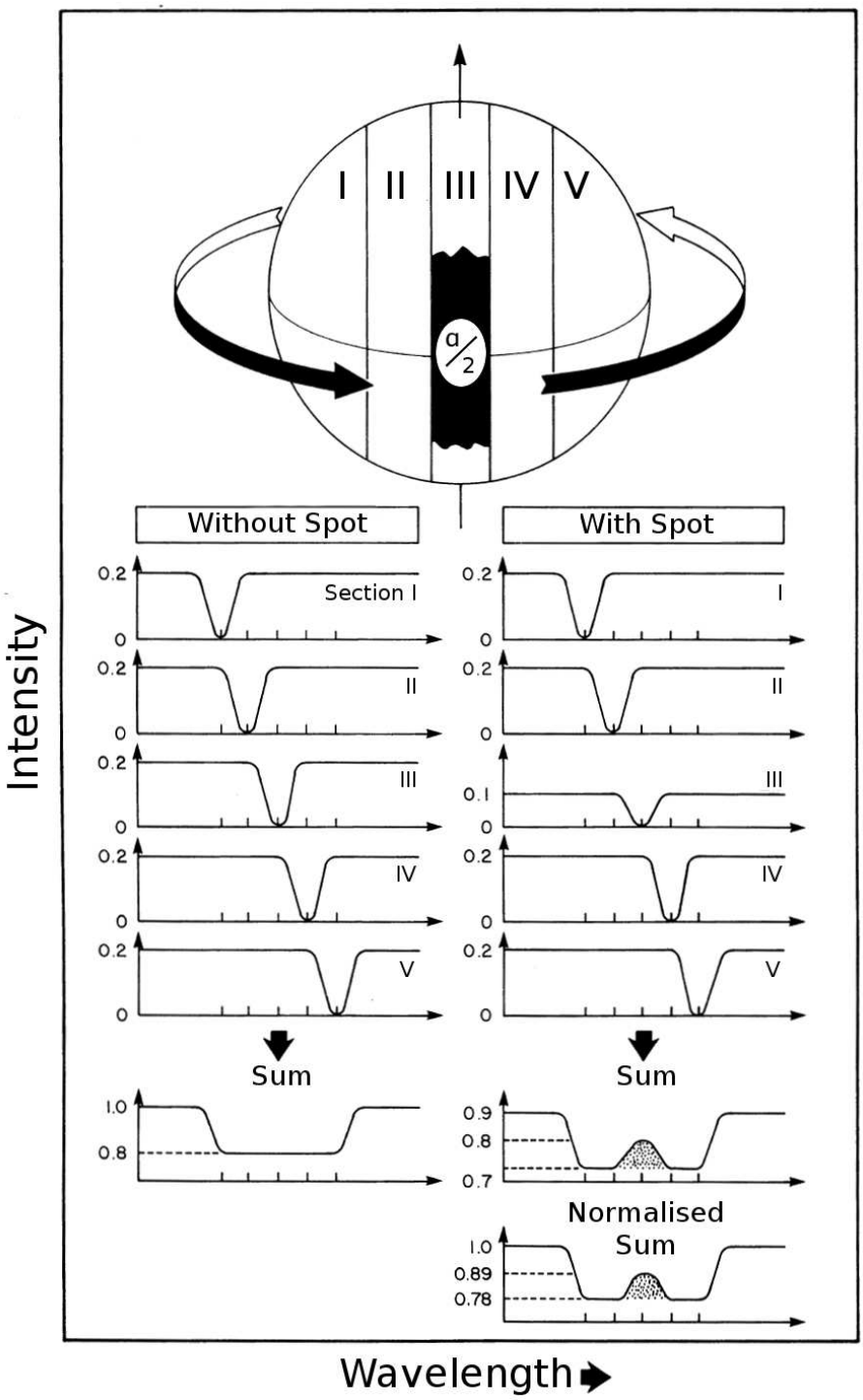

Figure 1.4: Adapted from Vogt & Penrod (1983), this illustration shows the effects of a spot being rotated through the angle of observation on an absorption line profile. Each section contributes a line with some degree of Doppler shifting due to rotation, summing to a broadened line. In the case where section III is 50% covered in an absolutely black spot, as depicted, a line of 50% depth from a continuum of 50% intensity causes an apparent emmision bump in the broadened line profile. As the star rotates, this bump will move through the line profile tracing the movement of the spot through the angle of observation as the star rotates, the speed at which it does indicative of its latitude.

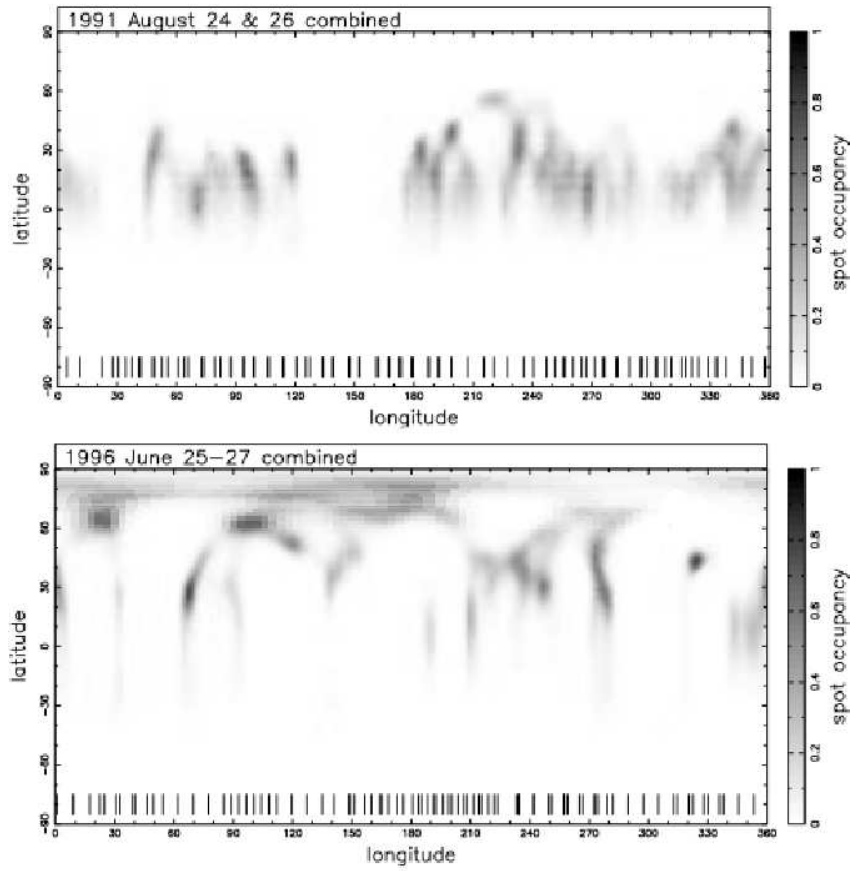

FIGURE 1.5: Doppler images of the stars HK Aqr (top) and RE 1816 1541 (bottom) from Barnes & Collier Cameron (2001).

a cool spot rotates with the spherical surface of a star, first distorting the blue side of the Doppler-broadened line and then the red, as shown in Figure 1.4. The change in flux due to spotted regions of the star being rotated into and out of view changes the profile of a line broadened by Doppler shifting due to rotation. The size of the bump created in the line is dependant on the spot area and temeperature, while the rate at which it transits the line is dependant on its latitude. Thus such features in absorption lines can be used to generate a surface map of the spottedness of a star. Doppler imaging is, however, limited to determining the spot patterns on only rapidly rotating M dwarfs. In order for the Doppler effects to be measurable the star is required to be rapidly rotating (which also observationally aids the attainment of a more complete phase coverage) and must be bright enough such that the signal to noise ratio is large enough for the effects to be detectable. The technique was first applied to M dwarfs by

Barnes & Collier Cameron (2001) to map spots on two rapidly rotating stars, HK Aqr (dM1.5e) and RE 1816 1541 (dM1-2), shown in Figure 1.5 revealing a latitudanally distributed spot pattern, that is, a spot pattern not necessarily restricted to a narrow range in latitudes. Further Doppler imaging of HK Aqr found that the differential rotation rate was essentially consistent with near-solid body rotation. The distribution of photospheric spots remained morphologically similar over 11 months (Barnes et al., 2004), although the exact spot patterns were found to have changed. Polar spots are a common phenomenon observed in Doppler images of rapidly rotating cool stars due to the aforementioned effect of the Coriolis force driving emergent flux tubes to higher latitudes dependent on the period (Schüssler et al., 1996), combined with a super-Solar meridional flow Mackay et al. (2004), but it is clear from the presence of low latitude spots in Doppler images that such effects can only be partially deterministic of spot patterns.

There are currently few such Doppler images for main-sequence stars of a later spectral type than this, and none for the latest M dwarfs, although ZDI observations (as discussed in Section 1.1.2) indicate that the magnetic fields can either take axisymmetric poloidal or distributed toroidal topologies. This suggests that the spot configurations could in fact be much like those found in partially radiative stars, with some showing distributed spot patterns and others showing polar cap like distributions (e.g Jeffers et al., 2007). Morin et al. (2008a) perform ZDI observations on the fully convective M4 dwarf V374 Peg and find a mostly poloidal magnetic field stable over year-long time scales. They find a distributed spot coverage of low-contrast spots occupying 2% of the photosphere. The possibility of unresolved small spots is not discounted however, and small scale magnetic fields cannot be constrained. Contrary to this, Phan-Bao et al. (2009) find a single area of spot coverage occupying one pole for the young M4V star G 164-31 in an incomplete DI, which they interpret as a single, low contrast spot. Similarly, this does not discount the possibility of smaller spots distributed across the photosphere.

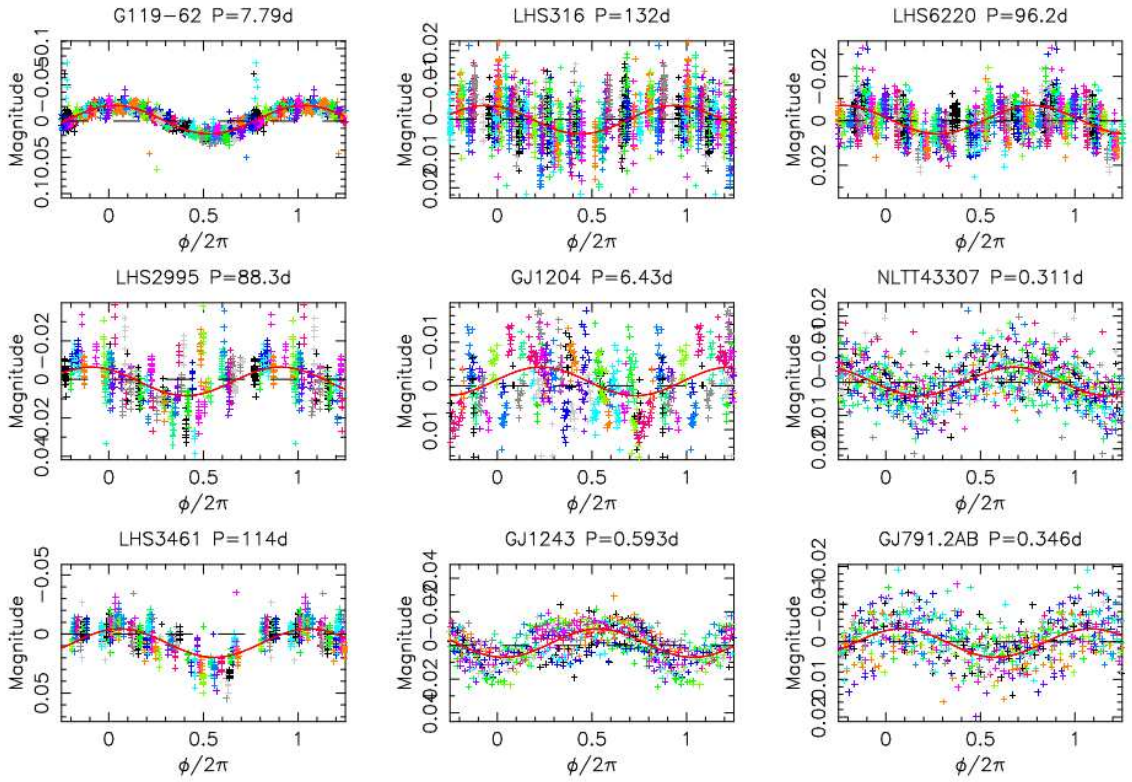

FIGURE 1.6: A selection of some of the phase folded M dwarf light curves presented by Irwin et al. (2011) showing spot modulation in the form of sinusoid-like variation over a range of periods.

1.2.3 Light curve modulation due to spots

The presence of cool star spots coupled with stellar rotation leads to photometric modulation as the starspots rotate into and out of view, as shown in Figure **??**. For light curve variation to be detected above the photon noise, the photosphere must be sufficiently covered in unevenly distributed spots. The designation of BY Dra type is occasionally used to refer to stars exhibiting this type of light curve modulation, after BY Draconis (Hełminiak et al., 2012). Many surveys designed for rotation studies, particularly of angular momentum evolution in open clusters have had an auxiliary result of providing a wealth of spot modulated light curves at varying wavelengths.

Messina et al. (2001) describe the factors that relate star spot coverage to light curve amplitude. The amplitude of any light curve is the product of the stars inclination, the contrast in temperature, and thus the brightness of the spotted and unspotted

photosphere, the spot areas, and the distribution of the spots over the photosphere, as follows:

Inclination: all stars will have some inclination between the two extremes of pole-on inclination, i=0°, and equator on inclination, i=90°, with a random distribution of inclinations typically assumed. In the case of pole-on inclination the amplitude as a product of rotation rate will be zero as the same hemisphere of the star will constantly be visible from the perspective of the observer. In the case of equator on inclination, the amplitude due to a given spot distribution will be maximal as the entirety of the photosphere is rotated through the angle of observation as the star rotates. Therefore, amplitude scales wholly between some maximum value and zero with an amplitude that approaches zero as the stellar inclination approaches zero for a fixed spot pattern. If the spot pattern evolves, changes in brightness will still occur, and any periodic behaviour occurring for a star orientated thusly could be due to some cycle analogous to the solar cycle.

Temperature contrast: the flux density of a star is determined as a first approximation, from the Stefan-Boltzmann equation, to be directly proportional to T^4 (assuming it behaves as black body). In reality this is modified by temperature-dependant molecular absorption lines, particularly so in M dwarfs. The sensitivity of the amplitude to changes in the contrast of the spotted to unspotted photospheric temperatures is greater when the contrast is lower, for example, a 100K change in spot temperature of ΔT=200K to ΔT=300K, where $\Delta T = T_p - T_s$ will cause a larger amplitude change than a similar 100K changes from ΔT=1200K to ΔT=1300K. This is because the contrast ratio at 1200K is already low. Stellar atmospheres are not black bodies however, and as the presence of different atomic and molecular species varies with temperature so too do absorption signatures in the photospheric and spot spectra, modifying the contrast ratios.

Spot distributions: a maximum possible amplitude would be the result of the entirety of the spotted photosphere being located on one hemisphere in the form of a large single equatorial spot. This would lead to a light curve with a flax maximum and a minimum morphologically similar to those of some eclipsing binaries (EBs).

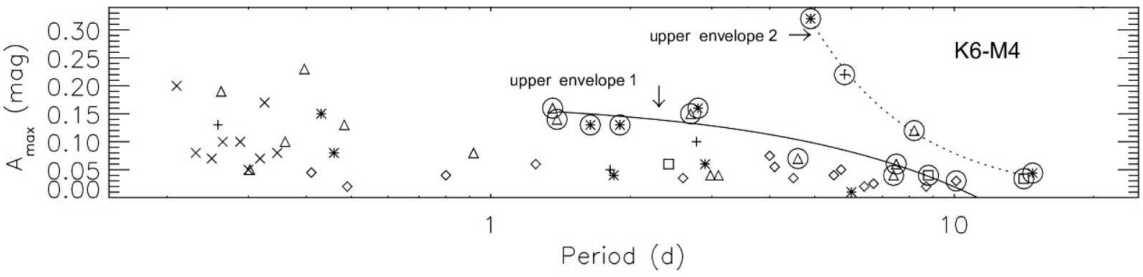

FIGURE 1.7: Maximum light curve amplitude versus rotation period for late type, partially radiative field and cluster dwarfs, adapted from Messina et al. (2003), showing the decrease in amplitude for longer rotation periods.

Conversely, the light curve amplitude may be minimised if the entirety of the spot coverage is distributed uniformly over the photosphere as infinitesimally spots. Intermediate cases could take forms that are strictly sinusoidal, or in the case of a large spot trailed by smaller spots, saw-toothed. Essentially, the presence of multiple spots or complex patterns adds higher order Fourier components to the light curve. Another interesting example is that of a star with two large spots on opposing hemispheres. Such a stars would have two different minima and maxima per phase. As such the amplitude, and crucially, the morphology of the light curve is determined by both the fractional area covered in spots and their distribution across the viewable surface of the star.

Because of the degeneracies between these three parameters, the amplitude of a light curve can only be a crude proxy for the true level of stellar activity. In considering the light curve amplitudes of samples of M dwarfs with respect to some other parameter it is therefore necessary to consider an upper envelope of a distribution of light curve amplitudes (Messina et al., 2001) as these are likely to be those less affected by the inclination of the star. Messina et al. (2003) fit two such envelopes to the late type dwarfs in a study of activity tracers of rotating stars in field and cluster stars of different ages, as shown in Figure 1.7. For each of their spectral type bins, a general trend of decreasing amplitude upper envelope with increasing rotation period was found. The V band amplitudes of these stars largely occupy a range from 0.01 to 0.2 with one larger than 0.3. Each of the stars considered in their work is also an X-ray source,

allowing for the use of the ratio between X-ray luminosity and bolometric luminosity as a tracer of chromospheric activity, finding a similar result of decreasing activity for longer periods. Kiraga & Stepień (2007) also find a decrease in activity for longer rotation periods. In studies of variable stars of type GV or later in the open cluster M11, Messina et al. (2011) find further evidence of the relation between decreasing light curve amplitude with increasing period. The dependence on activity levels with rotation period is expected due to the dependency of the dynamo in partially convective stars with the rotation rate. Rockenfeller et al. (2006) perform a periodogram analysis on multi-band observations of M and L dwarfs in order to probe a possible relation between spectral type and amplitude and establish variable fractions, finding no trend between amplitude and spectral type but finding variable fractions >0.25 for M dwarfs.

Ciardi et al. (2011) study the variability of all stars in the Kepler survey by determining the χ^2 statistic, testing for a significant deviation from the null hypothesis of no variability, for each light curve and binning them in $\chi^2 > 2$, 10 and 100 bins. In particular they seek to characterise the variability of the M dwarfs in the sample. They find that nearly 70% of M dwarfs fall into the $\chi^2 > 2$ bin considering stars where the Kepler mag < 14, and 47% fall into the $\chi^2 > 100$ bin. In this most variable bin, 90% of stars in a periodogram analysis exhibit some significant periodicity (although the nature of the periodicity is not explored) while in the lower variable bin the source of the variability was stochastic noise. While it is not discussed what the actual cause of this prevalent stochastic variation is, it is possible it could be an indication of transient photospheric features that exist on a time sale less than the rotation period such that no coherent modulation is ever established. The noise is described by the authors as being white, i.e., with amplitude independent of frequency.

Harrison et al. (2012) find a greater variable fraction of 79% for stars of spectral types later than K0V and earlier than M2V inclusively in the Kepler light curves. They note a few stars where it is clear there is some overall change in the spot configuration over month long time scales but a long term coherence is still maintained due to a dominant spot (group). If the Gnevyshev-Walder relation does hold for spots on other stars with solar-like dynamos then a prediction of this would be exactly this observed

behaviour where one large spot persists, taking a long time to decay, while smaller spots evolve on shorter time scales. In other stars in their sample it appears that the spots evolve or change location much faster, altering the morphology and amplitude of light curves on the time scales of ≤ 1 phase. Lane et al. (2007) find one of the first examples of an apparent change in spot morphology in a spot modulated M dwarf light curve. The light curve of the KOI-256, a post-common envelope binary system consisting of an M3V star and a transiting white dwarf shows a clear illustration of how large scale changes in the spot morphology can occur, as the light curve changes from being almost purely sinusoidal with one maximum and minimum per phase to having two maxima and two minima per phase, and then returning to a morphology similar to the former one over time scales of hundreds of days (Muirhead et al., 2013).

Another means of determining spot characteristics from light curves is by occultations of spots by transiting planets. This is discussed later in Section 1.3.

1.2.4 Light curve synthesis from spot modelling

Attempts to make deductions about the nature of the spottedness of a star from photometry are limited due to degeneracies between parameters. The number of free parameters causally linked to the observed light curve compounds the ability to directly measure any one of those parameters from photometry. The amplitude of a light curve is dependent on the configuration of the spot pattern and the filling factor of the photosphere, itself dependent on the difference between the unspotted and spotted photospheric temperatures and the percentage spot coverage of the photoshere, the latter of which is to some extent a dependency of the spot configuration. Spot configurations appear to only sometimes be connected to the dynamo and rotation rate of the star, with some stars showing only polar caps of spots while others show distributions over all latitudes in partially radiative stars, and expected spot coverages on fully convective stars with multi-polar or distributed dynamos are uncertain. Despite this, photometric monitoring of variable M dwarfs can make some a priori predictions about activity levels on M dwarfs and is a vital consideration for other light curve science such as planetary transit detection.

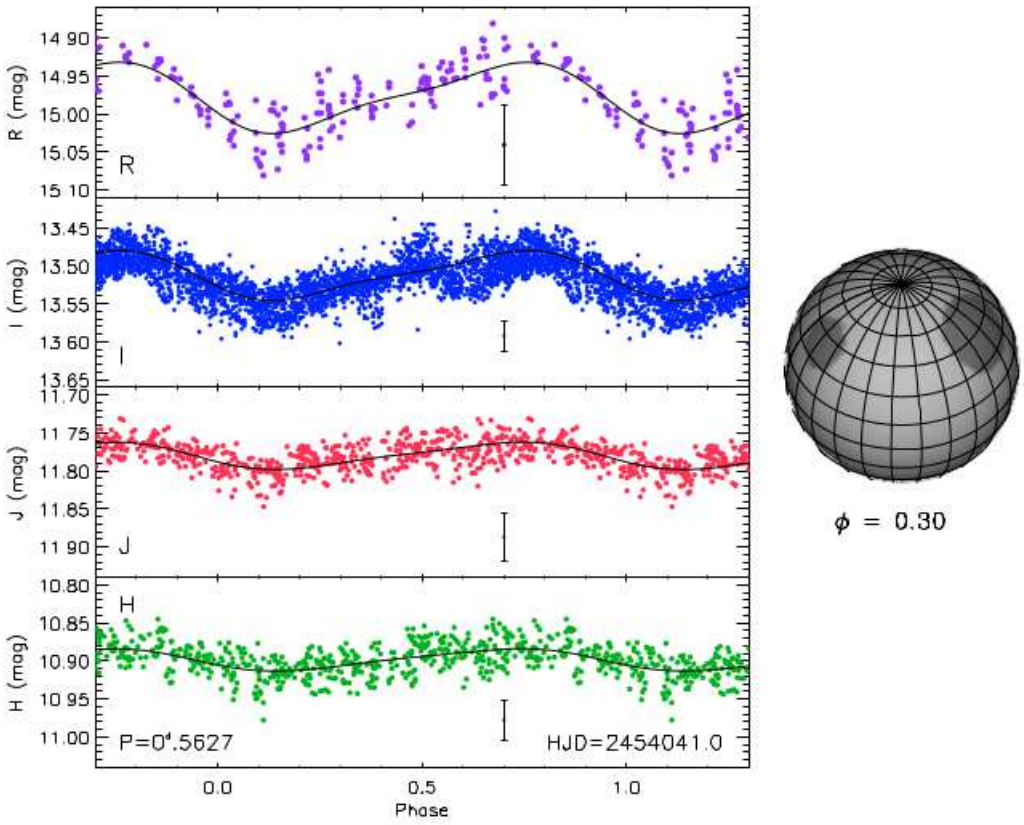

FIGURE 1.8: $RIJH$ light curves for an M3 pre-main-sequence star from Frasca et al. (2009) with the accompanying two-spot model fitted to the light curves, shown by the solid line.

Multicolour photometry combined with spot models can yield further parameterisation of spottedness. Strassmeier et al. (1994) use $UBVI$ photometry in conjunction with an iterative least squares model invoking rectangular spots to monitor changes in spot size and lifetime on the RS CVn binary HR 7275. Frasca et al. (2009) use the spot model code MACULA using two spots fitted to $RIJH$ light curves of pre-main-sequence variables in the Orion nebula cluster, as shown in Figure 1.8, following the work Frasca et al. (2005) that shows that light curves can be modelled with just two circular spots. Later use of MACULA by Kipping (2012), has enabled differential rotation to be estimated. This also relied on fitting small numbers of spots in order to model stellar light curves showing rotational modulation. Modelling of the late type dwarf Kepler light curves by Harrison et al. (2012) employ single spots due to the observation that many of the light curves have flat maxima indicating that one hemisphere of the star appears to be relatively spot free. It is noted that a single spot or

pair of spots cannot adequately reproduce the morphology observed in the light curves and they conclude that a pattern that is more complex with respect to longitude would be expected, and hence the above results are questionable.

It is apparent, therefore, that these models, while powerful at providing a possible solution for any given light curve, rely on the implementation of a small number of monolithic spots that minimise the entropy of the parameters to characterise a star with a dynamic model for analytic fitting, and may not be strictly physically justified given what is known about spot distributions on stars. That is, that the distributions imply that small spots contribute a significant fraction to the overall spottedness and ZDI observations of late M dwarfs indicate that the magnetic field of M dwarfs is either strongly poloidal or highly distributed. It is conceivable, though, given that it is known in the Sun's case that the form of the distributions that describe individual spots hold for spot groups and therefore models invoking large monolithic spots may do so validly as a proxy for unresolvable spot groups. These degeneracies will only be broken by high precision Doppler images of the spot patterns on active stars, and until then it remains to be seen whether models with parsimonious free parameters are genuine informers on the nature of spot patterns on active M dwarfs.

Given this, some approaches have used liberal parameterisations to predict parameters that observed stars may take. Jackson & Jeffries (2013) use a Monte Carlo approach to predict the distribution of light curve amplitudes for variable M dwarfs in NGC 2516. While using the commonly employed filling factor and T_p/T_s ratio they use a nearly equivocal scale length between spotted areas rather than spot distribution itself, with the spotted areas of the stars being modeled by filled, square bins. An interesting result from this approach is that it is the most heavily spotted stars that exhibit small light curve amplitudes as the spot placement distribution is more uniform over the surface. A uniform distribution would not be a realistic expectation of M dwarf spot sizes if there is any size distribution, however. If their spot sizes do follow a lognormal distribution, as they do on the Sun and other earlier stars, it would imply some combination of a few large spots with more medium and small spots. This would result in larger amplitude light curves if the total spot coverage is high. There

is therefore a need to examine how a non-uniformly sized random spot distribution would affect the resultant light curve distribution. These models are also static, and the evolution of spots on low-mass stars is yet to be well constrained.

1.3 Considerations for planet detection

The assessment of variability remains a challenge in many methods of planet detection. Recent conservative estimates of the 0.5-2$M_\oplus$ planet frequency around M dwarfs of $0.51^{+0.10}_{-0.20}$ by Kopparapu (2013) lend even more necessity to the proper characterisation of M dwarf variability.

Spots have the ability to change the shape and depth of planetary transits in two ways. The first, more simplistic way, is due to the overall change in brightness as spots rotat into view, changing the base brightness of the star which will effect the relative depth of the planetary transit. The second way is the result of the planet occulting spotted areas of the photosphere. As the planet moves from transiting unspotted to spotted photosphere the flux increases. For a single mid-transit spot this is manifested as a bump in the transit profile (e.g. Rabus et al., 2009), although for a heavily spotted photosphere it could appear as stochastic variations or noise depending on the spot pattern. The effects of spots on a transit are shown in Figures 1.9 and 1.10, the former an illustration of how spots can effect transit profiles, the latter a plot of a real transit for the planet COROT-2b showing variations due to real star spots (Silva-Valio et al., 2010). Observations and modelling by Barros et al. (2013) of the transit of the hot Jupiter WASP-10b orbiting its K5V star show that transit-timing variations (TTVs) suspected to be induced by perturbations by an additional, small planet in a resonant orbit are actually the results of spot occultation. Such TTVs can appear, for example, due to a planet transiting a spot near the stellar limb as the planet egresses causing the flux to increase earlier than expected. A proper assessment of the spot coverages, sizes and distribution expected across the spectral types can therefore inform us of the expected level of distortions expected in transit shapes and lead to a more informed constraint on planet size and orbital configuration.

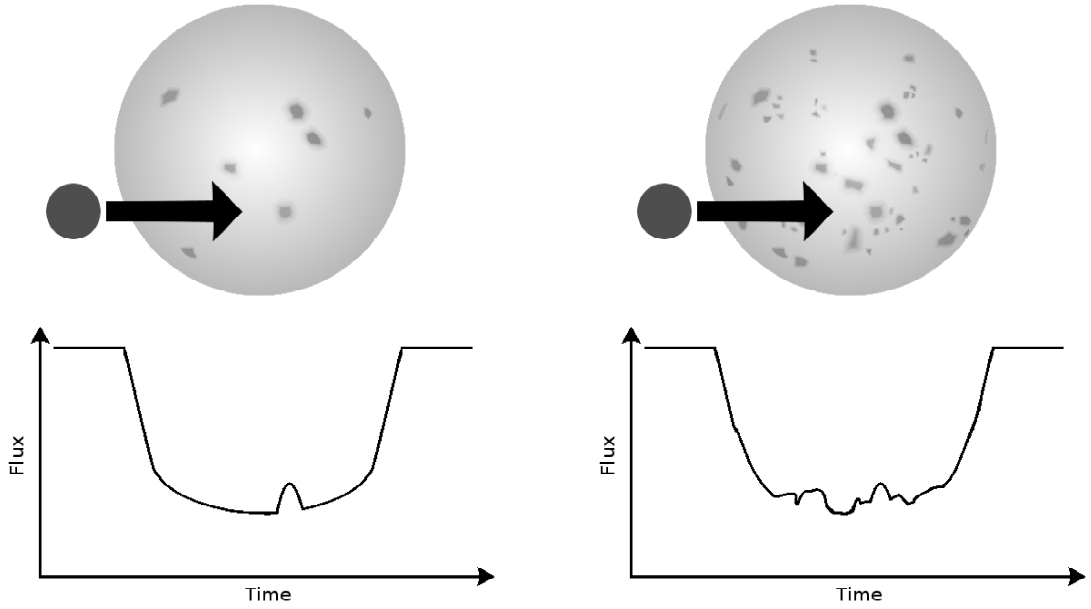

FIGURE 1.9: Illustrative cartoons of the effects of, in the first example, a planet occulting a single spot on a star, and in the second example, a planet occulting multiple spots of varying size on the star. In these examples it is assumed that the transit duration is much smaller than the rotation period of the star. As the planet begins to occult a darker area of the photosphere it ceases to occult a brighter area of the photosphere, decrease the overall depth of the transit as the net flux received from the star increases. Spots on the stellar limb similarly have the effect of changing the slopes of the transit profile. Over multiple transits, assuming the spot pattern changes with respect to the angle of observation and time, these effects would result in an apparent systematic noise and reducton in the depth of the transit, impeding planetary parameterisation.

Ballerini et al. (2012) show the necessity of multi-band transit photometry in order to alleviate the impact of spots on transit morphology due to the dependence of colour variability on photospheric spots. They model the relative change in flux in visible and infra-red bands with respect to the spot filling factor to show that in cases where the cadence of a transit survey is not sufficient to show discrete features associated with individual spots in a transit profile (under the assumption the spots are small and uniformly distributed) the true planetary radius given any filling factor can only be found through simultaneous multiband photometry.

Observations of spots occulted by the transiting hot Jupiter Kepler-17b are used

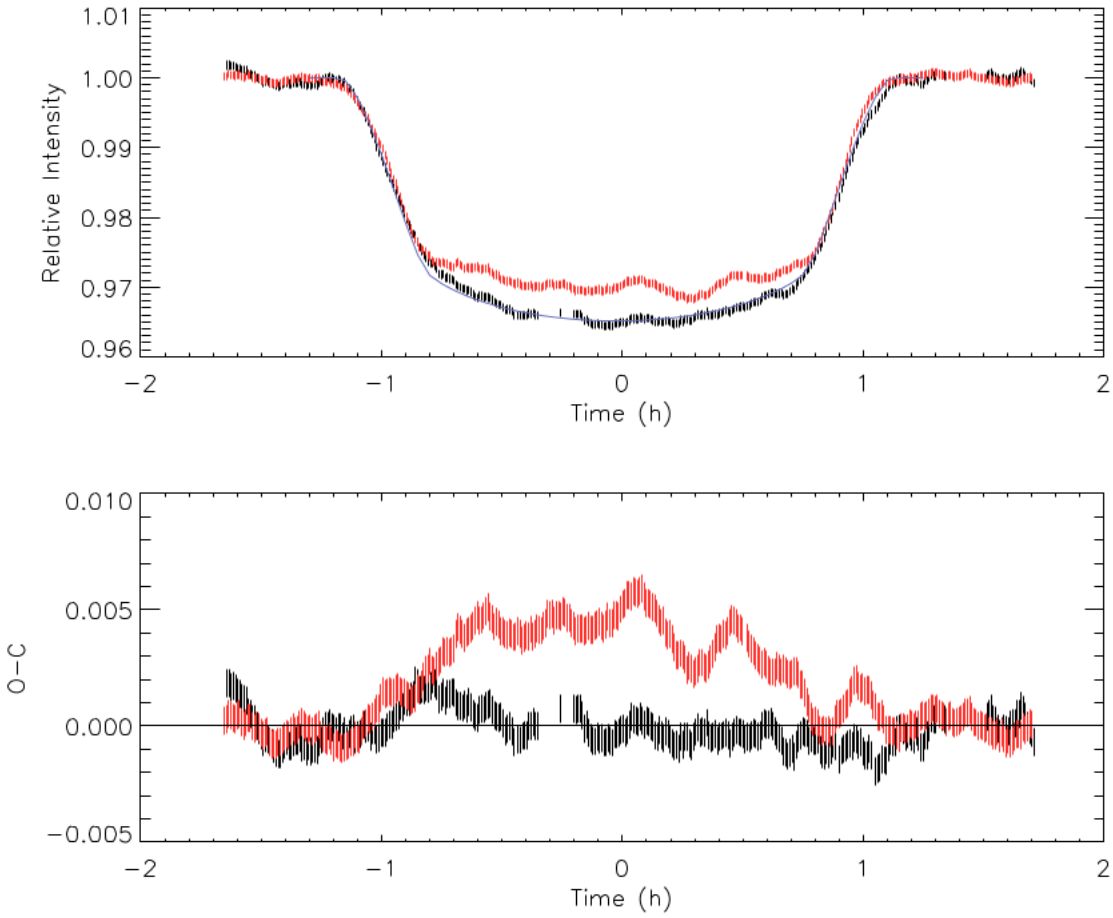

Figure 1.10: Light curves of the hot Jupiter COROT-2b transiting the young G7V star COROT-2 from **?**. The black points are from a transit at a time when the star is minimally spotted atr the transit latitude and the red points are from a typical transit. The lower panel shows the residual light curve of the data with a model transit subtracted. The spottedness for the star at the transit latitudes is found to be 10-20%.

by Désert et al. (2011) to constrain spot lifetimes on the G2V star to at least 100 days as the 5 detected spots persist throughout observations. In instances such as these, it is possible to predict when a spot will affect a transit, although in cases where there is a large angular offset between the orbital inclination and the equatorial plane of the star, such as in the case of HAT-P-11b as discussed by Winn et al. (2010), a transiting planet and spot will rarely intersect repeatedly. Llama et al. (2012) have shown, through modelling, that is ispossible to use changes in transit shape due to spots to map variations in the spot distribution in the case of rapid and solar-like rotation. This would enable reconstructions of solar butterfly-like diagrams for spotted stars from

3.5 years of Kepler observations. Assuming planets orbiting M dwarfs are detected by Kepler systems where such observations of spot distortions in transit can be made they will provide a useful accompaniment to direct Doppler imaging of spotted M dwarfs in informing the general picture of M dwarf spottedness and magnetic activity.

The activity of M dwarfs is also an important consideration for radial velocity detections of orbiting planets. Barnes et al. (2012) show that radial velocities measured at the reddest visible and NIR wavelengths with precisions of $<10\mathrm{ms}^{-1}$ are presently achievable, sufficient to detect super Earth mass (1-2 $\mathrm{M}_{\oplus}$) planets in M dwarf habitable zones assuming moderate rotation (assuming ≤ 50 epochs of observations). At these precisions spots can greatly effect the number of observations required to detect a planet. Barnes et al. (2011) model spotted M dwarfs and determine the RV variations expected at different levels of spottedness considering different $v\sin i$ and values of T_s/T_p at different wavelengths. Both the temperature contrasts and spot coverages can result in a planet being undetectable, even after hundreds of observations, i.e. moving from $\sim$10% spot coverage to $\sim$60% coverage can render a planet that could be detected with 50 observations to being undetected after hundreds of observations. The work also shows how even moderate rotation can rapidly decrease the efficiency at which detections can be made.

1.4 Summary and aims

Partially radiative low-mass stars possess a tachocline and are thought to have solar-like dynamos with a poloidal and toroidal component. They are predicted to have high latitude spots for faster rotation rates. This is the case in many observed stars, although some partially radiative M dwarfs show spots distributed across all latitudes. Fully convective M dwarfs are observed to have strong, dipolar fields or distributed toroidal fields, and modelling suggests they are capable of holding both. Like partially radiative stars, the few Doppler images of fully convective stars indicate that at least in terms of large, resolvable spots, both distributed and polar spot coverages can be formed.

The distributions of sunspot parameters are well characterised and can help inform the characterisation of spots on other stars. The inability to resolve small spots and magnetic fields through (Zeeman) Doppler Imaging currently means the true spot distributions of other stars can only be inferred from other techniques, like TiO band analysis for stars earlier than M, Doppler imaging and light curve analysis and modelling. Although Doppler imaging for early M dwarfs has provided some key benchmarks for the overall spot distributions for these spectral types, there is a lack of Doppler images for any star later than M4V.

Models of spotted M dwarfs can place constraints on the spots of M dwarfs through both analytic modelling and Monte Carlo simulations, although more work is needed to be done to understand the effects of spot size distributions and the evolution thereof on light curves. It is clear that only a minority of M dwarfs are periodically variable while a much larger fraction of them express changes in magnitude akin to white noise. Thus far M dwarf variability has been little observed in the near infra-red. The WFCAM Transit Survey (WTS) has produced light curves for thousands of M dwarfs for three years and presents an opportunity to investigate the variability of M dwarfs over a longer time scale than has so far been conducted with aims to expand the number of known long-period M dwarfs and to detect large scale changes in the spotted surface coverage.

In Chapter 2 the means of selecting M dwarfs from their colour indexes and then selecting the periodically variable M dwarfs among them using periodograms is described. In Chapter 3 the observed variable M dwarfs are discussed including trends with spectral type, period, and amplitude, as well as new and novel examples of stars exhibiting evolving spot patterns. In Chapter 4 simulations to determine the sensitivity of the periodograms to varying periods and amplitudes are described. Simulations are then used to determine the nature of the spot distributions on the M dwarfs, to show how an evolving spot coverage can generate some of the light curve morphologies observed in WTS and Kepler.

2

Detection of Variable M Dwarfs

This chapter is composed of work published in "J-band Variability of M Dwarfs in the WFCAM Transit Survey", Goulding et al. (2012). Work presented pertaining to the selection of MV type stars was also used in contribution to the co-authored papers "Four ultra-short-period eclipsing M-dwarf binaries in the WFCAM Transit Survey" (Nefs et al., 2012), "Discovery and characterization of detached M dwarf eclipsing binaries in the WFCAM Transit Survey" (Birkby et al., 2012), "The first planet detected in the WTS: an inflated hot Jupiter in a 3.35 d orbit around a late F star" (Cappetta et al., 2012), and "WTS-2 b: a hot Jupiter orbiting near its tidal destruction radius around a K-dwarf" (Birkby et al., 2013, in prep) for the purpose of planetary transit and eclipsing binary candidate prioritisation.

2.1 Chapter Overview

The sources detected within the entirety of the WFCAM transit survey are selected on the basis of being bright, point-like sources. By making use of cross matched magnitudes of the Sloan Digital Sky Survey (SDSS) with the WTS observations the luminosity class and spectral type of the stars in the sample are found. A Lomb-Scargle periodogram is conducted on each of the late-type main-sequence stars in the sample to produce a final sample of periodically variable M dwarfs.

2.2 The WFCAM Transit Survey

Utilising the Wide Field Camera (WFCAM) on the UK infra-red Telescope (UKIRT), the WFCAM Transit Survey is a near infra-red survey designed for the detection of planets transiting M dwarfs. The survey was proposed by Pinfield (2007), and first described by Birkby (2010) with the first results published by Nefs et al. (2012), where the survey is first described in the literature. WTS is described in full by Kovács et al. (2013). The survey is complimentary to other contemporary transit surveys such as Corot and Kepler that target earlier main-sequence stars, with additional science goals of studying M dwarf variability, and detecting low-mass eclipsing binaries, Kuiper Belt objects, and high proper motion white dwarfs.

WFCAM's detectors are four 2048 × 2048 18μm HgCdTe Rockwell Hawaii-II infra-red detectors, each covering 13.65 × 13.65 arcmin^2 with a resolution of 0.4 arcsec pixel^{-1}. The light curve observations are made in the J band with single deep exposures additionally made in the $ZYJHK$ bands. The J band is used as this is near the location of the peak of the spectral energy distribution for M dwarfs, as shown in Figure 2.2. An M4 star is approximately 4 times brighter in J than in the V band. As shown by Ballerini et al. (2012) the ratio of the brightness between spotted and unspotted photosphere is also greatly reduced in the J band. While this is undesirable from the perspective of studying spots, it can partially mitigate the degree of obfuscation of transit signals due to spots. The sensitivity to spots in the WFCAM transit survey is

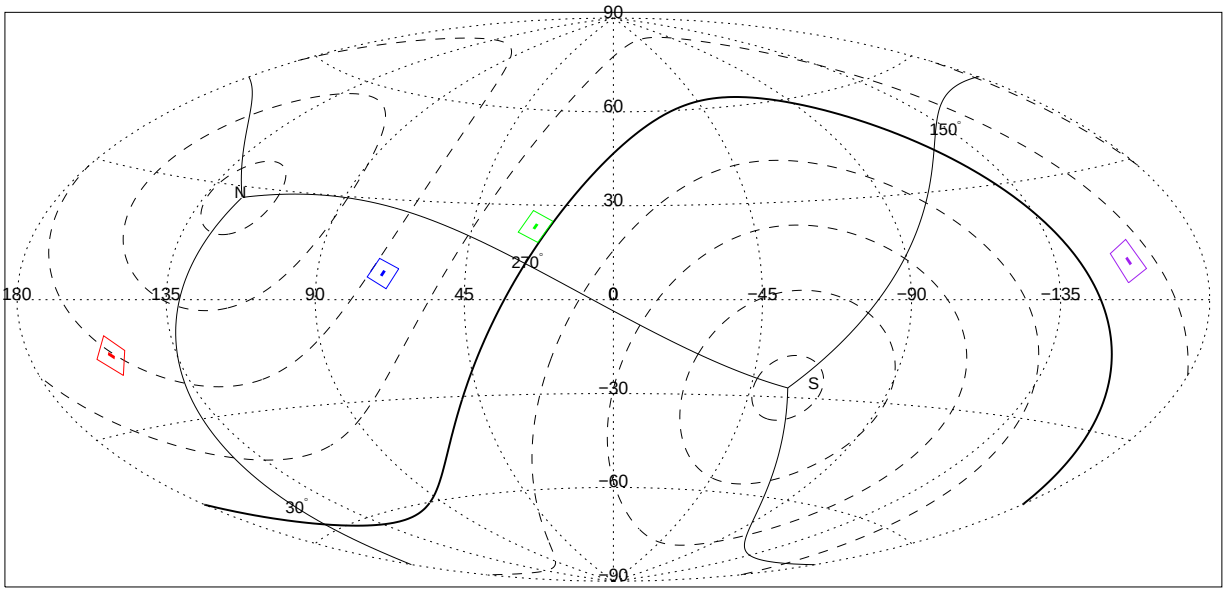

Figure 2.1: The WTS fields in Galactic coordinates with transformed celestial coordinates also shown. The 03hr, 07hr, 17hr and 19hr fields are covered by the red, purple, blue and green polygons respectively, surrounded by boxes to highlight their positions.

discussed in Chapter 4.

Four fields, the 03hr, 07, 17hr and 19hr fields, were selected, each 1.5 degrees^2, shown in Figure 2.1. Fields were selected to be outside (but still close to) the galactic plane, so as to reduce overcrowding and reddening in the fields, and to detect a high ratio of dwarfs to giants (Kovács et al., 2013). Each field is observed in eight pointings labelled a to g, each pointing itself being composed of the paw print from the four detectors labelled 1 to 4, such that an object observed is labelled, for example, 19b_3_23134, where the latter number is unique to each observed object on that detector. The data reduction is performed by the Cambridge Astronomical Survey Unit (CASU) pipeline and aperture photometry is used as described by Irwin et al. (2007) to derive the magnitudes constituting the light curves. The photometry is capable of $\sim$1% precision at J=16 and $\sim$0.25% at J =12, with saturation occurring at brighter magnitudes. The target number of epochs per field was 1000 and, as of the time of writing, this number has been reached for the 19hr field. Thus far there are two planet detections, WTS-1b, an inflated 4.01$\pm$0.35 M$_J$ hot Jupiter in a 3.35d orbit around an F7$\pm$1V type star Cappetta et al. (2012) and WTS-2b, a 1.12$\pm$0.13M$_J$ hot Jupiter in

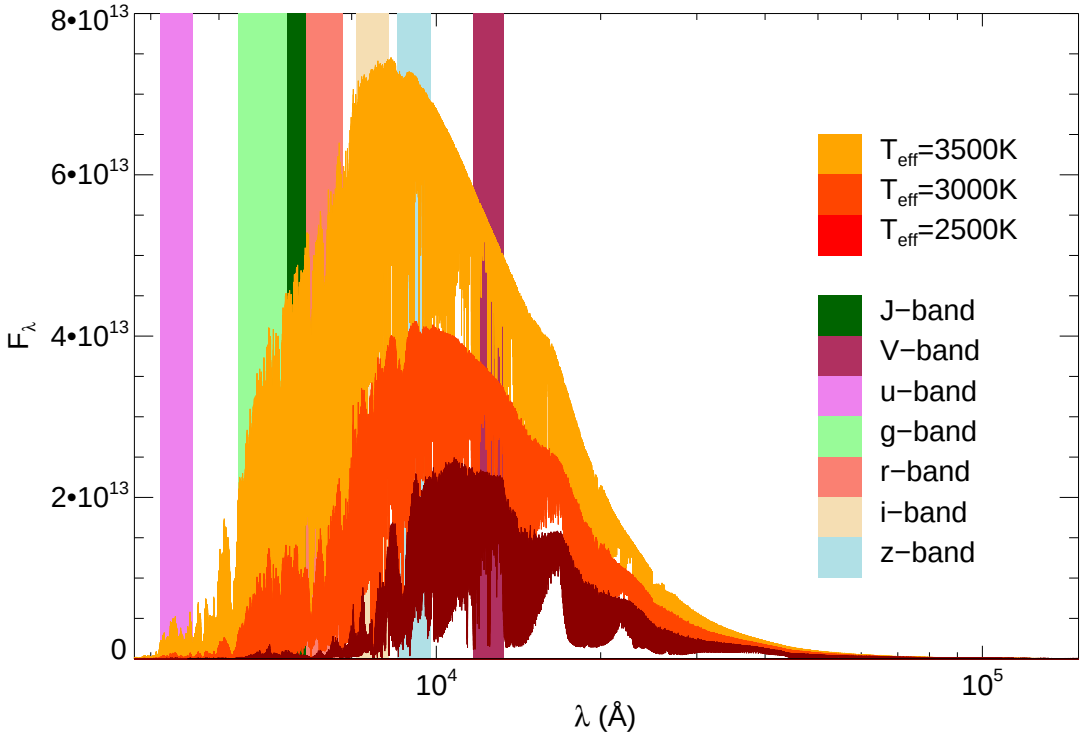

FIGURE 2.2: Synthetic spectra from Allard et al. (2012) for main-sequence stars of T_{eff} =2500K, 3000K and 3500K, approximately corresponding to spectral types M7V, M4V and M1V respectively. The peak of the SED approaches the J-band for later spectral types, where the J-band flux far exceeds that in the V-band.

a 1.02d orbit around a K2±2V star Birkby et al. (2013, in prep).

Although observations in the J-band are not optimised for spot detection, the long baseline of observations means WTS should be capable of detecting M dwarfs with periods of months such as those found by Irwin et al. (2011), and should be sensitive to detecting M dwarfs with periods corresponding to ages up to the Hubble time. The number of M dwarfs in WTS should provide a substantial addition to previous samples of variable M dwarfs, such as those presented by Irwin et al. (2011) and Kiraga & Stepień (2007). M dwarf photometric variability has thus far not been as extensively characterised in the near infra-red as it has at visible wavelengths. M dwarfs with varying amplitude light curves and morphologies should be found and the long baseline should be capable of detecting changes on time scales yet to be observed. The change in ratio of visible to infra-red fluxes with increased spot coverage (see Figure

3, Ballerini et al., 2012) indicates that the V band is more sensitive to spots than J, and as such the maximum amplitudes found should be less than those found at shorter wavelengths (e.g. Messina et al., 2011). This also means that WTS is less sensitive to lightly and moderately spotted M dwarfs and thus the fractions found may be smaller, although the same trends of decreasing maximum amplitude for later spectral types should be found. From $v\sin i$ and previous light curve surveys it can be expected that the fastest rotators are of a later spectral type and the dispersion of rotation periods increases with spectral type. WTS is sensitive to periods of potentially hundreds of days and provides a rare opportunity to discover long-period M dwarfs and populate a currently sparsely studied space.

2.3 M Dwarf Selection

The full WTS data set represents a total of 1,043,129 sources. The breakdown of source numbers per field can be found in Table 2.1. In order to make the search for variable M dwarfs in the WTS observations an efficient process, various sources that were not of interest or use are removed, as outlined in the following sections.

2.3.1 Initial Cuts

The initial step to greatly reduce the number of objects that would make for inappropriate targets for a variability search is to remove those where the random noise in the light curves occurs on a scale that inhibits the ability to detect any variable signal. As the noise increases as a function of magnitude (see Figure 3.1) this entails determining the minimum brightness at which it is possible to reliably detect a periodically variable signal by means of the method described in Section 2.4. As discussed in Section 1.2.2, variability found in the V band has an amplitude typically much less than 0.3 mag Messina et al. (e.g 2011) and J band amplitudes of variable M dwarfs will be less than this. Therefore sources fainter than the corresponding $J = 17.5$ were removed from the sample as at this point possible amplitudes for variable M dwarf will be less than

Field	No. of sources	$J < 17.5$	$J < 15$	Unblended	Retained sources
03hr	164235	25676	5131	140991	16845
07hr	201084	36311	7056	168919	23136
17hr	216102	26949	4355	184638	16923
19hr	461708	119522	17601	329296	59460
Total	1043129	208458	34143	208458	116364

TABLE 2.1: List of the number of sources, including number of sources where the J-band magnitude is less than 17.5, and where the J-band magnitude is less than 15. The retained sources are those for which $J < 17.5$ and are flagged as unblended, and these are the objects that are subject to the spectral typing procedures described in Section 2.3.3.

the scale of the noise in the light curve. A complete analysis of the effects of the random noise in each magnitude bin is detailed in Section 4.1. The number of remaining sources per field is shown in Table 2.1, as is the number of sources where $J < 15$ for comparison.

The data reduction pipeline flags sources that appear to be blended, and these blends were removed from the sample as it would not be possible to precisely determine the nature of any of the objects comprising the blended source, and the number of these found in the full sample is shown in Table 2.1.

The process of removing these faint or blended objects leaves a total of 116364 sources with light curves observed by WTS.

2.3.2 main-sequence Star Selection

After magnitude and blended-source cuts, the data still contain objects yet to be confirmed as stellar, such as galaxies or observational artifacts. Objects that are not main-sequence stars must next be removed. In order to do this the sample of objects is first cross matched with the Sloan Digital Sky Survey Data Release 7 (DR7) catalogue (Abazajian et al., 2009). The coverage of the SDSS extends only to the 03hr, 07hr and 19hr WTS fields.

The cross match was done by means of an SQL query selection of the nearest star observed in the SDSS within 0.5 arcminutes of the object observed in WTS, where

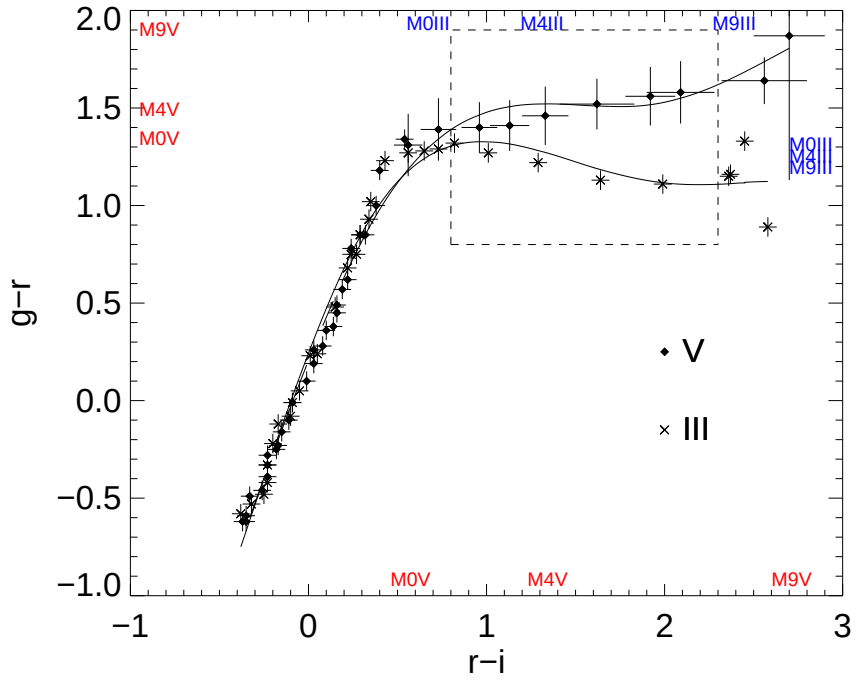

Figure 2.3: A plot of SDSS $r-i$ versus $g-r$ with the useful region, where the dwarf (diamonds) and giant (crosses) colour sequences diverge, is indicated by the dashed box. The solid lines are the spline fits to each sequence. The blue limit is set at the value of $r-i$ corresponding to M1V as at blue colours the dwarf and giant fits converge, althought there is likely some degeneracy still in this region due to the larger error bars on the main-sequence series, although the effection should be small due to the robustness of using multiple colours. While the spline fits are separated by 0.5 in $g-r$ in the red end, the dispersion of the giant colours here warrants curtailing the useful region (at ≈M6V) so as not to erroneously identify any giant stars lying between the two sequences as belonging to the main-sequence.

the difference between the WTS $Z-$band magnitude (882 nm) and the SDSS $z'-$band magnitude (905 nm) is less than 0.1 mag to reject false matches. Objects flagged by the SDSS pipeline as being galaxies are also removed from the sample. The 03hr, 07hr and 19hr fields fully overlap with SDSS observations, and $\sim 96\%$ of the $J<17$ objects have corresponding SDSS magnitudes, whereas the 17hr field is not covered by SDSS (see Section 2.3.4), and a spectral type was only assigned to those with SDSS observations.

As the aim is to obtain a pure sample of M dwarf stars on which to conduct a variability search, the primary concern is to eliminated as many potential interlopers as possible. Here the work of Covey et al. (2007) who make use of the solar metallicity spectral standards as determined by Pickles (1998) is used to ascertain the colours of

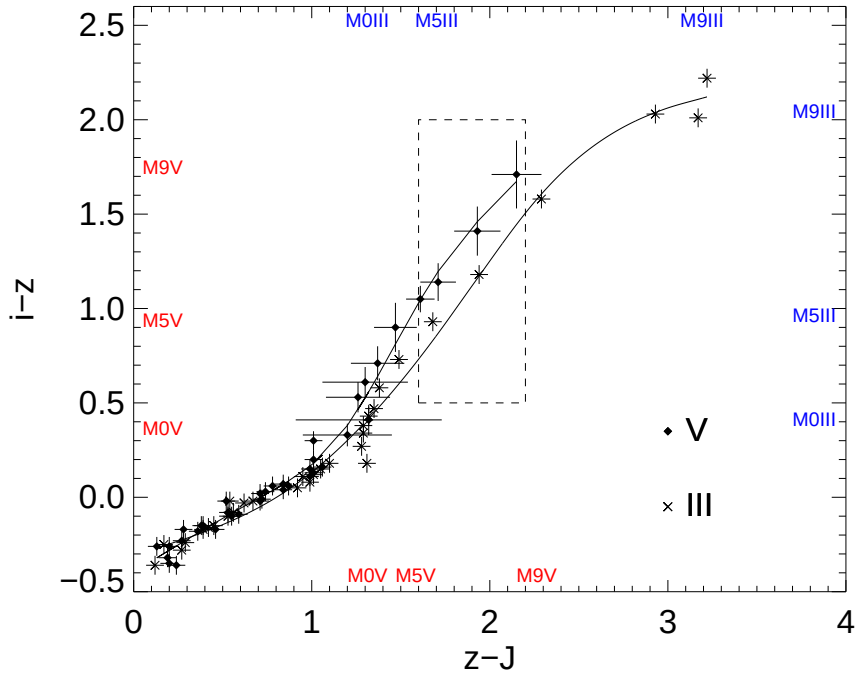

FIGURE 2.4: As with Figure 2.3; a plot of SDSS and 2MASS $z-J$ versus $i-z$. The useful region is narrowed by the redder point of divergence between the sequences and the termination of the dwarf sequence at a bluer colour than the giant sequence. Whilst the two sequences lie close in colour space with a difference of 0.3 in $i-z$, meaning faint objects with large error bars will be identified as being ambiguous, the sequence still allows for positive identification of brighter stars.

main-sequence and giant stars across the spectral types from O5V to M6V and from O8III to M10III. The colour sequence for dwarf stars is extended to M9V by use of the median colours of late M dwarfs as found from 70841 spectroscopically identified M dwarfs by West et al. (2011).

In order to make make use of techniques employed in the literature for stellar identification, it is necessary to convert from the Mauna Kea Observatory (MKO) system to the Two Micron All Sky Survey (2MASS) system using the empirical relations described by Hodgkin et al. (2009):

$$J_W = J_2 - 0.065(J_2 - H_2), \tag{2.1}$$

$$H_W = H_2 + 0.07(J_2 - H_2) - 0.03, \tag{2.2}$$

$$K_W = K_2 + 0.010(J_2 - K_2), \tag{2.3}$$

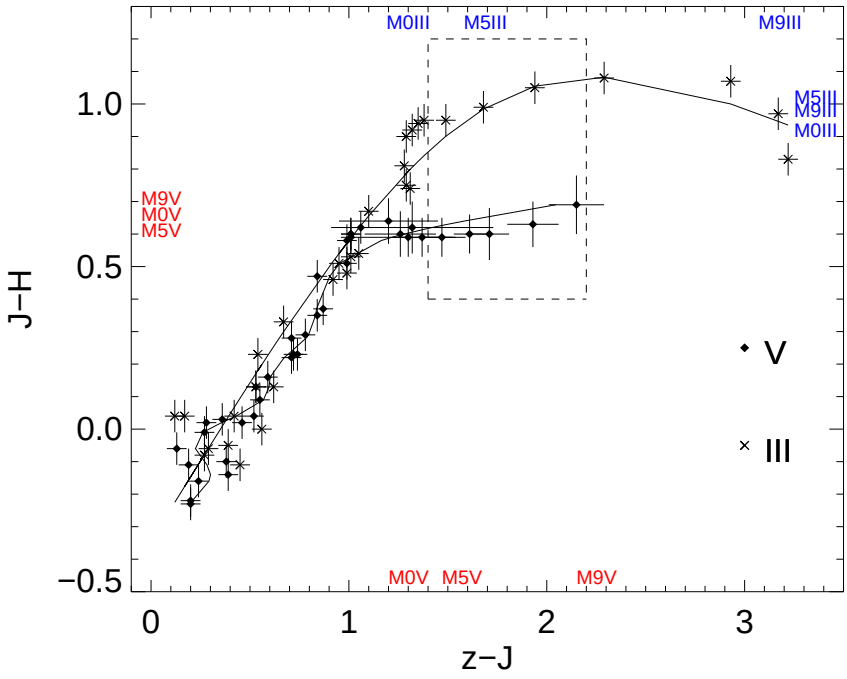

Figure 2.5: As with Figure 2.3; a plot of SDSS and 2MASS $z-J$ versus $i-z$. The two sequences diverge rapidly for $z-J>1.3$ with M dwarfs appearing bluer than M giants of equivalent subtype in $J-H$, and with the M dwarfs series terminating at bluer values of $z-J$.

which can be rearranged to give:

$$J_2 = 1.064J_W - 0.074H_W - 0.002, \tag{2.4}$$

$$H_2 = 1.070H_W - 0.080J_W + 0.032, \tag{2.5}$$

$$K_2 = 0.990K_W - 0.010J_2, \tag{2.6}$$

where W suffixes WFCAM magnitudes and 2 suffixes 2MASS magnitudes.

Each bright, point like WTS source now has *ugriz* SDSS magnitudes and equivalent 2MASS JHK_S magnitudes. On SDSS/2MASS $ugrizJHK_S$ colour-colour diagrams, as presented by Covey et al. (2007), the loci of main-sequence and giant stars are discernible enough to fit discrete tracks. The relative positions of each WTS star to these tracks are used to estimate whether a star is on the main-sequence or not. Regions where the tracks are discrete are found on plots of the colours of consecutive passbands: $r-i$ versus $g-r$, $z-J$ versus $i-z$, $J-H$ versus $z-J$, $H-K_s$ versus

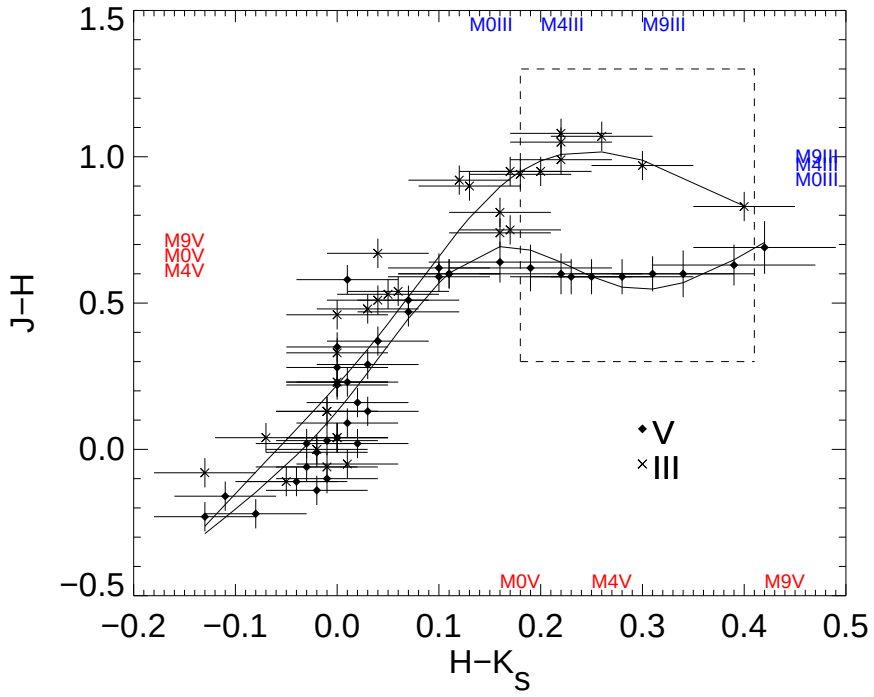

FIGURE 2.6: As with Figure 2.3; a plot of SDSS and 2MASS $z - J$ versus $i - z$. As with other colour-colour relations, the two sequences digress from their degeneracy from one another for redder colours.

$J - H$; additionally colours of wider baselines were used: $i - K_s$ versus $g - i$, $r - z$ versus $J - H$. These colour-colour relations are plotted in Figures 2.3 to 2.8. The use of multiple colour-colour plots allows for greater robustness in the identification, in particular where the trends for giants and dwarfs are more divergent at the red end of the trends where it is necessary to distinguish between M dwarfs and M giants.

Cubic splines are least-squares fitted to each of the trends to create fits for giants and dwarfs in colour-colour space using seven knots. An area where the fits are divergent is chosen, generally corresponding to the stars of spectral types M. The areas, as indicated by the boxes on the figures, are limited in the x direction by the approximate point of divergence of the colour series in the blue and either by the termination of a series or increasing degeneracy in the red end. In the y direction the boundaries are effectively arbitrary and are set so as to contain the stars to be typed. A quantified comparison between a star's colours and the interpolated equivalent colours on the dwarf and giant tracks in each diagram can then be made by finding the residuals of

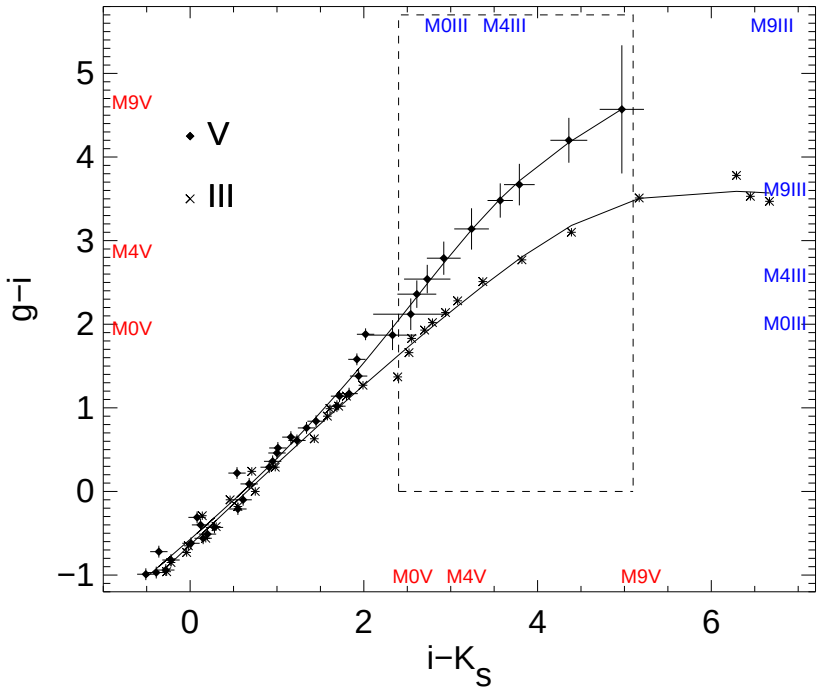

FIGURE 2.7: As with Figure 2.3; a plot of SDSS and 2MASS $z - J$ versus $i - z$.

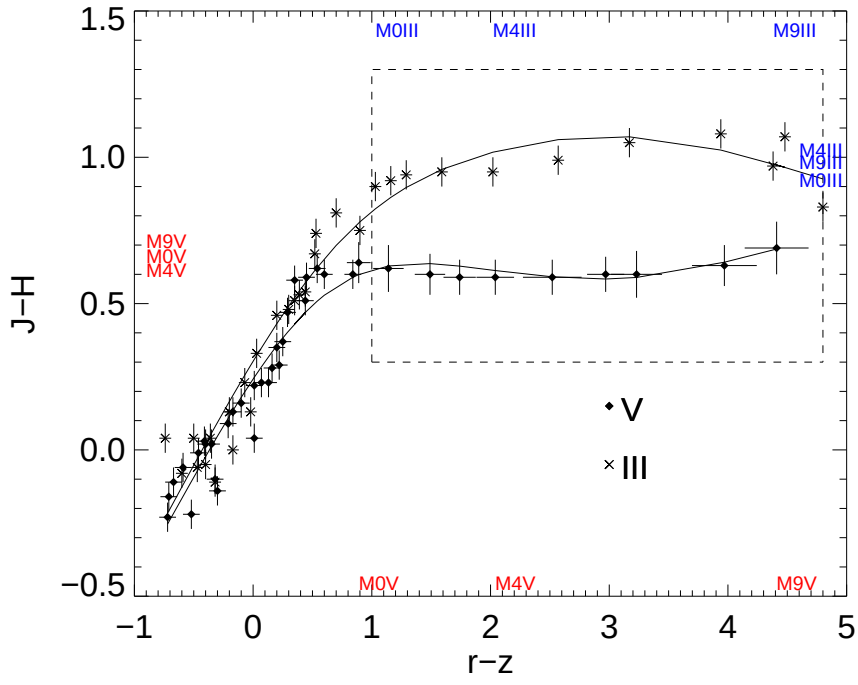

FIGURE 2.8: As with Figure 2.3; a plot of SDSS and 2MASS $z - J$ versus $i - z$.

a star from each track. A star's separation in colour space from each track is found and divided by the 2σ error on the star's colour index to identify which track a star lies closest to. Stars that lie within 2σ of one of the spline fits are assigned as being a dwarf or giant, respectively, whereas all other stars are flagged as being ambiguous under that colour-colour regime. The modal identification from the comparisons with the seven colour-colour relations is found giving each star an overall categorisation as either dwarf, giant or ambiguous. Using colours from across the visible and NIR bands increases the robustness of the identification beyond that which could be obtained from a single colour-colour relation, as well as increasing the number of stars whose spectral types can be identified. As most stars occupy a degenerate position on the tracks this serves primarily to eliminate any star from the sample that can be positively identified as being a giant. 5.6% of the stars are identified as being giants and are removed from the sample.

2.3.3 Spectral Type Selection

The spectral types of the majority of stars in the WTS data are unknown. Although colour cuts, which are latterly used, have shown to be a useful tool for extracting samples of M dwarfs while eliminating sources of contamination (Plavchan et al., 2008), an estimation of spectral subtypes is preferential for analysing relations between spectral type and other parameters. Spectral classifications using colour-spectral type relations to identify the WTS M dwarfs are therefore made. For the process of selecting M dwarfs from the sample a method similar to that used by Kowalski et al. (2009) is implemented. Covey et al. 2007 find the location of main-sequence stars across the Morgan-Keenan spectral types from near infrared 2MASS JHK_s and visual Sloan Digital Sky Survey (SDSS) *ugriz* photometry. They find the median position of stars across spectral type O to M for main-sequence, giant and supergiant stars in a 7 dimensional colour space and the relationship between spectral type and colour. Using these relationships it is possible to estimate a spectral type for any given star providing it is observed in SDSS.

Hawley et al. (2002) discuss the usefulness of SDSS and 2MASS colours from $rizJK$ magnitudes as spectral type diagnostics. While $r-i$ does not perform well as an indicator of spectral types later than M8 due to degeneracies with the increasingly blue early L dwarfs, $i-z$ and $z-J$ allow for discrimination between late M and early L subtypes, and conclude that combinations of optical and near-infrared photometry suffice for the identification of low-mass dwarf spectral types. The colour indices therefore used to identify the M dwarfs and the subtypes thereof in the WTS are the consecutive $r-i$, $i-z$, and $z-J$ (e.g. Figure 2.3.3); other SDSS and 2MASS colours being either too metallicity dependent or having too large uncertainties. Indeed, ugr photometry has been shown to be an estimator of metallicity (Ivezić et al., 2008) and thus if a metallicity dependency exists for these bands it is prudent to minimise potential sources of dispersion in the colour-spectral type space by utilising only the riz SDSS magnitudes.

The method for finding the spectral type is similar to that used to find the luminosity class, where smoothing splines were fitted to the colour index-spectral type relations and a spectral type for each star in the sample is found by interpolation. The mean and standard deviation of the spectral types interpolated for each colour index give an estimation for spectral type and error in spectral type of each star in the sample. Because of the continuous nature of output interpolated spectral types, the types were rounded to the nearest subtype.

2.3.4 Additional Colour Cuts

In their selection of a sample of M dwarfs using data from the 2MASS, Plavchan et al. (2008) make use of a series of colour cuts to remove contamination in the form of reddened background sources and M giants. Although the WTS fields were chosen to minimise such contamination, to further ensure the sample contained no such contaminants, these colour cuts are applied to the sample of stars to further identify and remove any potential contaminating objects.

One constituent field of the WTS, the 17hr field, was not observed in the SDSS, and therefore spectral sub-type estimates are not made, although a variability selection described in the following section is made for the reddest stars at $H-K>0.175$

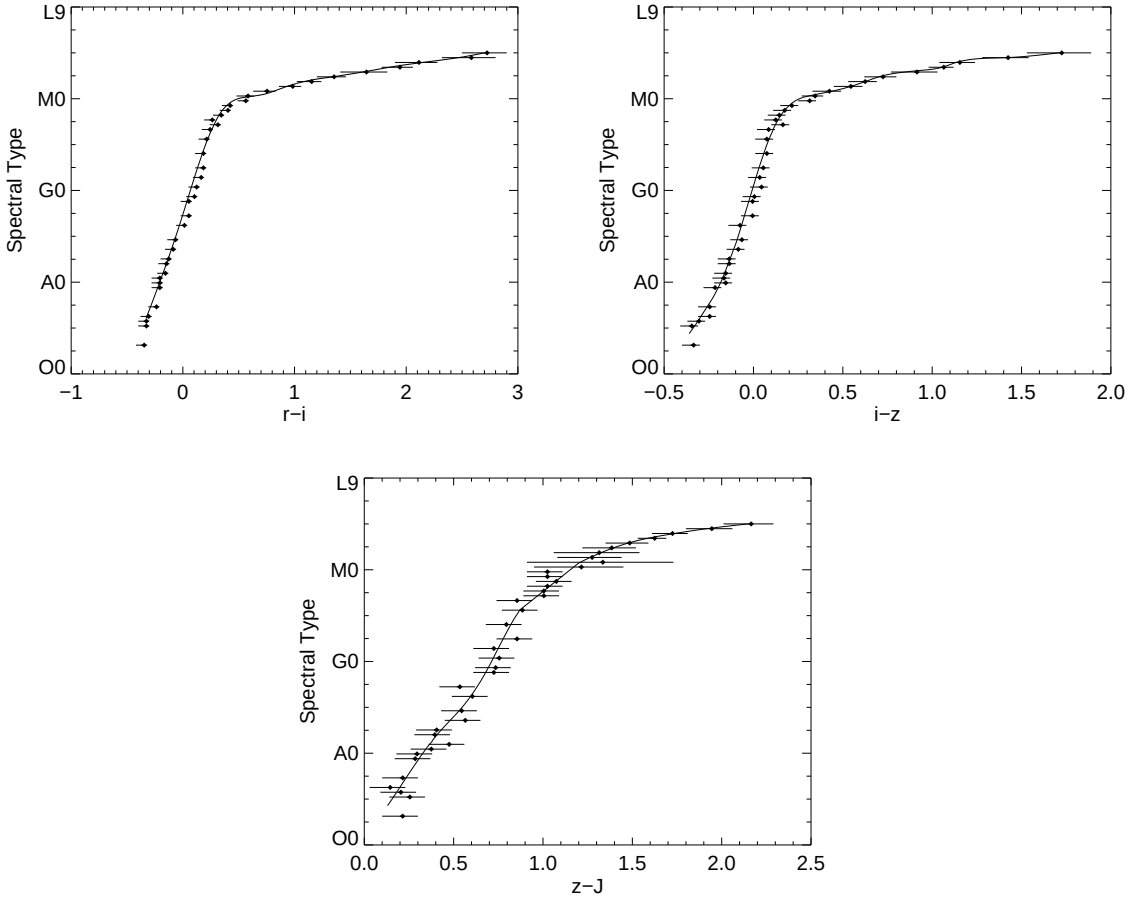

FIGURE 2.9: The colour-spectral type relations used to estimate spectral types for the WTS sample. The points are the colour indices for types, earlier than M0 from Covey et al. (2007) and for later types from West et al. (2011) which extend the series to M10. The fitted spline was used to infer spectral types for the stars in the WTS sample.

(corresponding approximately to K7V and later), combined with other colours cuts presented by Plavchan et al. (2008) to eliminate M giants and background, reddened sources from this sample. While sources from this field are also included in the variability search, they therefore are only identified as being M dwarfs, with the sub-type unknown.

2.3.5 M dwarf Identification

To assess the reliability of the classification of M dwarf subtypes using the colour-spectral type relations, the method is applied to 44084 low-mass dwarfs of known

spectral types from catalogues published by West et al. (2008). Figure 2.10 shows that the match between the estimated spectral type and the spectroscopically determined spectral type follows a 1:1 relation with an error of approximately ±1 sub-type.

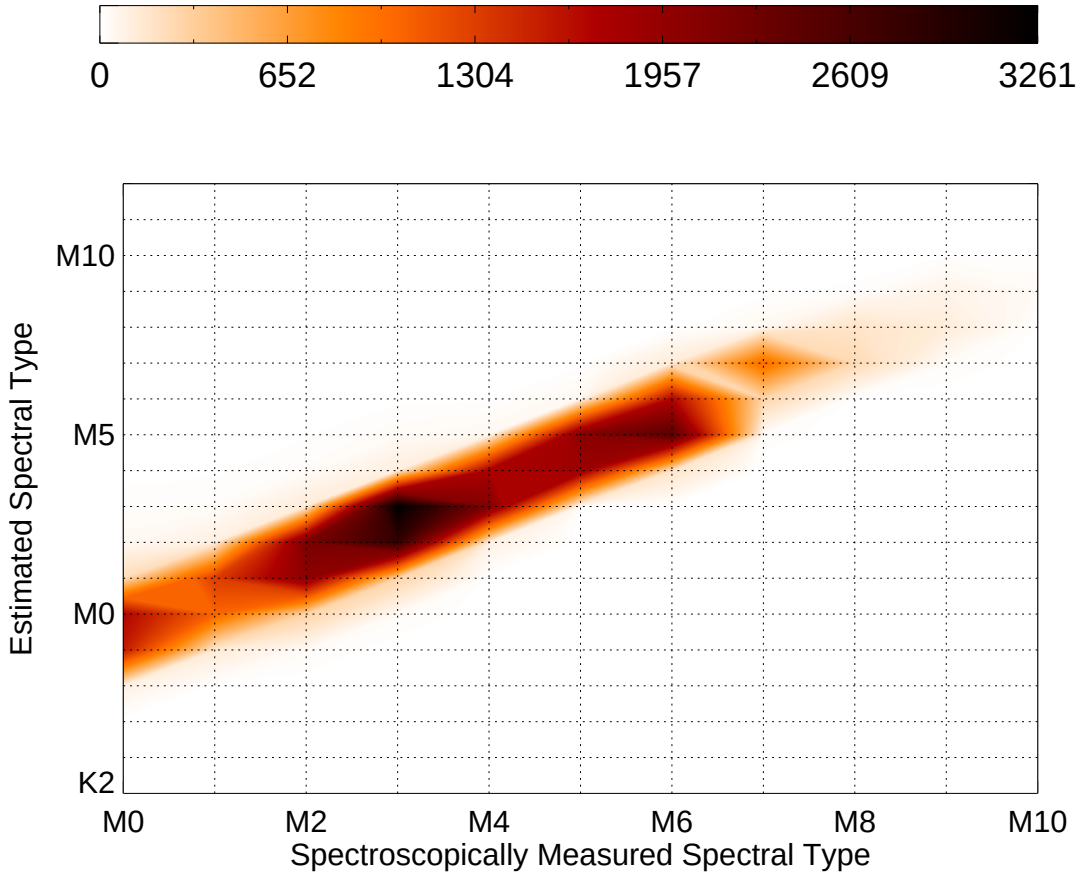

Figure 2.10: A 2-D histogram of the spectral types of known M dwarfs versus the spectral types found from the methods presented here, showing the accuracy of our spectral typing is $\sim \pm 1$. A bin size of one sub-type is used. The colours from white through to black indicate the number of stars.

For later spectral subtypes the identification method did not perform as well, estimating a spectral type $\sim$ 1.0 subtypes earlier for M9V and 0.5 for M5V, as shown in Figure 2.11. This effect may in part be caused by the use of $r - i$ which does not perform as well as an indicator of spectral type for M6V and later (Hawley et al., 2002), as stars later than this become degenerate in $r - i$ at they are increasing blue from M8V. This effect, however, is of little overall impact as the method finds very few stars later than M5V. Some stars are assigned spectral subtypes ±5 from their true

Table 2.2: Number of M dwarfs with $J < 17.5$ found per field. In the case of the 17hr fields $H - K$ colour was used as a means of distinguishing the late type stars as this field does not have SDSS coverage, cf. ∼6600 M dwarfs found by Nefs et al. (2012) at $J < 16$ in WTS.

Field	Number of M dwarfs
03hr	5970
07hr	3061
17hr	6633
19hr	2535
Total	18199

type. While this constituted $< 0.1\%$ of the stars, it indicates that stars identified as being earlier than M0V may in fact be misidentified M dwarfs, especially if there is a large error on the spectral type as found from the colours. Therefore, all the WTS stars that fall within the colour cuts used by Plavchan et al. (2008) are included in the variability search, and the spectral type (and error thereof) estimation serves to inform the reliability that a star is indeed an M dwarf. As described in Section 2.4.2, further constraints placed on the nature of the variability found serve to provide a source of stellar identification. In other work including the identifying the spectral types of WTS stars, e.g. Birkby et al. (2013, in prep) and Cappetta et al. (2012), broad band spectral energy distribution fitting is used to estimate T_{eff} for candidate planet hosts and eclipsing binaries (EBs) using, SDSS and UKIRT bands (as also used here). The estimates of T_{eff} for these stars typically have errors of one to several hundred K, or $0.5 - 1$ spectral subtypes, and thus do not yield significant gains in accuracy over the methods used here.

The majority of the stars found by the aforementioned methods are of spectral type MV4 and earlier (Figure 2.12). This can be accounted for by the luminosity function of low-mass stars in the galactic disk. The luminosity function of M dwarfs peaks at $M_r \approx 11$ (Bochanski et al., 2011) which corresponds approximately to M3V-M4V (Bochanski et al., 2010). The breakdown of stars per spectral type found in the three fields with SDSS coverage is shown in Figure 2.12. The results of the spectral typing reveal in total 15664 stars identified as M dwarfs from the 03hr, 07hr and 19hr fields. In addition 2535 that were sufficiently red in $H - K$ were selected, as shown in Table 2.2, giving a total of 18199 stars subject to the variability search described in Section 2.4.

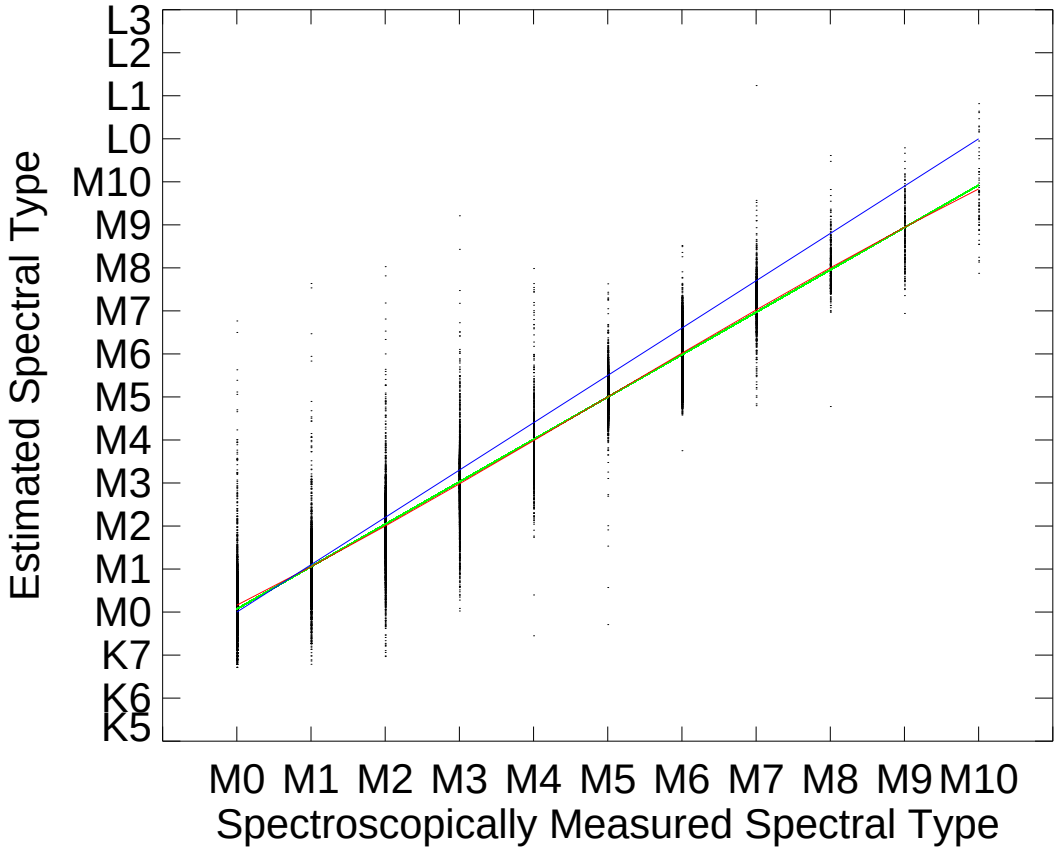

Figure 2.11: A plot of the all the estimated spectral types with a linear fit (green) and a third order polynomial fit (red). The blue line indicates where spectral type is equal to estimated spectral type.

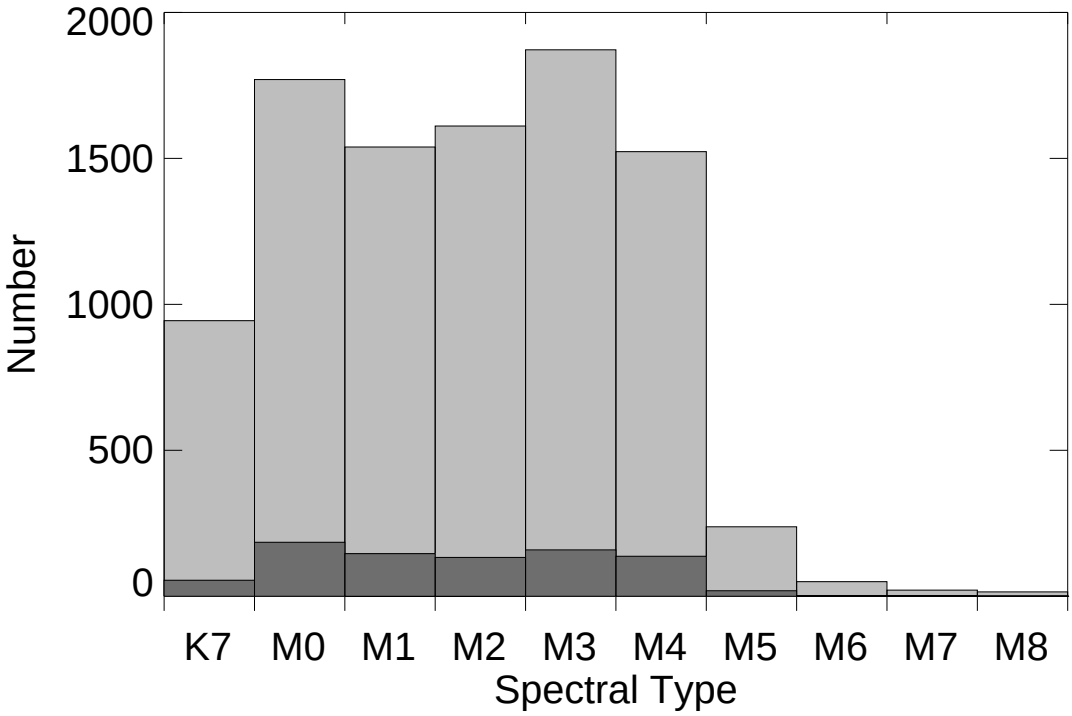

FIGURE 2.12: Histograms showing the frequency of each spectral type in the sample. The light grey represents all stars with magnitude $J<17$, the dark grey $J<15$.

2.4 Variability Selection

As discussed in Section 1.2.3, periodic variability is characterised by a repetitive change in a star's magnitude typically, to a first approximation, taking the form of a repeating function such as a sine or saw-tooth wave. Given the ubiquity of repetitive cycles in stars, from rotation periods and binarity to activity cycles and cataclysmic variation, the study of stellar variability has been a focus for research since the discovery of the periodic variability of Mira at least four centuries ago. The variability found in observations of M dwarfs takes the form of both periodically variable fluctuations in brightness and stochastic, noise-like variability (e.g. Ciardi et al., 2011). Here the aim is to detect the former of those occurring in the WTS sample of M dwarfs.

Regardless of the wavelength at which observations of variable M dwarfs are made, the morphology of the light curve variability appears as a sine curve or summation of sine curves. Methods to detect such variations in time series observations therefore usually employ some kind of fitting of sine-like functions. Such methods produce a periodogram which displays a frequency or period against a power spectrum of peaks of varying significance which can inform the process of determining whether a periodicity exists in the light curve. For evenly spaced observations, or where observations are closely enough spaced such that even sampling rates can be interpolated, the discrete Fourier transform (DFT) and fast Fourier transform (FFT) algorithms can be used to form a periodogram. This Fourier analysis is done by means of deconstructing a light curve into constituent harmonics and expressing the amplitude of these as a function of the frequency. These periodograms remain popular today after being shown to be superior to comparable methods for astronomical purposes, such as the Jerkevich periodogram (Swingler, 1989), although these still see some use in astronomy. Examples of astronomical use of Fourier analysis include the detection and Fourier synthesis of variability in the light curve of the M3$\sim$4.5I star S Persei (Chipps et al., 2004), where both DFT and FFT are used, and in the analysis of the light curve modulation of the cataclysmic variable triple star system FS Aurigae (Chavez et al., 2012). Less commonly used algorithms include AoVHarm, as implemented by Hartman et al. (2011),

and Supersmoother (e.g Becker et al., 2011), both used to select variable, low-mass stars.

One of the most popular algorithms for periodogram analysis is the Lomb-Scargle periodogram (Lomb, 1976; Scargle, 1982), which is optimised for finding sinusoidal shaped periodic signals. This efficient algorithm (e.g. Press & Rybicki, 1989) has been widely used in astronomy and implemented in FORTRAN 77, Python, IDL, C and R, as well as others, in particular for the analysis of variable M dwarf light curves (e.g. Lane et al., 2007; Frasca et al., 2009; Messina et al., 2011). It has also seen use in spectroscopic observations of M dwarfs, for example, measuring the variation in the Ca II K flux line as a tracer of chromospheric activity cycles (Buccino et al., 2011), and in determining the periods of planets by use of the radial velocity method (e.g. Dumusque et al., 2012). The periodogram calculates a normalised power spectrum across a defined range of periods and frequency intervals; the peaks corresponding to periodic variations in the light curve with varying significance. It is robust with respect to a varying amplitude in that, while a linear change in amplitude will attenuate a signal and a periodic change in amplitude will introduce a second signal, the signal corresponding to the primary variability period will still be detected.

The periodogram as defined by Scargle (1982) is:

$$P_x(\omega) = \frac{1}{2}\left(\frac{\left[\sum_i X_i \cos\omega(t_i-\tau)\right]^2}{\sum_i \cos^2\omega(t_i-\tau)} + \frac{\left[\sum_i X_i \sin\omega(t_i-\tau)\right]^2}{\sum_i \sin^2\omega(t_i-\tau)}\right), \tag{2.7}$$

where t_i is the time of a measurement, ‘ω is the frequency to be tested, and X_i is the measured variable, in this instance the magnitude of a star, defined such that:

$$X_i = X_s(t_i) + R(t_i). \tag{2.8}$$

In this case $X_s(t_i)$ is the signal to be found and $R(t_i)$ is the random observational error on the measurement, where τ is defined such that:

$$\tan 2\omega\tau = \frac{\sum_i \sin 2\omega t_i}{\sum_i \cos 2\omega t_i} \tag{2.9}$$

and is the time delay such that when the data are evenly sampled $\tau = 0$.

2.4.1 Implementation of the Lomb-Scargle Periodogram

Due to its prevalent use and previous implementation the Lomb-Scargle method is the preferred choice for the analysis of the WTS light curves, through the use of an IDL routine that allows for the calculation of a false alarm probability (FAP). The FAP threshold, as described by Horne & Baliunas (1986), is determined to enable the peaks in the periodogram to be identified with a given level of confidence and to filter out peaks that are probably caused by noise. The threshold is defined such that all peaks in the periodogram with a value greater than this value correspond to a real signal with 99 per cent confidence or better. By this means all peaks in the periodogram lower than the maximum peak obtainable from Guassian noise are discarded as they likely pertain to spurious signals. An example of the output periogogram from the Lomb-Scargle procedure used is shown in Figure 2.13.

While this method tends to reject most of the peaks as insignificant and, therefore, likely products of random errors in the measurements, a number of peaks that do not correspond to the rotation period are found. These additional peaks are the product of three phenomena: spectral leakage, aliasing with the observational period, and unknown but real sources of variation.

Although the uneven sampling of the WTS prevents aliasing on scales of less than a day, the ability to only observe the stars for a limited window once a day often results in a peak at 1 day in the periodogram. This is simply because a sinusoidal function with a period of 1 day where the point at which the sinusoid crosses the mean value of the magnitudes lies temporally at the mid point of the observations. Deviations from this that do not correspond to real frequencies in the data will have greater residuals. The significant one day periods also suffer from spectral leakage such that significant peaks will appear at n and $1/n$ where n is an integer, often but not always to 2 or 3 significant figures. Furthermore, because observations occur at a range of times during each one day observational period, these peaks corresponding to the observation period can be broadened or split such that there may instead be peaks at $\sim 1 \pm 0.1$ which further complicates their identification. The significant yet still false positives are not by default eliminated, as it is entirely possible that a star does

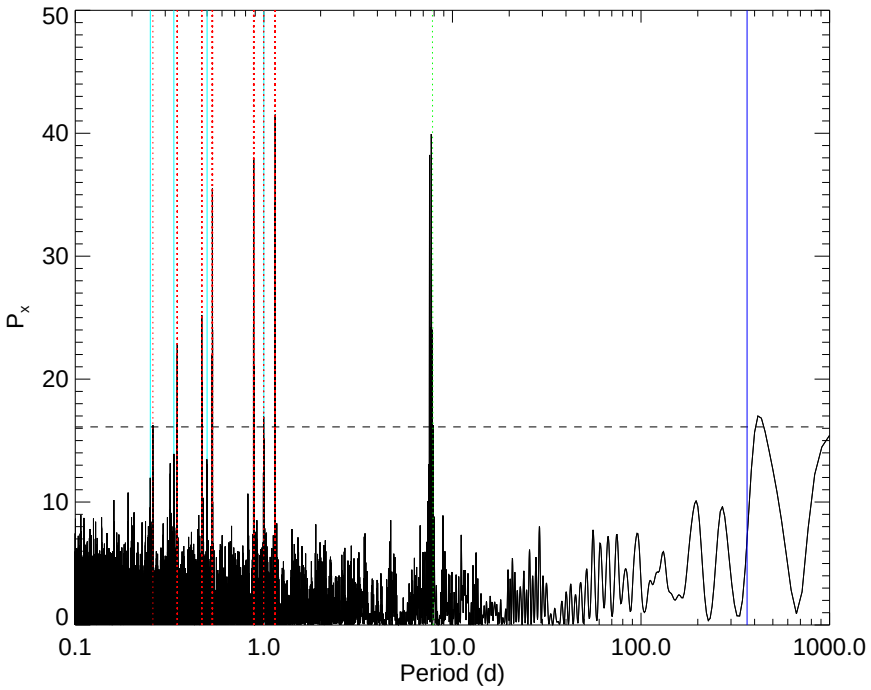

FIGURE 2.13: Example periodogram for the WTS star 19h_3_16170. This periodogram is the result of performing a Lomb-Scargle analysis over periods of 0.1 to 1000 days testing 1×10^5 frequencies. The solid cyan lines indicate $\frac{1}{4}, \frac{1}{3}, \frac{1}{2}$ and 1 days and the solid blue line indicates 1 year. The dotted red lines indicate the peaks more significant than necessitated by a false alarm probability of 0.01 and the green dotted line indicates the maximum peak corresponding to the real periodicity of the star. The peaks aliasing with the observational period for this periodogram are split due to spectral leakage or due to the range of observation timings during the observational period, or both. There is another significant peak at ∼400 days that may correspond to the expected ∼1 year period.

happen to rotate with a period of $\sim n$ or $\sim 1/n$, and indeed, the presence of these peaks may hide the true period of the star. Therefore, all light curves with significant peaks are folded about those significant peaks. At the other end of the period scale, some aliasing with 1 year and 1/2 year periods can be detected as individual stars are only observable for limited periods during a year, although this is of less concern as it is beyond the range of expected periods for rotating M dwarfs.

From the light curves in the sample a peak to peak amplitude for each light curve is obtained by binning the folded light curve, while the period is obtained directly from the highest peak in the periodogram not to have been previously discounted.

Each light curve is then broken down into three separate consecutive epoch ranges

each containing a third of the observations and each range is again tested for variability. While the significance of the peak in the periodogram varies for each epoch range, its presence tests whether the periodic signal is maintained in the photometry of the star for the duration of observations. This process also enables the discovery of some examples of evolving variability as discussed in Section 3.5.

Since the Lomb-Scargle periodogram, while fast and thus efficient for detecting periodicities in large data sets, suffers from spectral leakage and aliasing, the CLEAN algorithm is used on each light curve showing significant periodicity. The CLEAN algorithm was initially developed for deconvolution of radio data (Högbom, 1974) and was later adapted for use on dimensional data by Roberts et al. (1987), specifically for the purposes of time series analysis. Much like the Lomb-Scargle periodogram, CLEAN finds the power spectrum of a time series but works to remove artifacts generated by unevenly sampled data with gaps. It is, however, much slower to implement and thus unsuitable for efficiently analysing large data sets, and more suitable for a second order refinement of the periods initially detected by the Lomb-Scargle periodogram. For each of the variables found in WTS, the CLEAN algorithm is performed in the light curve and the period is found from the highest peak in the periodogram. The Lomb-Scargle and CLEAN periodograms for 72 variable M dwarfs in the WTS can be found in Figures A1–A72.

2.4.2 Variability Contamination

After systematic sources of confusion in the periodogram have been eliminated, there remain real sources of variability in the photometry for some objects which are the result of genuine astrophysical processes, namely, variables of other varieties such as CVs and Miras, and eclipsing binaries.

Most eclipsing binaries can be identified due to the morphology of their light curves. Clark et al. (2012) find, using spectroscopic data from the Sloan Digital Sky Survey (SDSS), that the fraction of M dwarfs that are close binaries (defined as a<0.4AU) to be $2.9^{+0.6}_{-0.8}\%$. Binaries that are not in contact have light curves that are punctuated by non-contiguous drops in magnitude of alternating depth due to the primary and secondary

eclipses of the system, and are thus different from the contiguous and sinusoid-like morphologies of spot modulated M dwarfs. Therefore, detached binaries are not treated as a potential source of confusion. Systems with components earlier than M types should also be eliminated in the spectral typing procedures. In instances where both the components are both M type dwarfs this would not be the case, and close binaries could therefore prove a source of contamination. Contact binaries where the components have equalised temperatures, indeed including those observed in WTS (Nefs et al., 2012), do result in light curves that are nearly sinusoidal as from the point of observation, although so long as one star has a greater luminosity than the other the light curve will still display the dichotomous depths that are indicative of an eclipsing binary. In addition to this, the overall amplitude of the light curve far exceeds the values typically expected from spot modulation. Furthermore, confusion here should only be caused for very short periods. Nefs et al. (2012) show that periods for contact binary systems composed of M dwarfs of similar spectral types go from $\sim$0.05 days for an M5V star to $\sim$0.21 days for an M1 star. Any variables with such short periods should be treated with caution, although the work by Nefs et al. (2012) should have found any such eclipsing binaries in the WTS variable sample, making potential confusion unlikely. For eclipsing binaries that vary on time scales greater than these the components will be detached and therefore break the sinusoid-like light curve morphology.

Many known types of variable star, such as Beta Cephei and Alpha Cygni are of spectral types O and B and can be simply discounted as being too blue to remain in the sample after colour cuts and spectral type selection, while others such as SRa and Mira variables, being red and potentially evading the aforementioned cuts, rotate with amplitudes of $\Delta V \geq 2$ which greatly exceeds the V-band amplitudes of late-type, main-sequence stars (e.g. Messina et al., 2010), and indeed the amplitudes found at any wavelength for M dwarfs in other sources. Other SR type stars do not rotate with a regular period. Despite these stars not being direct constituents of the variable M dwarf sample, it is possible that photometric artifacts such as diffraction spikes or the encroachment of the bright, variable star's point spread function into the aperture centred on the M dwarf could contaminate the photometry of the M dwarf and invoke

a periodic signal. Each variable star candidate is inspected by eye in the WTS images of the field to reduce the potential of having any variations in magnitude invoked by variability in other sources.

There are few instances when the periodic variability of an M dwarf is not due to spot modulation. It is conceivable that a circumstellar disk around an M dwarf could produce periodic variations in the brightness if it was of variable density or if the disk was warped Muzerolle et al. (2009). This possibility can be largely excluded however; Gautier et al. (2007) find no evidence for dust disks around M dwarfs older than 1Gyr of more than $10^{-9} - 10^{-4} M_{\oplus}$ from Spitzer 24μm observations. Observations of M dwarf dust disks are exceptionally rare and limited to M dwarfs tens of Myr old (e.g. Forbrich et al., 2008), and a side-on geometry would be required for any influence on the WTS light curves. Therefore, this is discounted as a likely explanation for the variability of any of the M dwarfs in WTS, and ongoing space motions analyses of the WTS stars will place more formal age constraints on them.

2.5 Summary and results of the Lomb-Scargle search

WTS JHK_s colours combined with SDSS *ugriz* colours are used to to classify the stars in WTS. In particular, the M stars are identified and giants are eliminated through use of spectral type and luminosity colour relations and colour cuts. The Lomb-Scargle periodogram is used to identify stars that exhibit significant variability and extract a sample of periodically variable M dwarfs. The light curves are reviewed by eye and the CLEAN algorithm is used to deconvolve the periodogram power spectrum and identify the periods.

From the results of the Lomb-Scargle search of the WTS M dwarf sample, a total of 3192 light curves with a significant peak in the periodogram are found by the Lomb-Scargle search. This is inclusive of spurious peaks such as those imposed by aliasing as discussed previously. After reviewing them by the above described method, a total of 84 stars with clear periodic variability are found. The remaining light curves are primarily eliminated because the periodic signals corresponded to one day or fractions thereof,

and are therefore imposed by the observation period, while others were elimininated because upon folding the light curve it showed no obvious variability, and thus the significant peaks are likely due to random noise or an unaccounted systematic. As the FAP is set for a significance corresponding to a probability that the signal is genuine of 0.99, it is expected that 0.1 (i.e. $\sim$32) of the variable light curves can be accounted for purely by signals emmerging from random noise.

From these remaining 81, one star was excluded as it was blended with the diffraction spike from a known Mira type star V1134 Cyg (Miller, 1966) evoking a period of 327.01 days, close to the previously published period for V1134 Cyg of 340 days. All other potential identities for the variables are discounted through the reasoning above. A total of 9 suspected or known eclipsing binaries are identified in the sample as having light curves with periodic troughs of two distinct depths, indicative of the primary and secondary eclipse of the system, or periodic magnitude variations of ΔJ>0.02. THese EBs are shown in Figures A73-A81. This leaves a remaining sample of 72 stars, 68 of which have SDSS photometry and therefore spectral sub-type estimates. The remaining four are in the 17hr field, with infra-red colours indicative of them being M dwarfs.

3

Periodic Variability of WFCAM Transit Survey M Dwarfs

This chapter is composed of work published in "J-band Variability of M Dwarfs in the WFCAM Transit Survey", Goulding et al. (2012), and "Periodic variability of spotted M dwarfs in WTS", Goulding et al. (2013).

3.1 Overview of results

From the selection process a total of 72 periodically variable M dwarfs are found, listed in Table 3.1. The light curves and periodograms are plotted in Figures A1 to A72. The periods found range from several hours to several months. Irwin et al. (2011) similarly find long periods, in a wavelength region approximately corresponding to the $i+z$ bands

for M dwarfs ranging between 0.28 and 154 days in their study of rotating M dwarfs in the MEarth Transit Survey. Benedict et al. (1998) find evidence for periodicity in Barnard's Star of ∼130 days and Proxima Centauri of ∼40 and ∼83 days, the latter confirmed by Kiraga & Stepień (2007). Whilst the WTS periodic variable M dwarf sample produced no convincing evidence of a large number of stars exhibiting periodicity on these time scales, a large number of periods > 80 days were found in the periodicity search and subsequently rejected when no sinusoidal variability was seen. Such peaks in the periodogram may, however, correspond to seasons over which any given star is observed during a year and WTS may, therefore, not be particularly sensitive to periods of this length. In addition, phase incompleteness may prevent the detection of long periods as illustrated in Section **??**. WTS is not wholly insensitive to periods longer than this as evidenced by the detection of a 327.01 day period for the Mira V1134 Cyg. A diffraction spike from V1134 Cyg, which was itself saturated in the WTS observations, affected the photometry of an M dwarf in the initial colour-selected M dwarf sample; this was identified by the visual examination of the WTS images. As the entire sample selected by colour cuts was tested by periodicity a few variables detected (such as 03e_1_02053), while appearing as M dwarfs in the near infra-red, some have more dispersed colours in SDSS resulting in an overall identification as a K dwarf. These are retained in the sample presented below for the sake of completeness. Errors in the periods found are not quoted; the Lomb-Scargle periodogram does not find errors in period and typically finds precise periods, particularly for periods >10 days, while periods estimated by the CLEAN algorithm are of the order 1×10^{03} days and therefore are at least two orders of magnitude smaller than the shortest period found here.

The overall fraction of periodically variable M dwarfs found in WTS appears small, with just 72 variable stars found in the M dwarf sample. Considering only those 68 variables with spectral sub-type estimates, this represents just 0.007 of the stars searched for periodic variability. For comparison Hartman et al. (2011) finds the fraction of variables at 0.057, and 0.001 for just field M and K dwarfs, in the HATNet survey. Ciardi et al. (2011) finds a variability (but not necessarily periodic variability) fraction

of 0.367 in Kepler, while Rockenfeller finds the variable fraction of field M dwarfs to be 0.21±0.11. The fraction found in Kepler is likely much higher due to the better signal-to-noise ratio and observing at shorter wavelengths where the effects of spots are greater. From plots of magnitude versus light curve amplitude (Figure 3.1) it is clear there is a completeness dependency on brightness, although considering just the most complete magnitude bins of $12 < J < 14$ the fraction of variable M dwarfs found in WTS is 0.02. Simulations further exploring the completeness and the interaction of the Lomb-Scargle periodogram with light curves of varying amplitude and period are discussed in Section 4.1. No variable stars later than M4 were detected in the WTS sample. This is perhaps because while the fraction of active M dwarfs increased for later M types, the level of activity decreases (e.g. Reiners & Basri, 2008; Bell et al., 2012). Rockenfeller et al. (2006) find, in a compilation of variable M and L dwarfs, that I-band light curve amplitude increases greatly during the mid M to mid L types, so the non-detection of periodic variables in WTS is likely the result of the relatively small fraction of bright mid to late M dwarfs in the sample. Most variables are found in the 07 and 19hr fields, which are closest to the Galactic plane, where Ciardi et al. (2011) find a greater fraction of variability for M dwarfs.

Name	RA[a]	Dec[a]	J[b]	ST[c]	Period[d]	Amplitude[e]	RA (SDSS J2000)[f]	Dec (SDSS J2000)[f]	v_t (kms^{-1})[g]
03d_1_04395	55.115972	39.134701	14.32	M1 ± 1.01	4.880	0.017 ± 0.004	—	—	—
03e_1_02053	53.784274	38.954377	14.95	K5 ± 9.36	24.100	0.015 ± 0.006	—	—	—
03e_2_03325	54.204782	38.846530	14.08	M1 ± 1.01	7.090	0.024 ± 0.004	—	—	—
03f_1_03040	54.006089	38.807408	16.30	M4 ± 1.01	8.110	0.037 ± 0.014	—	—	—
03h_2_01177	55.772275	38.959886	14.64	M0 ± 7.64	12.440	0.020 ± 0.004	—	—	—
03h_4_04646	55.184813	39.423991	15.13	M3 ± 1.00	37.690	0.017 ± 0.006	—	—	—
07b_2_02081	106.059460	12.868579	15.69	M4 ± 1.00	2.120	0.029 ± 0.009	—	—	—
07b_2_02125	106.158970	12.867247	14.10	M3 ± 1.00	16.660	0.014 ± 0.004	-1.410 ± 2.642	-1.606 ± 2.642	3.047 ± 0.624
07b_2_02237	106.272010	12.863213	13.24	M4 ± 1.00	5.950	0.019 ± 0.003	-16.955 ± 2.547	6.120 ± 2.547	15.996 ± 1.925
07b_3_00631	106.072930	13.345031	14.31	M4 ± 1.01	0.490	0.011 ± 0.004	-1.657 ± 2.853	-1.733 ± 2.853	3.317 ± 0.705
07b_3_02281	106.137370	13.257735	15.64	M0 ± 1.06	4.670	0.043 ± 0.008	-4.709 ± 2.797	-3.696 ± 2.797	49.275 ± 9.840
07c_2_00282	106.827750	12.938019	13.71	M2 ± 1.00	14.920	0.013 ± 0.003	0.142 ± 2.421	-3.279 ± 2.421	115.837 ± 22.843
07c_2_00294	106.899370	12.937313	13.91	M3 ± 1.00	1.530	0.012 ± 0.003	9.569 ± 2.617	-2.292 ± 2.617	16.275 ± 2.652
07c_4_04250	106.459880	13.336219	14.76	M3 ± 1.00	52.490	0.009 ± 0.005	1.724 ± 2.924	-19.953 ± 2.924	42.274 ± 9.217

[a] Coordinates in SDSS (epoch J2000) if available [b] WTS average UKIDSS system J band magnitude MKO system [c] Spectral type estimate as determined by method described in Section 2.3.3 with error determined by standard deviation in colour-type space and minimum uncertainty of ±1 (see Figure 2.10) [d] Period in days as determined by maximum peak in CLEAN periodogram [e] Amplitude in J band magnitude [f] Proper motion in mas yr^{-1} from SDSS [g] Tangential velocity in kms^{-1}

Table 3.1: A table of the 72 variable M dwarfs found. Included are stars outside the M dwarf spectral type range but with H-K > 0.175 suggesting a redder, late type star that the spectral typing procedure erroneous assigned an earlier spectral type, and have been retained for maximum inclusivity.

Name	RA[a]	Dec[a]	J[b]	ST[c]	Period[d]	Amplitude[e]	RA (SDSS J2000)[f]	Dec (SDSS J2000)[f]	v_t (kms^{-1})[g]
07d_1_02956	106.627350	12.859053	13.83	M1 ± 1.00	2.780	0.037 ± 0.003	-3.240 ± 2.481	-1.363 ± 2.481	7.927 ± 1.486
07d_1_03180	106.617910	12.780124	16.04	M0 ± 1.11	1.190	0.042 ± 0.011	-3.872 ± 2.970	-0.899 ± 2.970	37.971 ± 8.498
07d_1_06063	106.510690	12.913766	15.35	M3 ± 1.00	7.800	0.013 ± 0.007	8.695 ± 3.114	-1.453 ± 3.114	22.054 ± 4.435
07d_4_03625	106.725960	13.303723	13.87	M3 ± 1.00	1.630	0.028 ± 0.004	5.903 ± 2.561	-16.933 ± 2.561	27.624 ± 4.870
07d_4_04577	106.692980	13.339136	16.70	M0 ± 1.01	1.410	0.047 ± 0.020	-1.171 ± 3.130	1.261 ± 3.130	25.460 ± 6.040
07e_2_01022	105.870700	12.686058	12.45	K2 ± 2.20	21.270	0.078 ± 0.002	-3.729 ± 2.322	1.183 ± 2.322	12.746 ± 2.243
07e_2_02466	105.869530	12.632173	14.99	K7 ± 1.44	12.860	0.110 ± 0.007	-1.946 ± 2.392	-0.524 ± 2.392	16.488 ± 3.097
07e_2_06232	105.994080	12.512096	15.27	M0 ± 1.01	2.290	0.023 ± 0.011	0.327 ± 2.764	-0.321 ± 2.764	2.618 ± 0.580
07f_3_00675	106.076750	13.042346	12.62	M0 ± 10.21	3.870	0.051 ± 0.002	-11.750 ± 2.322	-1.021 ± 2.322	34.156 ± 4.526
07f_3_03235	106.172640	13.106071	14.94	M4 ± 1.00	6.310	0.019 ± 0.005	-4.006 ± 3.053	-6.566 ± 3.053	13.356 ± 2.988
07g_1_04615	106.386640	12.613818	14.49	M0 ± 1.03	35.790	0.012 ± 0.005	-14.678 ± 2.514	-8.399 ± 2.514	77.421 ± 10.105
07h_1_03267	106.617800	12.550436	14.59	M0 ± 1.08	1.290	0.022 ± 0.005	0.743 ± 2.616	-5.523 ± 2.616	22.316 ± 4.654
17a_1_01533	4.50169	0.064409	16.38	—	0.630	0.055 ± 0.018	—	—	—
17a_3_00950	4.50686	0.072623	14.96	—	41.63	0.060 ± 0.005	—	—	—
17a_3_03244	4.50811	0.070696	14.96	—	45.21	0.068 ± 0.005	—	—	—
17d_1_06032	4.50811	0.070696	13.12	—	1.66	0.022 ± 0.006	—	—	—
19a_1_00838	292.765130	36.419518	15.99	M0 ± 1.61	24.650	0.025 ± 0.011	1.516 ± 2.956	-3.306 ± 2.956	39.212 ± 3.310
19a_1_10932	292.511620	36.308370	16.08	M0 ± 1.02	8.410	0.030 ± 0.011	5.269 ± 4.318	2.332 ± 4.318	52.077 ± 6.235
19a_3_01981	293.095110	36.809146	15.64	M4 ± 1.00	1.680	0.027 ± 0.008	—	—	—
19a_3_10735	293.304660	36.915622	15.14	M0 ± 1.21	1.200	0.059 ± 0.006	—	—	—
19a_3_11735	293.329960	36.744529	16.78	M0 ± 1.00	0.160	0.081 ± 0.017	-36.959 ± 4.379	51.498 ± 4.379	813.932 ± 78.904

Table 3.1: Continued.

Name	RA[a]	Dec[a]	J[b]	ST[c]	Period[d]	Amplitude[e]	RA (SDSS J2000)[f]	Dec (SDSS J2000)[f]	v_t (kms^{-1})[g]
19b_1_10542	292.815320	36.294256	16.36	M1 ± 1.19	2.060	0.038 ± 0.014	—	—	—
19b_3_03003	293.389460	36.815246	15.58	M4 ± 1.00	1.480	0.015 ± 0.008	—	—	—
19b_3_08292	293.505170	36.904554	16.39	M0 ± 1.05	28.710	0.028 ± 0.013	1.228 ± 3.669	-3.199 ± 3.669	44.699 ± 4.699
19b_3_09282	293.527870	36.925772	16.99	M1 ± 1.06	7.680	0.028 ± 0.020	—	—	—
19b_3_12753	293.601230	36.745270	16.71	M3 ± 1.01	2.450	0.037 ± 0.016	—	—	—
19c_2_05428	294.422680	36.416670	15.91	K7 ± 1.00	20.680	0.115 ± 0.010	2.969 ± 2.681	-2.105 ± 2.681	41.374 ± 3.151
19c_3_01804	294.179440	36.758408	16.27	M3 ± 1.00	7.700	0.036 ± 0.012	—	—	—
19c_3_03299	294.205130	36.760331	13.17	M0 ± 1.00	5.620	0.016 ± 0.002	7.245 ± 2.438	-18.289 ± 2.438	42.647 ± 2.796
19c_3_04974	294.235120	36.750789	12.41	M2 ± 1.64	1.450	0.010 ± 0.002	-10.040 ± 2.393	0.388 ± 2.393	21.279 ± 1.379
19c_3_05921	294.252830	36.875064	15.37	M4 ± 1.05	42.400	0.016 ± 0.006	—	—	—
19c_3_11273	294.354460	36.709272	15.75	M3 ± 1.06	90.330	0.016 ± 0.008	—	—	—
19c_4_10571	293.851810	36.888130	15.92	M4 ± 1.02	1.440	0.032 ± 0.011	—	—	—
19c_4_12623	293.864930	36.921243	16.54	M3 ± 1.10	3.600	0.034 ± 0.016	3.934 ± 5.675	-17.812 ± 5.675	88.260 ± 14.006
19d_1_06078	294.046830	36.381880	15.14	M1 ± 1.00	15.490	0.023 ± 0.006	2.722 ± 3.513	2.695 ± 3.513	15.304 ± 1.497
19d_1_06603	294.036450	36.297312	16.21	M2 ± 1.10	5.360	0.027 ± 0.012	—	—	—
19d_1_12693	293.923010	36.287590	16.00	M4 ± 1.03	0.730	0.033 ± 0.010	—	—	—
19d_2_00740	294.453090	36.487943	15.54	M3 ± 1.00	8.050	0.025 ± 0.008	—	—	—
19d_3_01140	294.441370	36.901497	15.64	M4 ± 1.01	2.410	0.019 ± 0.008	—	—	—
19d_3_01271	294.445960	36.921308	16.38	M4 ± 1.00	0.560	0.026 ± 0.013	—	—	—
19d_3_02216	294.461610	36.796780	14.10	M4 ± 1.00	2.010	0.023 ± 0.003	12.883 ± 4.176	5.053 ± 4.176	14.979 ± 1.616
19d_3_03681	294.482160	36.713086	15.83	M0 ± 1.00	17.480	0.019 ± 0.009	—	—	—

Table 3.1: Continued.

Name	RA[a]	Dec[a]	J[b]	ST[c]	Period[d]	Amplitude[e]	RA (SDSS J2000)[f]	Dec (SDSS J2000)[f]	v_t (kms^{-1})[g]
19d_3_05922	294.526470	36.803361	16.08	M2 ± 1.12	23.060	0.029 ± 0.010	-0.337 ± 3.841	2.172 ± 3.841	11.717 ± 1.263
19d_3_07286	294.550410	36.755946	15.38	M0 ± 1.00	7.170	0.026 ± 0.007	1.442 ± 2.741	4.024 ± 2.741	25.633 ± 1.961
19e_1_03204	292.733110	36.090610	16.79	M1 ± 1.19	1.950	0.042 ± 0.018	—	—	—
19e_2_02880	293.130710	36.239925	15.18	M4 ± 1.00	50.020	0.013 ± 0.006	3.037 ± 3.696	3.874 ± 3.696	8.848 ± 0.920
19e_2_09200	293.301440	36.154486	15.22	M4 ± 1.00	1.350	0.018 ± 0.006	—	—	—
19e_3_09622	293.199860	36.614838	16.46	M4 ± 1.00	1.620	0.025 ± 0.014	—	—	—
19f_3_08798	293.508310	36.571411	15.98	M4 ± 1.00	65.390	0.026 ± 0.010	12.862 ± 4.506	13.205 ± 4.506	39.388 ± 4.858
19f_3_12800	293.593410	36.489227	15.97	M3 ± 1.18	3.890	0.018 ± 0.009	—	—	—
19f_4_06780	292.808650	36.620585	17.02	M0 ± 1.76	2.620	0.048 ± 0.022	—	—	—
19g_1_04348	293.805310	36.117012	16.34	M0 ± 1.06	1.420	0.042 ± 0.014	3.106 ± 3.109	1.070 ± 3.109	32.632 ± 2.962
19g_1_05313	293.787750	36.249911	16.76	M4 ± 1.00	34.220	0.041 ± 0.017	—	—	—
19g_1_10773	293.683380	36.080351	16.16	M4 ± 1.08	5.910	0.023 ± 0.011	—	—	—
19g_2_03649	294.179550	36.224328	16.47	M3 ± 1.00	9.420	0.053 ± 0.015	—	—	—
19g_3_06870	294.268510	36.556675	15.62	M4 ± 1.06	13.000	0.014 ± 0.008	-8.732 ± 3.748	-1.280 ± 3.748	18.177 ± 1.921
19g_4_00989	293.744820	36.504677	16.20	M4 ± 1.20	40.050	0.025 ± 0.012	—	—	—
19h_3_16170	294.703050	36.655522	16.99	M0 ± 1.31	7.560	0.052 ± 0.018	-5.934 ± 3.846	-12.512 ± 3.846	309.087 ± 34.741

Table 3.1: Continued

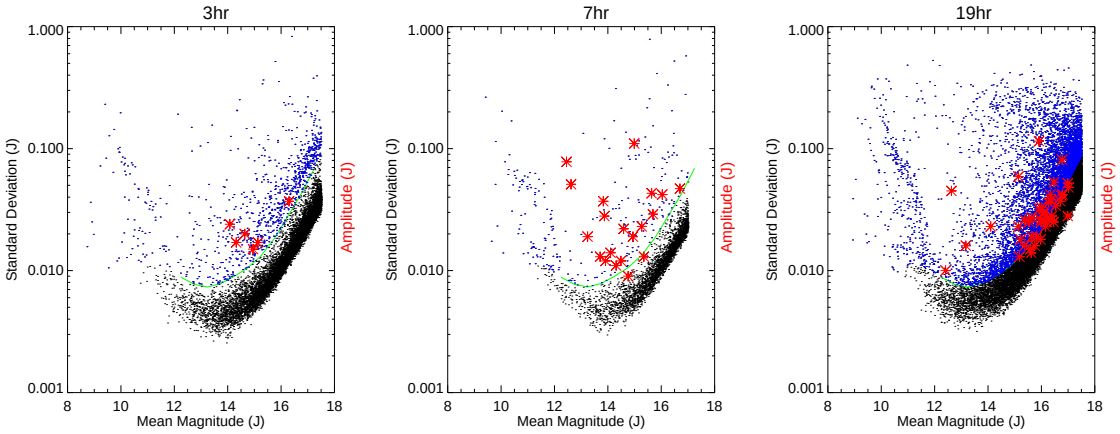

FIGURE 3.1: Plots of all the M dwarfs found in the three fields with SDSS coverage. The amplitudes of the variable stars found in WTS are shown as red stars. The green lines show the effective upper 1σ value for standard deviations of the lightcurves per magnitude bin. There is a clear dependency on magnitude for the minimum amplitude detected per magnitude bin closely following the trend in dispersion of lightcurves with magnitude.

3.2 Period versus spectral type

In order to take advantage of the variables detected and measured in WTS to enable comparisons with other works on the kinematic properties of variable M dwarfs, estimates of tangential velocity ($v_{\rm t}$) are used as tracers of population (e.g. Reiners & Basri, 2008). In the absence of radial velocity measurements of the WTS stars the full space motion cannot be estimated. The proper motions of most of the WTS stars are measured in the SDSS proper motion catalogue (Munn et al., 2004, 2008). To calculate $v_{\rm t}$ from the proper motions, distance estimates must be made. The distances are estimated using the empirical photometric parallax technique for SDSS M dwarfs by Bochanski et al. (2011) relating observational values of $r-z$ to M_r. A spline interpolation is used to find the values of M_r for the WTS M dwarfs from their SDSS $r-z$ values, and the distance is then estimated from M_r and r. Using these distance estimates the proper motions can be interpreted as tangential velocities; both are tabulated in Tables 3.1–**??**. Following Reiners & Basri (2008), stars with a $v_{\rm t} \gtrsim 30\,{\rm kms}^{-1}$ are considered probably old disk stars while any stars with $v_{\rm t} \lesssim 15\,{\rm kms}^{-1}$ are considered thin disk. Two of the faintest stars in the sample, one with $v_{\rm t} = 309 \pm 35\,{\rm kms}^{-1}$ and another with $v_{\rm t} = 814 \pm 89\,{\rm kms}^{-1}$, have velocities consistent with being members of the

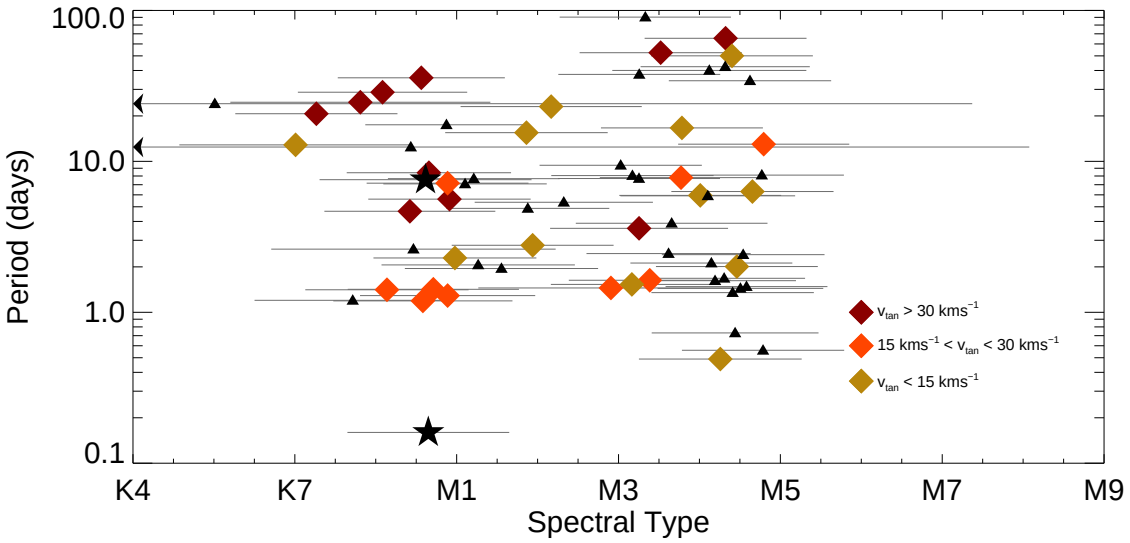

Figure 3.2: Spectral type versus period for the WTS periodically variable M dwarfs. Symbols are described in Section 3.2

halo (e.g. Lépine et al., 2003; Scholz et al., 2005). In Figures 3.3 to 3.5 depicting the periods, amplitudes and spectral types, the stars with $v_t \gtrsim 30\,\mathrm{kms}^{-1}$ are shown as red diamonds, the stars with $v_t \lesssim 15\,\mathrm{kms}^{-1}$ are shown as yellow diamonds, the stars with Halo-like v_t are shows as black stars, other stars are shown in orange, and stars with no SDSS proper motions are shown as black triangles.

The periods versus spectral types of the WTS variable M dwarfs are shown in Figure 3.3. While the standard deviation of the stars later than M3 is larger than those earlier than M4, a Kolmogorov-Smirnov (KS) test reveals that the probability they are drawn from the same distribution is 0.265. Thus it cannot be said with any great probability that the periods for early and mid M dwarfs are drawn from different distributions, and comparisons to the significantly different distributions of $v\sin i$ across the spectral types found by Jenkins et al. (2009) cannot be made. The WTS sample, however, is more lacking in mid to late M dwarfs. As Stelzer et al. (2013) finds for the M dwarfs within 10pc of the Sun, the dispersions of rotation rates is greater at M4 than it is for earlier M dwarfs; they also find an onset of more rapid rotation at M4V. With the exception of 19a_3_11735 (discussed below), this result is corroborated by the findings in WTS as all other stars for which $p < 1\,\mathrm{d}$ are of spectral type M4V,

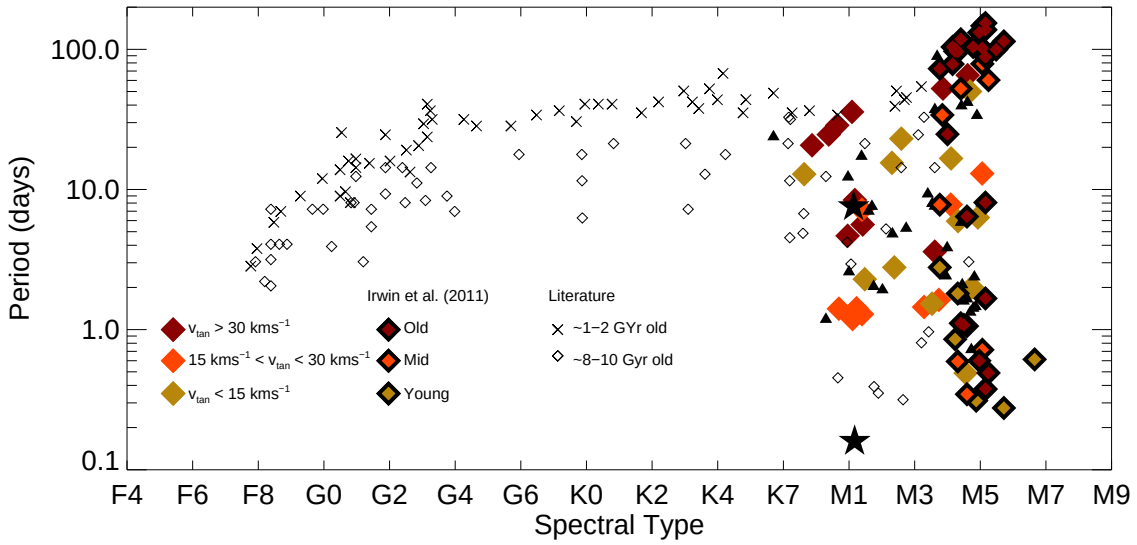

FIGURE 3.3: Spectral type versus period for the WTS dwarfs and those presented and compiled by Irwin et al. (2011). Black triangles are stars with no matched proper motions in SDSS, black stars are stars for which v_{tan} suggests a halo star, coloured symbols are described in the key and further exlained in Section 3.2. Old (∼1-2Gyr) main sequence stars from literature sources compiled in that paper are shown as crosses and old (∼8-10Gyr) main sequence stars are shown as unfilled diamonds. Stellar masses have been converted to spectral type by use of spectral standards compiled by Mamajek (2011). The star designated with the black star symbol with the shortest period is 19a_3_11735, as discussed in Section 3.2.

although the fraction of rapid rotators is smaller.

Comparisons between the early M variables found in WTS with the variable mid M dwarfs found by Irwin et al. (2011) can be made. They present the variable M dwarfs in the MEarth survey with other literature sources of periodically variable field M dwarfs. They compare their proper motions with those predicted by models for thin and thick disk stars (assumed to be old and young disk stars respectively) in order to assign population memberships to each. They find, via a KS test, that the period distributions for each classification are significantly different. A KS test performed analogously on the WTS stars does not show a high probability that the two distributions are different, with a probability that they are from the same population of 0.267. Despite this, it is found that most of the slowest rotators (p<20 d) are amongst the 'old' stars, while the 'young' stars show a greater range of periods. The mean period of the 'old' stars is 19.4 d, with a robust mean curtailed at 2σ of 12.7 d (σ=3.6 d). For the 'young'

stars the mean is 12.6 d with an alike robust mean of 3.6 d (σ=0.5 d). The six 'old' stars with periods >10 d appear on Figure 3.3 as expected for stars of their spectral type, although the presence of 3 'old' early M dwarfs with periods 5 d< p <10 d is noteworthy as no old M dwarfs have been detected in this parameter space before. In general, the result from Irwin et al. (2011), showing longer maximum rotation periods with decreasing mass, is corroborated, i.e. the longest rotation for the WTS mid M dwarfs is longer than the periods for the earlier WTS M dwarfs.

It is particularly unusual that the star, 19a_3_11735 (Figure A35), with the shortest period in the sample, has a velocity consistent with being a halo star. Such stars are 10-12 Gyr old (e.g. Jofré & Weiss, 2011), and as such a period this short would not be expected from models of M dwarf spin down time (Irwin et al., 2011). Using the $(r-z)-(g-r)$-metallicity dependent quantity (ζ, Lépine et al., 2007) from West et al. (2011) and the ζ-[Fe/H] relation from Woolf et al. (2009) this star appears not to be particularly metal poor ([Fe/H]>-0.34) and thus does not suggest an older, Population II star as might be expected from a star with such a large tangential velocity. This star also has the largest amplitude of all stars found in the sample, and may perhaps be a contact binary with components of equal temperature not found in previous searches for such systems in WTS by Nefs et al. (2012), although due to the dynamo dependency on rotation for early M dwarfs it is not surprising to see the largest light curve amplitude in the sample for the fastest rotator. Simulations discussed in Chapter 4 do indeed produce stars with this magnitude of light curve amplitude due to spot modulation. Future spectroscopic observations should provide further information as to the nature of this star and others in the WTS.

3.3 Amplitude versus spectral type

In order to estimate the amplitudes of the variable stars, the folded light curves are binned in 30-observation intervals and the difference between the minimum and maximum is found. The error on the amplitude is found from the standard deviation of the light curve after the variability has been subtracted. The amplitudes of the sample

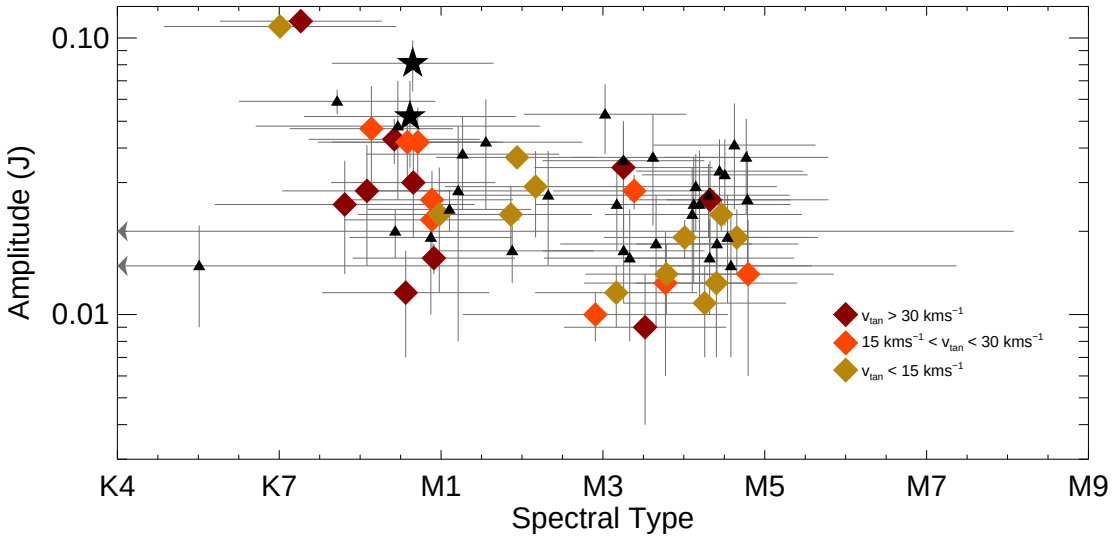

FIGURE 3.4: A plot of WTS variable M dwarf spectral types versus amplitudes. Black triangles are stars with no matched proper motions in SDSS, black stars are stars for which v_{tan} suggests a halo star, coloured symbols are described in the key and further exlained in Section 3.2.

range from 0.009±0.005 to 0.115±0.010 in the J-band. The amplitudes are plotted with respect to spectral type in Figure 3.4. A Spearman rank correlation coefficient calculated for the amplitudes with respect to spectral type indicates a weak trend for lesser amplitudes at later spectral types (R_S=-0.35, 99.7% significance), with the largest amplitudes detected from the earliest type stars. This is perhaps an indicator of lesser activity of stars with later spectral type, as a larger amplitude may result from a greater, less uniform spot coverage, as shown in Chapter 4. Alternatively, this could be because the contrast in spot and photosphere temperatures, thus brightnesses, is lesser for later spectral types (Berdyugina, 2005).

Observations of Hα emission, a tracer of chromospheric activity, in mid M to late L dwarfs have shown the normalised Hα luminosity decreases with later spectral types. Bell et al. (2012) find that while Hα emission decreased for later M spectral types the variability of the Hα emission increases, but suggest this is because small, transient emitters of Hα such as flares contribute a greater fractional change in Hα luminosity for lower activity stars that those with higher activity. Reiners et al. (2012a), Mohanty & Basri (2003) and others, however, find that the actual fraction of early

M dwarfs showing Hα activity is low, rising steeply at M3 to >50% while the normalised Hα luminosity decreases. Thus, while the Hα luminosity decrease with later spectral type, the fraction of active stars increases from early to mid M. The finding in WTS that the later M dwarfs have lower amplitude light curves is perhaps indicative of decreasing photospheric activity with later spectral type, although for periodically variable M dwarfs observed in the *GRI* bands by Rockenfeller et al. (2006), no definite trend is found with increasing spectral type. As so few periodically variable M dwarfs are found in WTS it is not possible to discern the relative fractions per spectral type.

3.4 Amplitude versus period

For early M dwarfs the stellar dynamo operates at the tachocline where convective and radiative zones meet as discussed in Section 1.1.1, and therefore it is expected that phenomena caused by magnetic activity will some exhibit rotation period dependent behaviour. In a study of field and cluster main sequence stars of varying ages Messina et al. (2003) study the dependence of X-ray emission on star spots and the subsequent dependence on rotation. X-rays are known to be a tracer of magnetic coronal activity and it is shown in that paper that relative X-ray luminosity is correlated with spot modulated light curve amplitude. For late K and early M dwarfs Messina et al. (2003) find that maximum amplitudes per period bin can be described with two envelopes defined as a power law of decreasing amplitude with increasing period. Envelopes are used as upper amplitude limits in that paper instead of trends to account for effect of amplitudes being lessened for $i < 90°$. A similar trend for decreasing amplitudes for longer periods is found in a sample of periodically variable M dwarfs in the HATNet survey by Hartman et al. (2011). Studies of Hα emission (e.g. Reiners, 2012) have shown an increase in activity for faster rotators, in that low activity is only found in slow rotators, although there is a large dispersion of activity levels amongst the faster rotators. Such studies have shown that rotation and activity are not absolutely interdependent, as some fast rotators show no Hα emission while some slow rotators are found to be active.

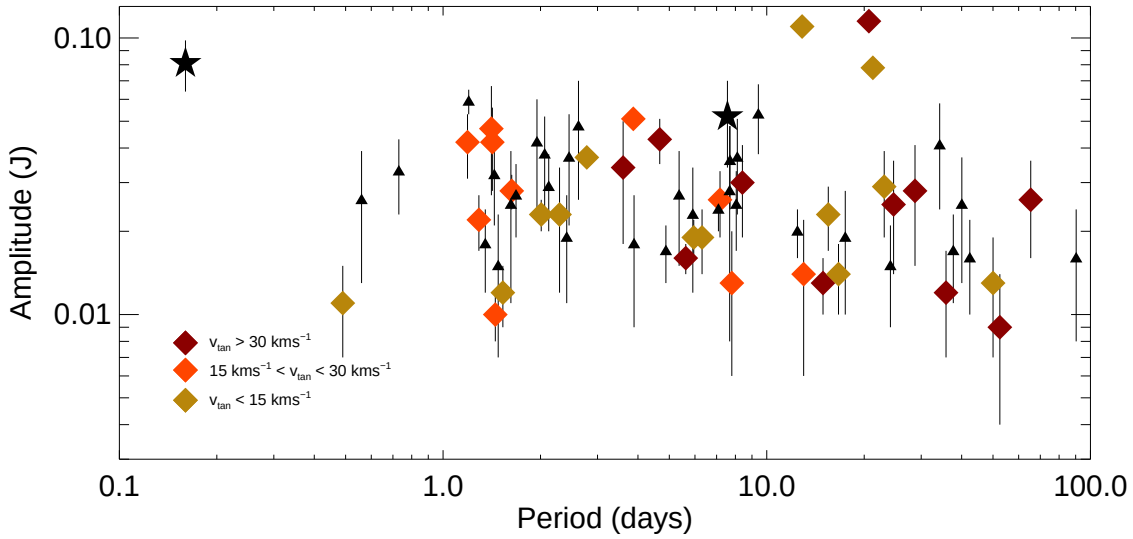

FIGURE 3.5: A plot of WTS variable M dwarf period versus amplitudes. Black triangles are stars with no matched proper motions in SDSS, black stars are stars for which v_{tan} suggests a halo star, coloured symbols are described in the key and further exlained in Section 3.2.

In the WTS variable M dwarfs, a weak trend, with smaller amplitudes at longer periods, is found using the same Spearman rank coefficient (R_S=-0.24, 95.5% significance), although as previously discussed this trend will have been affected by the varying inclinations of the stars reducing the amplitude. In Figure 3.5, showing the periods versus amplitudes, three stars with periods >10 d are found above the main series of amplitudes. A similar result is found by Messina et al. (2001), who find some some late K–early M dwarfs with large amplitudes far removed from the overal trend for main sequence dwarfs, as can be seen in Figure 1.7. Like other studies of photometrically variable M dwarfs such as Kiraga & Stepień (2007) and Irwin et al. (2011), M dwarf with very slow rotation rates on the order of months in length have been found to be sufficiently active to induce spot modulation.

3.5 Evolving light curves

Three of the light curves found in the sample show notable evidence of evolution. The star 07e_2_02466, shown in Figure 3.6, displays four different, distinct morphological

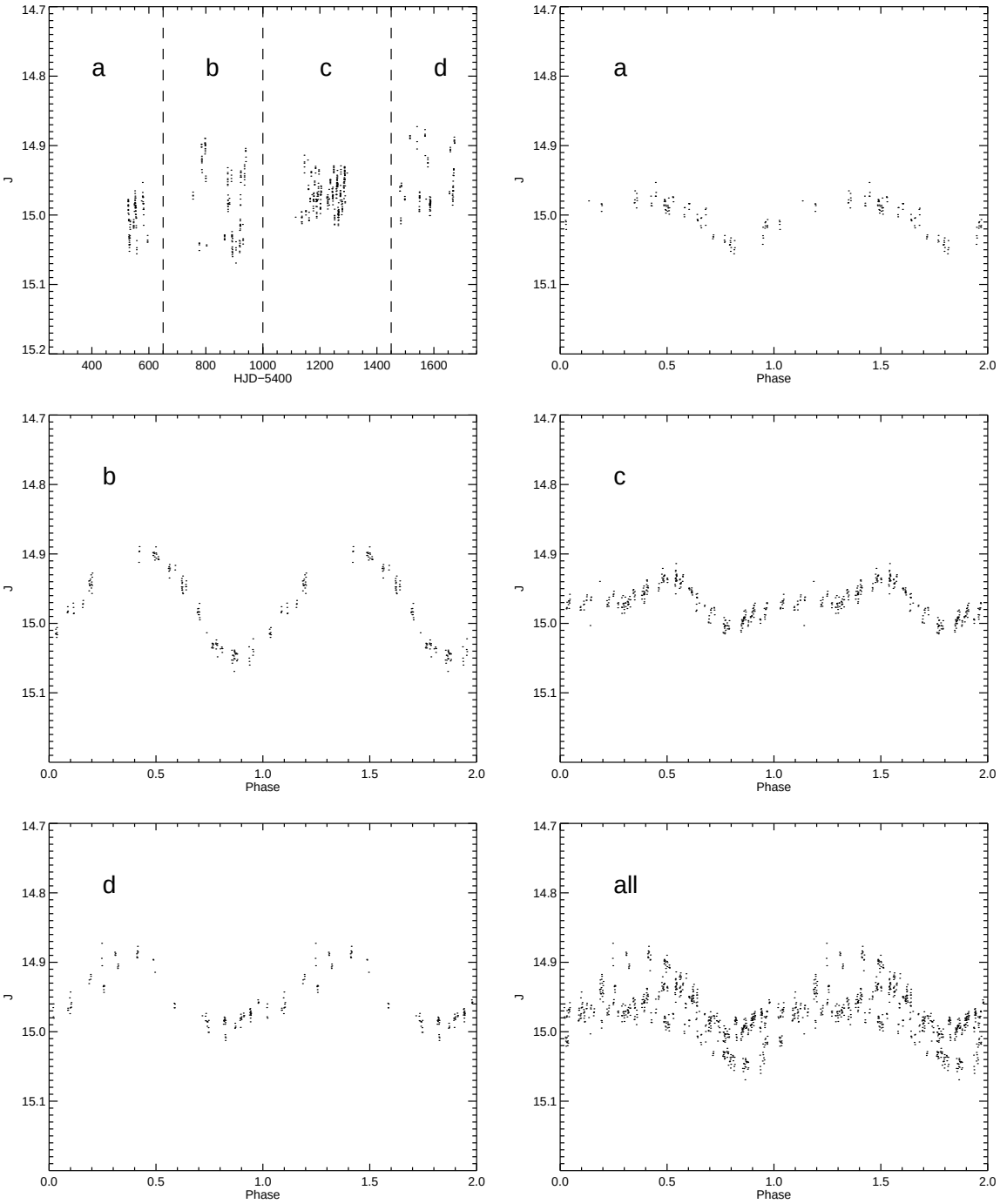

Figure 3.6: The unfolded light curve of the star 07e_2_02466, with subsequent plots phase folded over the 22.86 d period, each showing a distinct morphology, each corresponding to the labelled section of the original lightcurve. The final plot shows the overlayed folded lightcurves from all the periods of observation showing the dispersion that can occur in a light curve if long term spot evolution is not accounted for.

configurations in its light curve throughout the observations, each last for at least a few months. The first appears as a repeating arc shape, the second a sinusoid, the third as a saw tooth and the fourth as a zig-zag. In each instance the amplitude and mean brightness changes. Such changes in the lightcurve are clear evidence of a complex and evolving spot morphology.

The star 17d_1_06032, shown in Figure 3.7, shows a little periodic behaviour or an undetectably low amplitude in the first two observing periods of this field. In the first, no significant peak is found in the periodogram. In the second, however, a small but insignificant peak appears corresponding to the same period that is evident in the third observing period, showing a distinct sinusoid like variability. Such a change is evidence of reasonably rapid and large scale evolution in the spot pattern and/or coverage on the star, either indicating the star becoming more active and spotted, or the exact configuration of spots changing to become significantly less uniform in the $\sim$150 days between observation periods. 17d_1_06032 also served as a test for the ability of the Lomb-Scargle periodogram to detect a signal amongst an only partially variable light curve. The significant peak was detected in the periodogram for the entire light curve dependent only on the periodic variability established in the latter observations. The identification of a non-significant peak in the periodogram of the observations labelled *b* may indicate that the spot distribution had already begun to change sufficiently to invoke some modulation signal in the light curve despite this not being apparent in the folded light curve.

Another example is found in 19c_2_05428, shown in Figure 3.8. The changes in morphology are similar to those seen with 07e_2_02466 but on longer time scales. For the first two years of observations the light curve exhibits a morphology between sinusoidal and saw toothed. In the third year the amplitude doubles and the light curve becomes more arc shaped. On the darker hemisphere, between the temporal ranges *a* and *b*, a large spot, or group of associated spots, evolves decreasing the brightness of the darker hemisphere and increasing the amplitude of the light curve. The larger dispersion of points on the light curve maxima at this time may be indicative of spot evolution on the least spotted side of the star, although the maxima remains at approximately the

same brightness throughout the observations indicating that no large spots form on this hemisphere. During the fourth and fifth years of observations the large spots has seemingly decayed as the amplitude decreases and the morphology changes to a more complex one, with multiple minima on the darker hemisphere of the star. This may be due to evolution of mid to large sized spots or dense spot groups on this hemisphere of the star, or perhaps indicates the large spot that previous evolved has subsequently fragmented while decaying.

Among other stars in the WTS, several show some evidence of evolving morphology with time. Stars such as 17d_1_06032 , 19a_3_01981, 19a_3_10735, 19d_1_06078 (Figures A30, A33, A34, A49 respectively) and others all seem to show some time-dependent changes in amplitude and morphology. Such changes in light curves appear to take place over months and years. If this modulation is due to small spots then spot evolution requires growth and decay rates much slower than those observed on the Sun, however, if the spots are considerably larger than those on the Sun, such as those found in DI observations of M dwarfs, then decay rates may be much faster in order to invoke sufficient evolution in the spots to change light curve morphology. These possibilities are explored in more detail in Chapter 4. It may also be that M dwarfs undergo cycles of activity like the Sun, but on much shorter time scales.

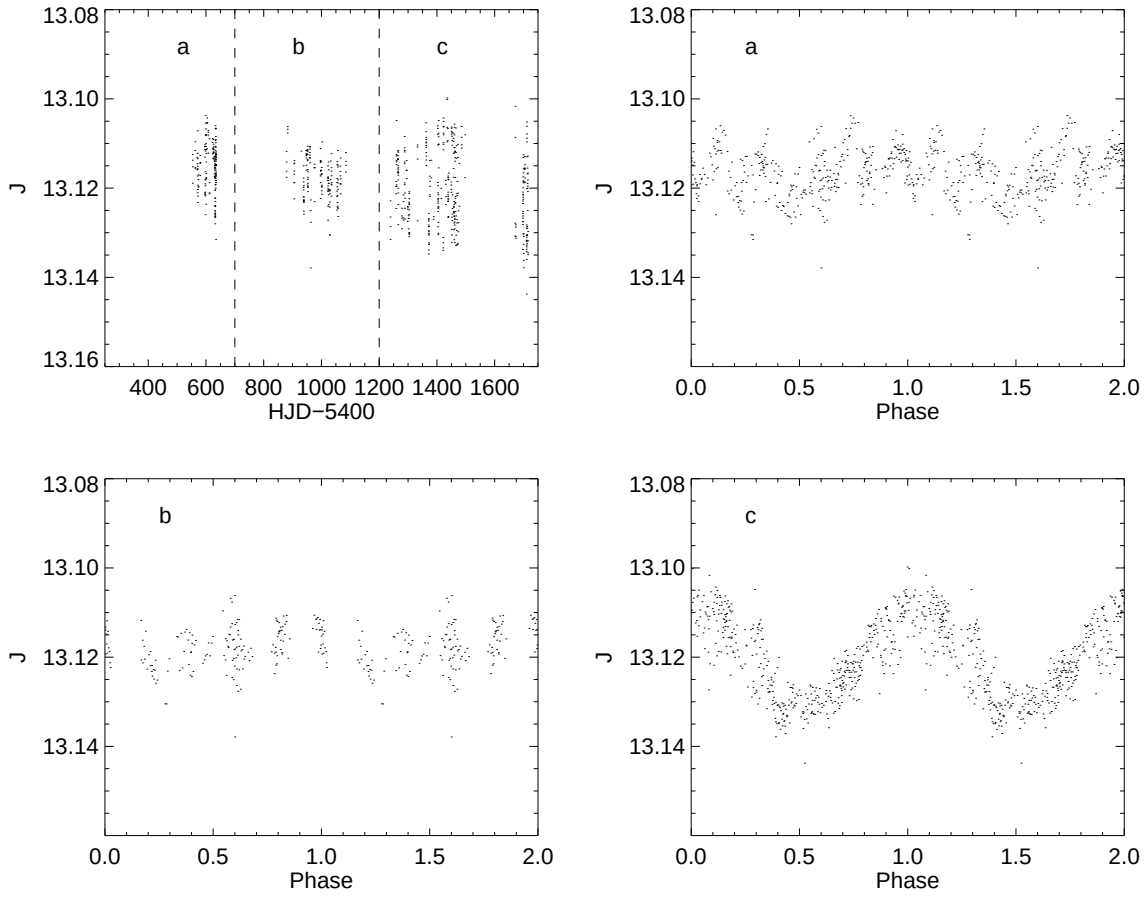

FIGURE 3.7: The unfolded light curve of the star 17d_1_06032, with subsequent plots phase folded over the 1.66 d period. The first two folded light curve plots (*a* and *b*) each show the light curve folded over the period found from the both periodograms performed over the entirity of the observations. These two folded light curve indicate no obvious periodic variability, although a separate periodogram performed on the observations labeled *b* shows a small but non-significant peak corresponding to the later period while a periodogram. The observations labelled *c* however show clear sinusoidal variation, and a seperate periodogram performed on *c* indicates it is these epochs alone contributing the significant 1.66 d peak in the periodogram. This, therefore, seems to be evidence of an inhomogeneity in the spot coverage of the star forming.

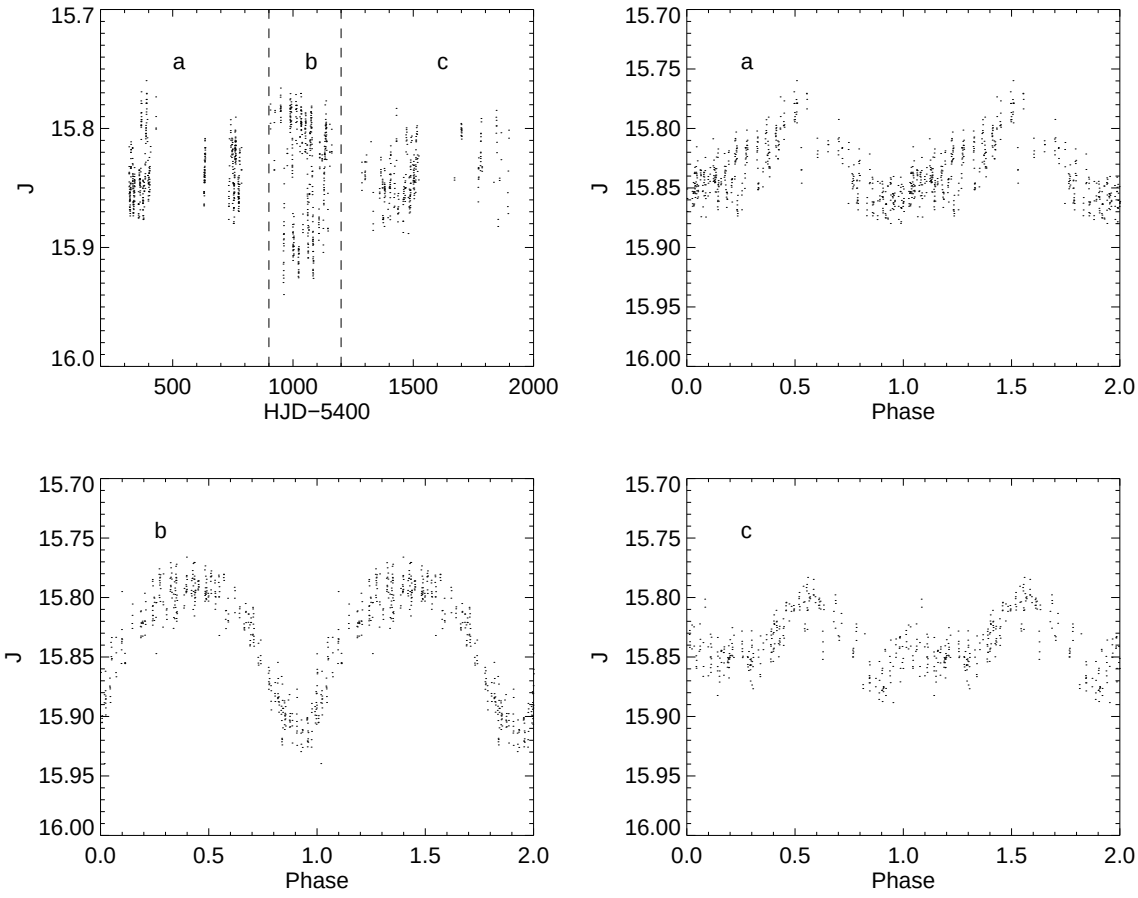

Figure 3.8: The unfolded light curve for 19c_2_05428 (top left) with folded light curves for each different morphology observed (panels *a*, *b* and *c*). Between *a* and *b* it appears as if a large spot, or group of associated spots, has evolved on the darker hemisphere of the star decreasing the brightness of the minima. For the epochs labelled *c* it that appears the large spot or spot group on the darkest hemisphere subsequently decays again over a period of $\sim$ 1yr. The morphology observed in *c* shows a distinctly non-sinusoid or saw tooth form with multiple minima flanking the peak in the light curve, indicating a spot morphology of several medium to large spots or associated spot groups. It is noteworthy that the maximum and minimum remain in phase and the maximum does not vary much in brightness, indicating that either no significant differential rotation has occurred on the time scale of the spot evolution, or that all spots on the star evolve at a constant latitude and that some aspects of spot pattern have remained stable.

3.6 Flaring

No attempt was made to detect transient events, such as flaring, in the M dwarfs in the WTS. The J-band is not optimal for observing flaring; Tofflemire et al. (2012) find no evidence of flaring in JHK_S bands during simultaneous optical and infrared monitoring of three M dwarf stars for 47 hours corresponding to the flaring events they detect in the U-band. One flaring event, as shown in Figure 3.9 is serendipitously found in the periodically variable M4V($\pm$1) star 19d_1_12693, of $\geq\Delta$0.2 in J band magnitude. The incomplete observations of the flare lasted for 49 minutes and thus the overall duration could have been several hours. The brightness of the flare is in contrast to the results of Tofflemire et al. (2012) who expect to find flaring events in the J band occurring on mmag scales, and would transform to a u-band response of > 6 magnitudes. By extrapolation of the frequencies of flaring events per magnitude found by Davenport et al. (2012) such an event would be expected to be observed less than once a year. Due to such a low rate of occurrence it is unlikely that such a flare would obfuscate the detection of periods or a planetary transit and contribute any significant noise, but such high intensity flares may have astrobiological significance (France et al., 2012) and considerations of such flares may help refine the definition of the habitable zone of active M dwarfs. A number of other potential flares are found in the light curves of the stars 19c_4_10571 (Figure A47), 19d_3_01271 (Figure A54), and 19d_3_02216 (Figure A55).

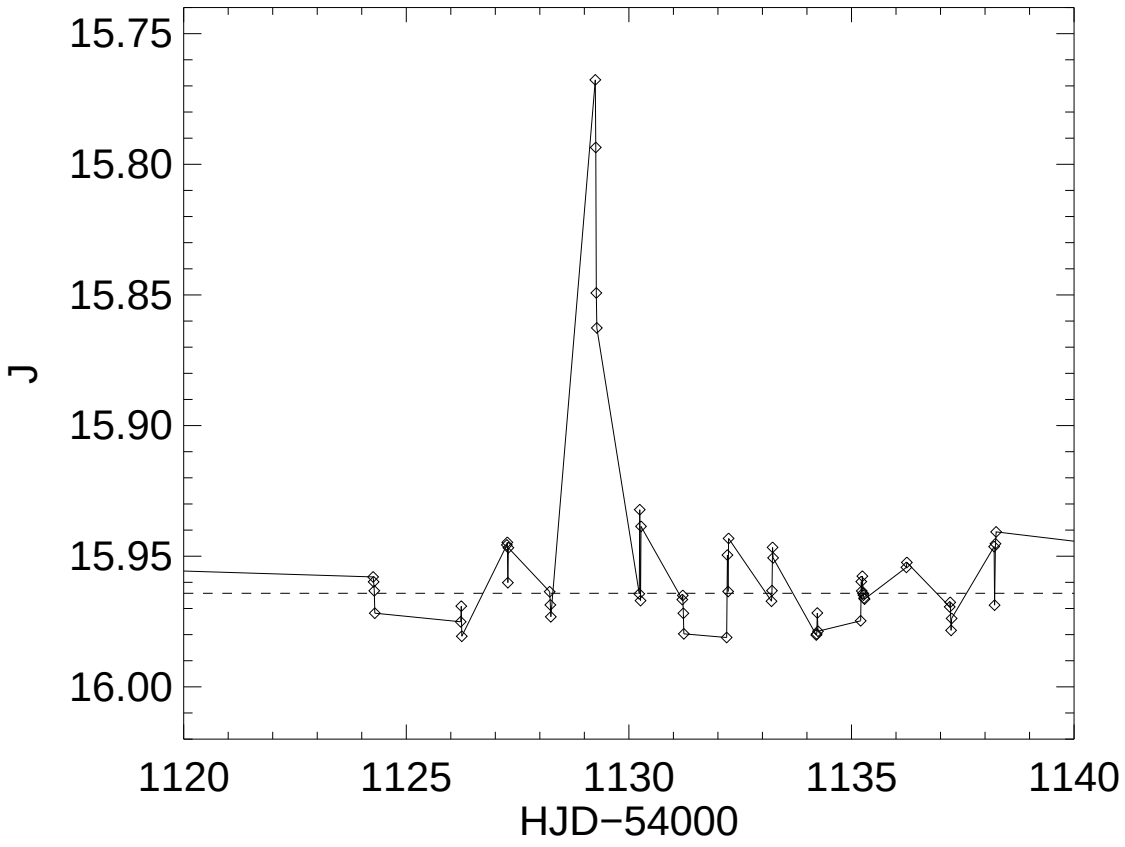

Figure 3.9: The flare observed from the variable M4V star 19d_1_12693. Consecutive observations are joined. The observation of the flare is partial but those observations composing it were made over a 49 minute period.

4

Simulations of Spotted M Dwarfs

The work in Sections 4.1 and 4.2 appears in "J-band Variability of M Dwarfs in the WFCAM Transit Survey", Goulding et al. (2012). Work appearing in Section 4.2 appears in "Periodic variability of spotted M dwarfs in WTS", Goulding et al. (2013).

4.1 Sensitivity analysis

It is important to establish some context for the relatively small fraction of periodically variable M dwarfs in WTS. This may be found by means of testing the sensitivity of the methods used for detecting M dwarfs in such a way that accounts not only for the amplitudes but also the periods. Given that the sample contains field stars of a mix of ages it is not possible to predict what the amplitude and period distribution should be for the sample of M dwarfs in WTS without prior knowledge of their ages.

However, a simulation can be employed to give greater insight into the sensitivity of the Lomb-Scargle periodogram across period and amplitude.

Light curves from each magnitude bin between J=12 and J=17 from the 07hr and 19hr field are selected with no significant peaks corresponding to any period in a Lomb Scargle periodogram. The observations are randomised with respect to time to maintain the same magnitude distribution but to further ensure that no real signal remains in the light curve. Sinusoids with random amplitudes between $\Delta J = 0$ and $\Delta J = 0.2$ and random periods between $P > 0$ and $P = 50$ days are chosen and added to the randomised WTS observation light curves, for 100,000 realisations. The same period detection procedure is performed as described in Section 2.4.1 on each of the 100,000 light curves. Any significant peak not corresponding to 1 d or a fraction thereof is constituted as a detection, since peaks that occur due to the real period but not necessarily corresponding to it (such as those due to aliasing) are found in the real WTS data.

The results of the simulations are shown in Figures 4.1 to 4.4. It is clear that the recovery rate as a function of amplitude is dependent on the noise of the light curve as expected. In the simulations at J=16 and J=17 the sensitivity is poor, reaching a maximum of ∼30% for some periods, up to $\Delta J = 0.03$. This is the range in which the majority of detected amplitudes for the WTS variables lie for brighter stars, and thus this explains the inability to detect many periods for stars dimmer than J=16 despite these stars constituting the majority of the sample. At J=12, however, the method performs relatively well for ΔJ >0.01 and $P < 20$ d and is able to retrieve all injected signals, and therefore it can be assumed that for the brightest stars in the sample the completeness approaches absolute in terms of amplitude dependence for short periods. The results of the simulations also shows the striking effects of the discontinuous observing strategy even in the most complete Winter (19hr) and Summer (07hr) fields. At certain period ranges the Lomb-Scargle periodogram is completely unable to detect any significant period in the light curve (it should be noted in these cases that significant peaks are found corresponding to 1 day and fractions thereof even in these ranges). The only cause for this can be due to aliasing with the windows of

observation in WTS. In the 19hr field, as the number of epochs has exceeded 1000, the periods at which detection is greater as phase coverage for light curves varying with larger periods is improved. The 07hr field suffers from greater period-dependent sensitivity as a result of fewer epochs of observations and therefore less phase coverage at certain periods. In the 07hr field, it is therefore possible that many variable stars with periods greater than 10 days are not detected due to the strong dependency of sensitivity with period. It is not surprising, therefore, that the number of variables detected in each field varies with the number of epochs of observations for each field. Long term variability studies that use continuous monitoring of targets, such as Kepler, should suffer increasingly less from these effects.

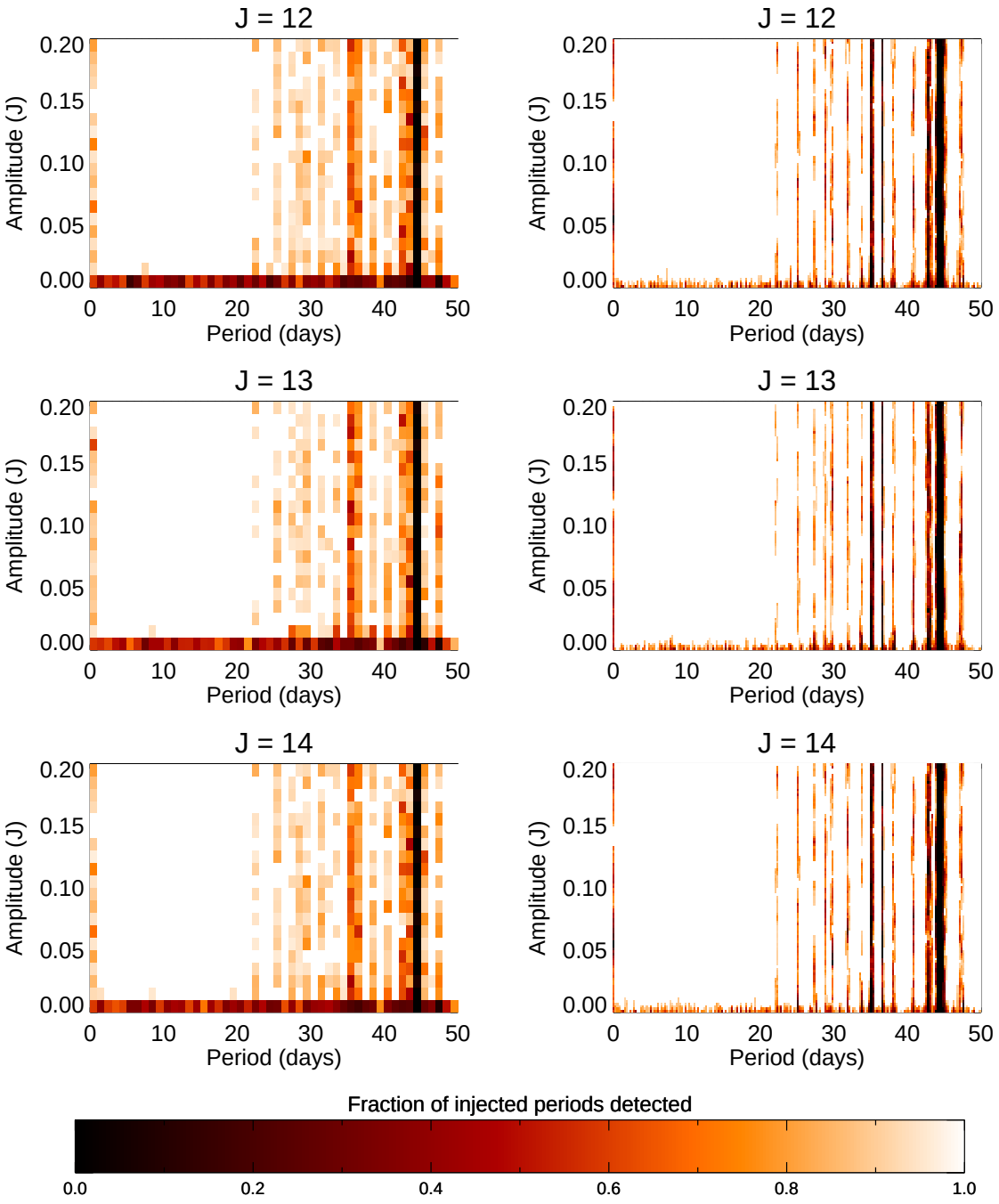

FIGURE 4.1: The binned results of the sensitivity simulation for the 19hr field showing the fraction of simulations in which a significant period not corresponding to the observation period is detected. In the plots on the left the bins are 1 day by 0.01 amplitude with an average of 1666.7 data per bin and on the right they are 0.25 day by 0.002 amplitude with an average of 83.3 data per bin. For magnitudes J=12-15 the insensitivity is dominated by aliasing effects with the period and only affected by noise at the lowest amplitude range.

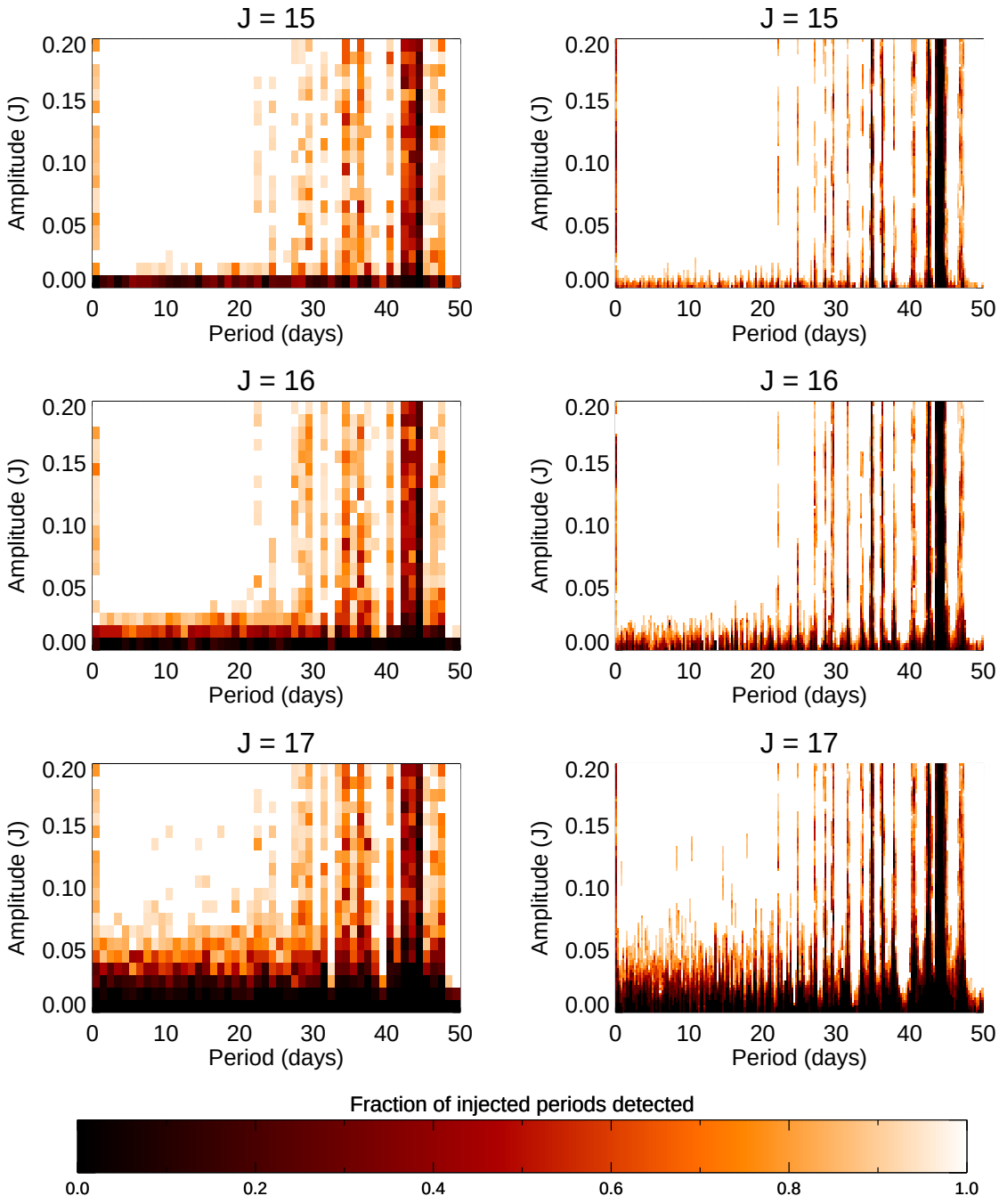

Figure 4.2: As in Figure 4.1. For magnitudes J=15-17 noise begins to become a greater source of insensitivity across the range of amplitudes at which variability in brighter stars was detected.

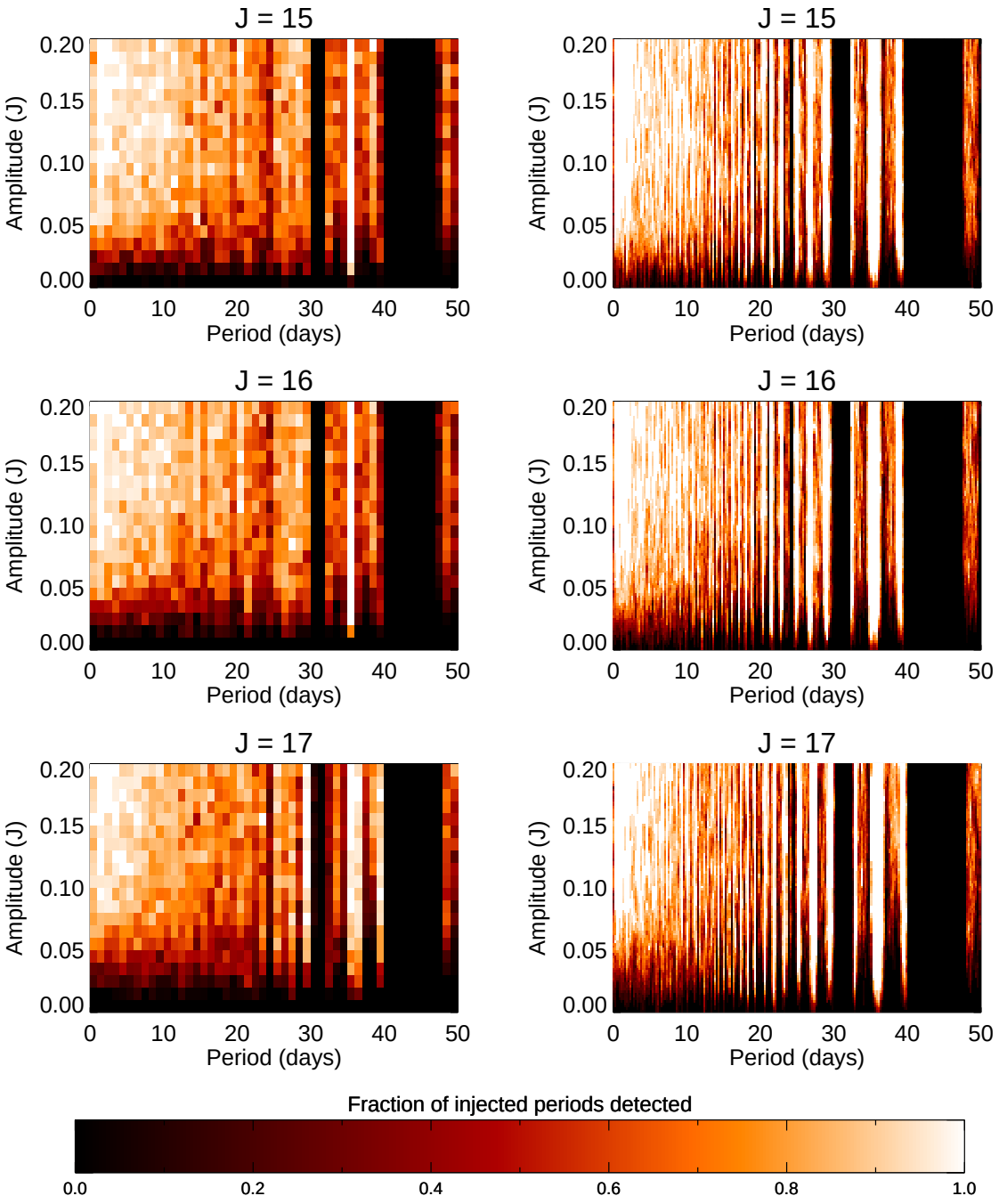

FIGURE 4.3: As in Figure 4.1 but for the 07hr field. There are less epochs of observations for the 07hr field and therefore there is less phase coverage.

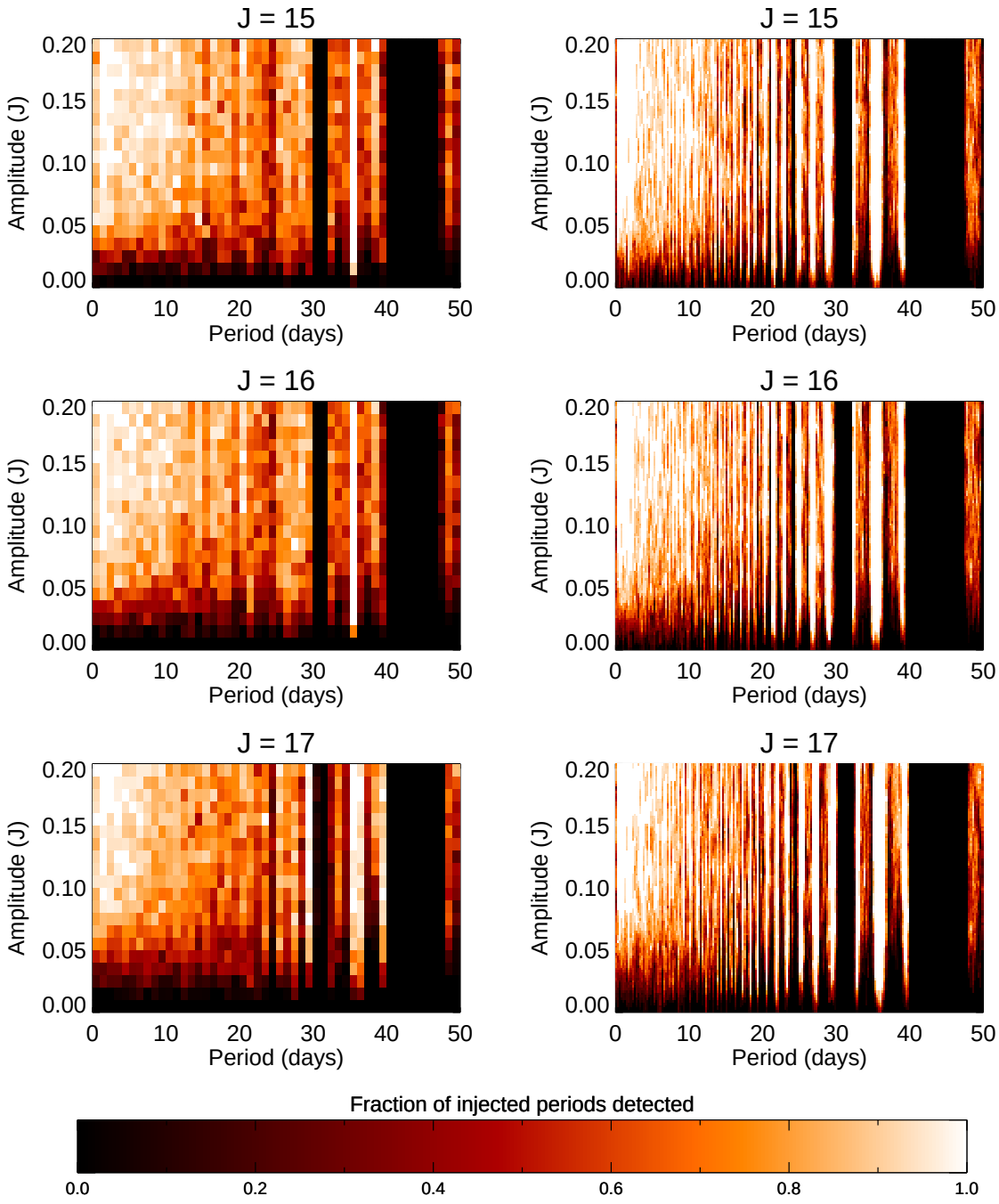

Figure 4.4: As in Figure 4.3.

4.2 Preliminary spot modelling

The results of the variability and period search in the WFCAM transit survey reveal some new and interesting behaviour for variable M dwarfs. Due to the degeneracies discussed in Section 1.2.3, specifically those factors listed by Messina et al. (2001) that contribute towards the amplitude and morphology of a light curve, it is difficult to retrieve much information about the spot coverage of M dwarfs with any certainty. Despite this, parameter windows for any given star can be established using benchmark models.

The star spot simulations utilise a Doppler imaging code called 'Doppler Tomography of Stars' (DOTS; Collier Cameron, 1997). The code can be used to construct a surface brightness map of a star using a two temperature model and spot filling factor. Spectroscopic or photometric data may be synthesised from a constructed spot model of a star. As a first approximation, models of spotted stars that were first introduced and compiled by Jeffers (2005) are used. These were created for testing the effects of unresolved spots on the RS CVn binary SV Cam in eclipsing mapping studies, and later developed and adapted by Barnes et al. (2011) for modelling spotted M dwarfs. The models use the solar spot distribution described in Section 1.2.1 as determined by Bogdan et al. (1988), that is:

$$\frac{\mathrm{d}N}{\mathrm{d}A} = \left(\frac{\mathrm{d}N}{\mathrm{d}A}\right)_{\max} \exp\left[\frac{(\ln A - \ln\langle A\rangle)^2}{2\ln\sigma_A}\right], \tag{4.1}$$

where N is the number of spots, A is the area of a spot umbra, $(dN/DA)_{\max}$ is the maximum height of the distribution, σ_A determines the width of the distribution, and $\langle A\rangle$ represents the mean spot size, and using values as tabulated in Barnes et al. (2011, Table 1) and reproduced here as Table **??**. Spots are distributed randomly latitude and longitude and an umbral to penumbral area ratio of 1:3 is used as per Solanki (1999), with the penumbral temperature set to be midway between the spot and umbral temperature. In addition to these models, a model with a single equatorial spot is used to gauge the effects of a very asymmetric spot coverage and to measure the relative amplitudes at different bands in the simulation. Spot coverage is defined as total fraction of the surface that contains some degree of spot filling. Spotting filling factor

Model	1	2	3	4	5	6
σ_A (MSH)	3.8	5.0	6.8	9.2	12.2	15.8
$(\mathrm{d}N/\mathrm{d}A)_{max}$	5	25	65	125	205	305
Umbral spot coverage	0.0003	0.003	0.016	0.061	0.18	0.48
Total spot filling	0.0003	0.003	0.019	0.009	0.295	0.624

Table 4.1: Relevant values taken from Table 2 in Barnes et al. (2011). Models 1 and 2 correspond to Solar minimum and maximum coverages and Model 6 extended to extremely active cases. MSH is defined as a micro Solar hemisphere, i.e. $5 \times 10^7 \mathrm{A}_\odot$, where $\mathrm{A}_\odot$ is the surface area of the Sun.

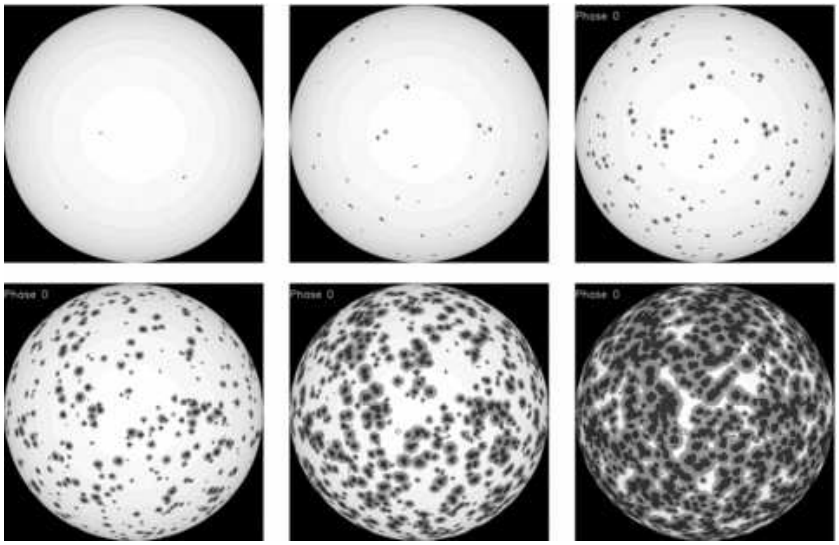

Figure 4.5: Images of the models used for the preliminary simulations as described in Table 4.1. Temperatures scale with brightness: white for the hottest part of the photosphere and black for the coolest.

is the mean spot filling of all the pixels over the surface of the model, where the unspotted photosphere is represented by a filling factor of 1.0 and the coldest area of spot by 0.0. Hence the total spot coverage may be 100% but the filling factor may be 80%. See Table 4.1 for the coverage and filling factors of the models used.

For each model a simulations is run under three different temperature rations: $T_\mathrm{p} - T_\mathrm{s}$ =250K, $T_\mathrm{s} = 0.8T_\mathrm{p}$ and $T_\mathrm{s} = 0.6T_\mathrm{p}$, rounded to the nearest 250K, for a range of photospheric temperatures from 2250K to 3750K at 250K intervals. A light curve is generated for each model by rotating the model at zero inclination and synthesising photometric observations in the J band from stellar SEDs as detailed in Collier Cameron

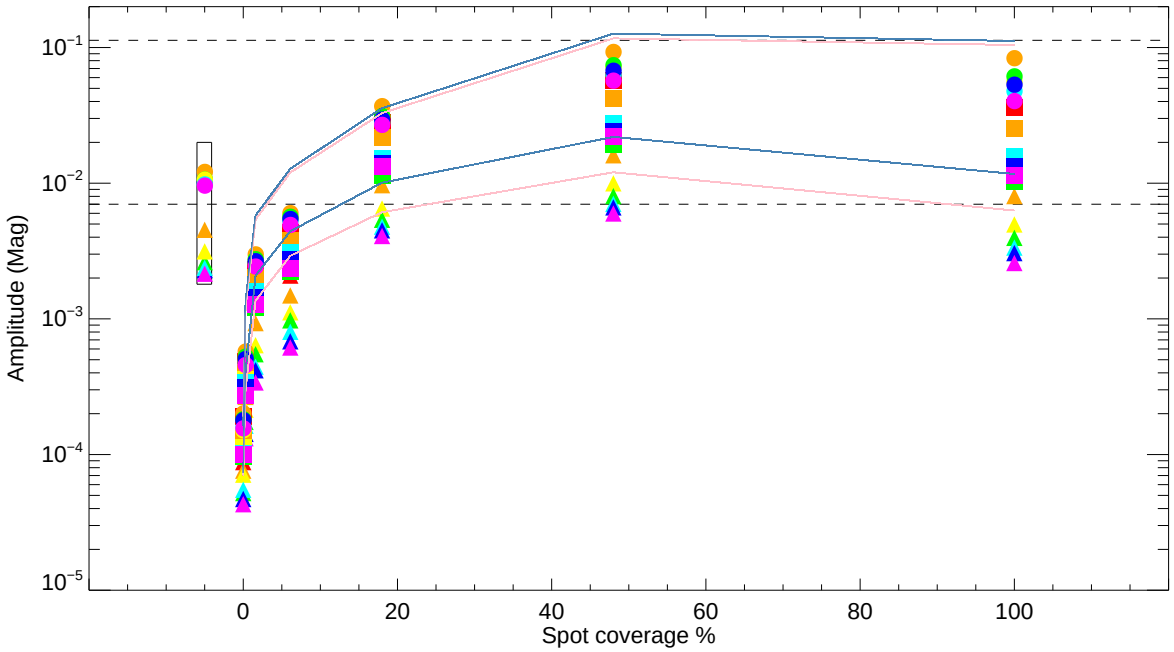

FIGURE 4.6: Output magnitudes for the 8 preliminary DoTS simulations (7 spotted simulations as described in the text and one additional single spot model). Triangles indicate the simulations where $T_s = T_p - 250$K, squares indicates simulations where $T_s = 0.8T_p$ and circles indicate simulations where $T_s = 0.6T_p$. T_s and T_p are always rounded to 250K intervals. The colours from red through green to magenta are from $T_p = 2250$K through $T_p = 3000$K to $T_p = 3500$K respectively. The boxed symbols indicate simulations where a single, large spot with a radius of 5° was placed on the equator. In all simulations i=90°. The pink and blue solid lines indicate the equivalent maximum and minimum range in the I band and V band, respectively, for comparison. The dashed lines indicate the maximum and minimum amplitude of the WTS variable M dwarfs. The downturn seen for the most heavily spotted M dwarfs is due to the increasingly homogeneous photosphere with increasing numbers of spots. The downturn never approaches zero however as contrast between umbrae and penumbrae result in varying photospheric brightness even at 100% spot coverage.

(1997), and the peak to peak amplitude for each light curve is found. The results are plotted in Figure 4.6. An additional model with 100% coverage (∼80% filling factor) was also used for the sake of completion, as well as a model with a single, uniformly dark spot with a width of 5 degrees on the equator.

The models show that a random spot coverage of the order of ∼10% is required in order to produce the amplitudes detected in WTS, with spot models corresponding to 18% coverage and 48% coverage being plausible for the lower T_S/T_p ratios and the 6.1% coverage model being plausible assuming higher contrast spots. There is a general

trend of increasing amplitude with increasing spot coverage. Amplitude increases with increased spot coverage, and for any given coverage with increasing ratio between spot and photospheric temperature ratio. For the most heavily spotted model there is a slight downturn in amplitude. This is because the surface becomes more uniform at high spot filling factors when the photosphere is covered in many spots leading to a lower amplitude brightness variation as the star rotates. The single spot model indicates the amplitudes possible due to a monolithic spot for comparison, and is able to generate a sufficiently large amplitude in there high contrast models albeit with a light curve morphology dissimilar to the sinusoidal and saw-tooth like morphologies indicative of the more complex spot distributions observed.

4.3 A new model for spotted stars

The previous models used invoke a fixed spot pattern on a rotating star in order to generate a light curve. As discussed in Section 1.2.2, the light curve morphology is heavily dependent on the latitudinal and longitudinal distribution of spots and therefore using single static models may not necessarily give a complete comparison to a sample of variable M dwarfs. In order to allow for a more thorough understanding of how correlated the relation between surface coverage, spot temperature and light curve amplitude is, a more dynamic means of modelling is required.

4.3.1 Constructing the model

The models used by Jeffers (2005) and Barnes et al. (2011) are based on a spot distribution parameterisation theoretically extrapolated to more active stars by Solanki (1999). Further means of extrapolating the changes observed between solar minimum and maximum activity are explored by Solanki & Unruh (2004), motivated by the disparity between the values of spot coverage obtained from TiO band monitoring and Doppler imaging. This was in order to address what distribution parameterisation would be capable of producing the correct number of spots detectable by DI for any given filling factor analogous to the one found by TiO observations. Two approaches

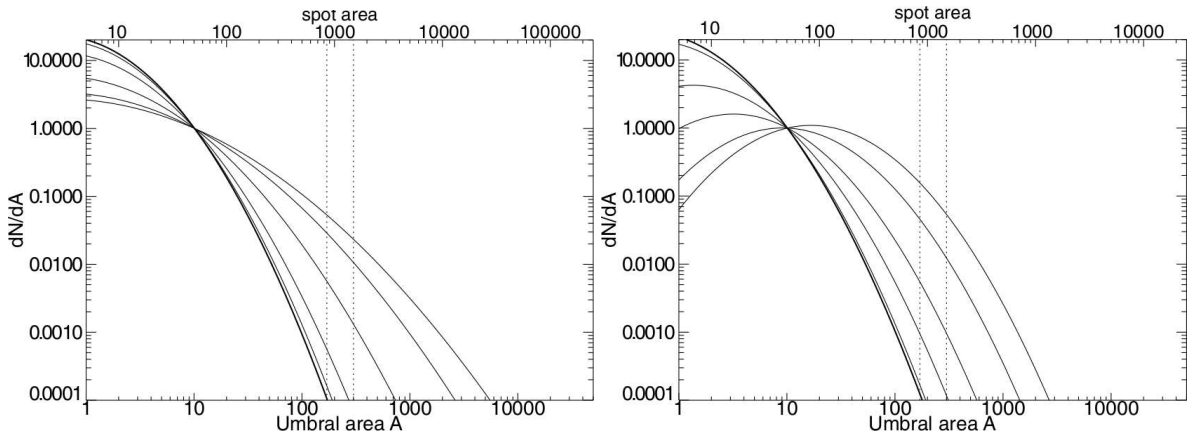

FIGURE 4.7: Excerpts of Figures 3 and 6 from Solanki & Unruh (2004) showing the distribution describing spot sizes for stars more active than the Sun with varying σ_A (left) and $\langle A \rangle$ (right). Solanki & Unruh (2004) finds that a distribution with varying σ_A more efficiently produces the larger spots found in DI observations in the proportion found relative to the filling factors found in TiO band observations.

are taken to extending the distribution to stars with a greater photospheric spot coverage: the first is to increase σ_A, the width of the distribution, which simultaneously produces larger and smaller spots about a fixed mean; the second is to increase the mean spot size $\langle A \rangle$, to produce spots that are on average larger for a distribution of fixed width. In both instances dN/dA is allowed to vary as a product of the coverage and variable parameter. The result of model distributions shows that varying σ_A is a more efficient means of reproducing observed spot distributions obtained from relative TiO and DI measured coverages assuming single spots, whereas varying $\langle A \rangle$ is less efficient at doing so and thus requires some grouping together of spots such that the groups can be resolved by DI. In reality, some combination of these two scenarios may occur. As discussed in Section 1.2.2, no reliable molecular band, analogous to the TiO band used for earlier spectral types, that can be reliably used as a spot filling factor diagnostic has been identified for M dwarfs. Therefore, there is no constrained disparity between spots detected by DI and actual spot filling factors for which a similar extrapolation can be performed. The parameter sets for a number of instances are given in Tables 7 and 8 in Solanki & Unruh (2004), and plotted examples of distributions are shown in Figure 4.7.

The ratio of 1:3 between umbra and penumbra areas assumed by Solanki (1999)

is in fact an under estimation of the size of the penumbra, as typical values in the solar case are approximately 1:5 (Table **??**) in the solar case. Indeed, Solanki & Unruh (2004) invoke spots where the umbral area contributes a fourth of the total spot area. DI observations of spotted M dwarfs by Barnes et al. (2004), Morin et al. (2008b) and Phan-Bao et al. (2009) superficially show that M dwarf spots are similarly constructed with a small, central region of high spot occupancy surrounded by extended penumbral regions of lower occupancy. Such effects, however, could be the result of the smoothing of spot occupancy inherent in Doppler Imaging, and the true umbra to penumbra area ratios are not truly known for stars other than the Sun. Given this, the solar case is assumed pending observation direction as to true nature of stellar spot structures.

In the context of an unclear picture of spot distribution with respect to latitude and longitude, the simplest approach of assigning spot locations randomly across the surface of the stellar sphere is taken. Each spot is assigned random longitudes between $0^\circ - 360^\circ$ and latitudes of $\theta = \arcsin(2x - 1)$ where $x \sim U([0, 1])$ such as to eliminate an artificial clustering of spots at the poles.

The model constraints are used to build a surface pattern for an M dwarf (by means of an IDL procedure). The input parameters are spot coverage, photospheric temperature and spot temperature. The temperatures are gridded at 250K intervals and are such that $\mathrm{T}_s < \mathrm{T}_p$ and $3750 > \mathrm{T}_p > 2250$ and $3500 > \mathrm{T}_s > 1500$. Previous works by Jackson & Jeffries (2013) assumed spot temperature ranges of $0.5 < \mathrm{T}_s/\mathrm{T}_p < 0.9$ and $1500\mathrm{K} \leq \mathrm{T}_s \leq \mathrm{T}_p - 250\mathrm{K}$ by Barnes et al. (2004). Solanki & Unruh (2004) quote values of $\mathrm{T}_s/\mathrm{T}_p \approx 0.7$ from TiO observations for early (late G to K) type active stars. In a review of star spots, Berdyugina (2005, and references therein) tabulates the known values of ΔT across spectral types and fits a trend of decreasing ΔT for cooler photospheric temperatures, with ΔT for M1V/M0V of $\sim$500K.

In the absence of a consensus on M dwarf spot temperatures due to degeneracies inherent in studies of M dwarf spots, the full ranges, as listed above, are initially assumed plausible inputs for the model.

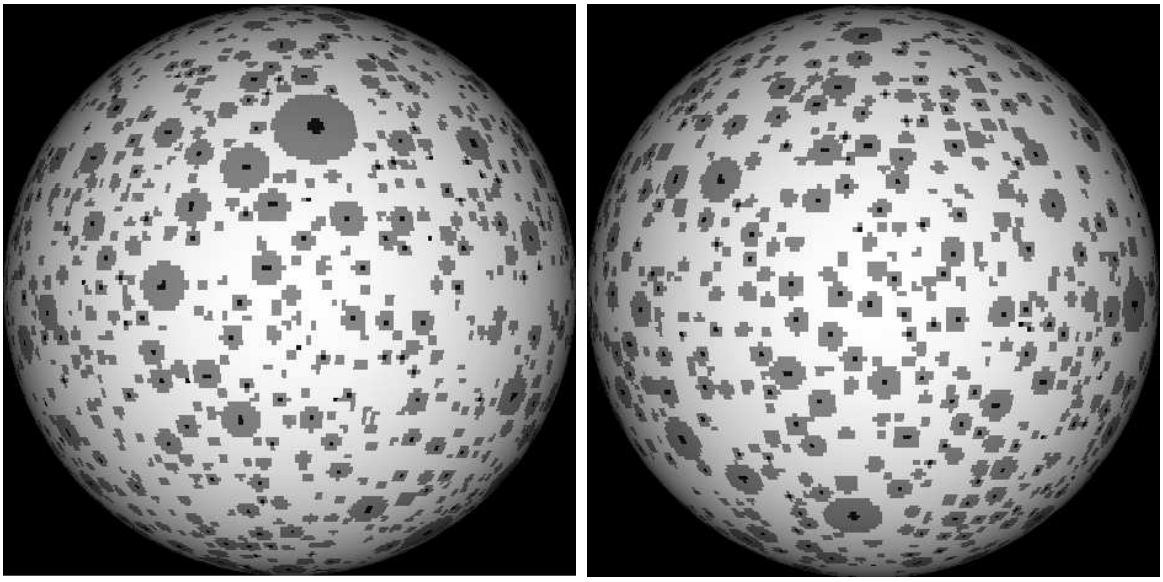

FIGURE 4.8: Example models set to 30% surface coverage, on the left, where σ_A varies with spot coverage, and on the right, where $\langle A \rangle$ varies with spot coverage. As can be seen, varying σ_A generates a model with a mix of larger spots and smaller spots as a wider distribution increases the diversity of spot sizes, whereas varying $\langle A \rangle$ increases the number of larger spots but restricts the diversity of spots, having a prohibitive effect on the generation of large spots. It should be noted that due to pixel resolution in the graphical display of the models, the smallest spots cannot be seen in these images.

4.3.2 Spot coverage and light curves

The simulations in Section 4.2 provide an insight into the general trends expected between spot coverage and light curve amplitude but only reflect the results of eight individual spot patterns. In order to more fully explore this parameter space, simulations are run whereby random spot coverages are generated 14,000 times by the above method for ranges of spot coverage from 0% to 70%. A surface coverage of 70% assuming maximal spot temperature in these models ($T_s = T_p - 250K$) would result in a filling factor of $\sim$0.6, just larger than the upper limit of filling factors found in TiO studies of active stars at 0.56. All input parameters are chosen randomly within the constrains of the conditions described previously. Both cases where either σ_A or $\langle A \rangle$ are allowed to vary with increasing spot coverage are employed in order to establish by which means a spot coverage capable of generating the range of amplitudes found in WTS and other light curves studies is formed.

The spotted star model generated is the input to DoTS which synthesises a light

curve for a complete phase of the star's rotation for an arbitrary period with 120 observations across the entire phase, i.e. one observations for every 3°. A peak-to-peak amplitude is calculated in the V and J bands for the output light curve ($\Delta J, \Delta V$). The complete output amplitudes for the simulations are plotted in Figures 4.9 and 4.10. As can been seen in the figures, the amplitudes generated by stars where the spot distribution changes with spot coverage by varying σ_A are much greater than those for varying $\langle A \rangle$. This is because, as found by Solanki & Unruh (2004), varying σ_A more efficiently produces the larger spots or spot groups observed in Doppler Images of active stars, as shown in the models in Figure 4.8. Such large spots result in less homogeneity in the brightness of the photosphere, as opposed to the spot distribution being accounted for by a peppering of many small spots. This in turns results in larger overall amplitudes in the light curves.

In Figures 4.9 and 4.10, the upper envelope, that is, the minimum boundary that contains all the simulated amplitudes, is plotted in each figure. The upper envelope is found by fitting a power law to the maximum point for each 0.05 width coverage bin. The boundary can be described by a power law with differing parameters for each wavelength and for each case where σ_A and $\langle A \rangle$ vary:

$$\Delta M = nC^m \tag{4.2}$$

where ΔM is amplitude in magnitude, C is the fractional spot coverage, and the values for the variables n and m are given in Table 4.3.2. Ideally, such a power law is obtained so that the envelope is minimised per amplitude bin, so that no amplitude as found from the simulations is greater than the power law for any given coverage. Assuming the model represents a realistic approximation of the spottedness of active M dwarfs then this power law can be used to predict the minimum spot coverage required to generate such an amplitude. In practice, however, the coverage is likely to be greater as all points lie below the envelope, and because the models assume $i = 90°$. Inclination differing from this would attenuate the amplitude of the light curve by reducing the fraction of the photosphere that is rotated through the viewing angle.

The results of the simulations for the case of varying σ_A are plotted in Figures 4.11

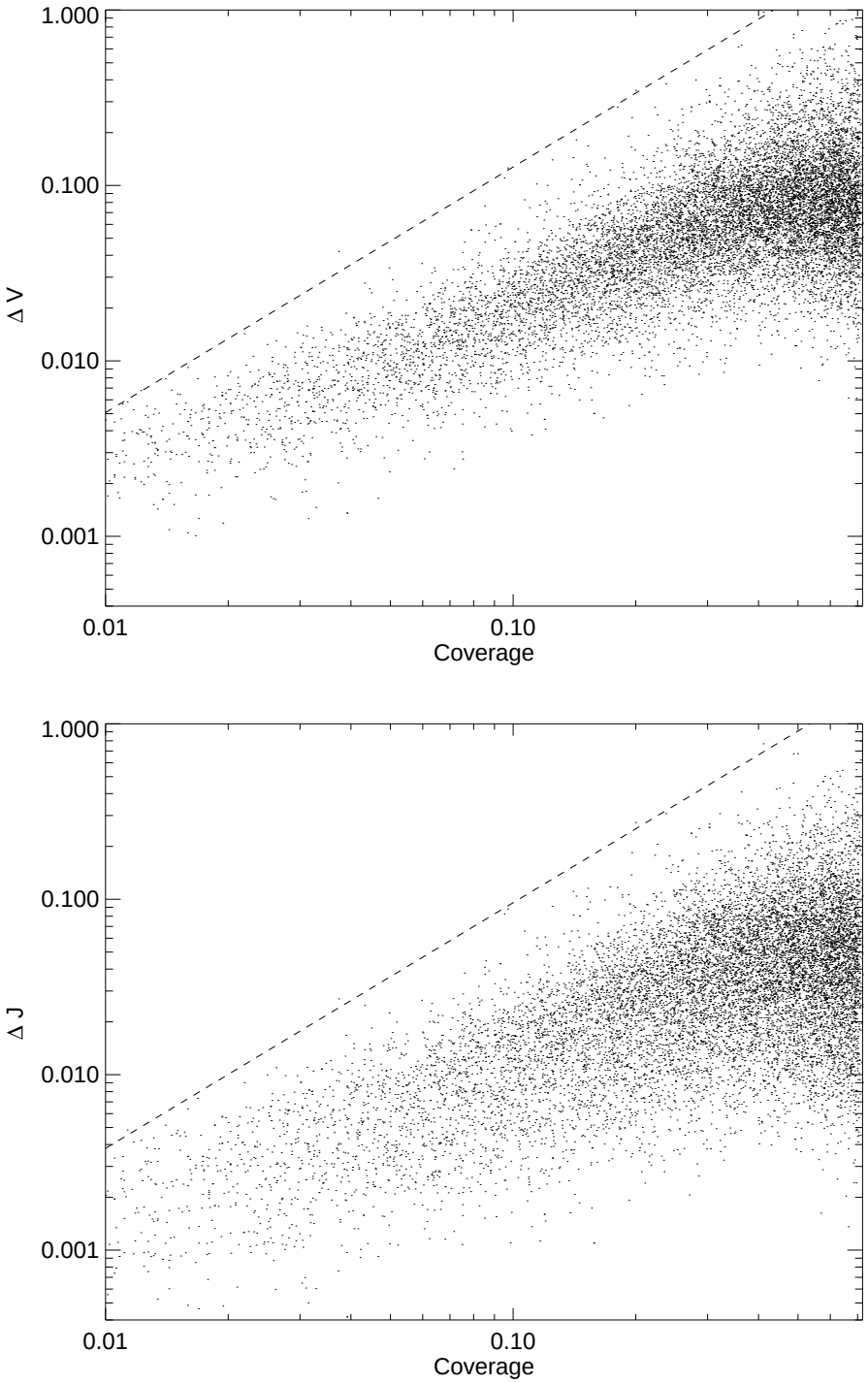

FIGURE 4.9: The overall output of amplitudes (ΔV, ΔJ) for the simulations of spotted M dwarfs in log-log space for σ_A varying with coverage. The upper envelope for each band is marked by the dashed line. There is a downturn in amplitudes at $\sim$0.5 spot coverage as increasing the spottedness decreases the unspotted photosphere and surface brightness becomes more homogeneous. This is not accounted for in the power law as spot coverages $>$0.5 are still capable of producing increasingly larger amplitudes if the spot coverage is sufficiently asymmetric.

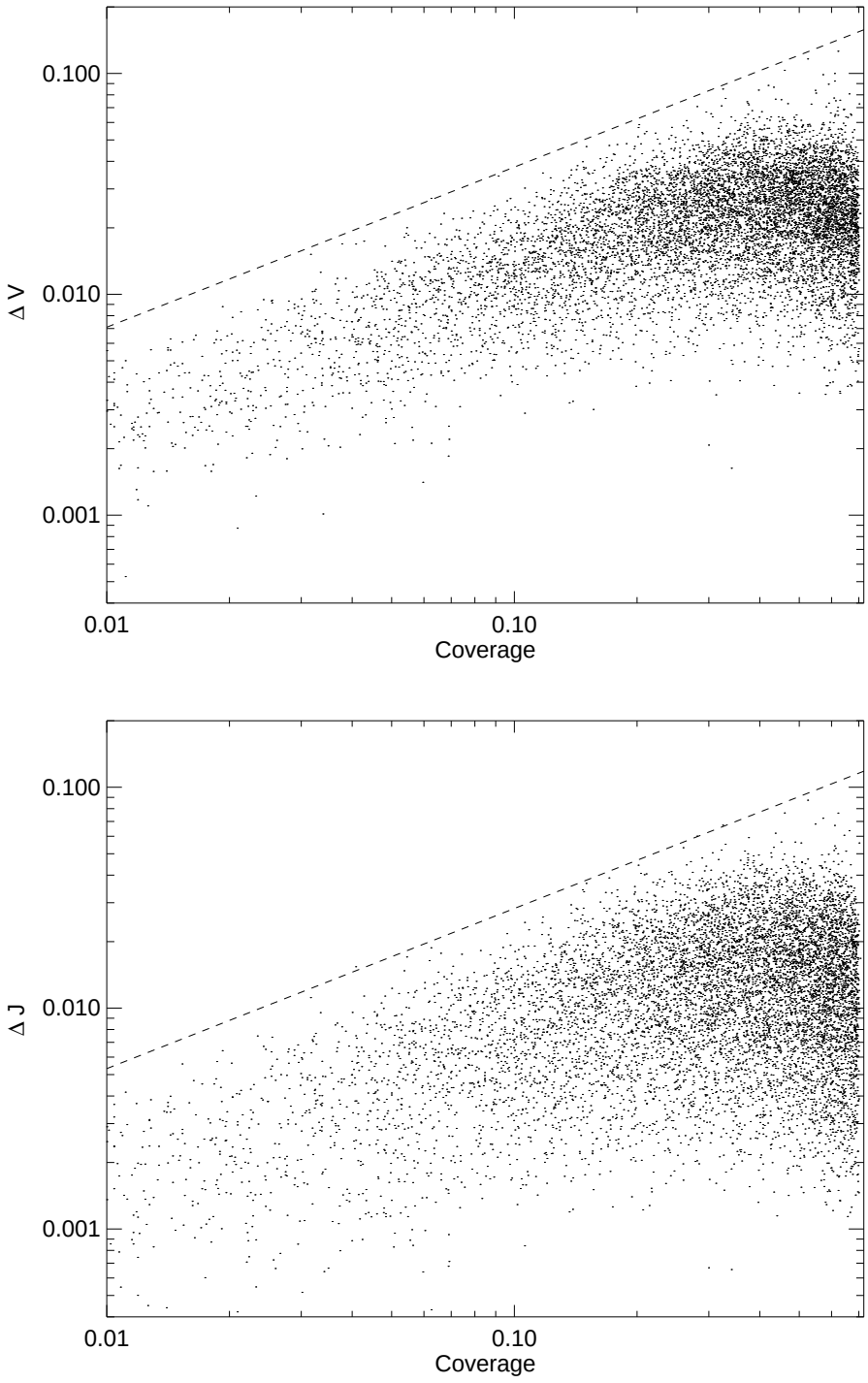

FIGURE 4.10: As for Figure 4.9 but for varying $\langle A \rangle$.

Parameters	n	m
$\langle A \rangle$, V	0.20	0.725
$\langle A \rangle$, J	0.15	0.725
σ_a, V	3.2	1.4
σ_a, J	2.4	1.4

TABLE 4.2: The values of power law in equation 4.2 for each parameter set.

(V) and 4.12 (J) and for the case of varying $\langle A \rangle$ in Figures 4.11 to 4.14. The data are binned according to the difference between the photospheric and spot temperatures. The ΔT=250K bin shows the greatest degree of dispersion due to the disparities in the range of photospheric temperatures which could occupy it, whereas the ΔT=1750K bin shows limited dispersion because only the hottest models could occupy it. The dispersions per bin are a consequence of the limits placed on the model by the maximum photospheric temperature allowed and the minimum spot temperature allowed.

The reason for the dispersion of any given ΔT is due to the non-linear dependence on flux with temperature. By the Stefan-Boltzmann law, the flux is dependent on T^4. Thus, to illustrate this, if we assume two cases in which $\Delta T = 250K$ where in one case we have $1750^4/2000^4 = 0.586$ and in the other $3750^4/3500^4 = 0.759$ we can see the proportional contribution to luminosity attenuation due to some spotted fraction of the photosphere is greater for a lower T_p. This is interesting to note in the context of the observed *decrease* in amplitude with respect to later spectral types (Section 3.3). The rate at which amplitudes change is different for the V and J band. In the V band, the rate of change of amplitude with respect to increasing ΔT is non-linear and is much greater for small values of ΔT than it is for larger values due to the sensitivity of the V band to small changes in temperature, such that moderate increases in ΔT, for example, on the scale sampled in these simulations, produce very small gains in amplitude. In the J band the rate of change of flux with ΔT is more linear and thus the amplitudes are more dispersed as moderate changes in flux effect moderate changes in amplitude. This additionally results in the larger overall amplitudes in the V band.

The comparison between the two sets of results for varying σ_A and varying $\langle A \rangle$ allows

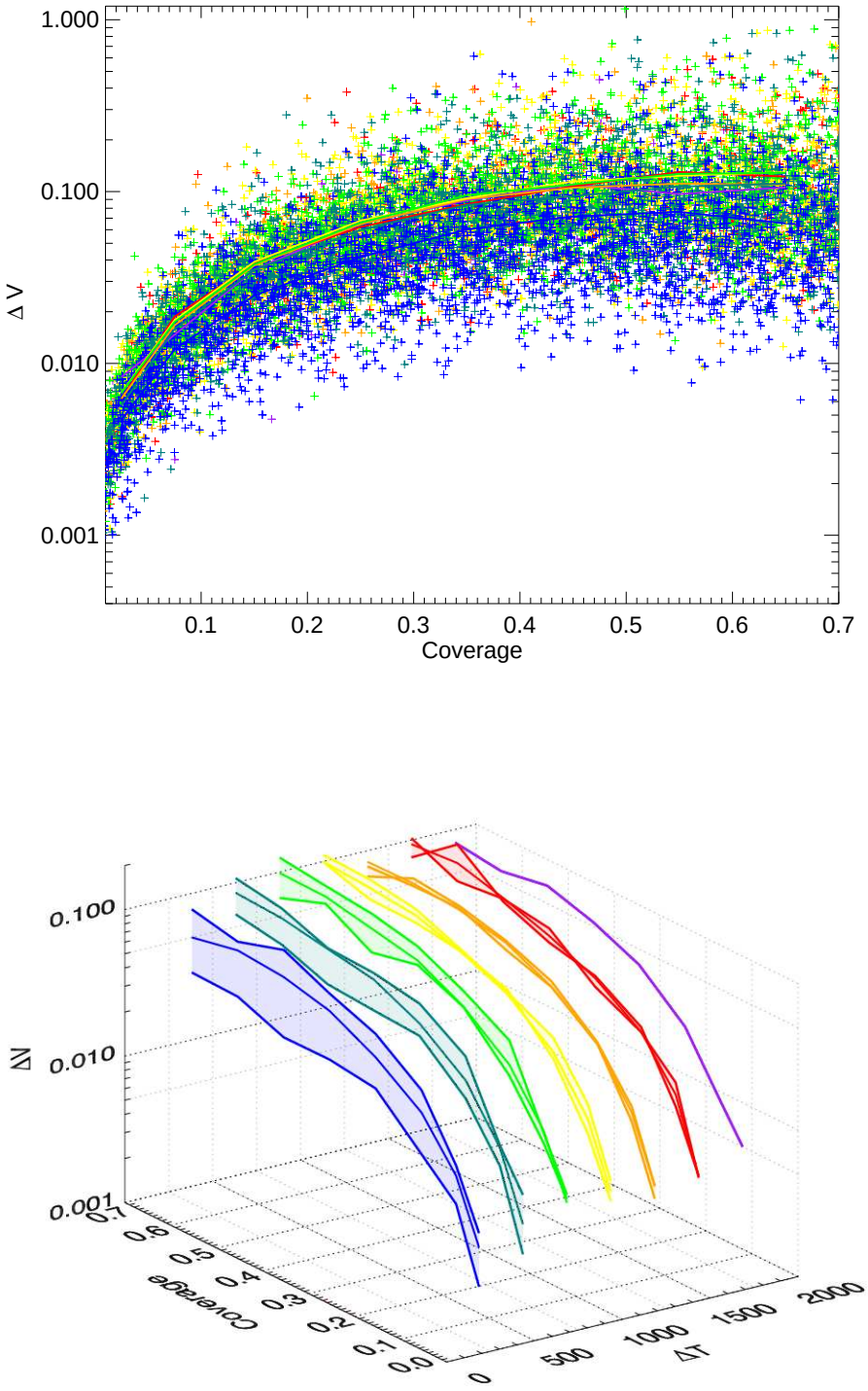

FIGURE 4.11: *Key* : ΔT = 1750K, 1500K. 1250K, 1000K, 750K, 500K, 250K where $\Delta T = T_p - T_s$. The upper plot shows all the V band amplitudes found from the simulation where $\sigma_A$varies. The solid lines show the average for each ΔT bin. In the lower plot each polygon represents the range of amplitudes resulting from the simulations, the upper solid line in each polygon is for the minimum T_p, and lower line is for the maximum T_p, and the middle solid line is the average as per the upper figure.

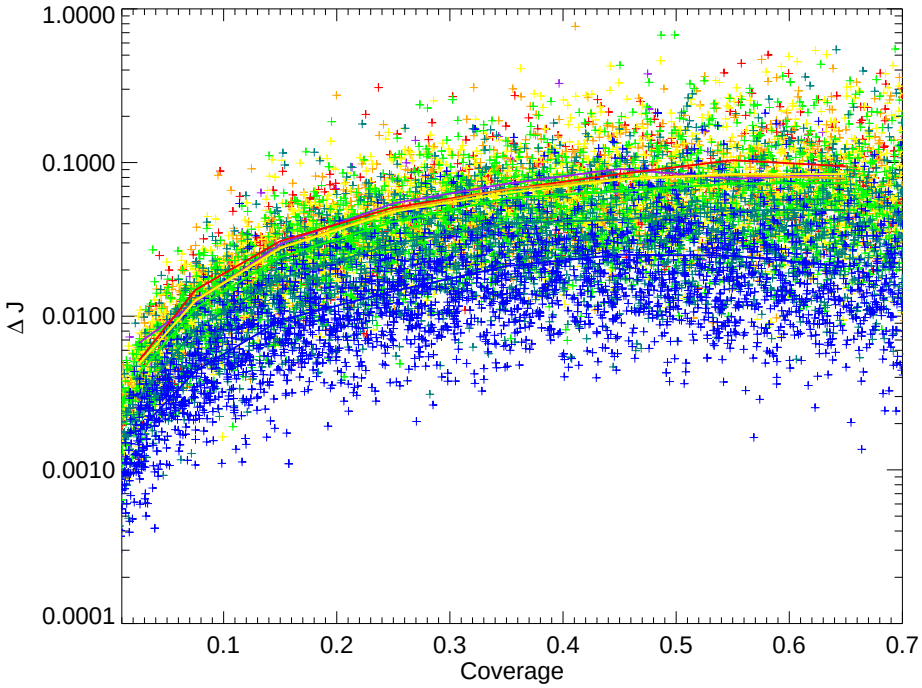

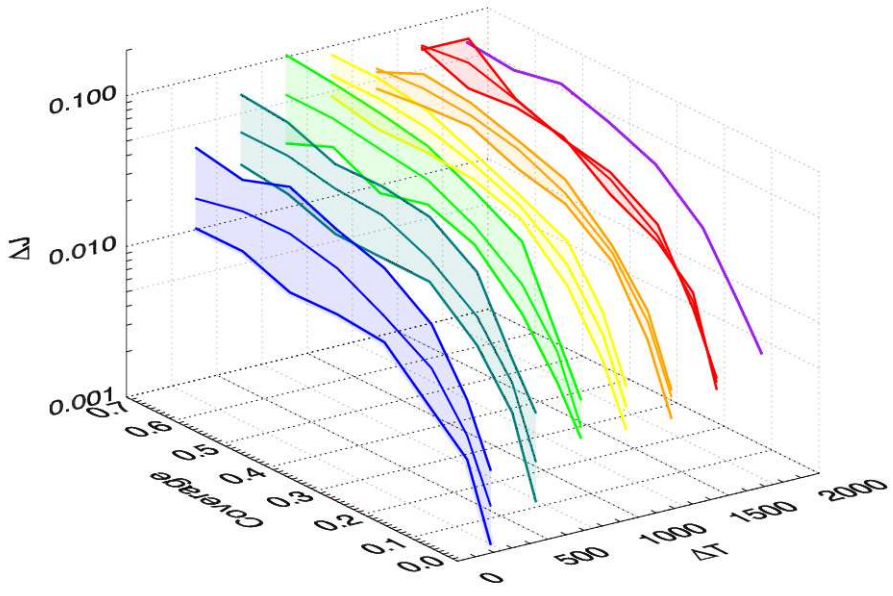

FIGURE 4.12: As for Figure 4.11 but for the J band amplitudes.

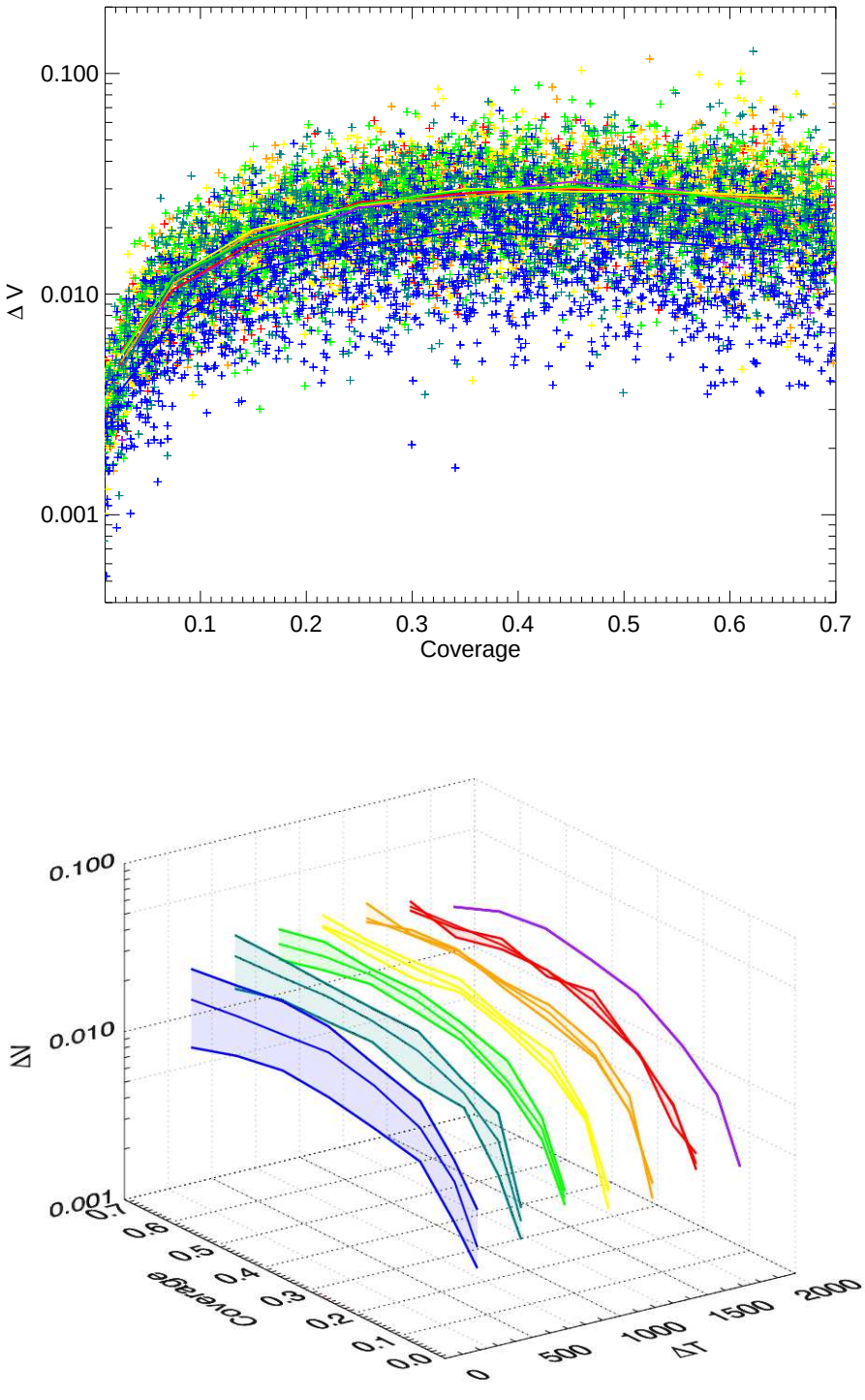

FIGURE 4.13: As for Figure 4.11 but for varying $\langle A \rangle$.

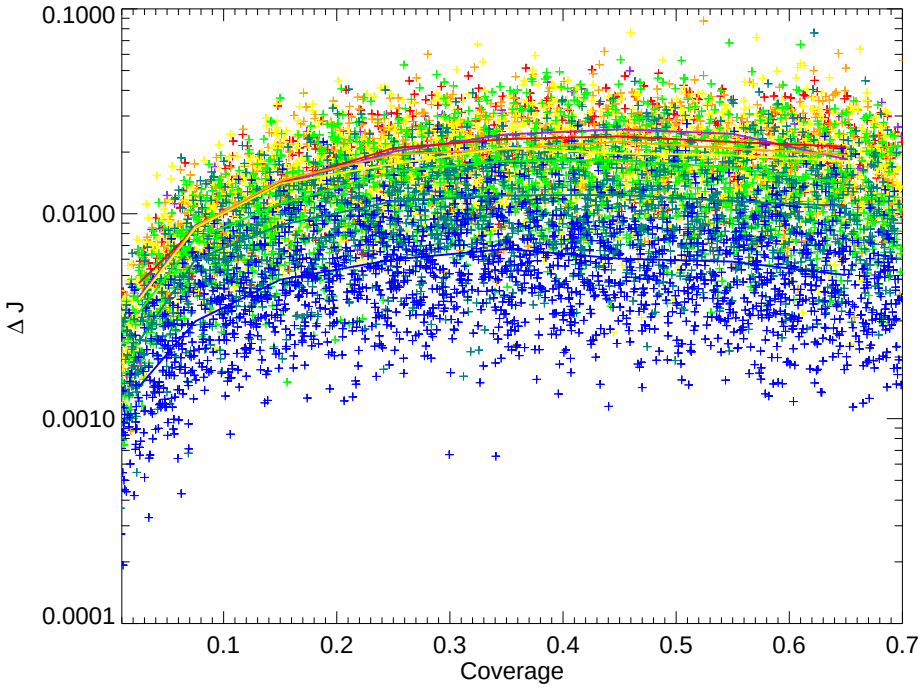

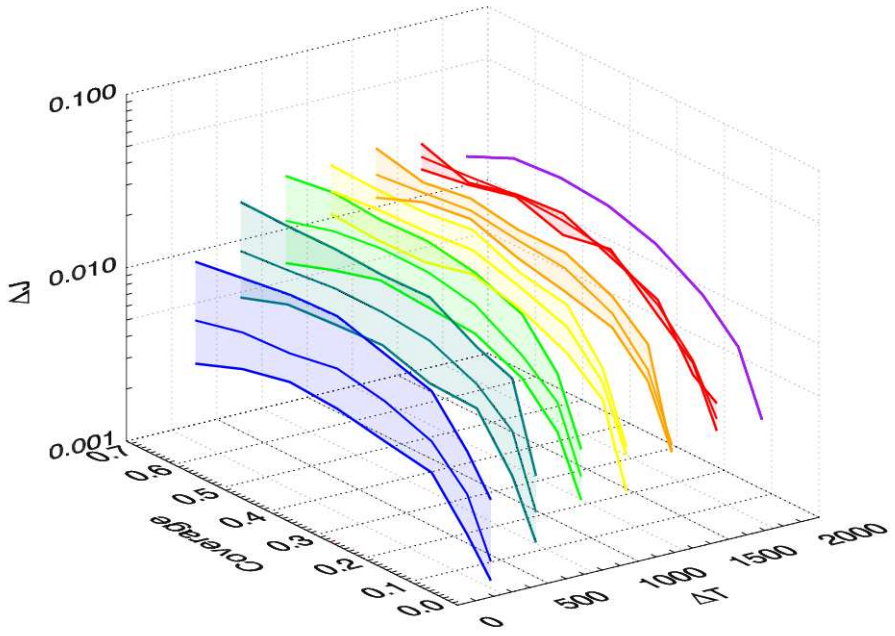

FIGURE 4.14: As for Figure 4.13 but for the J band amplitudes.

for comparisons of the effectiveness of each scenario in explaining the results of the periodically variable M dwarf sample in WTS. For values of $\langle A \rangle$ that vary linearly with increased activity, the simulations achieve the range of amplitudes found in WTS only for the larger values of ΔT. For ΔT = 250K and 500K only the coolest stars had amplitudes of $\sim$0.01 in J and simulations for larger values of ΔT only managed to produce amplitudes of the scale of the largest found in WTS as outliers typically for the cooler stars in those bins. This is expected from the simulations made by Solanki & Unruh (2004) who show that larger $\langle A \rangle$ is typically unable to produce the large spots observed in DIs of active stars. A lack of larger spots necessarily means that, withholding large groups of spots approximating larger spots, the spot coverage is more evenly distributed over the photosphere and thus cannot cause large amplitude modulation. Conversely, varying σ_A with activity, which increases the proportion of larger spots, efficiently populates the range of amplitudes found in WTS for all values of ΔT. A notable conclusion to be derived from this is that large light curve amplitudes are necessarily either indicative of large spots or large spot groups acting as effective proxies for large spots.

The interpretation of these simulations in terms of inferring which case is truly representative of active M dwarfs is mired through the lack of knowing the true fraction of periodically variable M dwarfs. For example, it could be the case that a spot distribution that is driven by varying $\langle A \rangle$ does indeed best describe the distributions found on M dwarfs and the very small fraction found in WTS represents the extreme outliers with the greatest amplitudes, as WTS is not sensitive to the ranges of amplitudes most efficiently populated by varying $\langle A \rangle$. The opposing case would imply that varying σ_A is a more realistic parameterisation but the absolute variable M dwarf fraction is small. The ability of the latter case to better explain DI observations of a disparity between the spot area accounted for by large spots and the true filling factor of earlier active stars supports this parameterisation, however. It is not possible to use the simulations to infer a true value of completeness for the methods used to detect the variable sample. Samples of variable M dwarfs in the literature, in more complete surveys (i.e. those conducted in the V band or another band where amplitudes are

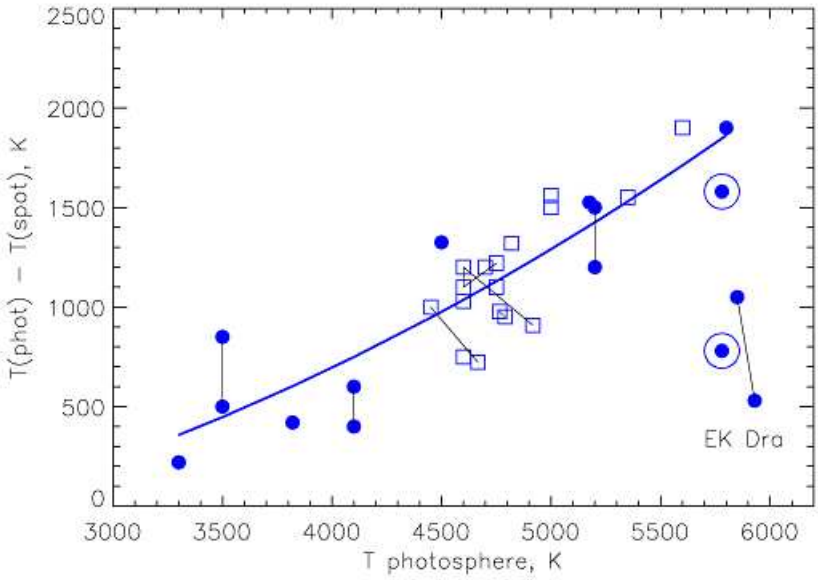

FIGURE 4.15: Figure 7 from Berdyugina (2005) showing compiled empirical values for ΔT illustrating the decreasing trend in ΔT for cooler photospheres. While few observations of spot temperatures have been made for early M dwarfs and none have been made for mid to late M dwarfs, these observations can be used to inform estimates of spot coverages for given amplitudes by constraining which models likely represent realistic combinations of T_s for a given T_p .

typically larger), either lack a quantification of the completeness themselves or lack sufficient details to extrapolate a completeness to a predicted real fraction of periodically variable M dwarfs. Assuming the simulations here can be taken as being representative of real spot modulation on M dwarfs, surveys such as Kepler, which are sensitive to even the lowest amplitudes found here, should be able to definitively provide a fraction of periodically variable M dwarfs.

The expanded simulations can constrain the possible range of surface coverages for variable M dwarfs found in WTS. In order to make estimates of the surface coverage a value for ΔT must be assumed. Assuming the values of ΔT compiled by Berdyugina (2005, see Figure 4.15) hold for the WTS variables, and that σ_A is the driver behind the larger spots observed on M dwarfs, surface coverages can be interpolated from the ΔT binned results of the simulations. The WTS variable M dwarfs are of spectral types M0 to M4, approximately corresponding to the T_p values of 3750K to 3000K respectively. For this range of T_p the value of ΔT is shown by Berdyugina (2005) to be 250K-500K,

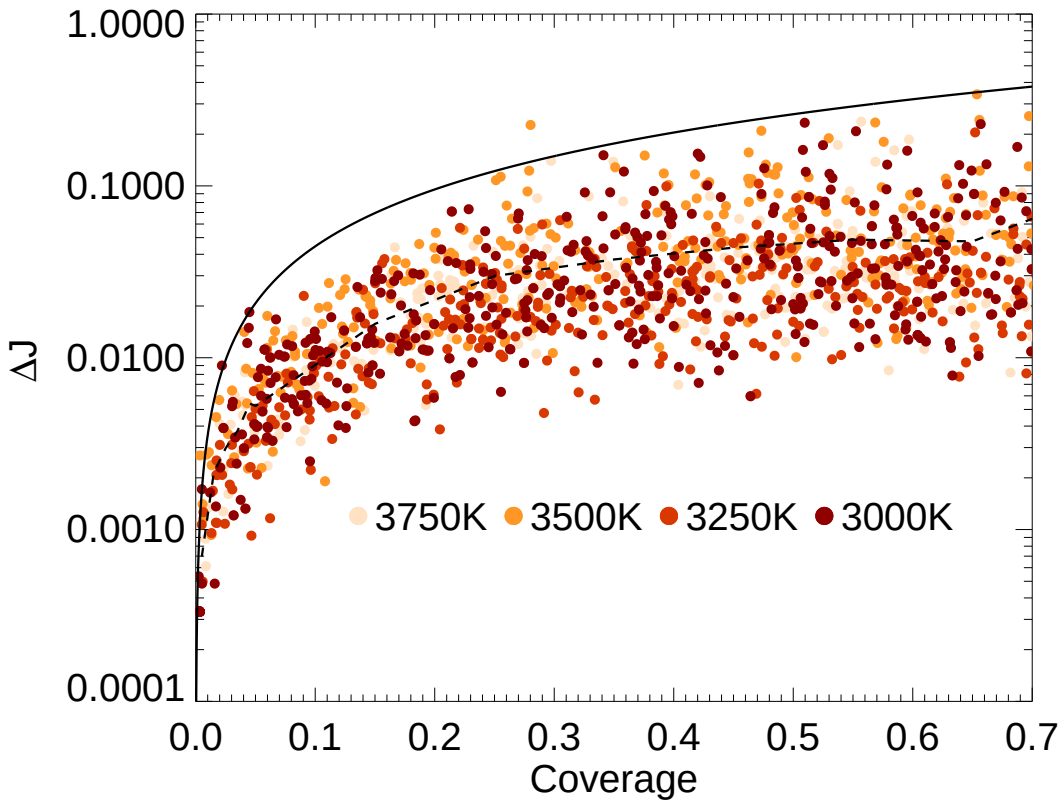

FIGURE 4.16: The amplitudes and surface coverages of the simulated variables in the bins used to predict surface coverages for the WTS variable M dwarfs. The mean value is indicated by the dashed line and the maximum value power law by the solid line. The colours indicate the photospheric temperatures of the simulated stars as follow: 3750K, 3500K, 3250K, 3000K.

corroborated by later DI observations by Morin et al. (2008a). For the purposes of these estimates, it is assumed that WTS M dwarfs typically obey the trend compiled by Berdyugina (2005). For the estimates of surface coverage for the WTS variable M dwarfs, therefore, only four bins of the simulations are considered: T_p=3750K, ΔT =500K; T_p=3500K, ΔT =500K; T_p=3250K, ΔT =500K; and T_p=3000K, ΔT =250K. The data for these bins are plotted in Figure 4.16 and approximately occupy the same distribution. The minimum surface coverage for any amplitude is found by a power law with values adapted for these data with n =0.62 and m =1.2, and the mean of the amplitudes for varying surface coverage predicts a mean surface coverage for each star. The coverages interpolated from the light curve amplitudes are shown in Table 4.3.

The ranges of minimum amplitudes found here indicates the somewhat obvious

result that surface coverage of spots on these M dwarfs is considerably larger than that of the Sun, ranging between 3.0% and 25.2%. It is important to again consider these values as minima in the context of inclination; as these simulations were performed at $i = 90°$, the interpolated coverages of the real M dwarfs will be less than the real surface coverages so long as their inclination is $< 90°$. The interpolated mean surface coverages also attenuate due to this effect. The minimum value found here is 9.2% while the uppermost values exceed the range of simulations at >70%. It may be the case that the simulations used here do in fact underestimate the true ΔT for these stars and the largest amplitude examples are just those that happen to exhibit a $\Delta T > 500K$. To take into account this possibility surface coverages were interpolated assuming the power law with parameters as described in Table 4.3.2. For this case the surface coverages vary between 1.8% and 11.4%. This range of surface coverages is similar to that compiled from DI observations by Solanki & Unruh (2004) for late G and early K dwarfs, while the mean values found from these simulations occupy a range more comparable to the filling factors obtained from TiO observations.

Another noteworthy result of the simulations is the range of surface coverages that are not detectable in the WTS. Even in the brightest unsaturated M dwarfs ($J = 12$) it becomes difficult to detect stars where the amplitude is small (i.e. $\Delta J < 0.1$) where periodicity detection rates are at best $\sim 60\%$. Assuming that the least spotted star found in WTS represents the lower amplitude limit to that which could be detected in WTS, with a minimum surface coverage of >1.8%, it could be the case that the majority of M dwarfs, while considerably more heavily spotted than the Sun, have spot coverages below this value. This bodes well for planetary transit surveys. For such surface coverages the maximum spot sizes are typically <1000 MSH. An Earth-radius planet eclipsing an M dwarf, for comparison, eclipses ∼10% this portion of the stellar disc. Assuming these models hold true and it is the case that the majority of M dwarfs lack a spotted coverage of more than a few per cent, the assumptions made by Ballerini et al. (2012) regarding spot coverage as a uniform factor of transit depth alteration seem an appropriate treatment. Therefore effects of individual spots on transit profiles should be small and transient due to the relative size and darkness

Name	ST	ΔJ	C_{min}	C_{mean}	Name	ST	ΔJ	C_{min}	C_{mean}
03d_1_04395	M1	0.017	0.042	0.159	19b_3_03003	M4	0.015	0.037	0.143
03e_1_02053	K5	0.015	0.037	0.143	19b_3_08292	M0	0.028	0.066	0.237
03e_2_03325	M1	0.024	0.057	0.208	19b_3_09282	M1	0.028	0.066	0.237
03f_1_03040	M4	0.037	0.085	0.346	19b_3_12753	M3	0.037	0.085	0.346
03h_2_01177	M0	0.020	0.048	0.180	19c_2_05428	K7	0.115	0.237	0.823
03h_4_04646	M3	0.017	0.042	0.159	19c_3_01804	M3	0.036	0.083	0.332
07b_2_02081	M4	0.029	0.068	0.244	19c_3_03299	M0	0.016	0.039	0.152
07b_2_02125	M3	0.014	0.035	0.133	19c_3_04974	M2	0.010	0.026	0.095
07b_2_02237	M4	0.019	0.046	0.173	19c_3_05921	M4	0.016	0.039	0.152
07b_3_00631	M4	0.011	0.028	0.105	19c_3_11273	M3	0.016	0.039	0.152
07b_3_02281	M0	0.043	0.097	0.439	19c_4_10571	M4	0.032	0.074	0.278
07c_2_00282	M2	0.013	0.033	0.124	19c_4_12623	M3	0.034	0.078	0.305
07c_2_00294	M3	0.012	0.030	0.114	19d_1_06078	M1	0.023	0.055	0.201
07c_4_04250	M3	0.009	0.023	0.086	19d_1_06603	M2	0.027	0.064	0.230
07d_1_02956	M1	0.037	0.085	0.346	19d_1_12693	M4	0.033	0.076	0.292
07d_1_03180	M0	0.042	0.095	0.423	19d_2_00740	M3	0.025	0.059	0.216
07d_1_06063	M3	0.013	0.033	0.124	19d_3_01140	M4	0.019	0.046	0.173
07d_4_03625	M3	0.028	0.066	0.237	19d_3_01271	M4	0.026	0.061	0.223
07d_4_04577	M0	0.047	0.105	0.517	19d_3_02216	M4	0.023	0.055	0.201
07e_2_01022	K2	0.078	0.167	0.727	19d_3_03681	M0	0.019	0.046	0.173
07e_2_02466	K7	0.110	0.228	0.833	19d_3_05922	M2	0.029	0.068	0.244
07e_2_06232	M0	0.023	0.055	0.201	19d_3_07286	M0	0.026	0.061	0.223
07f_3_00675	M1	0.051	0.113	0.659	19e_1_03204	M1	0.042	0.095	0.423
07f_3_03235	M4	0.019	0.046	0.173	19e_2_02880	M4	0.013	0.033	0.124
07g_1_04615	M0	0.012	0.030	0.114	19e_2_09200	M4	0.018	0.044	0.166
07h_1_03267	M0	0.022	0.053	0.194	19e_3_09622	M4	0.025	0.059	0.216
71a_1_01533	—	0.055	0.121	0.669	19f_3_08798	M4	0.026	0.061	0.223
17a_3_00950	—	0.060	0.131	0.682	19f_3_12800	M3	0.018	0.044	0.166
17a_3_03244	—	0.068	0.147	0.702	19f_4_06780	M0	0.048	0.107	0.651
17d_1_06032	—	0.022	0.053	0.194	19g_1_04348	M0	0.042	0.095	0.423
19a_1_00838	M0	0.025	0.059	0.216	19g_1_05313	M4	0.041	0.093	0.408
19a_1_10932	M0	0.030	0.070	0.252	19g_1_10773	M4	0.023	0.055	0.201
19a_3_01981	M4	0.027	0.064	0.230	19g_2_03649	M3	0.053	0.117	0.664
19a_3_10735	M0	0.059	0.129	0.679	19g_3_06870	M4	0.014	0.035	0.133
19a_3_11735	M0	0.081	0.172	0.735	19g_4_00989	M4	0.025	0.059	0.216
19b_1_10542	M1	0.038	0.087	0.361	19h_3_16170	M0	0.052	0.115	0.661

TABLE 4.3: The interpolated spot coverage fractions for the WTS variable M dwarfs. C_{min} is the minimum surface coverage interpolated from the upper envelope power law as described in the text and C_{mean} is the interpolated from the mean amplitudes from each surface 0.05 width surface coverage bin in the simulations.

of the largest spots in these cases. For more heavily spotted M dwarfs, effects such as those described in Section 1.3 would become greater considerations.

4.4 Dynamic models of evolving spot patterns

Another potential explanation for the small fraction of variable M dwarfs is the possibility that spot modulated variabilities in M dwarf light curve do not remain coherent over the time scales over which WTS observations are made due to evolving spots on the stars. Examples in WTS as shown in Section 3.5 show dramatic changes in amplitude and morphology over time scales of months to years, and Kepler observations have shown that such changes can wholly distort a M dwarf light curve such that it would not remain coherent for more than a few months (Muirhead et al., 2013). The observation by Ciardi et al. (2011) that $\sim$75% of the variable M dwarfs observed by Kepler exhibit low-level white-noise-like variability raises the possibility that the variability on these stars is due to a small and continuously evolving spot coverage.

As discussed in Section 1.2.1, while our undertsanbding of the evolution of Sun spots has benefited from centuries of observations, no comparable studies have been possible for other stars. Knowledge of spot distributions and evolution on stars cooler than the Sun has been derived from only a few DI observations performed over the last two decades and very recent light curve observations made in transit surveys such as Kepler and WTS. As such there are no parameterisations, for example, of the distribution of spot decay rates or the life times of spots on M dwarfs. It is therefore not possible to quantitatively relate the changes in spot morphology observed in light curves to some description of spot evolution on M dwarfs. In order to explore possible scenarios for the observed variable behaviour it is therefore necessary to employ speculative models evolving spot patterns on M dwarfs. As discussed in Section 1.2.3, previous attempts to model spotted M dwarfs have been dependent on analytically fitting the evolution of the minimum number of spots required to explain the morphology of a light curve (e.g. Frasca et al., 2009). It is known that large spots (i.e. those that can be detected by Doppler Imaging) only account for some fraction of the total spot coverage derived

from TiO band filling factors (Solanki & Unruh, 2004), and that in some cases models with limited numbers of spots are not complex enough to describe the full morphology of some light curves (Harrison et al., 2012). Here, therefore, the approach is taken to applying varying rates of spot evolution to the Solanki & Unruh (2004) models extrapolated to active stars.

Baumann & Solanki (2005) model the log normally distributed decay rates of spots, previously postulated by Howard (1992) and Martinez Pillet et al. (1993) and find their models capable of reproducing observations. Due to the ubiquity of log normality in spot parameterisations in the Sun and the ability of such distributions to be usefully applicable for describing the spot size distributions on more active stars, it seems appropriate to assume that spots on M dwarfs decay with a lognormal distribution of decay rates for the purpose of simulations. These decay rates are modelled following Baumann & Solanki (2005) using the linear decay law for spots, who find results that are indistinguishable from a quadratic treatment. As well as applying solar decay rates to M dwarfs, cases where the decay rates are 10 and 100 times greater than the solar case are also modelled. For the relatively rapid growth rates of spots, the assumption is made that they are 70% greater than the decay rates following observations by Javaraiah (2011).

To meet the criteria that both the instantaneous distribution and the maximum distribution both obey the same lognormal distribution, the maximum sizes of the spots are given the initial condition of having a random fractional area of maximum extent which each spot can grow to from, and decay from to, zero. This additionally simplifies the placement of spots, such that they do not overlap, and thus the constrainment of a fractional surface coverage. In effect this means that the surface coverage of the star is free to vary between zero and the maximum input coverage and at any given epoch will on average be at 50% of the maximum input coverage. The evolution of the penumbra and the umbra follow the evolution of each component as observed in sunspots, following Schlichenmaier et al. (2010b) and Gafeira et al. (2012), with the umbra emerging first and the penumbra growing after the umbra has reached maximum size. Both umbra and penumbra decay uniformly.

In order to limit the variables in the simulations, as described in Table 4.4, to just those that are subject to the evolving spots single values of T_p , T_s and ΔT are chosen to provide a range of amplitudes characterised by the simulations in Section 4.3, specifically T_p =3500K, T_s =2500K such that ΔT =1000K. These values are effectively arbitrary, but keeping them constant enables the effects only from varying spot coverages to be analysed. Two cases, one where maximum spot coverage is 0.2 and another where it is 0.6 are considered. These values should give average coverages of 0.1 and 0.3, typical values for the spot coverages of the WTS variable M dwarfs. Periods occupying the range of those found in WTS are sampled, specifically 1.62d, 12.74d, 22.34d and 51.84d, and are chosen to avoid effects of picking near-integer day periods outside of period-space regions in which the Lomb-Scargle performs poorly in the 19hr field. Decay rates distributions are set to either 1, 10, or 100 times the solar decay rates.

A program written primarily in IDL builds the spot pattern as per previous simulations with additional subroutines to evolve and monitor the individual spots on a 0.001d temporal resolution. The coordinates of the spots are rotated about the sphere of the star with the rotation period. The "observing strategy" is to run DoTS for a snapshot of the model at epochs identical to those of the 19hr field star observations. The output simulated flux values from DoTS are converted into a magnitude and normalised to give a light curve varying relative to an arbitrary mean. Each simulation is performed 20 times so as to produce examples of different spot patterns and thus different light curve morphologies.

For reference, simulated stars are given names that reflect the input parameters: maximum surface coverage, period, and solar decay rate factor, and iteration. For example, c0.2_p12.74_d10.0_4 is the fourth instance under the same parameterisation of the simulation with a surface maximum coverage of 20%, a period of 12.74 days and an average spot decay rate 10 times that of the Sun.

4.4.1 Morphological results

The results of the simulations provide some interesting cases that are both quantitatively and qualitatively similar to observed instances of varying variability in Kepler

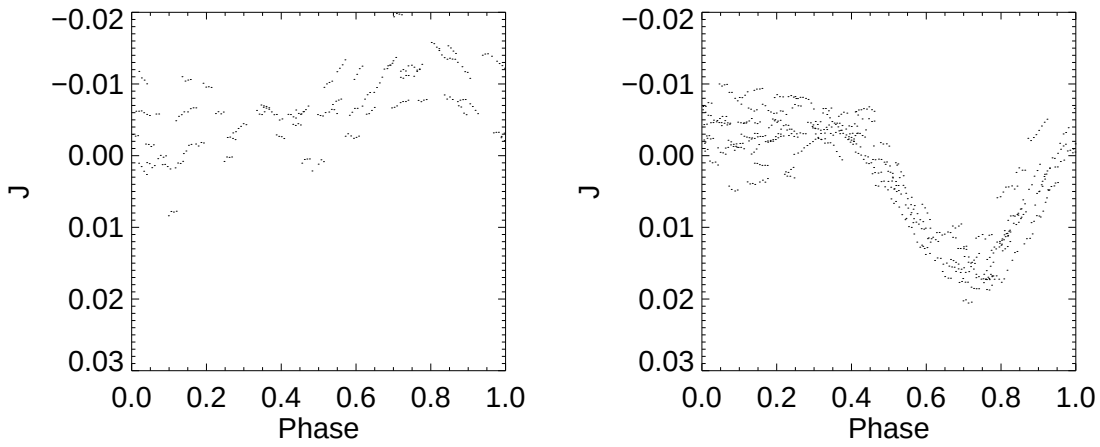

Figure 4.17: The simulation c0.20_p1.62_d10.00_1. The plot on the left shows the data from the first 200 days of observation, the data on the right the subsequent observations. The dichotomous nature and the lack of transition between the two states is simply due to the rapid emergence of the largest spot occurring during the analogous Summer month observations when the star would not be observed in the 19hr field.

and WTS. The simulation c0.20_p1.62_d10.00_1 (Figure 4.17) bears an extremely similar resemblance to the variability seen in 17d_1_06032 (Figure 3.7), which shows no apparent variability in the earliest section of the light curve and then a very significant, sinusoid-like variability in the latter part of amplitude ∼0.02. The same behaviour is seen in the simulation of c0.20_p12.74_d100.00_3 and others. This is driven by the change in spot coverage from that dominated by medium sized spots distributed across the star to one with medium spots and one large spot emerging. The transition is not seen as it occurs during a period when no observations are made, effectively the Summer months for the 19hr field, and thus the light curve appears to exist in two distinct states as with the example found in the 17hr field. Similar scenarios are found in a variety of other simulations where a star with low amplitude variability changes seemingly dichotomously to one with a pronounced, larger amplitude sinusoidal variability, driven by the emergence of large spot. In some cases the reverse can be seen, where a large spot decays and a strong sinusoidal signal disappears.

Other examples show changes in light curve morphology similar to that seen in the stars 19c_2_05428 (Figure 3.8) and 07e_2_02466 (Figure 3.6). Simulations such as c0.60_p12.74_d10.00_3 maintain the same morphology but vary in amplitude throughout

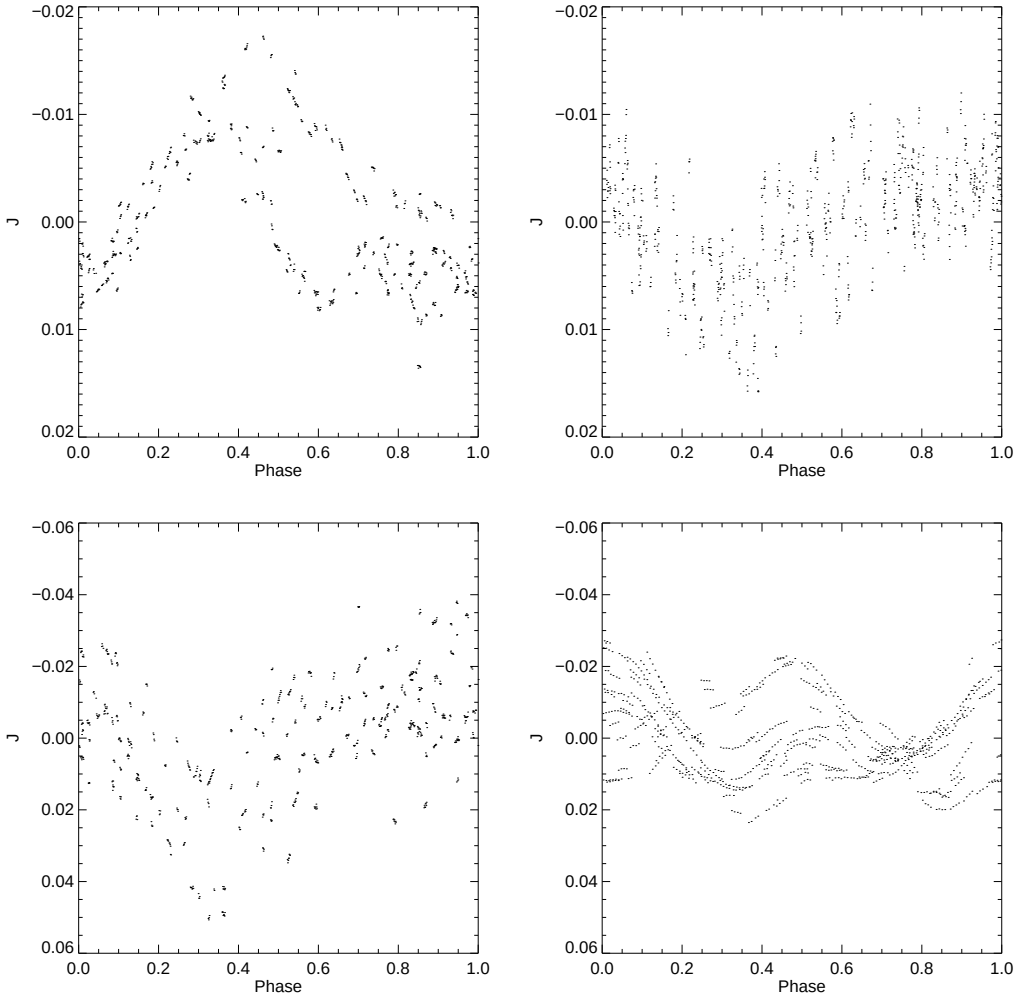

FIGURE 4.18: Examples of synthetic light curves referred to in the text, from the top left going clockwise: c0.20_p12.74_d1.00_1, c0.20_p22.34_d100.00_3, c0.60_p1.62_d1.00_6, c0.60_p12.74_d10.00_3.

the simulation as medium sized and small spots evolve over the surface mimicking other simulations such as c0.2_p12.74_d1.00_1 and c0.2_p22.34_d100.00_3 mimic 07e_2_02466, similarly transitioning between one morphology to another (Figure 4.18) . A few simulations, such as c60_p1.62_d1.00_6, resemble the evolving spot coverage observed by Muirhead et al. (2013) in the white dwarf-M dwarf binary KOI-256 where light curve morphology switches from having one peak and trough per phase to two. The examples are shown in Figure 4.18.

The overall morphological picture emergent from the simulations is a diverse one. The variety of morphologies produced by the simulations includes many examples that

bare no resemblance to those found in WTS and other M dwarf variability surveys. Although there is a superficial resemblance of some light curves to eclipsing binaries, these can be distinguished from effects due to spots either by their short periods, in the case of contact binaries, or by wholly flat maxima. It may be that some scenarios are not physically possible and that sinusoid and saw-tooth like morphologies are prevalent for physical reasons. Conversely, it could be that common methods for detecting M dwarfs are not sensitive to the more complex morphologies that can emerge from distributed, evolving spot patterns. Such simulations do not necessarily exist in a specific parameter space, although instances where the light curve appears to move through several morphologies typical require lower decay rates where $D = 1$ or $D = 10$. Many of the simulations have a morphology that mimics that of eclipsing binaries with two peaks and troughs per phase but with much longer periods caused by having spots dimming the star on opposing East-West hemispheres.

4.4.2 Noise resulting from spot evolution

Small variations in spot coverage can be expected to invoke noise in the light curve that would appear as white-noise-like. Ciardi et al. (2011) find that for many M dwarfs in the Kepler sample white noise like variation is common. The simulations of M dwarfs with varying spot coverage can be used to estimate the contribution to the noise from spot evolution for different spot coverages and decay rates. In order to measure this, a smoothing spline composed of eight parabolic segments is fitted to each phase folded light curve and subtracted, to remove the most significant trend due to spot modulation. The standard deviation of the light curve after this subtraction is then found. The remaining light curve is not strictly one of pure white noise but instead composed of fragments of the light curve at various superposed stages of spot evolution.

Figure 4.19 shows the mean standard deviation of each light curve after the average modulations have been subtracted. It is apparent in all instances that the noise increases with a greater decay rate; it is also expected that this effect is greater for long periods as more spot evolution would occur per phase as the time scale for spot

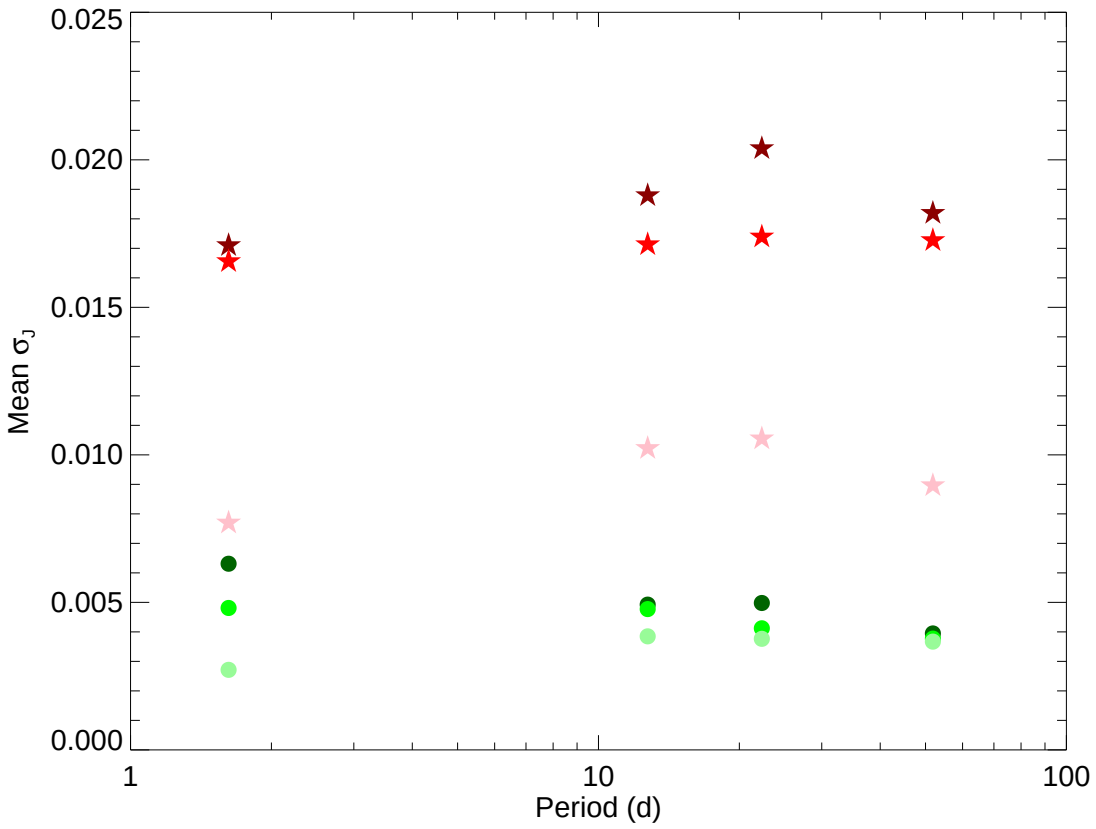

FIGURE 4.19: Period and spot evolution rate against mean light curve standard deviation for the simulations. Red stars are for $C = 0.6$ and green circles for $C = 0.2$. The colours go from light to dark for decay rates $D = 1$ to $D = 100$. For higher decay rates, the noise invoked in the light curve after the modulation is removed tends to be greater, although the relation of this to the period is not as well defined and no trend with increasing period is evident.

evolution approaches or is less than the period, although this is not evident in the simulations. The noise invoked by the spot evolution is in many cases an order of magnitude smaller than the amplitude of the light curve, with the exception of some of the $C = 0.6$ simulations (for which the average spot coverage during each simulation is 0.3) where the standard deviation of the light curve approaches the amplitude for the larger decay rates. The dispersion in the light curves caused by spots is of the same order as that found in WTS for the brightest unsaturated stars, suggesting that variation due to spots could contribute a significant component to the noise of heavily spotted M dwarf light curves in the J band, and more so at shorter wavelengths where the effects of spots are more pronounced.

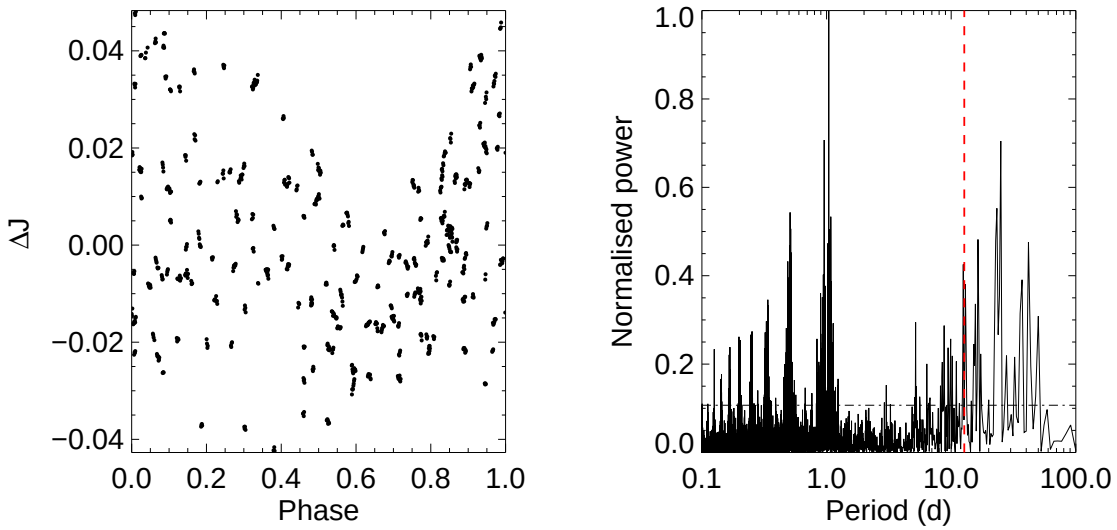

Figure 4.20: The phase folded light curve and Lomb-Scargle periodogram for simulation c0.60_p12.74_d10.00_5. A significant peak is found corresponding to the real period but is found amongst several other peaks of similar or greater significance.

The effects of the evolving spot coverage on the ability of the Lomb-Scargle periodogram to detect a period corresponding to the real period are also investigated. In order to obtain some measure of how the spot evolution affects the period retrieval, the height of the peak corresponding to the real period in each periodogram, if there indeed is one, is measured as a fraction of the height of the highest peak. In some instances the effects of spot evolution obfuscates the periodogram peak corresponding to the true period, for example in simulation c0.60_p12.74_d10.00_5 (Figure 4.20), where the peak corresponding to the real period is less significant than a number of other spurious peaks in the periodogram. This is only seen for stars in which the decay rates are on average greater than those found in the Sun. In Table 4.4, for each simulation, the mean height of the peak corresponding to the real period as a fraction of the highest peak is shown. This is also shown in Figure 4.21. This is averaged over all 20 instances of each parameterisation. In some individual instances the true period is detected as the highest peak, in some it is not detected as the highest peak but still occurs as a significant peak (for example, the highest peak may correspond to an alias), and in others it is not detected as a significant peak at all. For many period and coverage

combinations, this ratio decreases for increased decay rates, indicating the diminishing effect the rate at which the spot coverage evolves has on the ability to detect a period, although the dependency on decay rates is much less evident here than it is for the light curve noise, owing to the effects complex light curve morphologies can have on period detection. As an illustrative example, light curves where there are two maxima and minima per phase may have a period detected at half that of the actual period. In some instances no peak is detected as the spot evolution is sufficiently rapid to wash out the modulation due to rotation.

In addition, this was tested in the presence of additional noise equivalent to that found in the light curves at $J = 12$ and $J = 16$. When $J = 12$, 2% of the rotation periods could not be detected at $D = 100$ and for one simulation it could not be detected at $D = 10$; when $J = 16$, 8% could not be detected at $D = 100$ and 5% could not be detected at $D = 10$. This does not necessarily mean that some alike fraction of the WTS variables were undetected because of rapid spot evolution, since the real average decay rates of the WTS M dwarfs are unknown, but assuming that they are substantially super-Solar, it could be assumed that some fraction is not detected because of rapidly evolving spots. While some stars in the WTS do indeed exhibit morphological changes in the light curves explicitly necessitating super-solar spot evolution rates, many do not.

These results from the simulations suggest that some fraction of the real variable M dwarfs in WTS may have been discounted amongst the 3108 stars not included in the final sample for not appearing as periodically variable, as spot evolution diminished the height or otherwise obfuscated the periodogram peak corresponding to the real period or altered the morphology of the light curve such that it did not appear to be a bona fide periodic variable. As the dispersion of the light curve due to spots is of a similar order of magnitude to that of the instrumental noise, however, it would prove difficult to distinguish these stars. Detecting noise on this level, however, perhaps has implications for the detection of planetary transits around heavily spotted M dwarfs. A Neptune radius planet transiting an M2V star could be expected to cause a 0.2% drop in magnitude, less than the largest values found for spot induced noise in case of

Coverage	Period	Decay Rate	Peak height	$(J = 12)$	$(J = 16)$	σ
0.200000	1.62000	100	0.876029	0.850939	0.676787	0.00630985
0.200000	1.62000	10	0.939541	0.876997	0.636997	0.00481057
0.200000	1.62000	1	0.963150	0.974710	0.586898	0.00271366
0.200000	12.7400	100	0.723544	0.659425	0.309202	0.00492369
0.200000	12.7400	10	0.700949	0.736282	0.513035	0.00477283
0.200000	12.7400	1	0.682717	0.692102	0.462517	0.00384849
0.200000	22.3400	100	0.987579	0.980752	0.746632	0.00497909
0.200000	22.3400	10	0.937210	0.936867	0.662749	0.00412148
0.200000	22.3400	1	0.780431	0.796435	0.581832	0.00376473
0.200000	51.8400	100	0.710258	0.637744	0.410469	0.00394735
0.200000	51.8400	10	0.829989	0.836371	0.598433	0.00377187
0.200000	51.8400	1	0.869530	0.875191	0.715849	0.00367006
0.600000	1.62000	100	0.819529	0.826167	0.826931	0.0171010
0.600000	1.62000	10	0.852807	0.854689	0.826915	0.0165583
0.600000	1.62000	1	0.874127	0.872887	0.872844	0.00769817
0.600000	12.7400	100	0.610109	0.608994	0.619248	0.0187932
0.600000	12.7400	10	0.787950	0.785160	0.802491	0.0171317
0.600000	12.7400	1	0.668704	0.674172	0.657562	0.0102244
0.600000	22.3400	100	0.651275	0.643140	0.645037	0.0203869
0.600000	22.3400	10	0.855784	0.857860	0.854992	0.0173928
0.600000	22.3400	1	0.869314	0.873004	0.846856	0.0105497
0.600000	51.8400	100	0.729557	0.726880	0.705235	0.0181943
0.600000	51.8400	10	0.756079	0.758195	0.742377	0.0172717
0.600000	51.8400	1	0.836344	0.832575	0.833486	0.00896410

Table 4.4: Results from the simulations averaged over the six iterations of each parameter set; σ is the mean standard deviation of the light curve after the rotational modulation has been subtracted and peak height is the mean normalised height of the peak corresponding to the period as a fraction of the next highest peak in the periodogram. The adjacent column indicate this same parameter if noise equivalent to that found in light curves at $J = 12$ and $J = 16$ is added to the simulated light curves. In most instances, except at the highest decay rate, this has little impact on the ability to detect the period as the surface coverages used are typically sufficient for a detectable signal at these noise levels. For each period, σ tends to increase for greater decay rates while peak height decreases.

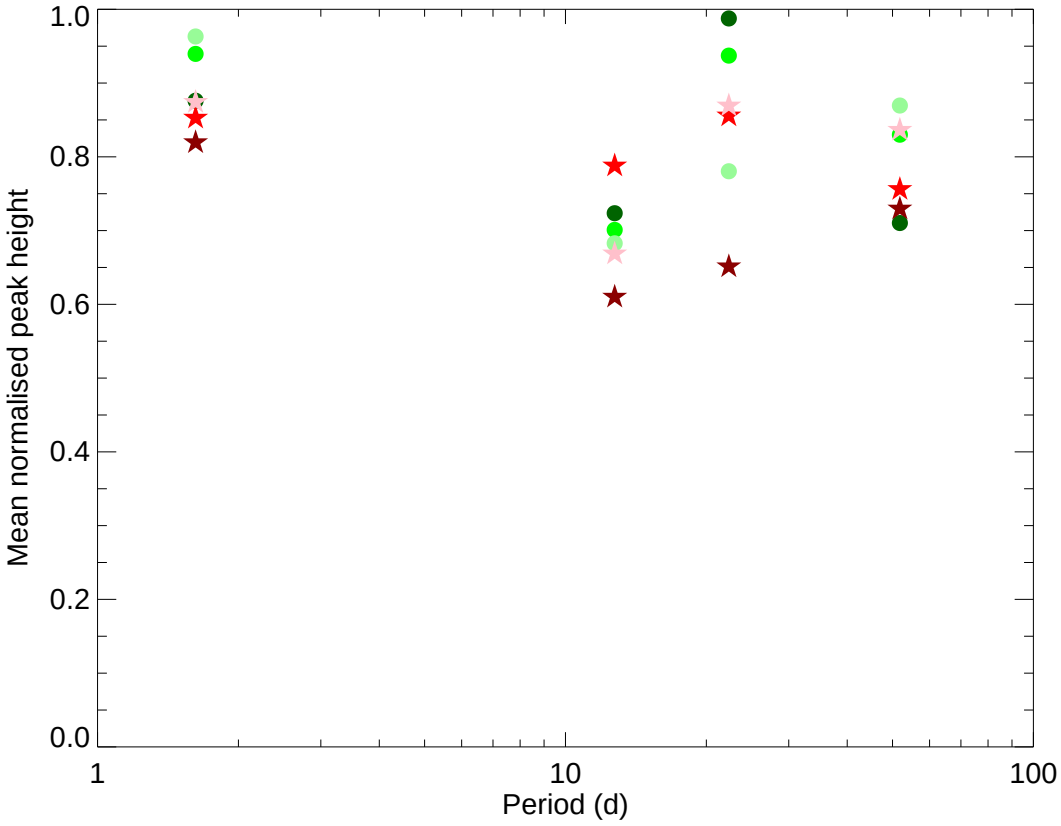

FIGURE 4.21: A plot of the mean periodogram peak height corresponding to the true period as a fraction of the height of the most significant peak. Symbols as in Figure 4.19. No clear trend is present indicating that other factors such as the exact spot pattern of a star may effect the ability of the Lomb-Scargle periodogram to detect the correct period rather than purely the noise present in the light curve.

moderately large coverage (∼30%) and super Solar spot evolution rates. Continuous tracking of a varying light curve (i.e. as with Kepler) would allow for the removal of these effects, whereas intermittent observations (i.e. as with WTS and other ground based surveys) would not allow for the monitoring of an evolving spot pattern, and would thus show up as noise over long periods of observations.

From Hα observations of variable M dwarfs discussed in Section 1.1.3, the variability of the activity in M dwarfs increases with later spectral type while the magnitude of the activity decreases (Lee et al., 2010; Kruse et al., 2010). Activity is also found to vary on more rapid time scales for later M dwarfs (Bell et al., 2012). It could therefore be expected that spot evolution on these stars is also far more rapid and well described

by simulations of stars with a relatively low spot coverage and rapidly evolving spots. If the trend in spot temperature contrasts, as found by Berdyugina (2005), continues to the late M dwarfs then it could be expected that by M5V, ΔT = 200K, and by late M it would perhaps by < 100K. Therefore, even if these stars are heavily spotted with rapidly evolving spots the noise expected to be found would be of a very low level owing to the very low brightness contrast expected between the spotted and unspotted photosphere. Thus in the context of detectable fractions of M dwarfs there may be a trade off between the absolute fraction of active stars and the fraction of active stars with long duration, high contrast spots with increasing spectral type.

4.5 Spot evolution on the WTS M dwarfs

As is apparent from the simulations, stars with a higher surface fraction of spotted photosphere have noisier light curves due to spot evolution. As such, the WTS light curves are reanalysed to see whether this holds true in real M dwarfs. In order to measure spot evolution on the WTS M dwarfs, the modulation due to rotation is subtracted in the same manner as in the simulations to leave a flat light curve with no modulation, and the raw standard deviation σ_r of it is found. As the WTS M dwarfs are observed at different magnitudes, the light curves will have different levels of random noise. The noise corresponding to the magnitude of the star σ_J is subtracted from σ_r to find the excess noise for that star σ_e, such that $\sigma_e = \sqrt{\sigma_r^2 - \sigma_J^2}$. This σ_e is therefore presumably due to real astrophysical processes such as spot evolution. The values of σ_e for the WTS variable M dwarfs are plotted in Figure 4.22 as a function of the mean estimated spot coverage. The Spearman rank coefficient is calculated for the trend to be 0.768 with a significance of $>8\sigma$. The excess noise in the light curves is therefore quite strongly correlated with the surface coverage of the light curve to a high degree of significance, as expected, showing that more heavily spotted stars have noisier light curves. This provides further evidence for the description of M dwarf spot coverage being best described as composed of a pattern of many evolving spots instead of a few monolithic spots. With further simulations at different levels of spottedness

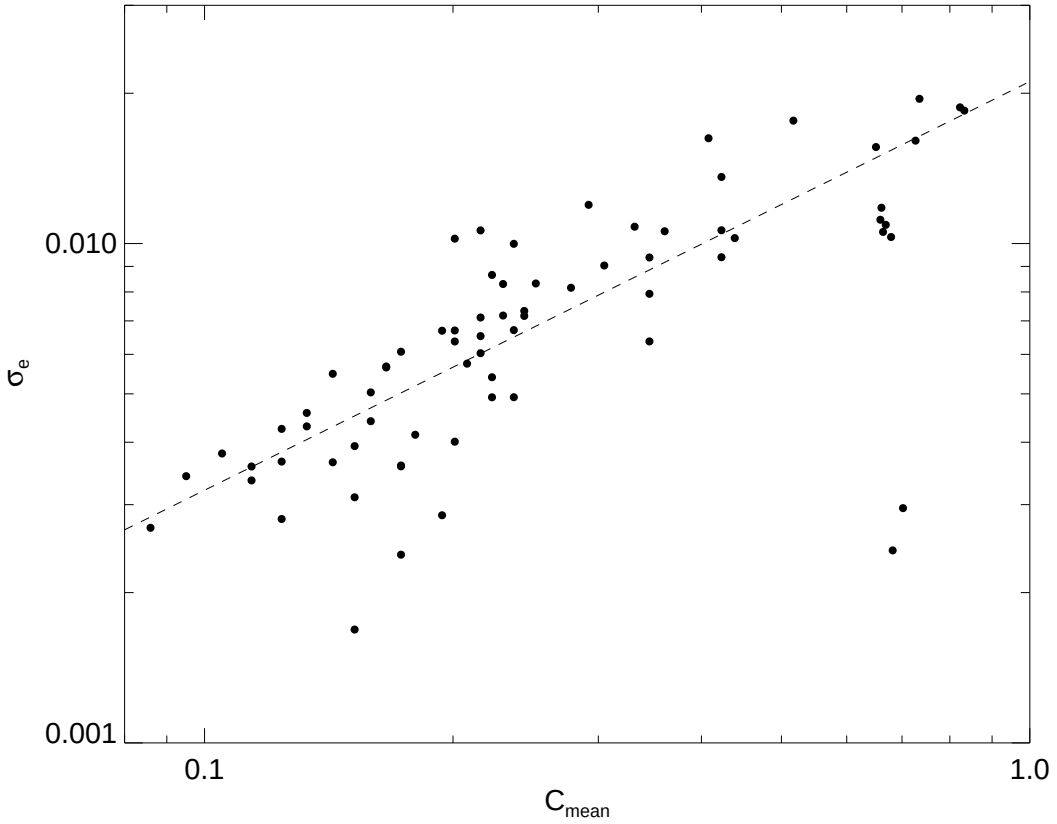

FIGURE 4.22: A plot of the mean coverage C_{mean} as tabulated in Table 4.3 versus σ_e. The trend appears to be linearly correlated in log-log space and thus a power law $\sigma_e = 0.0211{C_{mean}}^{0.818}$ is fitted and shown by the dashed line. The two outlying points are possibly instances where the modulation is the result of a single large spot or spot group evolving slowing as opposed to being dependent on a number of independently evolving spots.

it should be possible to infer mean spot decay rates as a function of the mean solar decay rate for the WTS M dwarfs. As the trend found appears linear in log-log space a power law $\sigma_e = 0.0211{C_{mean}}^{0.818}$ is fitted to the data.

4.6 Summary

In order to gauge how well the Lomb-Scargle periodogram could detect light curves of varying amplitudes and periods, simulations whereby sinusoids were injected into randomised, none-period WTS light curves were tested for period detection. The strong

amplitude-magnitude dependence (as seen in Figure 3.1) due to noise becomes apparent, as do the effects of the seasonal observation strategy of the WTS. Aliasing with the observation periods results in the periodogram being unable to detect certain periods greater than 20 d. This effect is magnified for the fields where less observations have been made, as variable light curves will have poorer phase coverage.

Simulations using single, static models from Barnes et al. (2011) are used to gauge how light curve amplitude varies with spot coverage and wavelength. Using spot distribution models extrapolated to more active stars by Solanki & Unruh (2004), new models are created to test two different means of creating spot distributions, namely by varying the width or the mean of the spot size distribution, for more heavily spotted stars, which can reproduce light curve amplitudes as observed in WTS. Solanki & Unruh (2004) find models that vary the spot size distribution by linearly varying the width of the distribution with increasing activity levels better reproduce the fraction of large spots as observed in Doppler images. Similarly, it is found that this can also more efficiently replicate the WTS variables, and indeed is required to generate spot modulated light curves of the amplitude range observed in WTS. Minimum and average spot coverages are then predicted for the WTS stars based on their light curve amplitudes.

The models are then adapted to produce evolving spot patterns based on spot evolution observations of the Sun at three different magnitudes of evolutionary rate, and WTS-like observations of stars with evolving spot patterns are simulated. Stars with a greater spot coverage and larger decay rates are shown to have noisier light curves. The estimated spot coverages for the WTS M dwarfs are shown to be strongly correlated with the excess noise in the light curves evidencing the paradigm of M dwarfs with many evolving spots. While M dwarfs do not exhibit large degrees of differential rotation, improvements to the models to include this, as well as meridional drift, if significant, will improve the model predictions for the effects of long term spot evolution on light curves.

5

Conclusions and Future Work

Solar activity has for centuries been the subject of much study and with improved technology in more recent times the study of the activity of small, fainter stars has become increasingly possible. Fruitful exoplanet detections around early type main sequence stars and efforts to detect terrestrial planets around M dwarfs has renewed the interest in the variability of these most common stars, and data from transit surveys has made such studies increasingly possible. Of particular interest is the spottedness of these M dwarfs, both in the context of understanding magnetic activity and field morphology across the partially radiative and fully convective regimes, and also for the assessment of its impact on transit and radial velocity planet detection surveys.

Through use of tracers for chromospheric activity, such as Hα, it is known that the fraction of active M dwarfs increases with later spectral type while the magnitude of the activity decreases (e.g. Reiners et al., 2012a). The spottedness of M dwarfs, however, is

relatively poorly understood in comparison to that of earlier type stars. A diverse range of magnetic topologies are found in fully and partially convective M dwarfs (Donati, 2011) and it remains unclear how spots are formed in the varying contexts of these. The formation, parameterisation, and evolution of sun spots is well characterised by long running campaigns of solar observations such as that of the Mt. Wilson Observatory (Bogdan et al., 1988). Doppler Imaging of G and K dwarfs, whereby the largest spots of a reasonably rapidly rotating star are mapped, has allowed for some characterisation of the spots of these stars. Combined with the use of molecular bands such as TiO as diagnostics of total spot coverage filling factors (O'Neal et al., 1996), this has allowed for tentative characterisation of spot size distributions for more active stars Solanki & Unruh (2004). A few such Doppler Images of early M dwarfs have been made (e.g. Barnes et al., 2002) although the lack of any such filling factor diagnostic prevents the true spot coverage from being measured, although observations made have shown large spots or spot groups distributed uniformly across the stellar surface, rather than being contained at specific latitudes or longitudes as in earlier spectral types. As the targets are faint, however, follow up may be difficult. Additional high resolution spectroscopy, (e.g. using an instrument such as Hectochelle, Szentgyorgyi et al., 2011) may help to characterise the WTS sample.

5.1 Results from the WFCAM Transit Survey

The WFCAM Transit Survey provides a long baseline of M dwarf observations with sensitivity to periods of hundreds of days. The M dwarfs in the survey are identified by means of a robust typing procedure that relies on spectral standard colour index relations from Covey et al. (2007) and West et al. (2011). The variables in the M dwarf sample are then identified with a Lomb-Scargle periodogram to detected periodicity in the light curve. A total of 72 periodically variable stars with colours indicative of being M dwarfs are detected with periods of 0.16 to 90.33 days and amplitudes of up to 0.115 in the J-band. Photometric parallaxes (Bochanski et al., 2011) and SDSS proper motions are used to estimate the population membership for the stars in the sample.

While the stars of different age estimated groups do not appear to be drawn from statistically distinct populations, some comparison to other periodicities samples can be made. The stars of later spectral type have a greater range of periods than the earlier spectral types, corroborating results from Irwin et al. (2011). Pending observations using the Large Sky Area Multi-Object Fibre Spectroscopic Telescope (LAMOST, also known as the Guō Shǒujìng Telescope, Cui et al., 2012) will aid the further characterisation of the periodically variable sample (and other M dwarfs in WTS). If $v\sin i$ can be measured, for example, if assumptions of the stellar radii are made inclinations can be estimated. Other activity indicators such as Hα or other chromospheric lines will enable direct comparisons of chromospheric activity with the photometric variability. Radial velocities measurements, combined with improved proper motions for the 19hr field obtained directly from the WTS images, will allow the calculation of the space motions for the variable M dwarfs, and thus provide a means of assessing the proper kinematic population membership of these stars.

The amplitudes of the light curves are found, on average, to decrease with later spectral types. This decrease is perhaps analogous to the decrease in Hα luminosity observed by Mohanty & Basri (2003) and subsequent sources with later spectral types; as the cooler atmosphere becomes increasingly neutral, magnetic effects can become increasingly damped Mohanty et al. (2002). The amplitude decrease seen for later spectral types in WTS may be due to the decrease in the difference between the temperatures (and therefore brightnesses) of the unspotted photosphere and the star spots, ΔT . Berdyugina (2005) finds a trend for decreasing ΔT for decreasing photospheric temperatures, and thus by mid-M the low temperature difference results in a low contrast in brightness. This is perhaps an aspect of the same effect of magnetic damping that could result in the decrease of relative Hα emission moving from mid to late M dwarfs, although this will require extensive magneto-hydrodynamic modelling to be substantiated; MHD models by Chabrier & Küker (2006) do predict that an α^2 dynamo would manifest in the form of small, low contrast photospheric spots too small to be detected in the form of light curve modulation. These effects therefore would conspire to result in a much lower amplitude spot modulation, and may also explain

the lack of variable M dwarfs later than M4 in the WTS sample. Besides the relative scarcity of late M dwarfs in the sample, as the amplitudes resulting from spot modulation are already much lower in the J-band than at shorter wavelengths, and as late M dwarfs are intrinsically faint, any spot modulation is likely of lower amplitude than the limiting noise of the observations. For example, at $J = 17$, where most of the WTS stars later than M4 are found (Figure 2.12) the sensitivity to amplitudes < 0.05 is poor, and for < 0.03 is zero (Figures 4.2 and 4.4). Irwin et al. (2011) detect variable mid to late M dwarfs in the MEarth sample with amplitudes of the order of 0.02 magnitudes at shorter wavelengths than the J-band (the MEarth pass band is centered at 715nm), indeed indicative of smaller amplitudes for later M dwarfs. As shown in Figure 4.6, even in the I-band (806nm) amplitudes for spot modulated M dwarfs are considerably greater than in the J-band and thus it does seem to be the case that WTS is not sensitive to variable M dwarfs later than M4. The detection of spot modulation for stars with periods of weeks to months long, as found in similar mid to late M dwarf studies by Kiraga & Stepień (2007) and Irwin et al. (2011), indicates that at least in some instances magnetic activity is not wholly dependent on rapid rotation in early M dwarfs.

Some light curves for the variable M dwarfs show clear examples of evolving spot patterns as the light curve morphology and amplitude varies over time. The morphologies are indicative of complex spot patterns composed of a number of spots evolving independently on times scales of months to years. Examples showing saw-tooth like morphologies and multiple minima and maxima require spot patterns composed of multiple small and medium sized spots, not just a few large spots as modelled in earlier works. In one instance, a star with no apparent periodic variability for the first two years of observations evolves into a state exhibiting spot modulation over the latter year of observations.

5.2 Simulations of spotted M dwarfs

Simulations are carried out to assess the sensitivity of the methods used for detecting periodic variability. It is found that due to the seasonal blocks of observation epochs in the WTS observations some ranges of periods cannot be detected by the Lomb-Scargle periodogram, and there is a strong dependence on the light curve noise on the low limit of the amplitudes that can be detected. WTS fields with fewer epochs are less complete on average due to poorer phase coverage for longer period M dwarfs.

Attempts to model periodically variable M dwarf light curves, with models invoking just a few large spots, fail to account for the complex morphologies and evolution some variables exhibit (Harrison et al., 2012), while models based on a pattern of uniform spot sizes similarly lack an observational precedent or support from spot size distributions (Jackson & Jeffries, 2013). The results found here somewhat contradict the general conclusions of Jackson & Jeffries (2013) from their simulations of spotted M dwarfs that use uniform dark pixels on a stellar surface as a proxy for spots. They conclude that low amplitude M dwarf modulations is due to a heavily spotted photosphere. While the models used here do indicate a down turn in amplitudes for the most heavily spotted stars as the surface becomes more wholly spotted, the lowest amplitudes are in fact found for M dwarfs with small fractional surface coverages. This is likely due to their treatment of spots as randomly distributed dark pixels peppering the photosphere. As the authors suggest, Doppler images provide motivation against the treatment of spots in this manner. As shown by Solanki & Unruh (2004), comparisons between Doppler images and TiO derived filling factors indicate that some portion of the spots is accounted for by larger spots with some fraction composed of smaller spots not resolved by Doppler imaging. If spots were to be described purely as uniform spots, the evolution as seen in WTS could not be explained. Transitions between morphologies in light curves require reasonably large changes in East-West hemispheric brightness of the stars that would require the simultaneous growth and decay of many of these spots with respect to the stellar hemispheres. Nor can they be explained by a few large spots evolving, as the morphologies require more complex spot

patterns. Instead they necessitate a range of medium to large of spot sizes undergoing dynamic evolution.

New models with an empirical precedent for many spots of varying sizes are used. Extrapolations to more active stars as described by Solanki & Unruh (2004) form the basis for these new models of variable M dwarfs and, assuming models under which the width of the spot size distribution increases with activity, successfully reproduce the range of amplitudes and morphologies observed in WTS and other surveys, through spot patterns composed of a combination of large and small spots. Power laws are found to describe the upper limit of the amplitudes with respect to spot coverage and thus provide a limit on the minimum spot coverage required to generate any given amplitude in absence of knowledge about a star's photospheric and spot temperatures. Using these models, spot coverage fractions are estimated making assumptions about the likely ranges of spot and photospheric temperatures of the WTS M dwarfs. The coverage fractions are generally of the same order as those found in K dwarfs from TiO band filling factors (Solanki & Unruh, 2004, and references therein), and in some instances are higher. The minimum spot coverages for variable M dwarfs indicate that the surfaces of many of the variable M dwarfs have a fractional surface spot coverage of > 0.1. In these models, larger amplitudes are generated by medium to large sized spots capable of reproducing the morphologies observed in WTS and Kepler.

Simulations modelling the evolution of spots at Solar and super-Solar rates quantitatively reproduce the behaviour as observed in WTS and Kepler M dwarfs. These models could be used further to study the effects of spot evolution on transit surveys conducted in a similar manner to WTS. The effects of evolving spots on the noise of the light curve are quantified, and a connection between spot coverage and noise invoked from spot evolution is established. It is found that the M dwarfs with the larger modulation amplitudes have noisier light curves after the modulation is subtracted. This is interpreted as being the result of many spots evolving over the duration of the observations. The picture of variable M dwarfs that emerges from the observations and simulations is of heavily spotted stars, typically with > 0.1 fractional surface coverage. The spots sizes are best described as a mix of a small number of large and medium

spots with many small spots, quantified by a log-normal distribution that grows wider with increasing levels of activity. The difference between the spot and photospheric temperature becomes increasingly smaller with later spectral types.

5.3 Future work

A firm observational mandate for the assumptions of the simulated models is still lacking as there are few Doppler images of M dwarfs and no known diagnostic for determining spot filling factor. Photometry alone is not alone able resolve many issues, although future Doppler Images of mid to late M dwarfs would break the degeneracies between spot and photospheric temperature and establish the sizes of the largest spots in the distributions for these stars. Such Doppler images of late type M dwarfs would indeed help to verify predictions made by the models of turbulent dynamos thought to operate in fully convective stars. High resolution observations with the VLT using UVES will enable the better characterisation of spot patterns on late M dwarfs, more so with next generation instruments such as HIRES proposed for the E-ELT (Pasquini et al., 2008), due to begin operation some time in the next decade. The FeH band at 9900Å represents a potential choice for determining the spot filling factors of M dwarf (O'Neal et al., 2005) which would firmly establish both the total spottedness of M dwarfs and place limits of the parameterisation of the spot size distributions. Multi-colour photometry of the variable M dwarfs can also aid the breaking of degeneracies with regards to spot temperature and coverage and empirically explore the dependency of light curve amplitudes on spot coverage at different wavelengths. This is particularly important for determining the impact of spots on transit detections and planet parameterisations (Ballerini et al., 2012).

The wealth of data from NASA's Kepler telescope provides observations of M dwarfs that are unequalled in their cadence and overall time baseline and light curves from this survey will prove a major informer to understanding of M dwarf variability and activity. Kepler's observations at shorter wavelengths also result in a greater sensitivity to spots. An analysis of the variability of M dwarfs in Kepler can be used to better

inform models of spotted M dwarfs. As the observations are continuous, rapid spot evolution would not result in a noise like dispersion in light curves and dispenses of the need to fold light curves over long periods of observations in order to obtain complete phase coverage. This could enable stricter constraints to be placed on the NASA's planned Transiting Exoplanet Survey Satellite (TESS) will provide further long term, near infra red (600-1000 nm) photometric monitoring of the closest $I < 13$ M dwarfs (Ricker et al., 2010) and will provide a further wealth of M dwarf light curves that will enable a more detailed study of the long term variability of these stars.

The WFCAM Transit Survey contains extensive light curves of main sequence stars observed in the near infra red and can potentially provide a wealth of additional science, for example, the variability of stars both of an earlier spectral type and other luminosity classes and how these compare to the M dwarf sample. No full detection and analysis of flares in the near infra red was carried out. While literature sources suggest that bright J-band flares should be very rare (e.g. Tofflemire et al., 2012), one example of a particular bright flare was nevertheless found serendipitously and more may be found in the data to place better constraints on the near infra red flaring of M dwarfs. The simulations of spotted M dwarfs can be extended to include planetary transits to better determine the ability of ground based transit surveys at detecting and characterising planets of varying radii and periods in the presence of varying levels of stellar activity and spot size distributions. Other improvements to the simulations could include differential rotation, if this is indeed significant for M dwarfs, or the conglomeration and fragmentation of spots. Further spectroscopic observations of the periodically variable WTS M dwarfs, as well as the other M dwarfs with noisy light curves for which no periodic variability is detected, may further characterise the nature of active M dwarfs.

Bibliography

Abazajian, K. N., et al. 2009, ApJS, 182, 543

Allard, F., Homeier, D., & Freytag, B. 2012, Royal Society of London Philosophical Transactions Series A, 370, 2765

Antalová, A. 1991, Bulletin of the Astronomical Institutes of Czechoslovakia, 42, 316

Ballerini, P., Micela, G., Lanza, A. F., & Pagano, I. 2012, A&A, 539, A140

Barnes, J., Collier Cameron, A., Donati, J.-F., James, D., Marsden, S., & Petit, P. 2005, Mon. Not. R. Astron. Soc., 357, L1

Barnes, J., James, D., & Cameron, A. 2002, Astronomische Nachrichten, 323, 333

Barnes, J. R. & Collier Cameron, A. 2001, MNRAS, 326, 950

Barnes, J. R., James, D. J., & Collier Cameron, A. 2004, MNRAS, 352, 589

Barnes, J. R., Jeffers, S. V., & Jones, H. R. A. 2011, MNRAS, 412, 1599

Barnes, J. R., et al. 2012, MNRAS, 424, 591

Barros, S. C. C., Boué, G., Gibson, N. P., Pollacco, D. L., Santerne, A., Keenan, F. P., Skillen, I., & Street, R. A. 2013, MNRAS, 430, 3032

Baumann, I. & Solanki, S. K. 2005, A&A, 443, 1061

Beck, J. G. & Chapman, G. A. 1993, Sol. Phys., 146, 49

Becker, A. C., Bochanski, J. J., Hawley, S. L., Ivezić, Ž., Kowalski, A. F., Sesar, B., & West, A. A. 2011, ApJ, 731, 17

Bell, K. J., Hilton, E. J., Davenport, J. R. A., Hawley, S. L., West, A. A., & Rogel, A. B. 2012, PASP, 124, 14

Benedict, G. F., et al. 1998, AJ, 116, 429

Berdyugina, S. V. 2005, Living Reviews in Solar Physics, 2, 8

Birkby, J. 2010, in JENAM 2010, Joint European and National Astronomy Meeting

Birkby, J., et al. 2012, MNRAS, 426, 1507

Birkby, J. L., et al. 2013, in prep, MNRAS

Bochanski, J. J., Hawley, S. L., Covey, K. R., West, A. A., Reid, I. N., Golimowski, D. A., & Ivezić, Ž. 2010, AJ, 139, 2679

Bochanski, J. J., Hawley, S. L., & West, A. A. 2011, AJ, 141, 98

Bogdan, T. J., Gilman, P. A., Lerche, I., & Howard, R. 1988, ApJ, 327, 451

Borucki, W. J., et al. 2011, ApJ, 736, 19

Brandt, P. N., Schmidt, W., & Steinegger, M. 1990, Sol. Phys., 129, 191

Browning, M. K. 2008, ApJ, 676, 1262

Browning, M. K., Basri, G., Marcy, G. W., West, A. A., & Zhang, J. 2010, AJ, 139, 504

Buccino, A. P., Díaz, R. F., Luoni, M. L., Abrevaya, X. C., & Mauas, P. J. D. 2011, AJ, 141, 34

Bumba, V. 1963, Bulletin of the Astronomical Institutes of Czechoslovakia, 14, 91

Cappetta, M., et al. 2012, MNRAS, 427, 1877

Carpano, S., Aigrain, S., & Favata, F. 2003, A&A, 401, 743

Chabrier, G. & Baraffe, I. 2000, ARA&A, 38, 337

Chabrier, G. & Küker, M. 2006, A&A, 446, 1027

Chavez, C. E., Tovmassian, G., Aguilar, L. A., Zharikov, S., & Henden, A. A. 2012, A&A, 538, A122

Chipps, K. A., Stencel, R. E., & Mattei, J. A. 2004, Journal of the American Association of Variable Star Observers (JAAVSO), 32, 1

Ciardi, D. R., et al. 2011, AJ, 141, 108

Clark, B. M., Blake, C. H., & Knapp, G. R. 2012, ApJ, 744, 119

Collier Cameron, A. 1997, MNRAS, 287, 556

Covey, K. R. et al. 2007, Astron. J., 134, 2398

Cowling, T. G. 1946, MNRAS, 106, 218

Cui, X.-Q., et al. 2012, Research in Astronomy and Astrophysics, 12, 1197

Davenport, J. R. A., Becker, A. C., Kowalski, A. F., Hawley, S. L., Schmidt, S. J., Hilton, E. J., Sesar, B., & Cutri, R. 2012, ApJ, 748, 58

Désert, J.-M., et al. 2011, ApJS, 197, 14

Dobler, W., Stix, M., & Brandenburg, A. 2006, ApJ, 638, 336

Donati, J.-F. 2011, in IAU Symposium, Vol. 271, IAU Symposium, ed. N. H. Brummell, A. S. Brun, M. S. Miesch, & Y. Ponty, 23–31

Dorch, S. B. F. & Ludwig, H.-G. 2002, Astronomische Nachrichten, 323, 402

Dressing, C. D. & Charbonneau, D. 2013, ApJ, 767, 95

Dumusque, X., et al. 2012, Nature, 491, 207

Durney, B. R., De Young, D. S., & Roxburgh, I. W. 1993, Sol. Phys., 145, 207

Fan, Y., Fisher, G. H., & Deluca, E. E. 1993, ApJ, 405, 390

Forbrich, J., Lada, C. J., Muench, A. A., & Teixeira, P. S. 2008, ApJ, 687, 1107

France, K., Linsky, J. L., Tian, F., Froning, C. S., & Roberge, A. 2012, ApJL, 750, L32

Frasca, A., Biazzo, K., Catalano, S., Marilli, E., Messina, S., & Rodonò, M. 2005, A&A, 432, 647

Frasca, A., Covino, E., Spezzi, L., Alcalá, J. M., Marilli, E., Fżrész, G., & Gandolfi, D. 2009, A&A, 508, 1313

Gafeira, R., Fonte, C. C., Pais, M. A., & Fernandes, J. 2012, ArXiv e-prints

Gautier, III, T. N., et al. 2007, ApJ, 667, 527

Gokhale, M. H. & Zwaan, C. 1972, Sol. Phys., 26, 52

Goulding, N. T., et al. 2013, in European Physical Journal Web of Conferences, Vol. 47, European Physical Journal Web of Conferences, 1006

Goulding, N. T., et al. 2012, MNRAS, 427, 3358

Harrison, T. E., Coughlin, J. L., Ule, N. M., & López-Morales, M. 2012, AJ, 143, 4

Hartman, J. D., Bakos, G. Á., Noyes, R. W., Sipőcz, B., Kovács, G., Mazeh, T., Shporer, A., & Pál, A. 2011, AJ, 141, 166

Hawley, S. L., et al. 2002, AJ, 123, 3409

Hełminiak, K. G., Konacki, M., Muterspaugh, M. W., Browne, S. E., Howard, A. W., & Kulkarni, S. R. 2012, MNRAS, 419, 1285

Henry, T. J., Jao, W.-C., Subasavage, J. P., Beaulieu, T. D., Ianna, P. A., Costa, E., & Méndez, R. A. 2006, AJ, 132, 2360

Hodgkin, S. T., Irwin, M. J., Hewett, P. C., & Warren, S. J. 2009, MNRAS, 394, 675

Högbom, J. A. 1974, A&AS, 15, 417

Horne, J. H. & Baliunas, S. L. 1986, ApJ, 302, 757

Howard, R. F. 1992, Sol. Phys., 137, 51

Irwin, J., Berta, Z. K., Burke, C. J., Charbonneau, D., Nutzman, P., West, A. A., & Falco, E. E. 2011, ApJ, 727, 56

Irwin, J., Irwin, M., Aigrain, S., Hodgkin, S., Hebb, L., & Moraux, E. 2007, MNRAS, 375, 1449

Ivezić, Ž., et al. 2008, ApJ, 684, 287

Jackson, R. J. & Jeffries, R. D. 2013, ArXiv e-prints

Javaraiah, J. 2011, Sol. Phys., 270, 463

Jeffers, S. V. 2005, MNRAS, 359, 729

Jeffers, S. V., Donati, J.-F., & Collier Cameron, A. 2007, MNRAS, 375, 567

Jenkins, J. S., Ramsey, L. W., Jones, H. R. A., Pavlenko, Y., Gallardo, J., Barnes, J. R., & Pinfield, D. J. 2009, ApJ, 704, 975

Jensen, E., Nordø, J., & Ringnes, T. S. 1955, Astrophysica Norvegica, 5, 167

Jofré, P. & Weiss, A. 2011, A&A, 533, A59

Kawaler, S. D. 1988, ApJ, 333, 236

Kipping, D. M. 2012, MNRAS, 427, 2487

Kiraga, M. & Stepień, K. 2007, Acta Astronomica, 57, 149

Kopparapu, R. k. 2013, ArXiv e-prints

Kovács, G., et al. 2013, ArXiv e-prints

Kowalski, A. F., Hawley, S. L., Hilton, E. J., Becker, A. C., West, A. A., Bochanski, J. J., & Sesar, B. 2009, AJ, 138, 633

Kruse, E. A., Berger, E., Knapp, G. R., Laskar, T., Gunn, J. E., Loomis, C. P., Lupton, R. H., & Schlegel, D. J. 2010, ApJ, 722, 1352

Lane, C., et al. 2007, ApJL, 668, L163

Lee, K.-G., Berger, E., & Knapp, G. R. 2010, ApJ, 708, 1482

Lépine, S., Rich, R. M., & Shara, M. M. 2007, ApJ, 669, 1235

Lépine, S., Shara, M. M., & Rich, R. M. 2003, AJ, 126, 921

Llama, J., Jardine, M., Mackay, D. H., & Fares, R. 2012, MNRAS, 422, L72

Lomb, N. R. 1976, APSS, 39, 447

Lustig, G. & Wohl, H. 1995, Sol. Phys., 157, 389

Mackay, D. H., Jardine, M., Collier Cameron, A., Donati, J.-F., & Hussain, G. A. J. 2004, MNRAS, 354, 737

Mamajek, E. 2011, A Modern Mean Stellar Color and Effective Temperatures (Teff) Sequence for O9V-Y0V Dwarf Stars, See http://www.pas.rochester.edu/∼emamajek/EEM_dwarf _UBVIJHK_colors_Teff.dat [Online; accessed 19-May-2013] and http://www.pas.rochester.edu/∼emamajek/spt [Online; accessed 19-May-2013]

Martinez Pillet, V., Moreno-Insertis, F., & Vazquez, M. 1993, A&A, 274, 521

Messina, S., Desidera, S., Lanzafame, A. C., Turatto, M., & Guinan, E. F. 2011, A&A, 532, A10+

Messina, S., Parihar, P., Koo, J.-R., Kim, S.-L., Rey, S.-C., & Lee, C.-U. 2010, A&A, 513, A29

Messina, S., Pizzolato, N., Guinan, E. F., & Rodonò, M. 2003, A&A, 410, 671

Messina, S., Rodonò, M., & Guinan, E. F. 2001, A&A, 366, 215

Miller, W. J. 1966, Ricerche Astronomiche, 7, 217

Mohanty, S. & Basri, G. 2003, ApJ, 583, 451

Mohanty, S., Basri, G., Shu, F., Allard, F., & Chabrier, G. 2002, ApJ, 571, 469

Moreno-Insertis, F., Schüssler, M., & Ferriz-Mas, A. 1992, A&A, 264, 686

Morin, J., et al. 2008a, MNRAS, 384, 77

Morin, J., et al. 2008b, MNRAS, 390, 567

Muirhead, P. S., et al. 2013, ArXiv e-prints

Munn, J. A., et al. 2004, AJ, 127, 3034

Munn, J. A., et al. 2008, AJ, 136, 895

Muzerolle, J., et al. 2009, ApJL, 704, L15

Nefs, S. V., et al. 2012, ArXiv e-prints

O'Neal, D., Neff, J. E., Saar, S. H., & Cuntz, M. 2004, AJ, 128, 1802

O'Neal, D., Saar, S. H., & Neff, J. E. 1996, ApJ, 463, 766

O'Neal, D., Saar, S. H., Neff, J. E., & Cuntz, M. 2005, in ESA Special Publication, Vol. 560, 13th Cambridge Workshop on Cool Stars, Stellar Systems and the Sun, ed. F. Favata, G. A. J. Hussain, & B. Battrick, 853

Osherovich, V. A. & Garcia, H. A. 1989, ApJ, 336, 468

Ossendrijver, M. 2003, AAPR, 11, 287

Parker, E. N. 1955, ApJ, 121, 491

Pasquini, L., et al. 2008, 70141I

Penn, M. J. & MacDonald, R. K. D. 2007, ApJL, 662, L123

Petit, P., Donati, J.-F., & Collier Cameron, A. 2004, Astron. Nachr., 325, 221

Petrovay, K. & van Driel-Gesztelyi, L. 1997, Sol. Phys., 176, 249

Phan-Bao, N., Lim, J., Donati, J.-F., Johns-Krull, C. M., & Martín, E. L. 2009, ApJ, 704, 1721

Pickles, A. J. 1998, PASP, 110, 863

Pinfield, D. J. 2007, The WFCAM Transit Survey (WTS), UKIRT campaign proposal, star.herts.ac.uk/RoPACS/Files/wts.pdf

Plavchan, P., Jura, M., Kirkpatrick, J. D., Cutri, R. M., & Gallagher, S. C. 2008, ApJS, 175, 191

Press, W. H. & Rybicki, G. B. 1989, ApJ, 338, 277

Rabus, M., et al. 2009, A&A, 494, 391

Reiners, A. 2012, Living Reviews in Solar Physics, 9, 1

Reiners, A. & Basri, G. 2008, ApJ, 684, 1390

Reiners, A., Joshi, N., & Goldman, B. 2012a, AJ, 143, 93

Reiners, A. & Mohanty, S. 2012b, ApJ, 746, 43

Ricker, G. R., et al. 2010, in Bulletin of the American Astronomical Society, Vol. 42, American Astronomical Society Meeting Abstracts #215, 450.06

Roberts, D. H., Lehar, J., & Dreher, J. W. 1987, AJ, 93, 968

Rockenfeller, B., Bailer-Jones, C. A. L., & Mundt, R. 2006, A&A, 448, 1111

Rodríguez Medina, R. 1983, Masters Thesis, Universidad de La Laguna

Scargle, J. D. 1982, ApJ, 263, 835

Schlichenmaier, R., Bello González, N., Rezaei, R., & Waldmann, T. A. 2010a, Astronomische Nachrichten, 331, 563

Schlichenmaier, R., Rezaei, R., Bello González, N., & Waldmann, T. A. 2010b, A&A, 512, L1

Scholz, R.-D., Meusinger, H., & Jahreiß, H. 2005, A&A, 442, 211

Schüssler, M., Caligari, P., Ferriz-Mas, A., Solanki, S. K., & Stix, M. 1996, A&A, 314, 503

Silva-Valio, A., Lanza, A. F., Alonso, R., & Barge, P. 2010, A&A, 510, A25

Solanki, S. K. 1999, in Astronomical Society of the Pacific Conference Series, Vol. 158, Solar and Stellar Activity: Similarities and Differences, ed. C. J. Butler & J. G. Doyle, 109

Solanki, S. K. 2003, AAPR, 11, 153

Solanki, S. K. & Unruh, Y. C. 2004, MNRAS, 348, 307

Spiegel, E. A. & Zahn, J.-P. 1992, A&A, 265, 106

Steinegger, M., Brandt, P. N., Schmidt, W., & Pap, J. 1990, APSS, 170, 127

Stelzer, B., Marino, A., Micela, G., López-Santiago, J., & Liefke, C. 2013, MNRAS, 431, 2063

Strassmeier, K. G., Hall, D. S., & Henry, G. W. 1994, A&A, 282, 535

Sütterlin, P. & Wiehr, E. 1998, A&A, 336, 367

Swingler, D. N. 1989, AJ, 97, 280

Szentgyorgyi, A., et al. 2011, PASP, 123, 1188

Tandberg-Hanssen, E. 1956, Astrophysica Norvegica, 5, 207

Tofflemire, B. M., Wisniewski, J. P., Kowalski, A. F., Schmidt, S. J., Kundurthy, P., Hilton, E. J., Holtzman, J. A., & Hawley, S. L. 2012, AJ, 143, 12

Vogt, S. S. & Penrod, G. D. 1983, PASP, 95, 565

Vogt, S. S., Penrod, G. D., & Hatzes, A. P. 1987, ApJ, 321, 496

Waldmeier, M. 1955, Ergebnisse und Probleme der Sonnenforschung.

West, A. A., Hawley, S. L., Bochanski, J. J., Covey, K. R., Reid, I. N., Dhital, S., Hilton, E. J., & Masuda, M. 2008, AJ, 135, 785

West, A. A., et al. 2011, AJ, 141, 97

Winn, J. N., et al. 2010, ApJL, 723, L223

Woolf, V. M., Lépine, S., & Wallerstein, G. 2009, PASP, 121, 117

Appendix

A1 Light Curves and Periodograms

This section lists the light curves and periodograms found for the stars in the WFCAM transit survey. The format for each of the figures is as follows: *Top*: plot shows the unfolded light curve with consecutive observations coloured in blocks. *Middle left*: The Lomb Scargle periodogram with the peak corresponding to the period marked by the red line and the dotted black line indicating the FAP threshold. *Middle right*: The CLEAN periodogram with the red line indicating the period as found from the Lomb-Scargle periodogram. *Lower left*: The light curve folded about the period as derived from the CLEAN periodogram maintaining the colours ascribed from the unfolded light curve. *Lower right*: The folded light curved binned to indicate the modulation. In each of the peridograms the vertical red line is indicative of the initial period as found by the Lomb-Scargle periodogram. The period found by the CLEAN algorithm is the period ultimately settled on, as indicated by the largest peak, although the red line indicates the Lomb-Scargle period for comparison in each CLEAN periodogram.

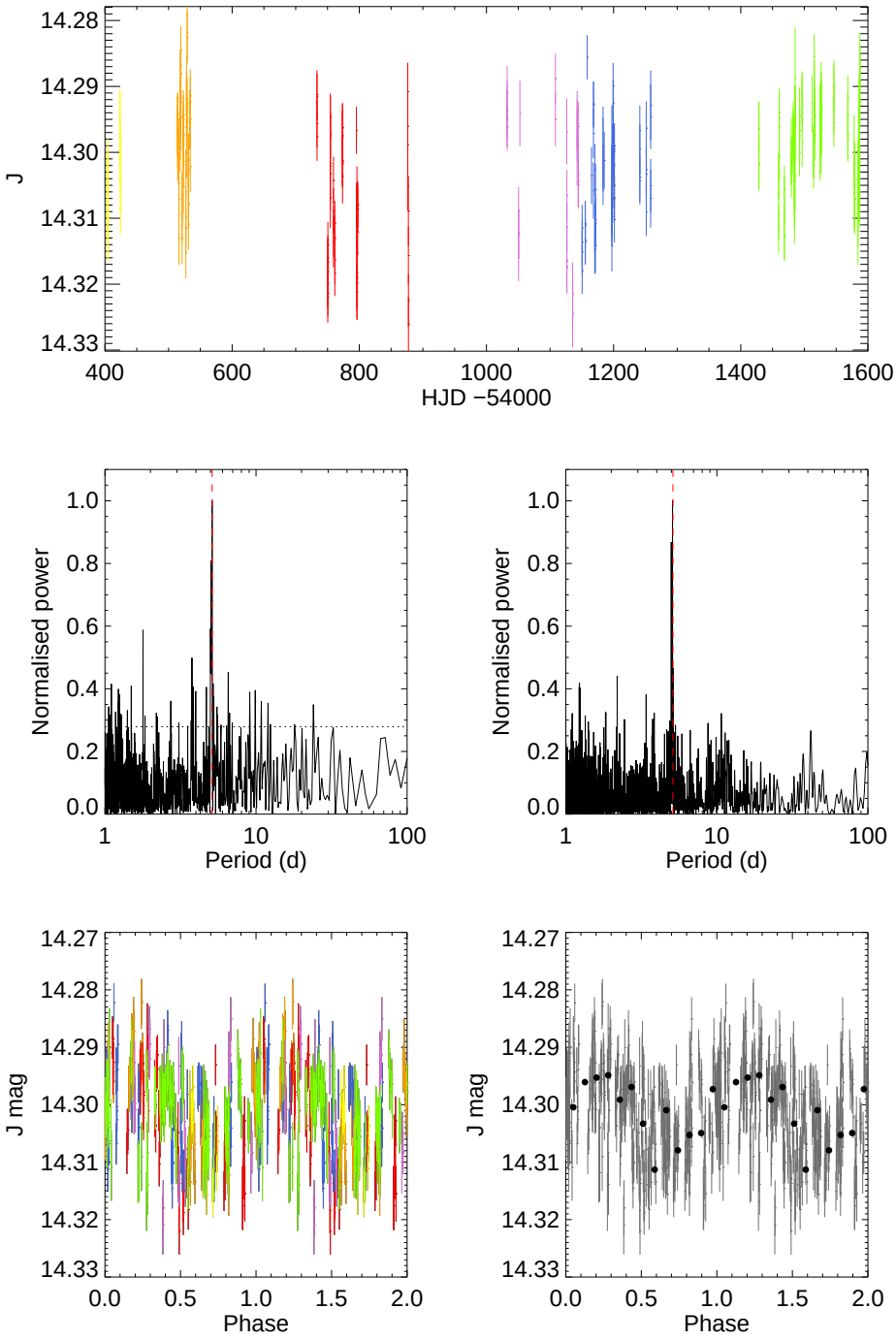

Period (d)	4.880
Amplitude (J)	0.017 ± 0.004
Spectral Type	M1 ± 1.01

FIGURE A1: Light curves and periodograms for the star 03d_1_04395. The most significant peak is ignored as it corresponds to the 1d aliasing period.

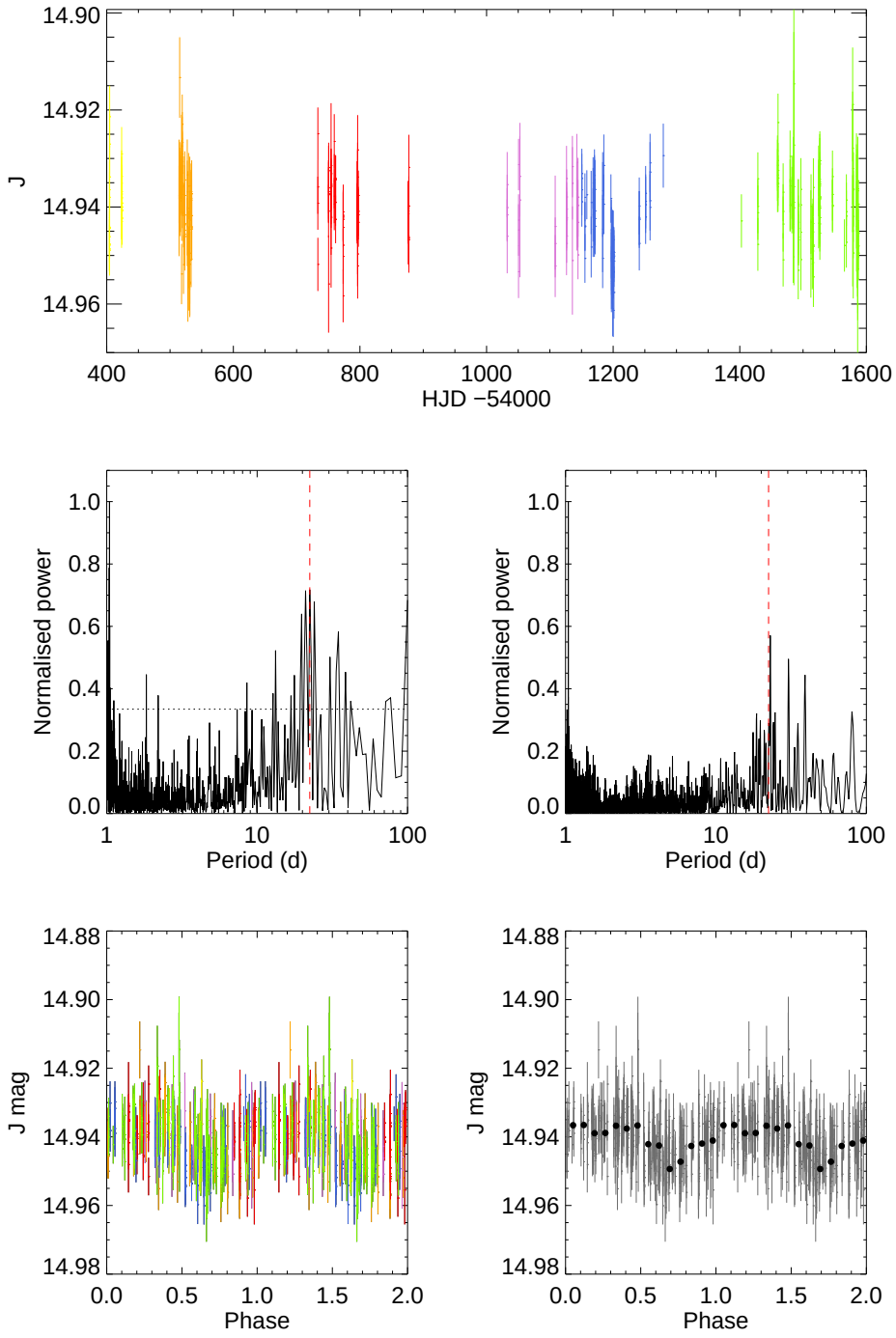

Period (d)	24.100
Amplitude (J)	0.015 ± 0.006
Spectral Type	K5 ± 9.36

Figure A2: As in Figure A1 for the star 03e_1_02053. The morphology of this light curve appears to be saw-toothed, although a differing morphology is seen for the red-coloured epochs, perhaps indicating spot evolution.

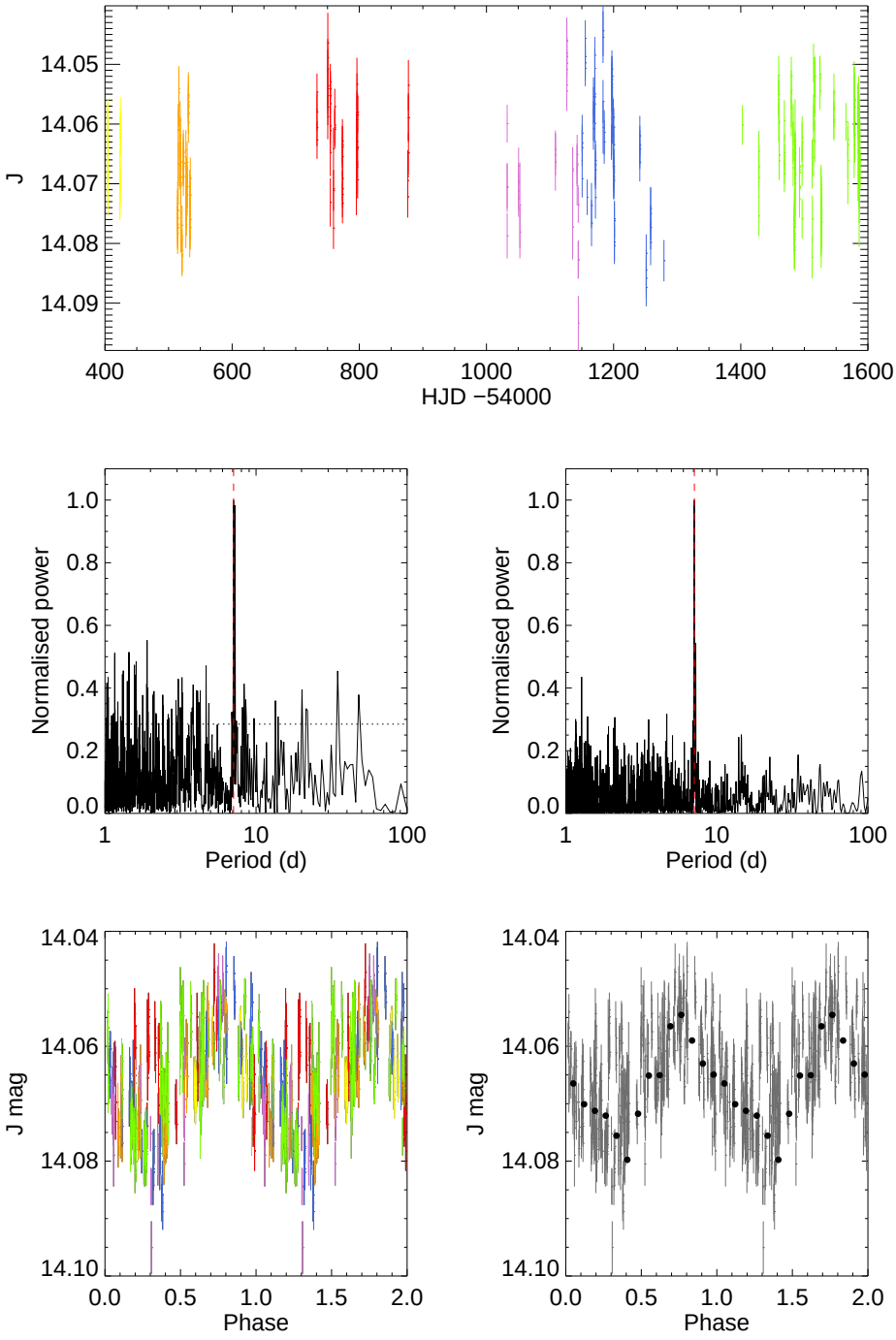

Period (d)	7.090
Amplitude (J)	0.024 ± 0.004
Spectral Type	M1 ± 1.01

FIGURE A3: As in Figure A2 for the star 03e_2_03325.

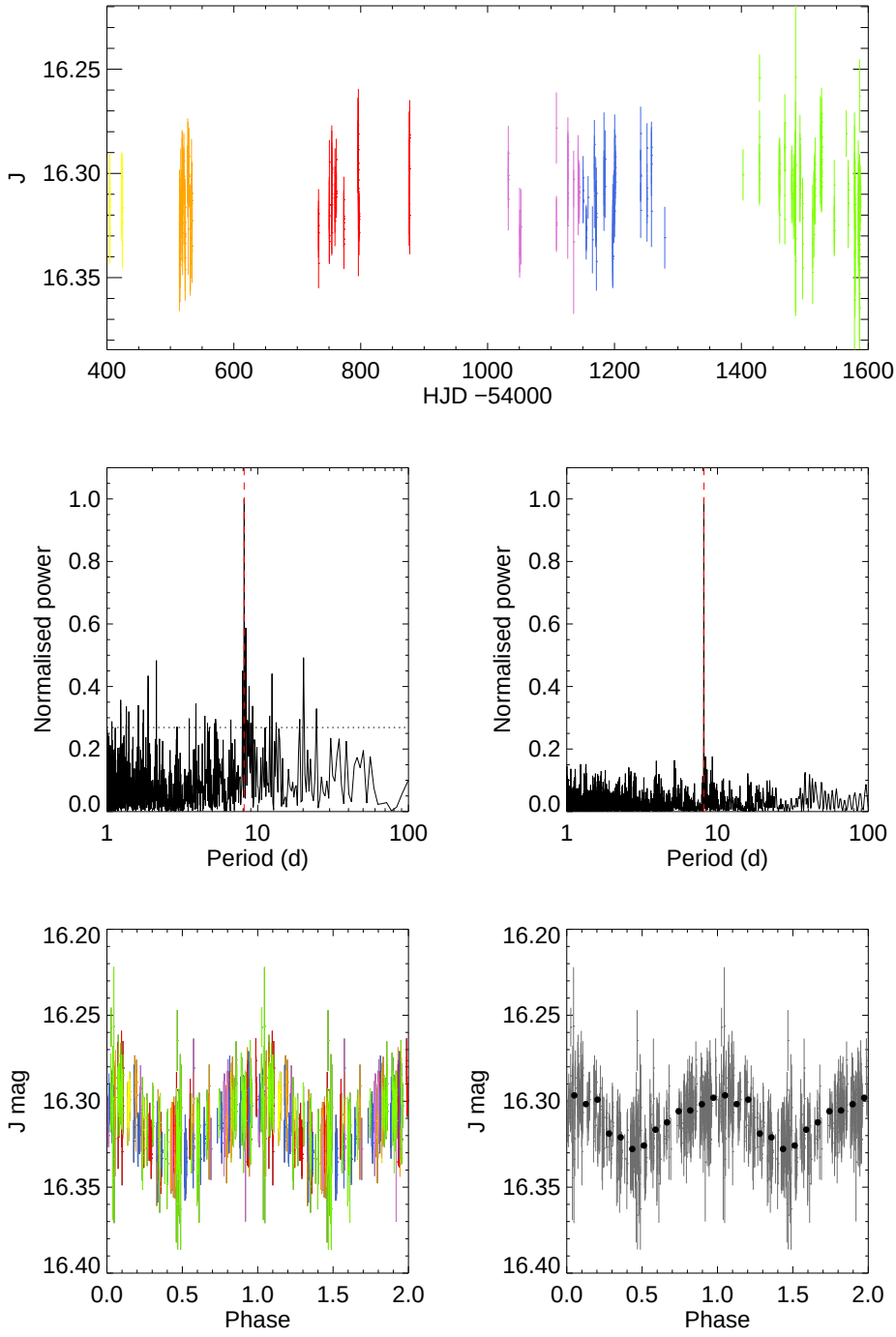

Period (d)	8.110
Amplitude (J)	0.037 ± 0.014
Spectral Type	M4 ± 1.01

Figure A4: As in Figure A3 for the star 03f_1_03040.

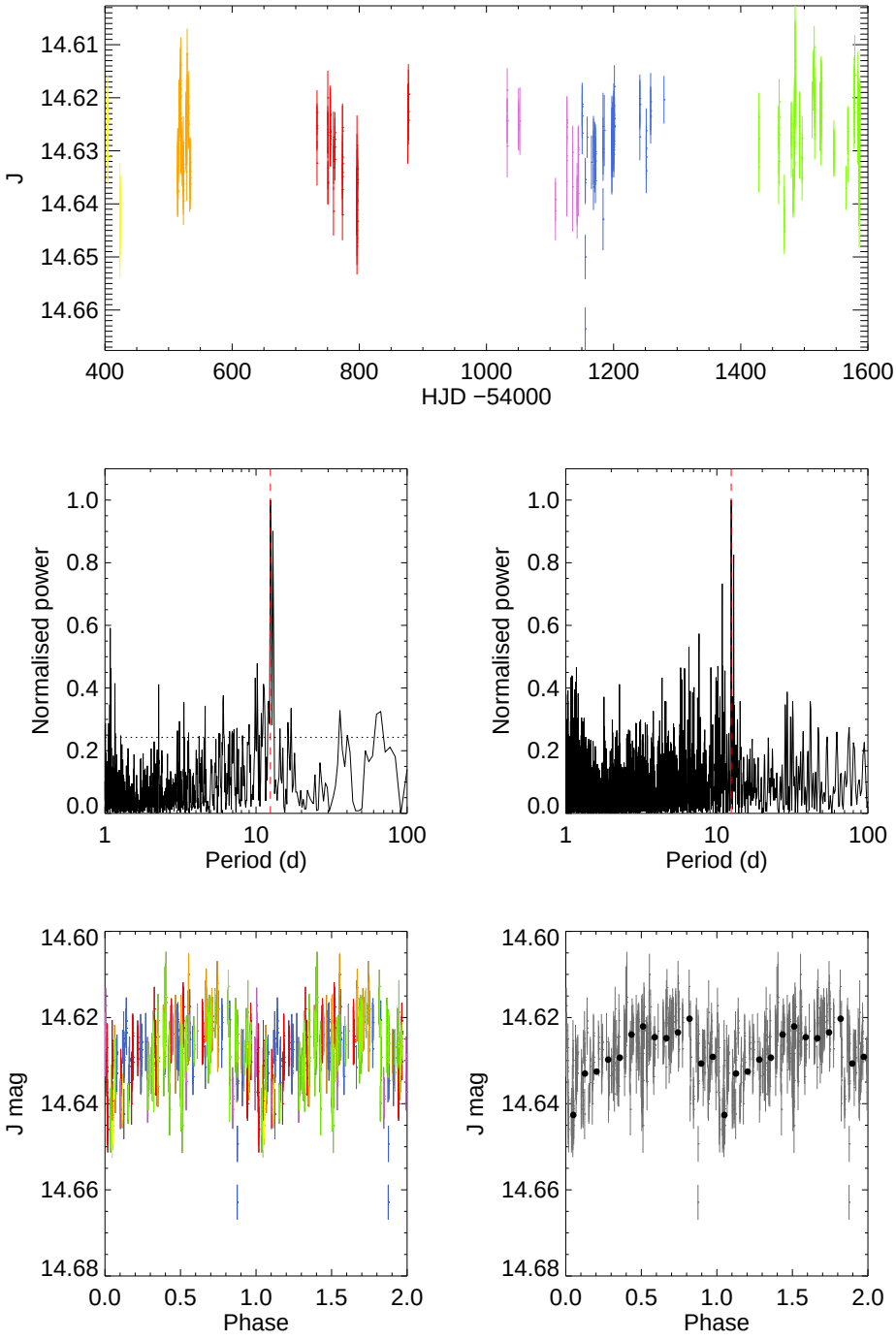

Period (d)	12.440
Amplitude (J)	0.020 ± 0.004
Spectral Type	M0 ± 7.64

FIGURE A5: As in Figure A4 for the star 03h_2_01177.

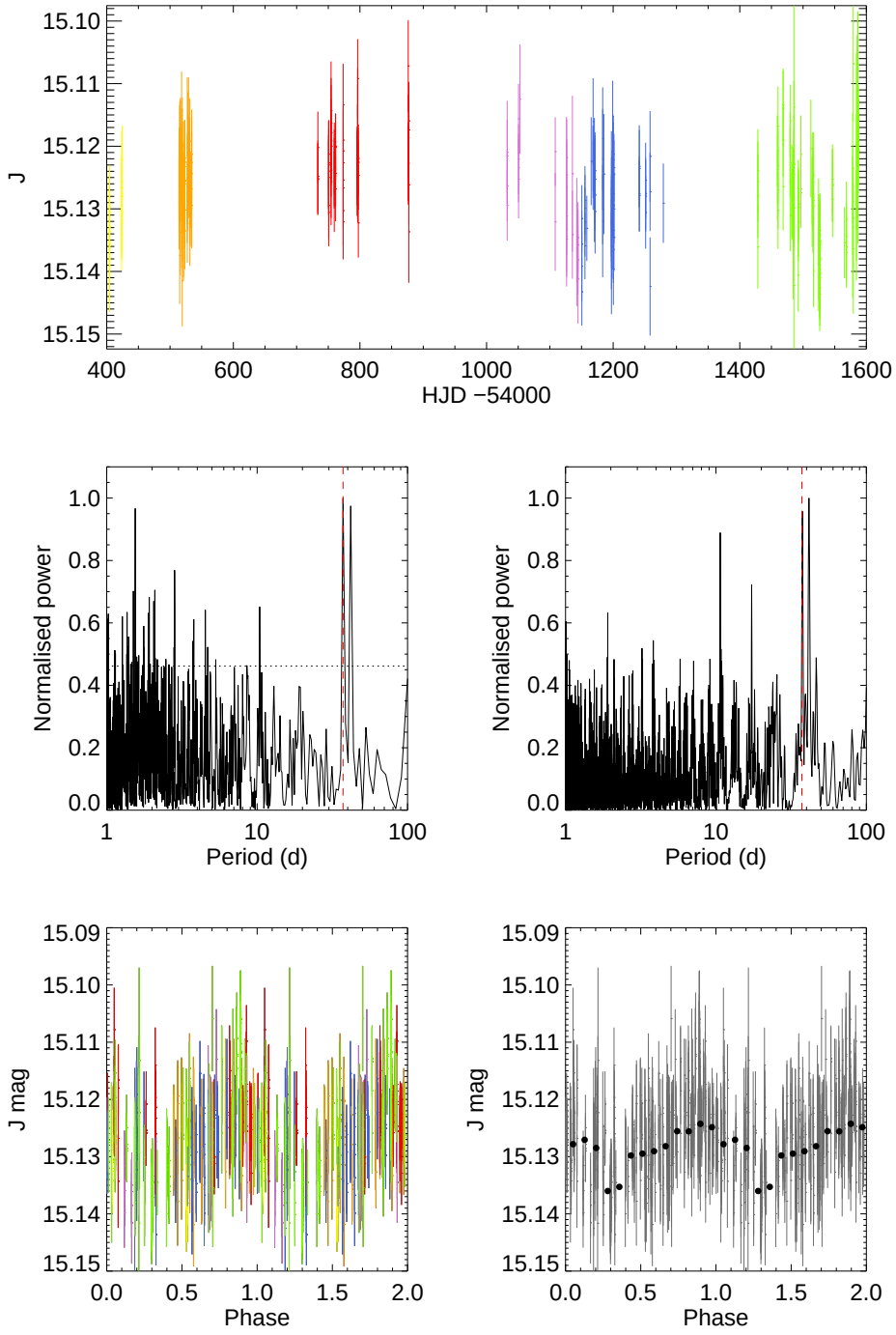

Period (d)	37.690
Amplitude (J)	0.017±0.006
Spectral Type	M3±1.00

Figure A6: As in Figure A5 for the star 03h_4_04646. As the light curve is noisy a number of spurious peaks are found at different significances in the Lomb-Scarlge and CLEAN periodograms. In both instances, the peak corresponding to the rotation period is fragmented.

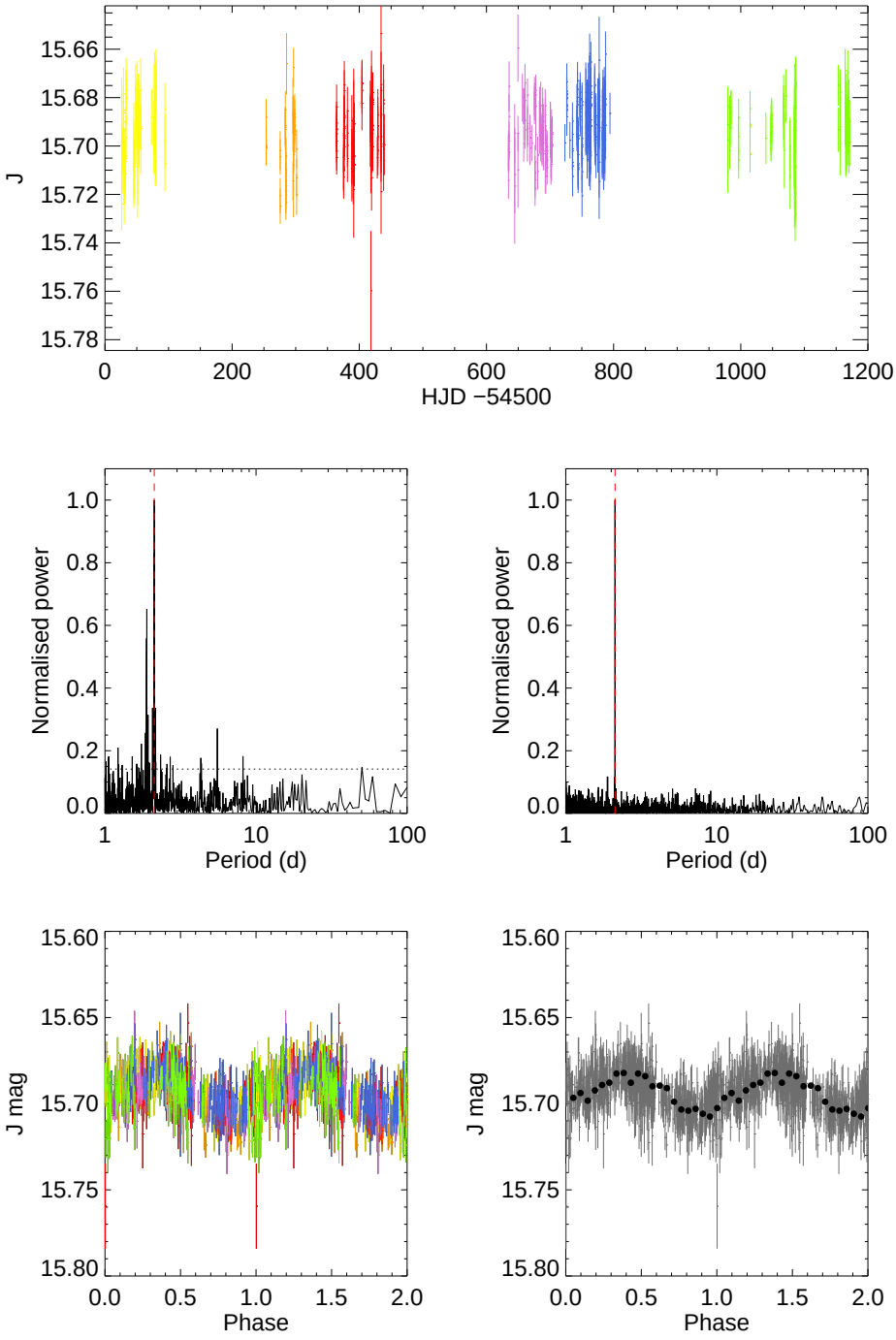

Period (d)	2.120
Amplitude (J)	0.029±0.009
Spectral Type	M4±1.00

FIGURE A7: As in Figure A6 for the star 07b_2_02081.

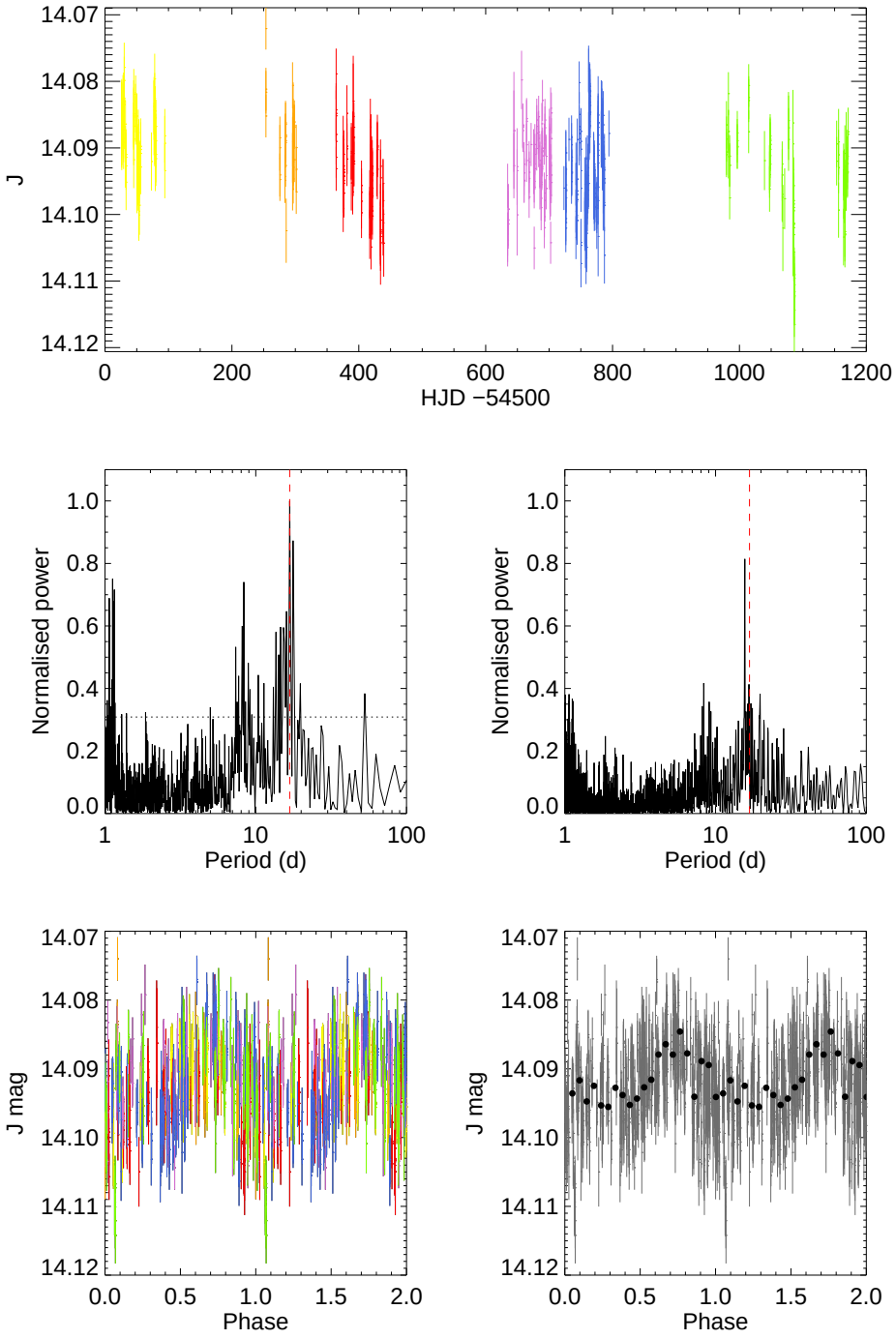

Period (d)	16.660
Amplitude (J)	0.014±0.004
Spectral Type	M3±1.00

Figure A8: As in Figure A7 for the star 07b_2_02125.

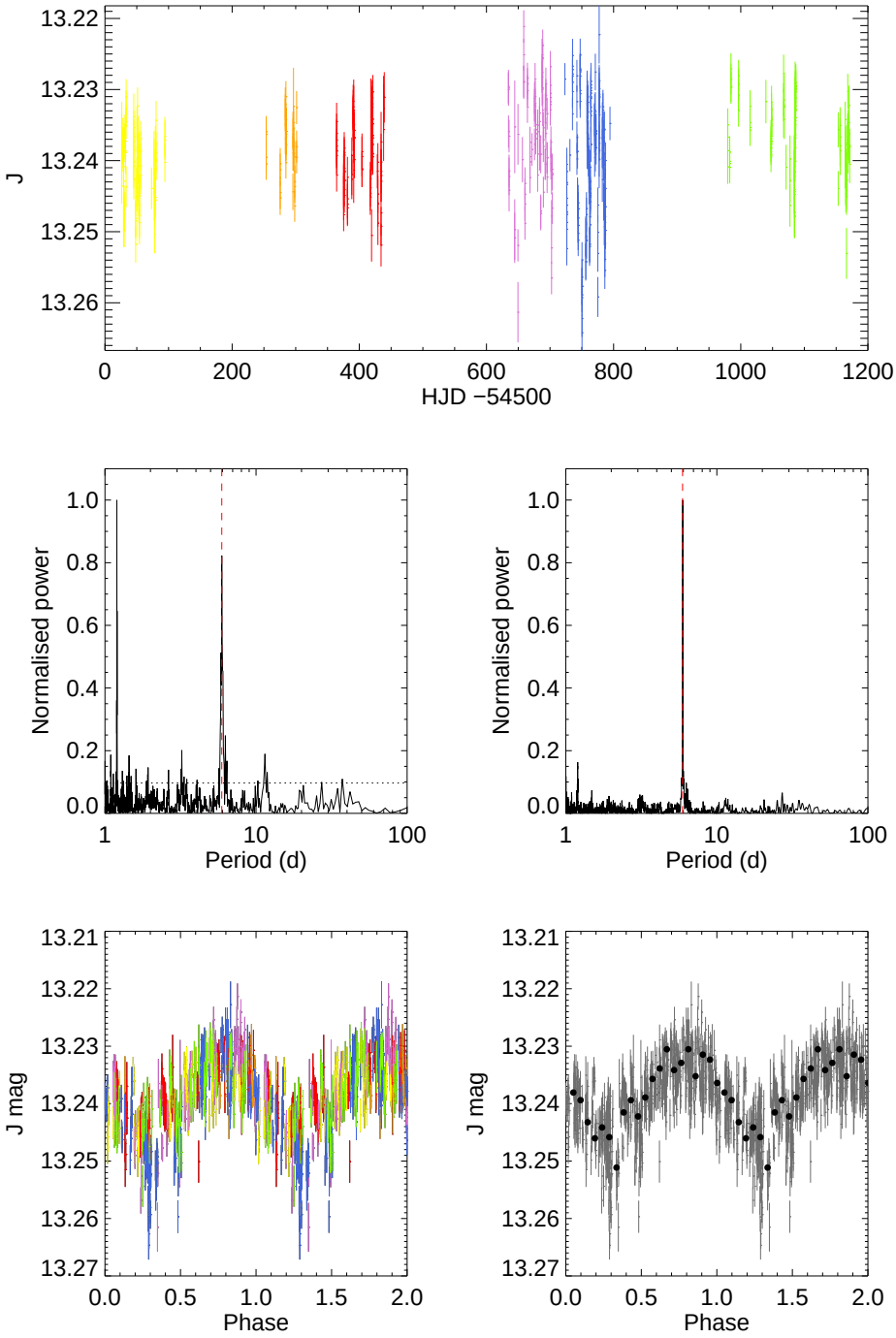

Period (d)	5.950
Amplitude (J)	0.019±0.003
Spectral Type	M4±1.00

FIGURE A9: As in Figure A8 for the star 07b_2_02237.

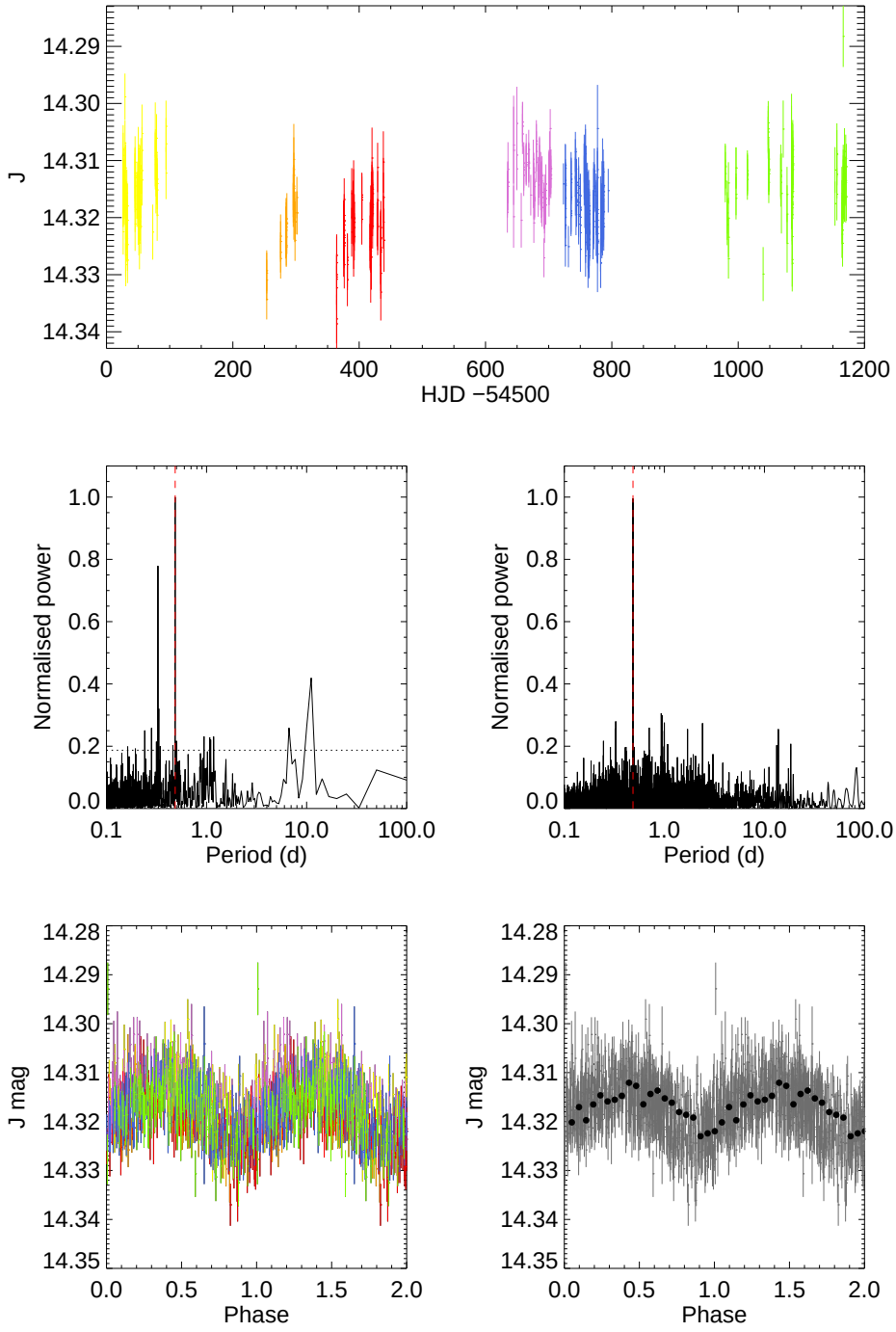

Period (d)	0.490
Amplitude (J)	0.011±0.004
Spectral Type	M4±1.01

Figure A10: As in Figure A9 for the star 07b_3_00631.

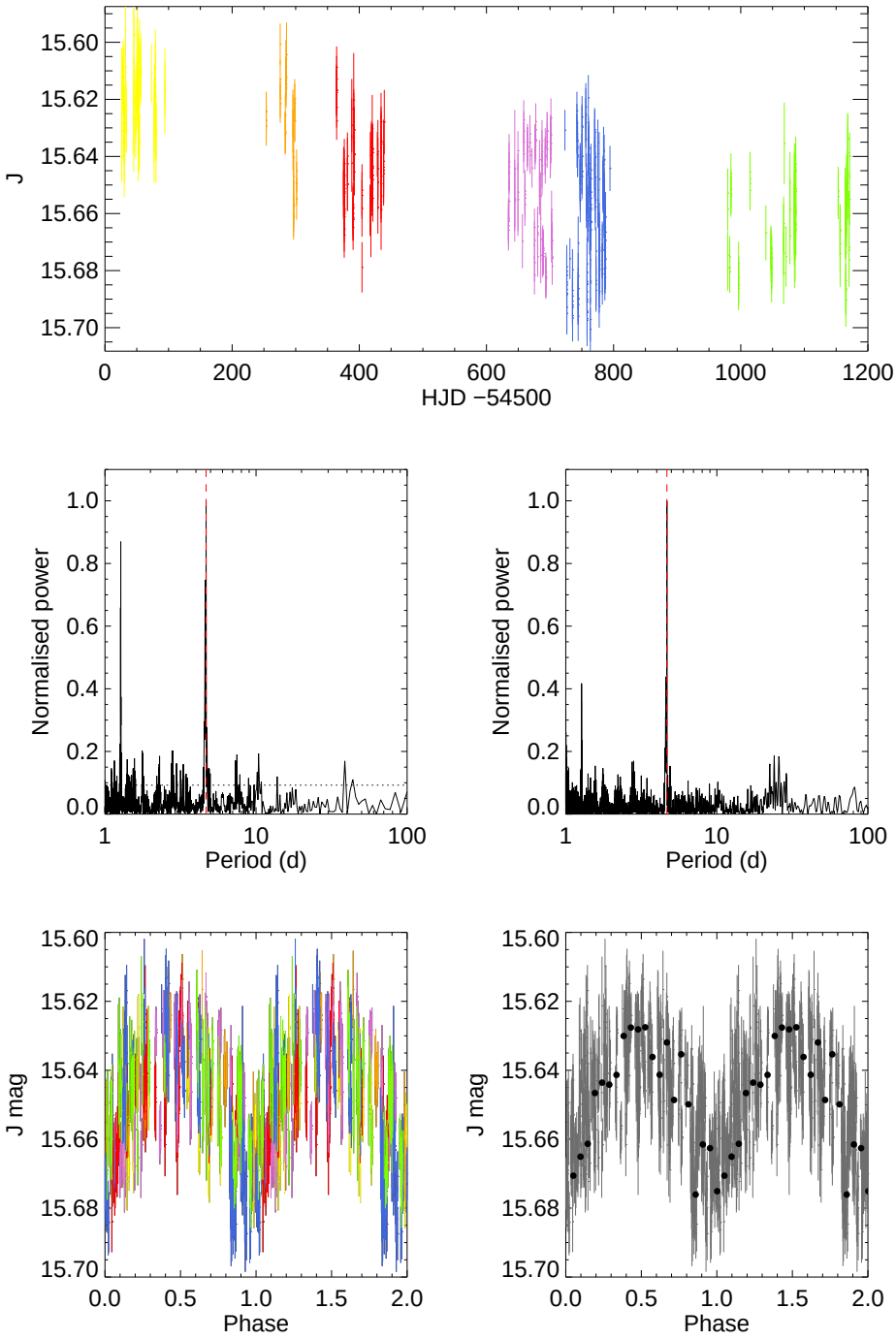

Period (d)	4.670
Amplitude (J)	0.043±0.008
Spectral Type	M0±1.06

FIGURE A11: As in Figure A10 for the star 07b_3_02281. A long term trend is also seen in the unfolded light curve showing the star decreasing in brightness over ∼3 years.

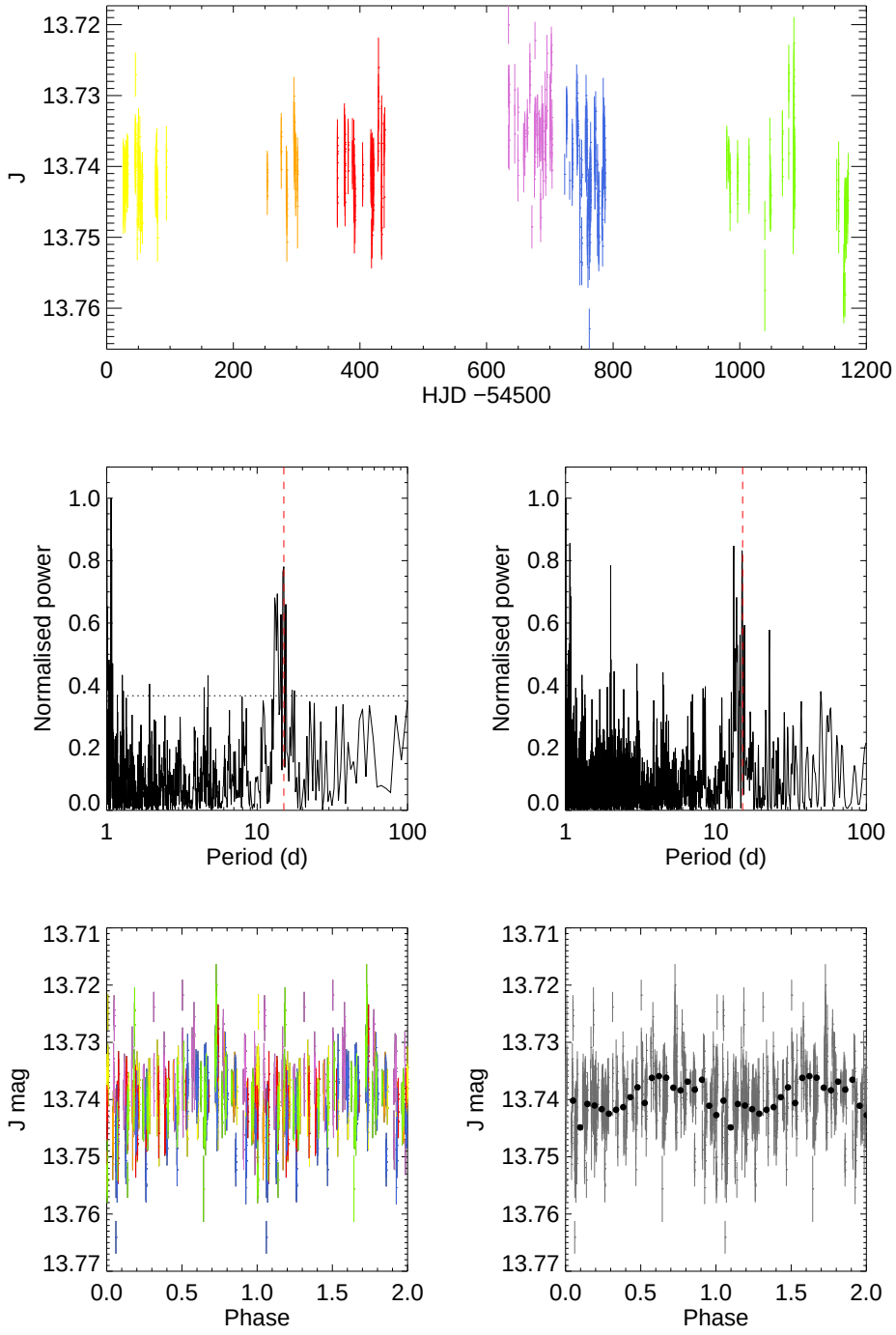

Period (d)	14.920
Amplitude (J)	0.013±0.003
Spectral Type	M2±1.00

Figure A12: As in Figure A11 for the star 07c_2_00282.

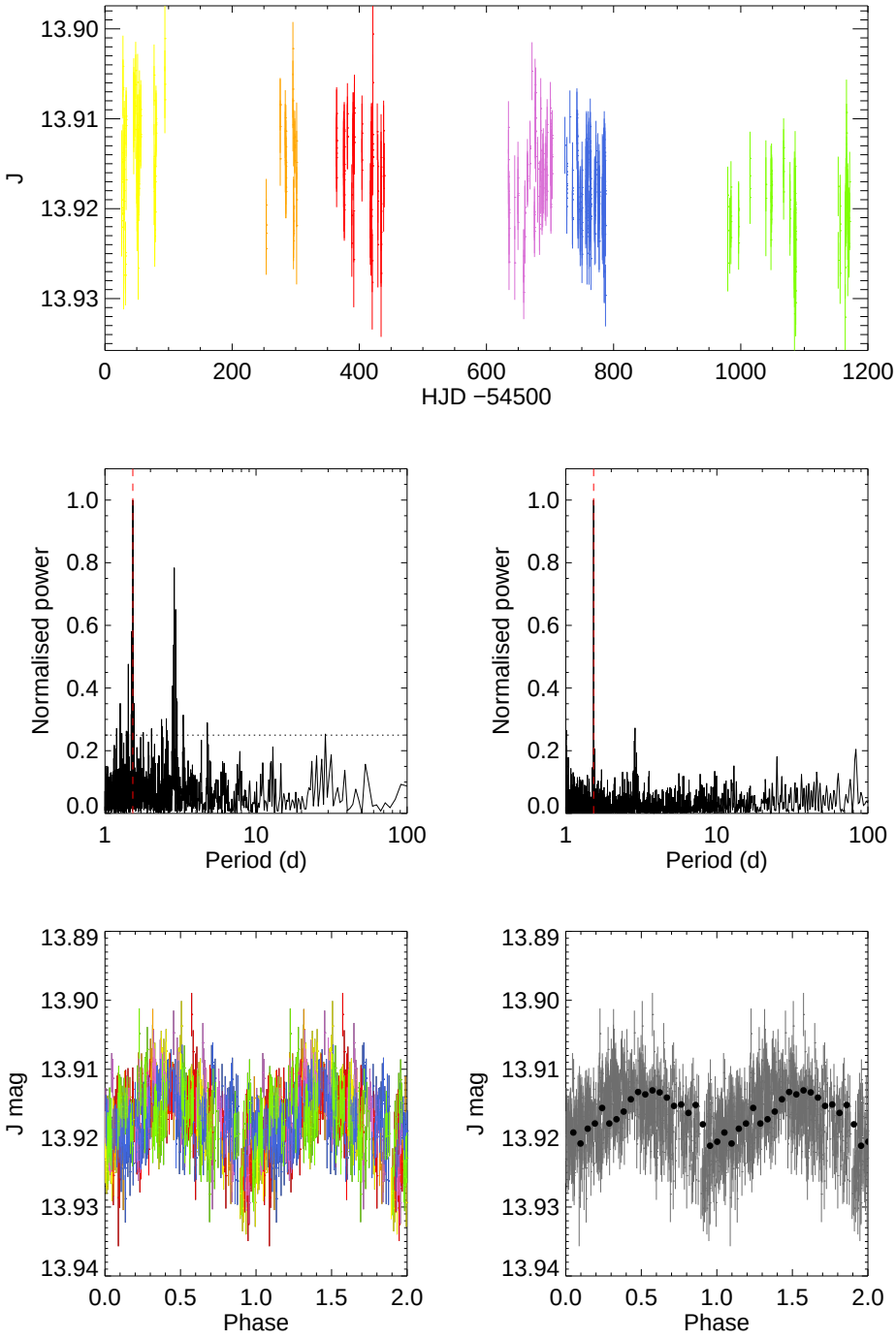

Period (d)	1.530
Amplitude (J)	0.012±0.003
Spectral Type	M3±1.00

FIGURE A13: As in Figure A12 for the star 07c_2_00294.

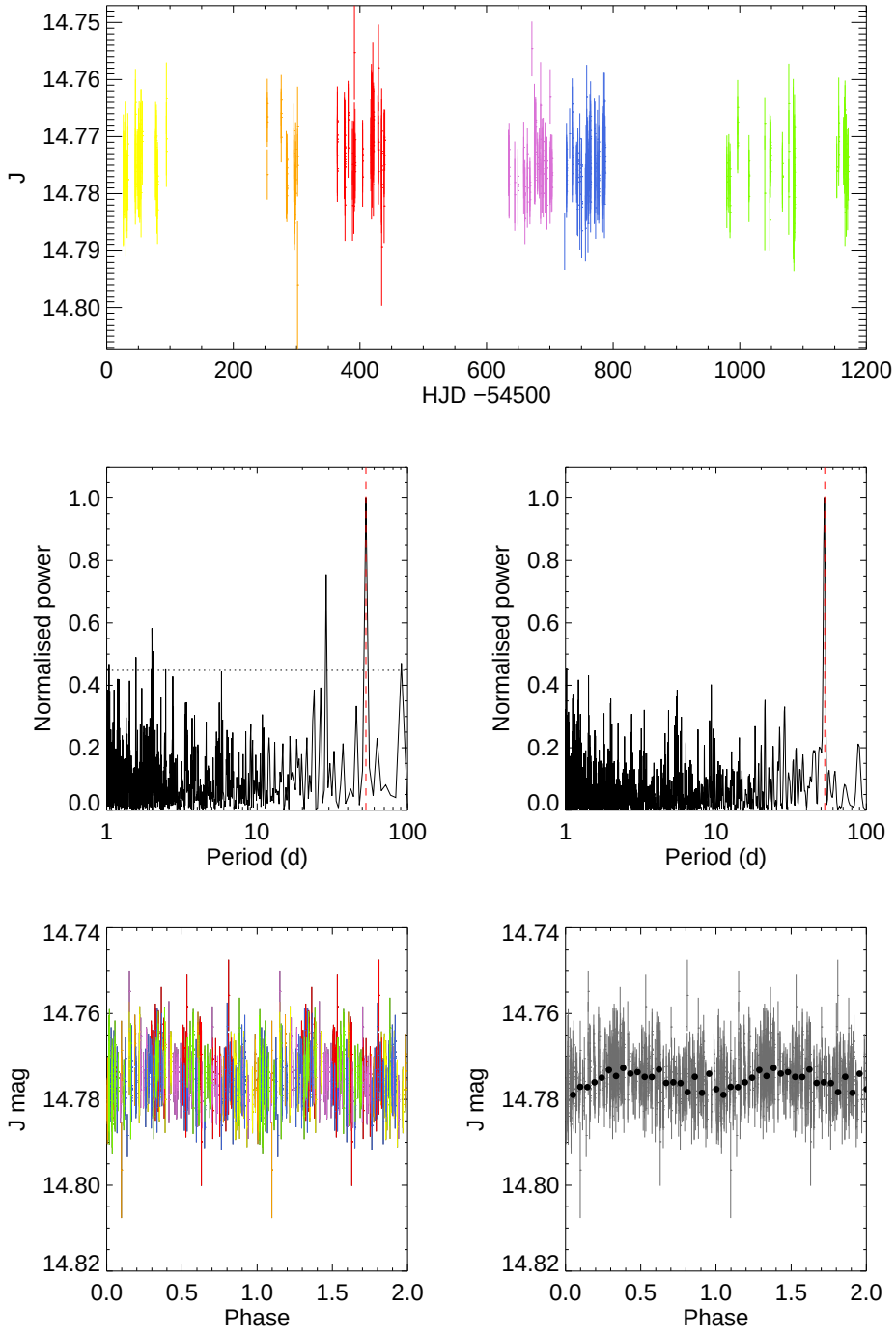

Period (d)	52.490
Amplitude (J)	0.009±0.005
Spectral Type	M3±1.00

Figure A14: As in Figure A13 for the star 07c_4_04250. The periodic nature of this star is not obvious in the folded light curve, although both the Lomb-Scargle and CLEAN periodograms and binned data reveal the low-amplitude variation.

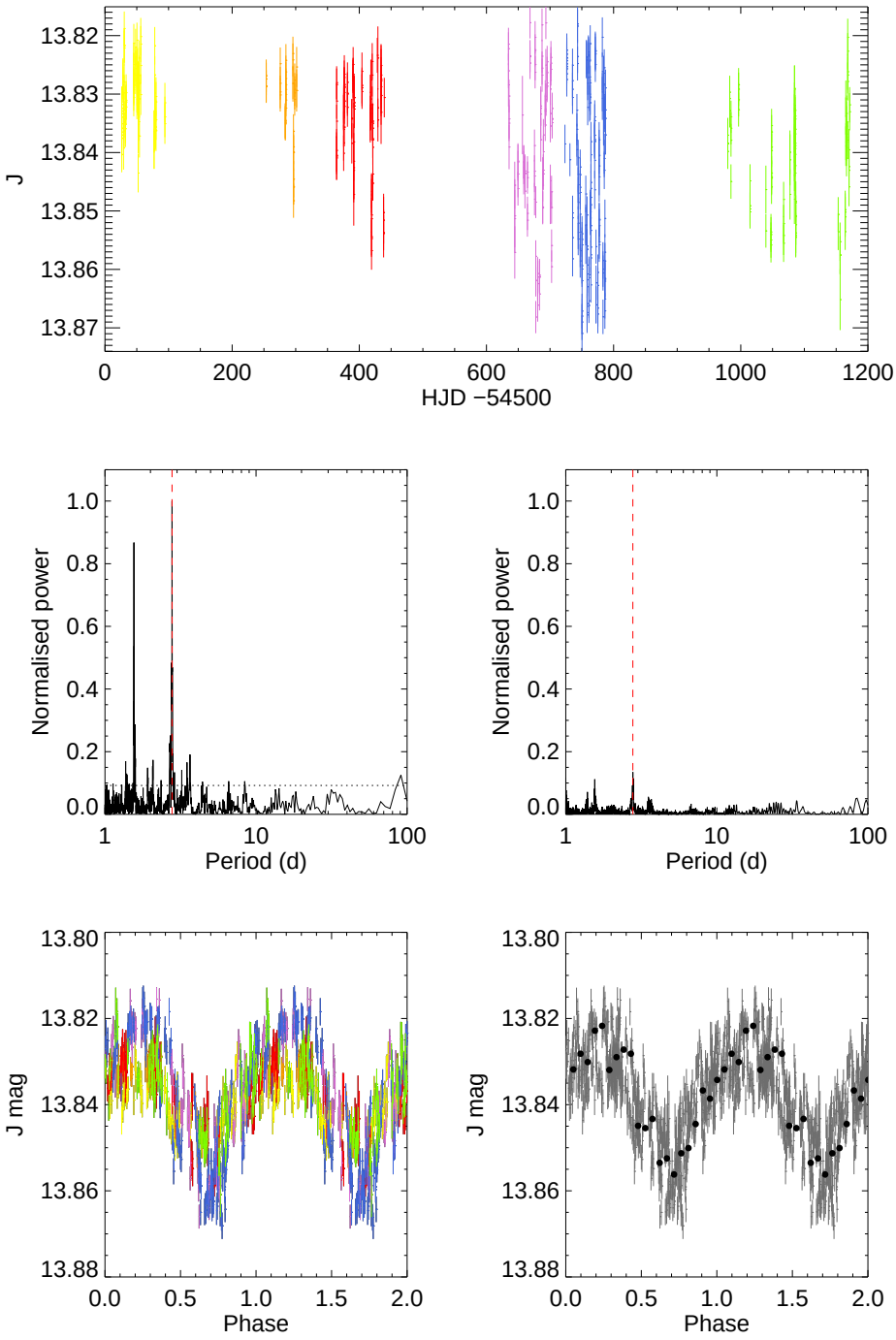

Period (d)	2.780
Amplitude (J)	0.037±0.003
Spectral Type	M1±1.00

FIGURE A15: As in Figure A14 for the star 07d_1_02956. This star shows obvious amplitude evolution with the amplitude in earlier observations (yellow) indicating a much smaller amplitude than is later seen after ∼ years of observations (purple and blue). As the average magnitude of the star decreases during this change, this is evidence of an increase in the number of dark spots on the stellar surface resulting in the change in amplitude.

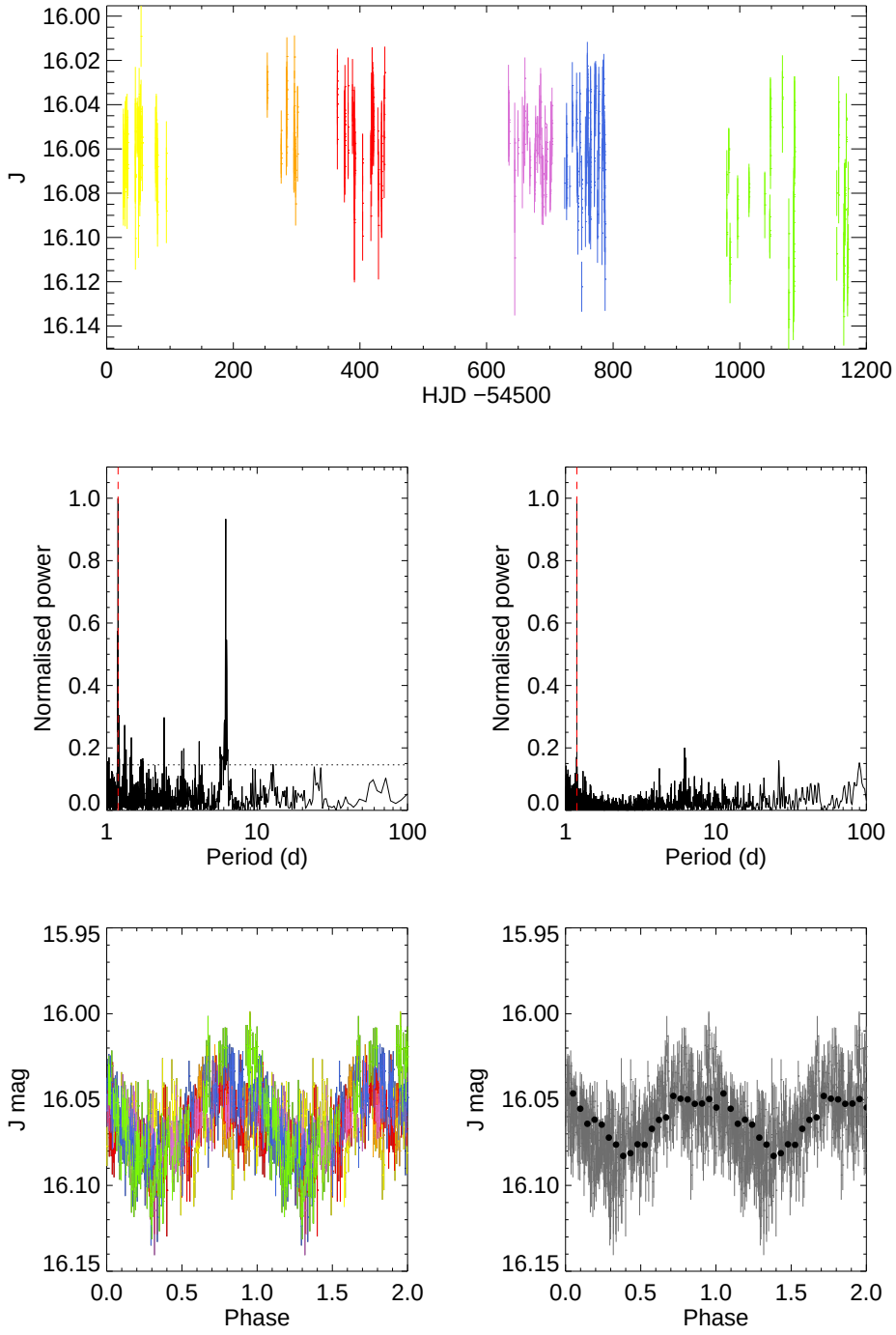

Period (d)	1.190
Amplitude (J)	0.042±0.011
Spectral Type	M0±1.11

Figure A16: As in Figure A15 for the star 07d_1_03180.

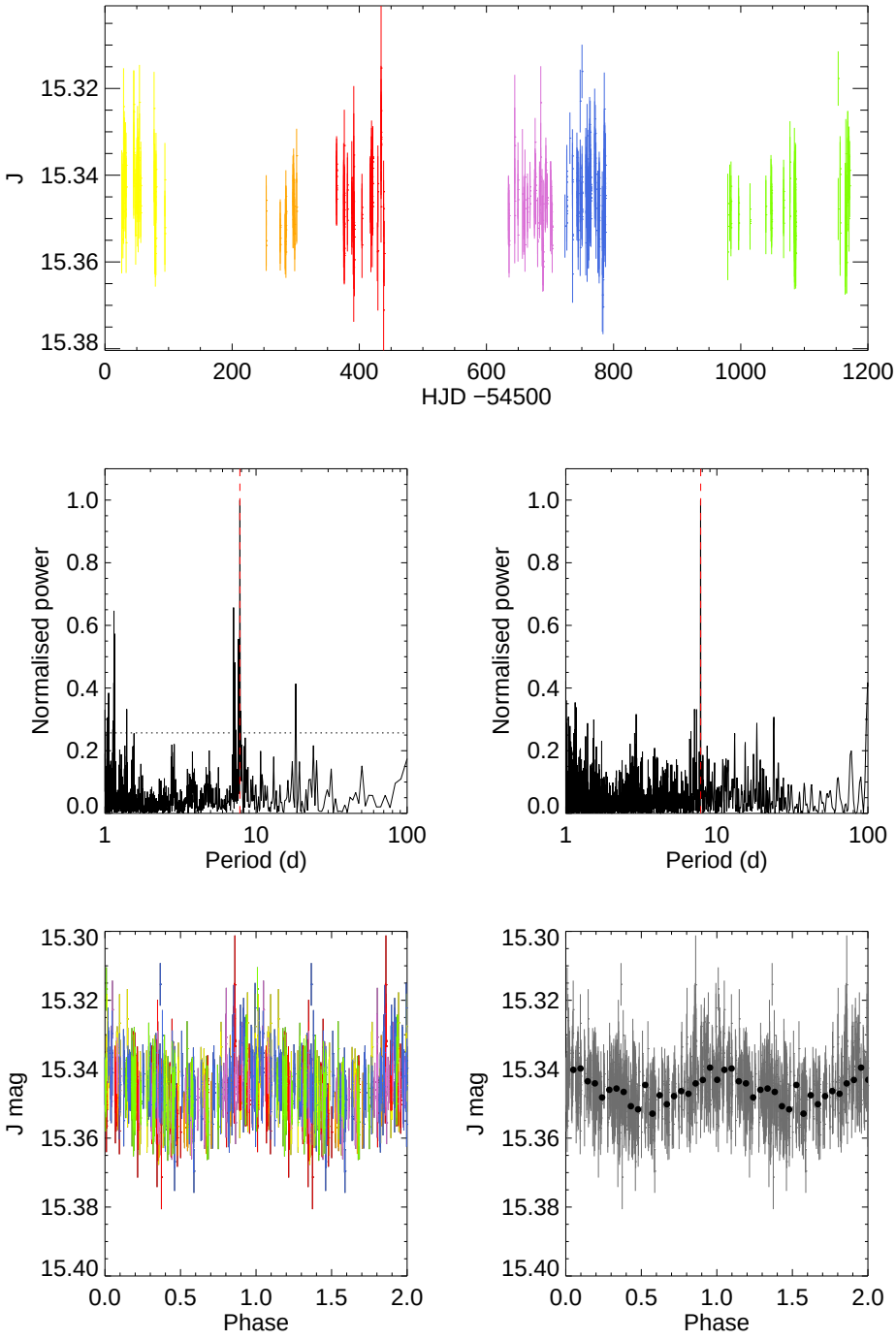

Period (d)	7.800
Amplitude (J)	0.013±0.007
Spectral Type	M3±1.00

FIGURE A17: As in Figure A16 for the star 07d_1_06063.

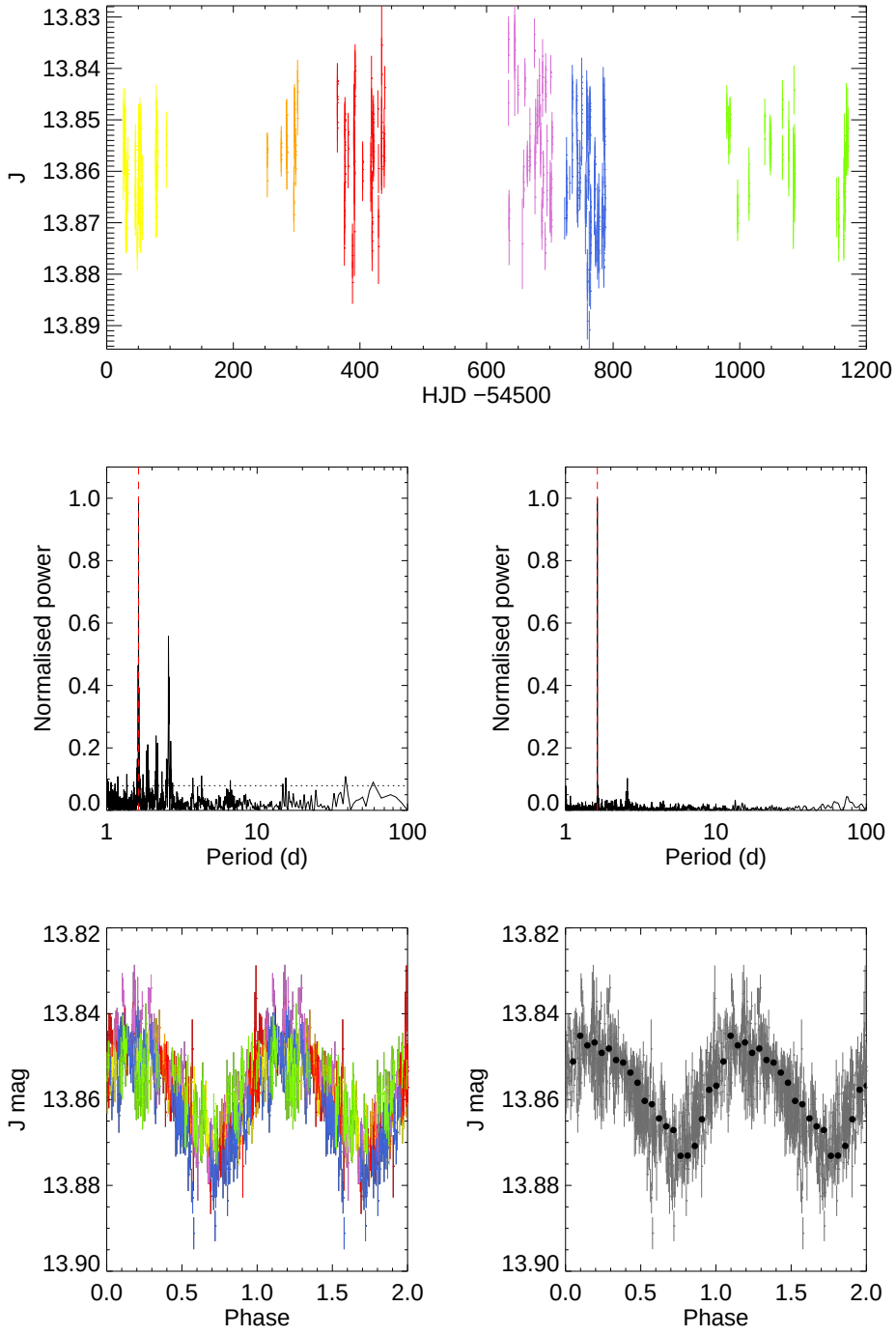

Period (d)	1.630
Amplitude (J)	0.028±0.004
Spectral Type	M3±1.00

Figure A18: As in Figure A17 for the star 07d_4_03625.

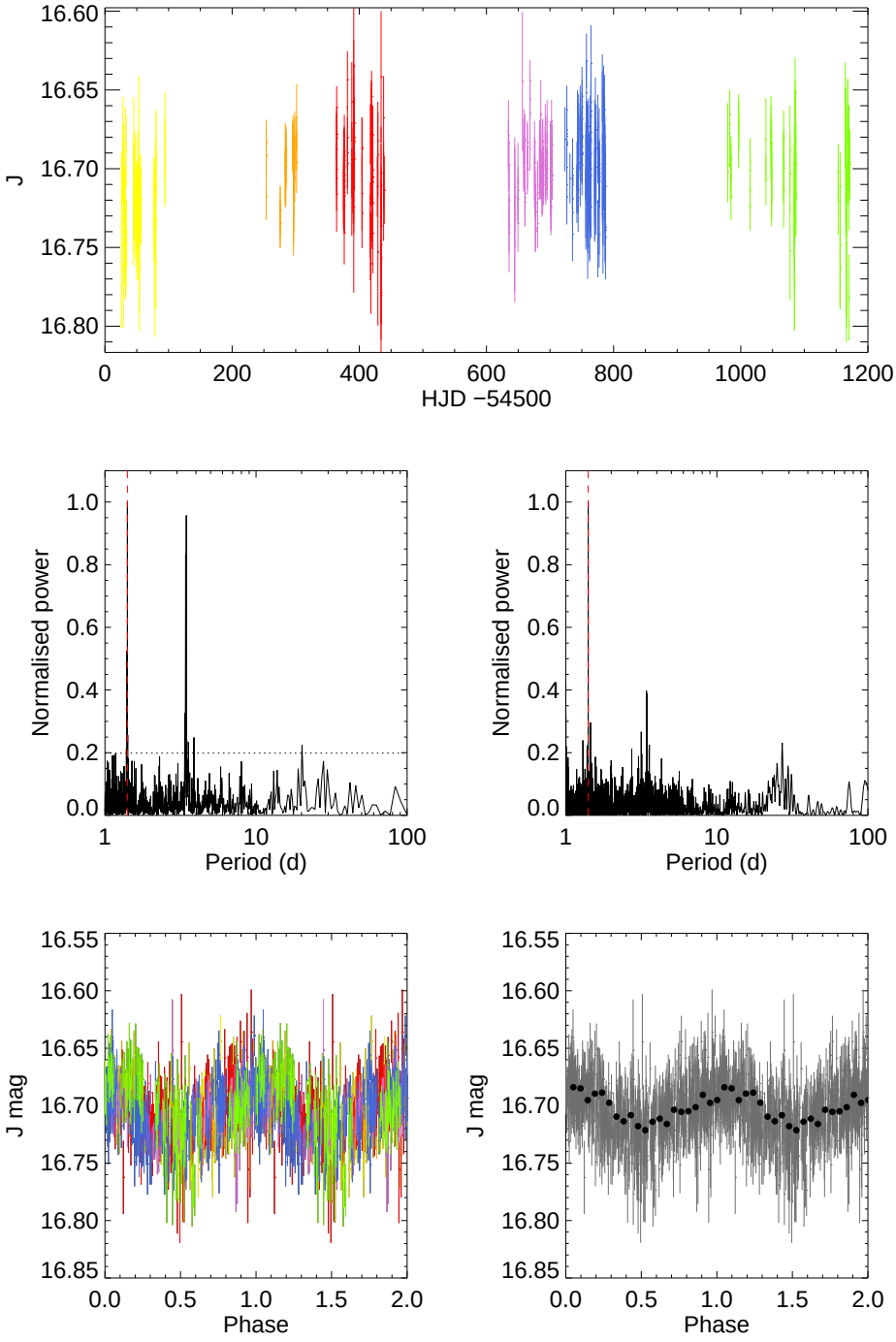

Period (d)	1.410
Amplitude (J)	0.047±0.020
Spectral Type	M0±1.01

FIGURE A19: As in Figure A18 for the star 07d_4_04577.

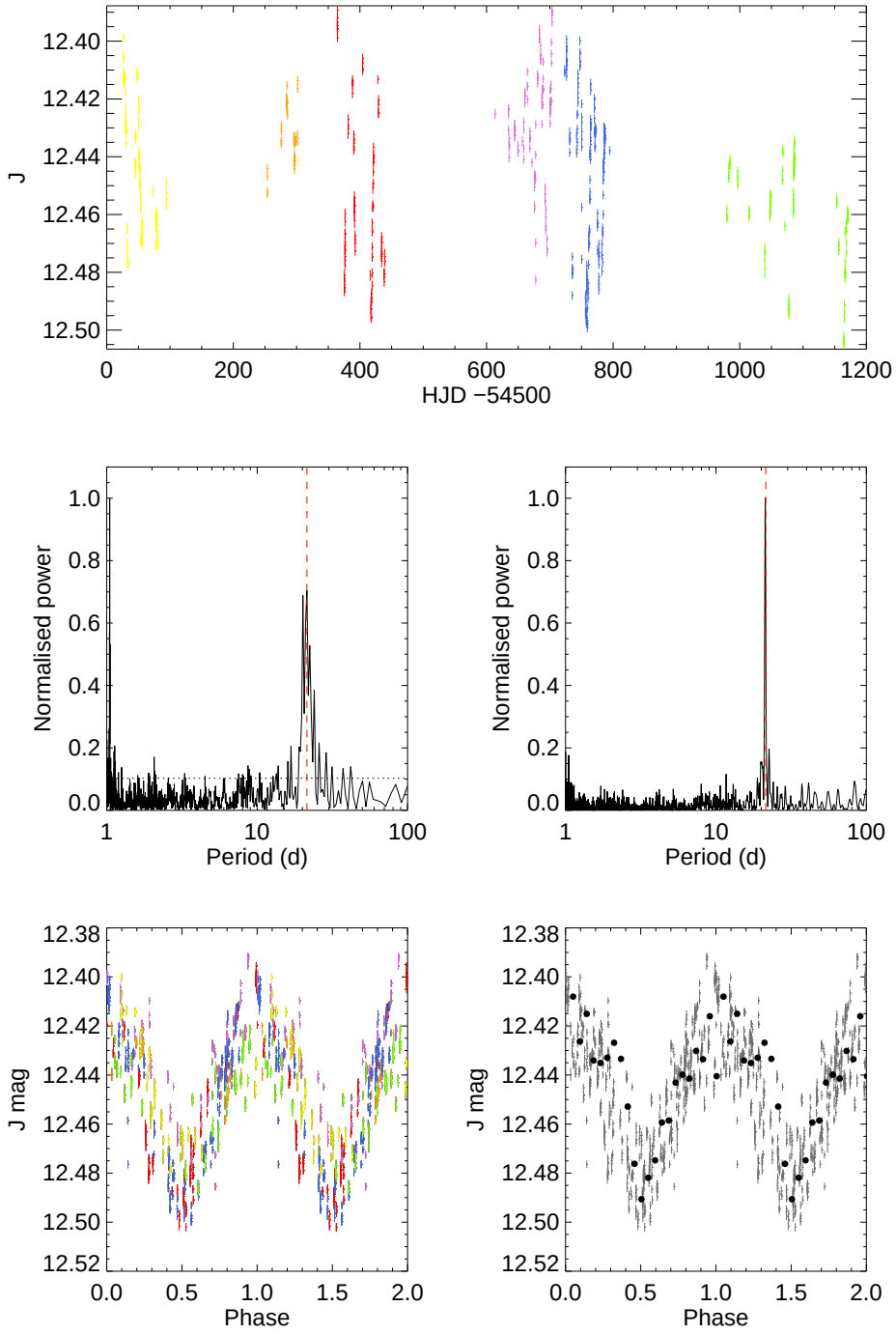

Period (d)	21.270
Amplitude (J)	0.078±0.002
Spectral Type	K2±2.20

Figure A20: As in Figure A19 for the star 07e_2_01022.

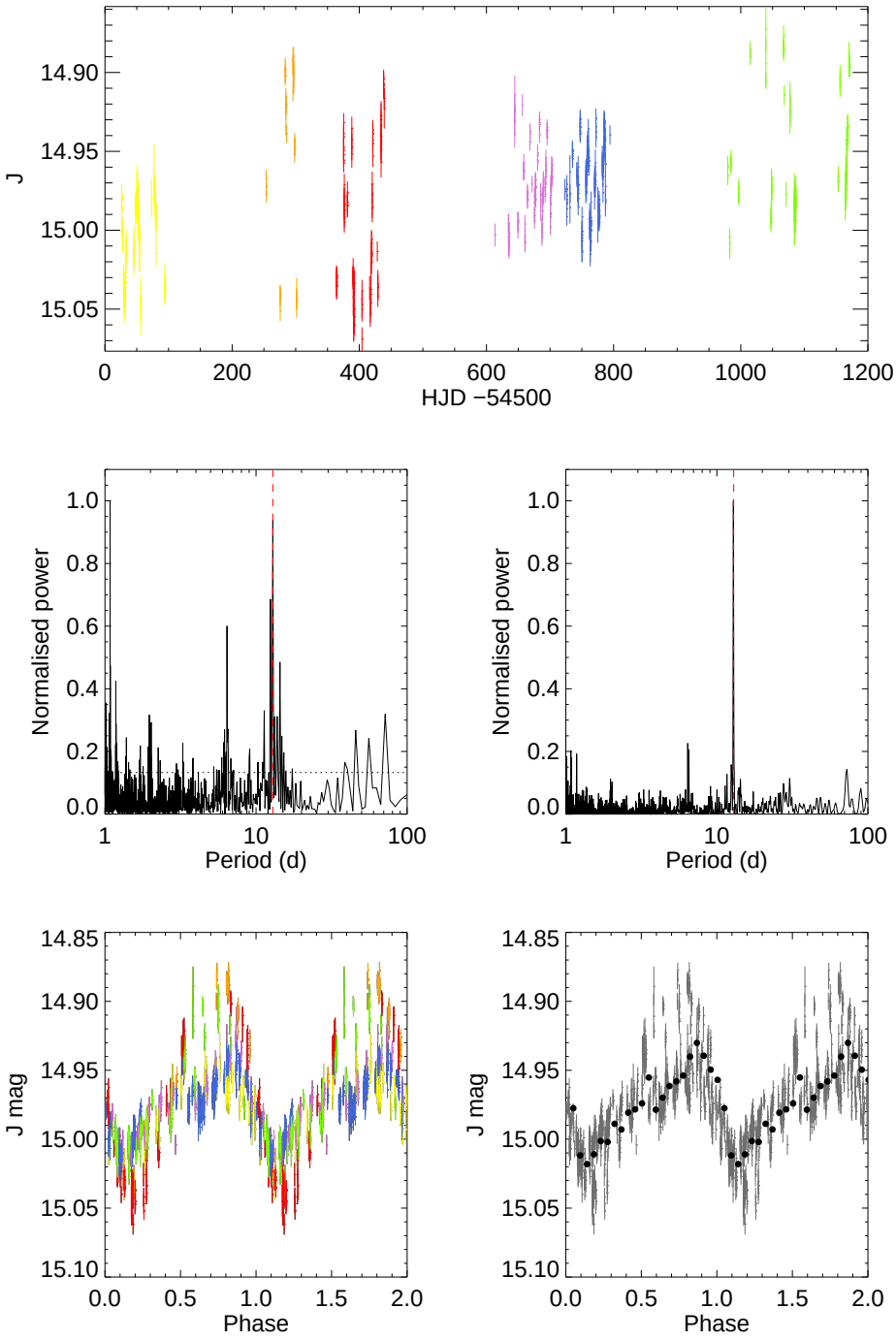

Period (d)	12.860
Amplitude (J)	0.110±0.007
Spectral Type	K7±1.44

FIGURE A21: As in Figure A20 for the star 07e_2_02466. As discussed in Section 3.5, this start shows clear evidence of spot evolution.

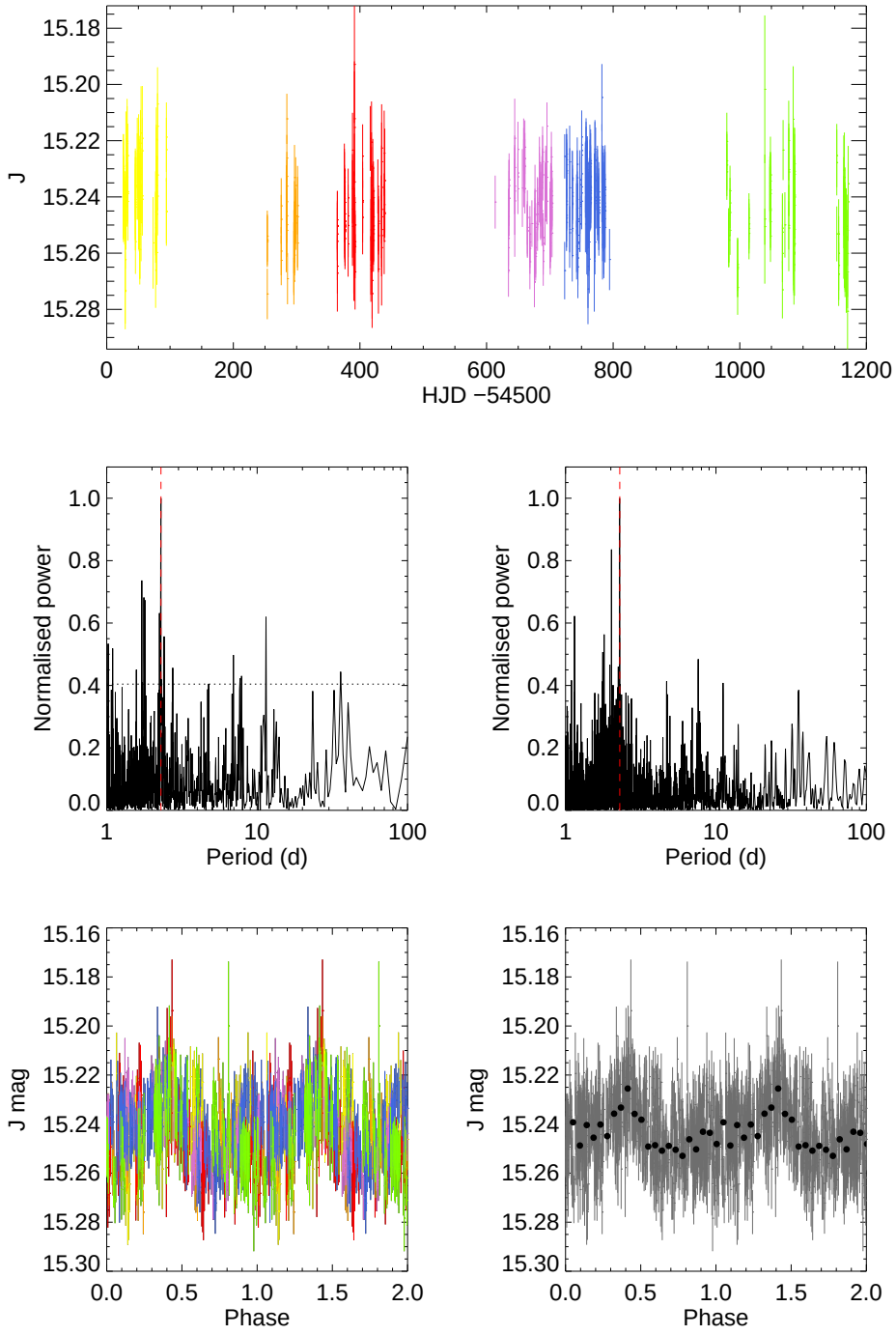

Period (d)	2.290
Amplitude (J)	0.023±0.011
Spectral Type	M0±1.01

Figure A22: As in Figure A21 for the star 07e_2_06232.

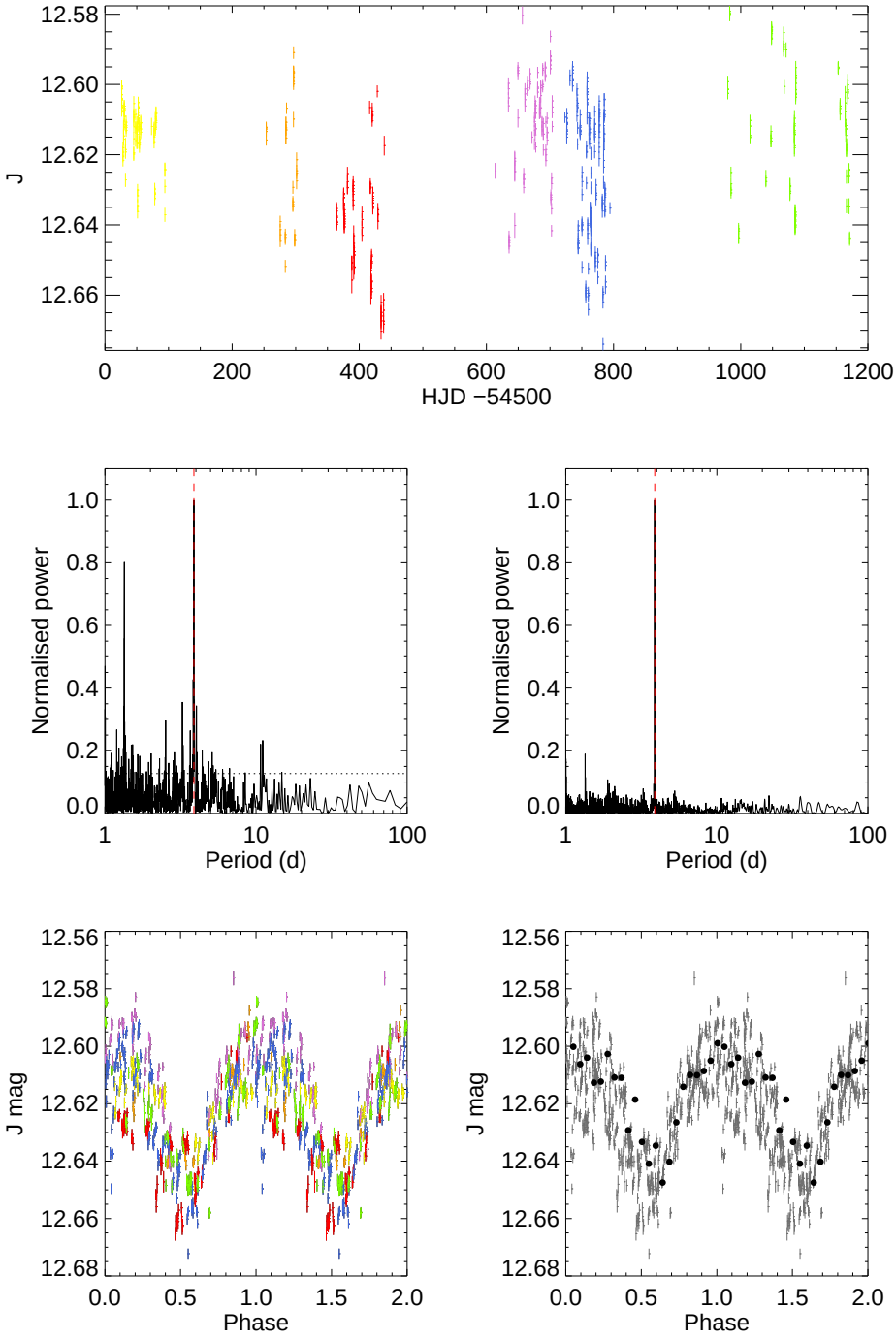

Period (d)	3.870
Amplitude (J)	0.051±0.002
Spectral Type	M0±10.21

FIGURE A23: As in Figure A22 for the star 07f_3_00675.

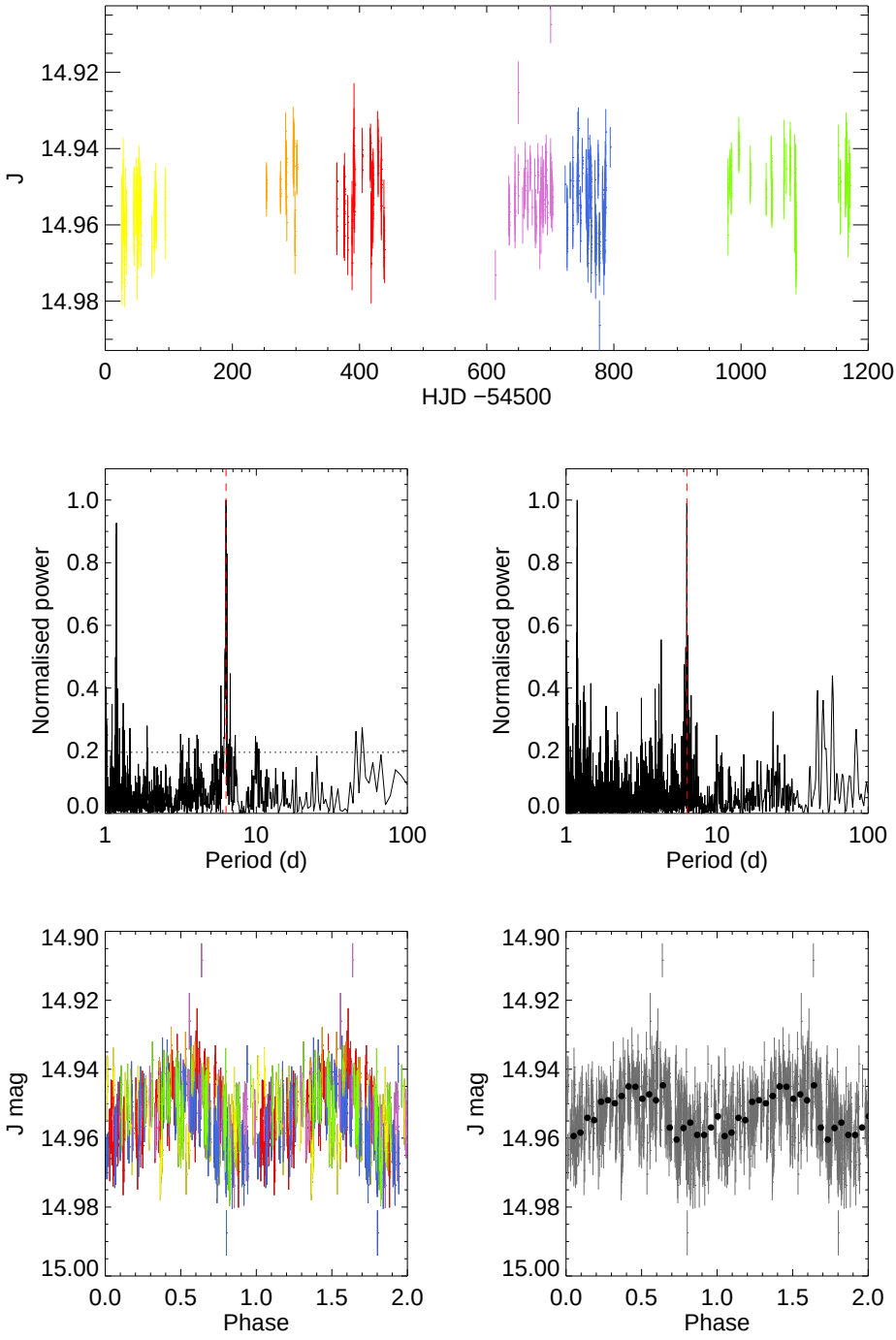

Period (d)	6.310
Amplitude (J)	0.019±0.005
Spectral Type	M4±1.00

Figure A24: As in Figure A23 for the star 07f_3_03235.

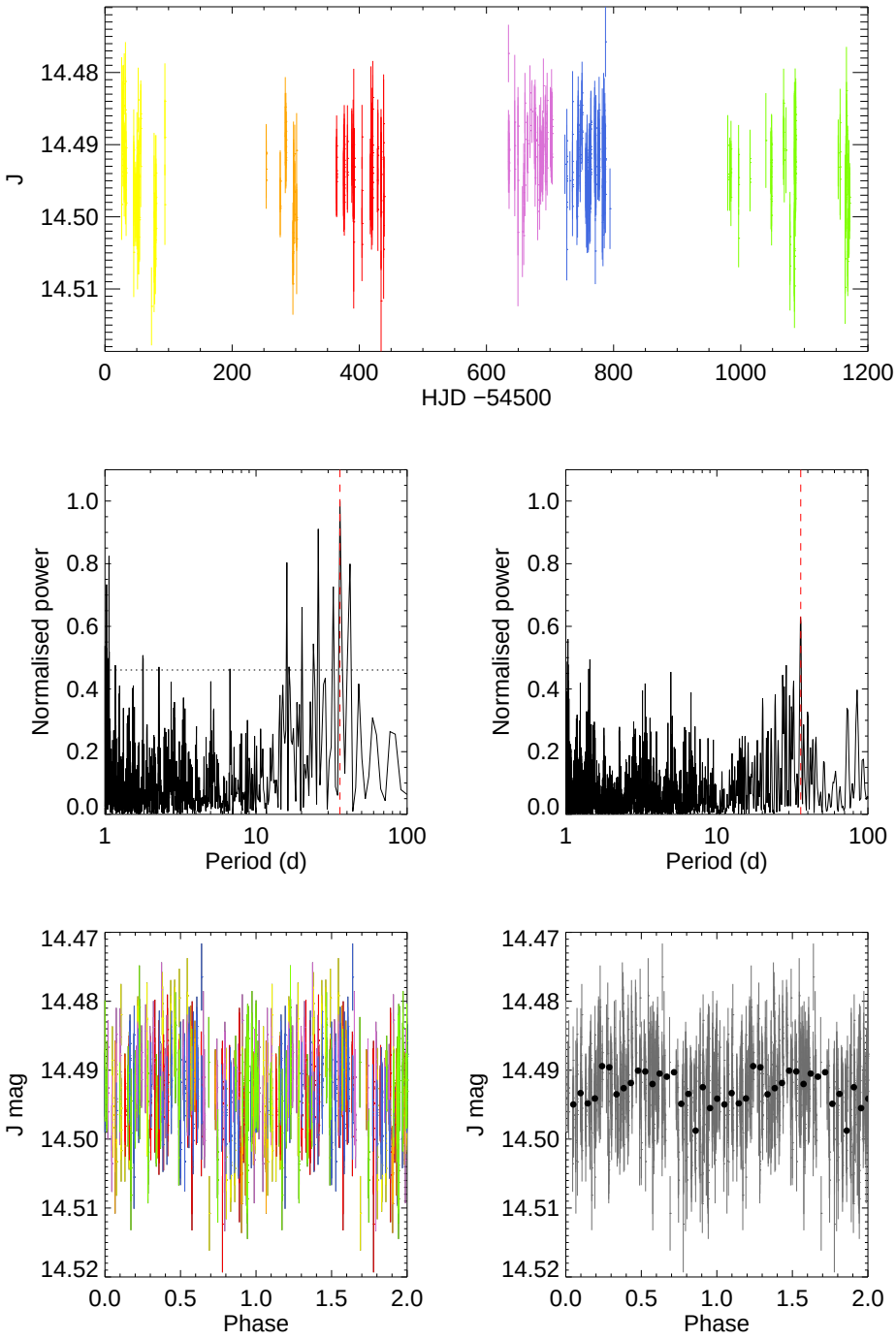

Period (d)	35.790
Amplitude (J)	0.012±0.005
Spectral Type	M0±1.03

FIGURE A25: As in Figure A24 for the star 07g_1_04615. While the periodic nature is not obvious in the folded light curve, the presence of a significant peak in any arbitrary grouping of observation epochs indicates that a periodic signal is in fact present throughout the entirity of the observations.

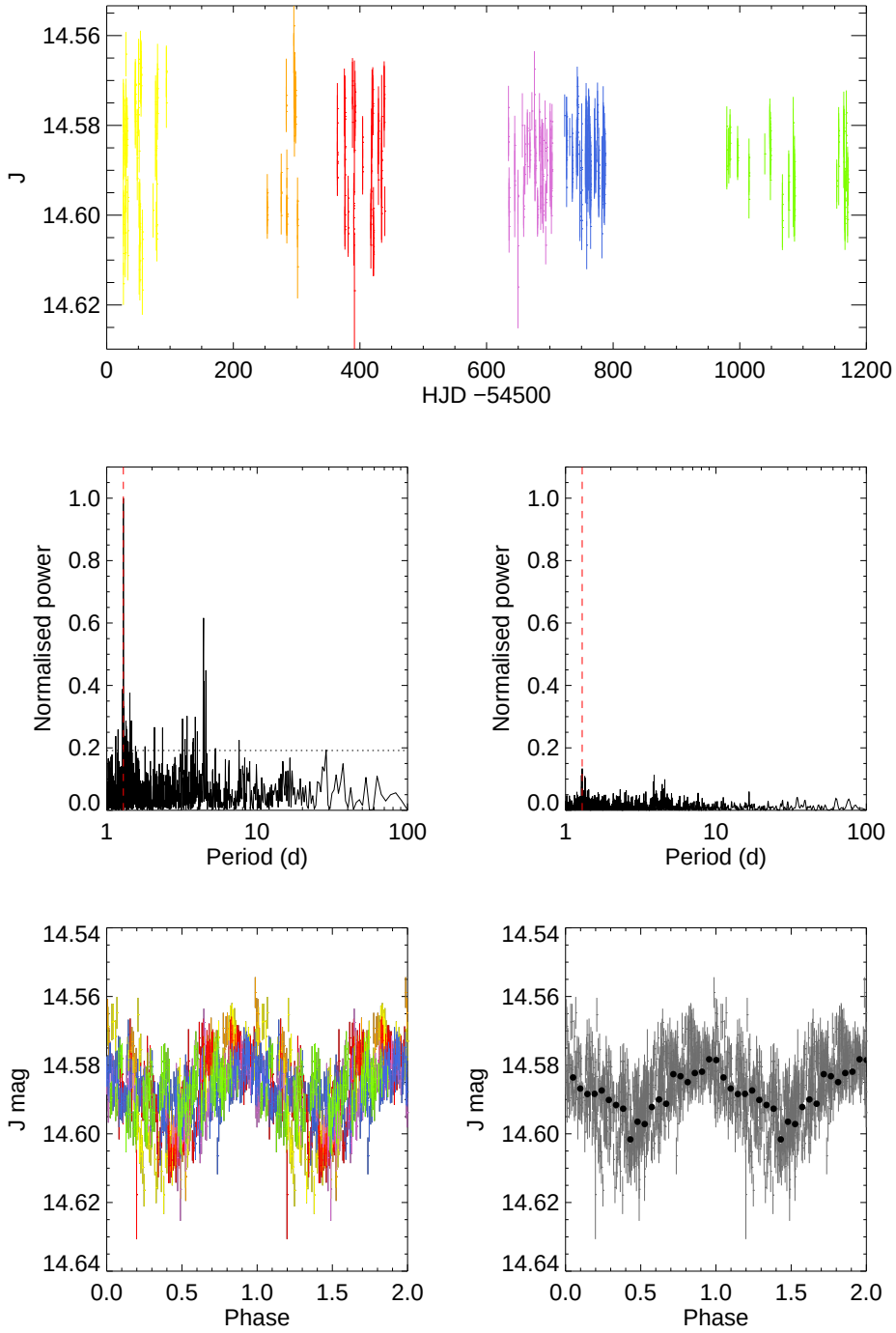

Period (d)	1.290
Amplitude (J)	0.022±0.005
Spectral Type	M0±1.08

Figure A26: As in Figure A25 for the star 07h_1_03267.

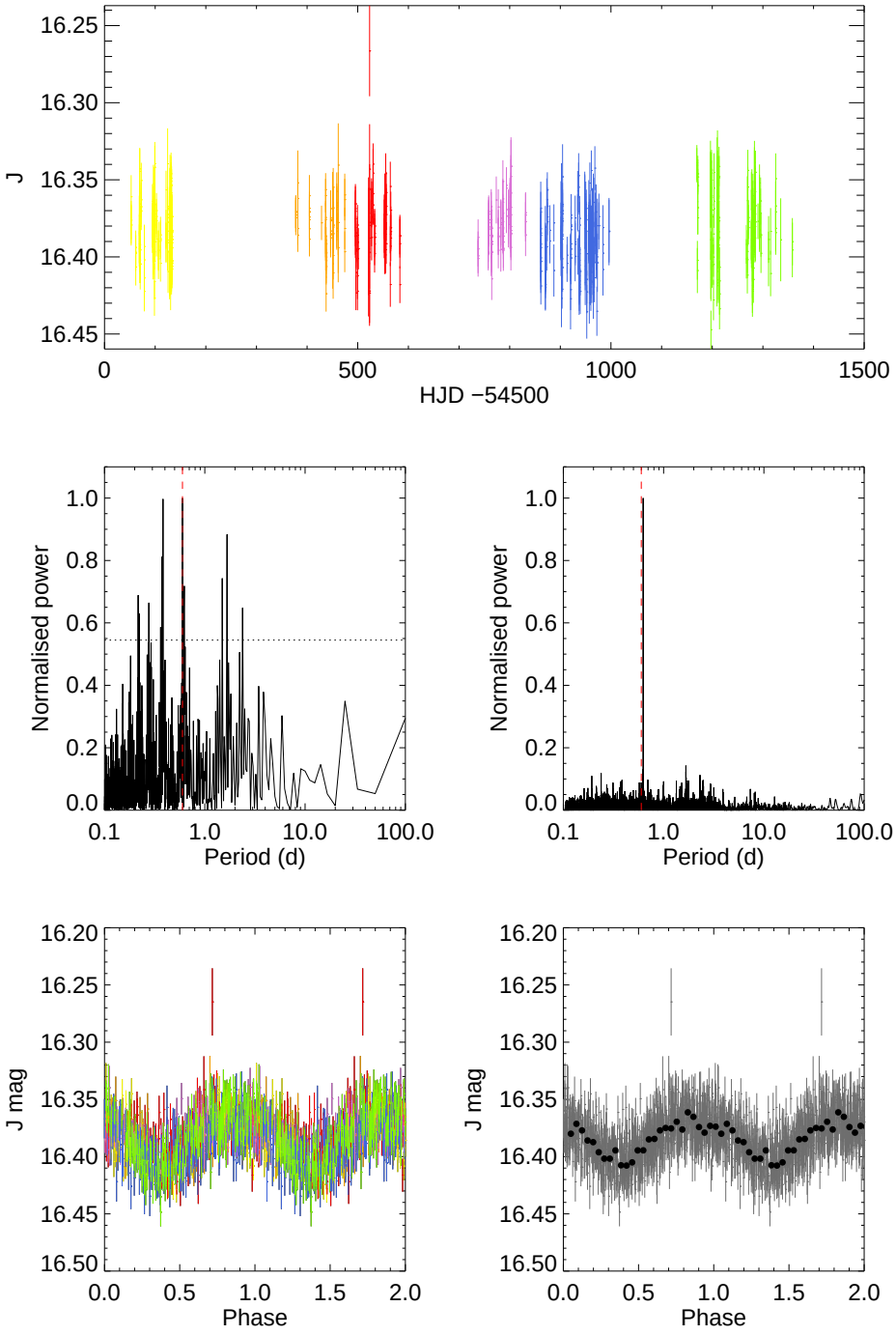

Period (d)	0.630
Amplitude (J)	0.055±0.018
Spectral Type	-±0.00

FIGURE A27: As in Figure A26 for the star 17a_1_01533. Comparing the periodograms for this star indicates the ability of CLEAN to derive the true period where Lomb-Scargle finds a crowded periodogram.

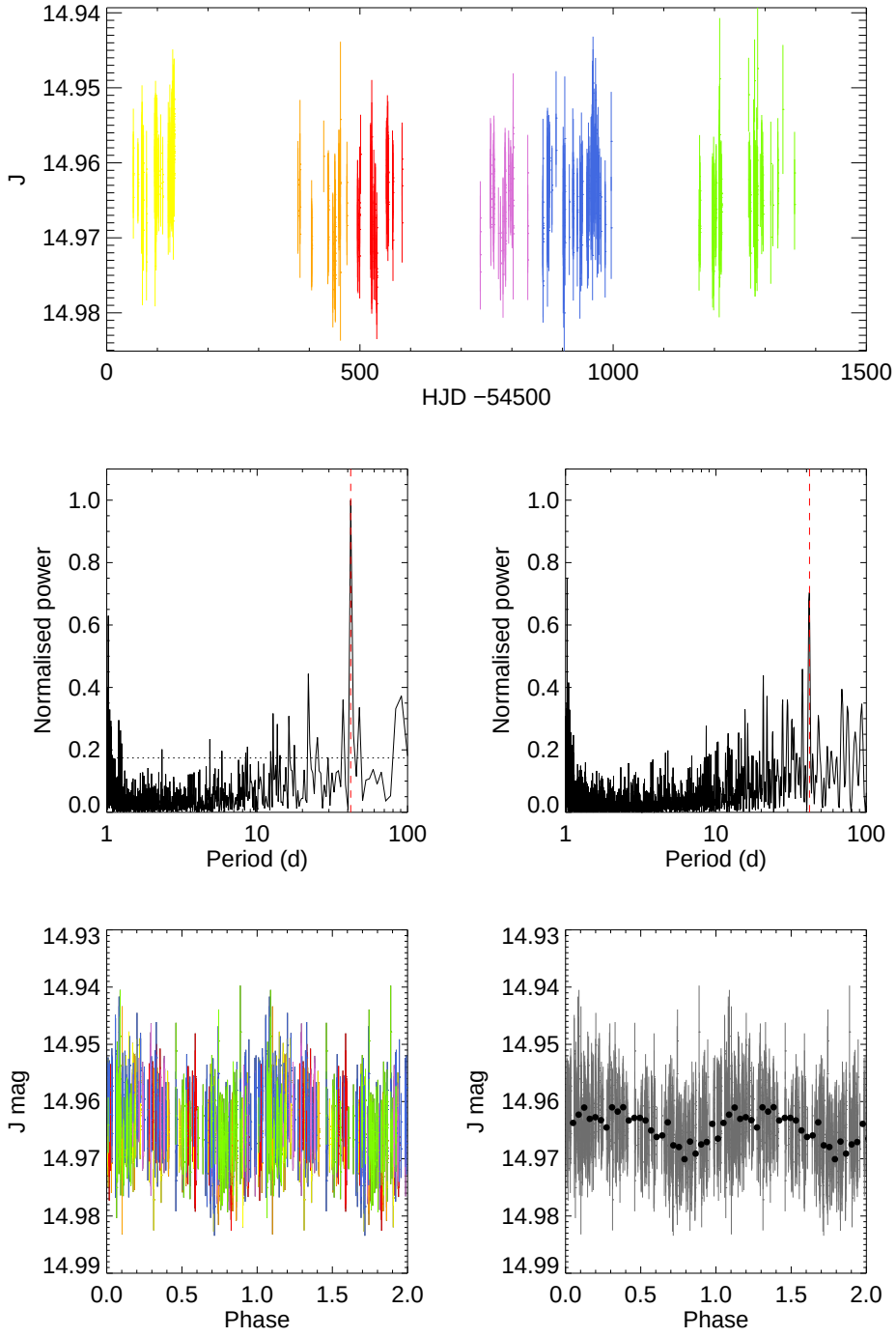

Period (d)	41.630
Amplitude (J)	0.060±0.005
Spectral Type	-±0.00

Figure A28: As in Figure A27 for the star 17a_3_00950.

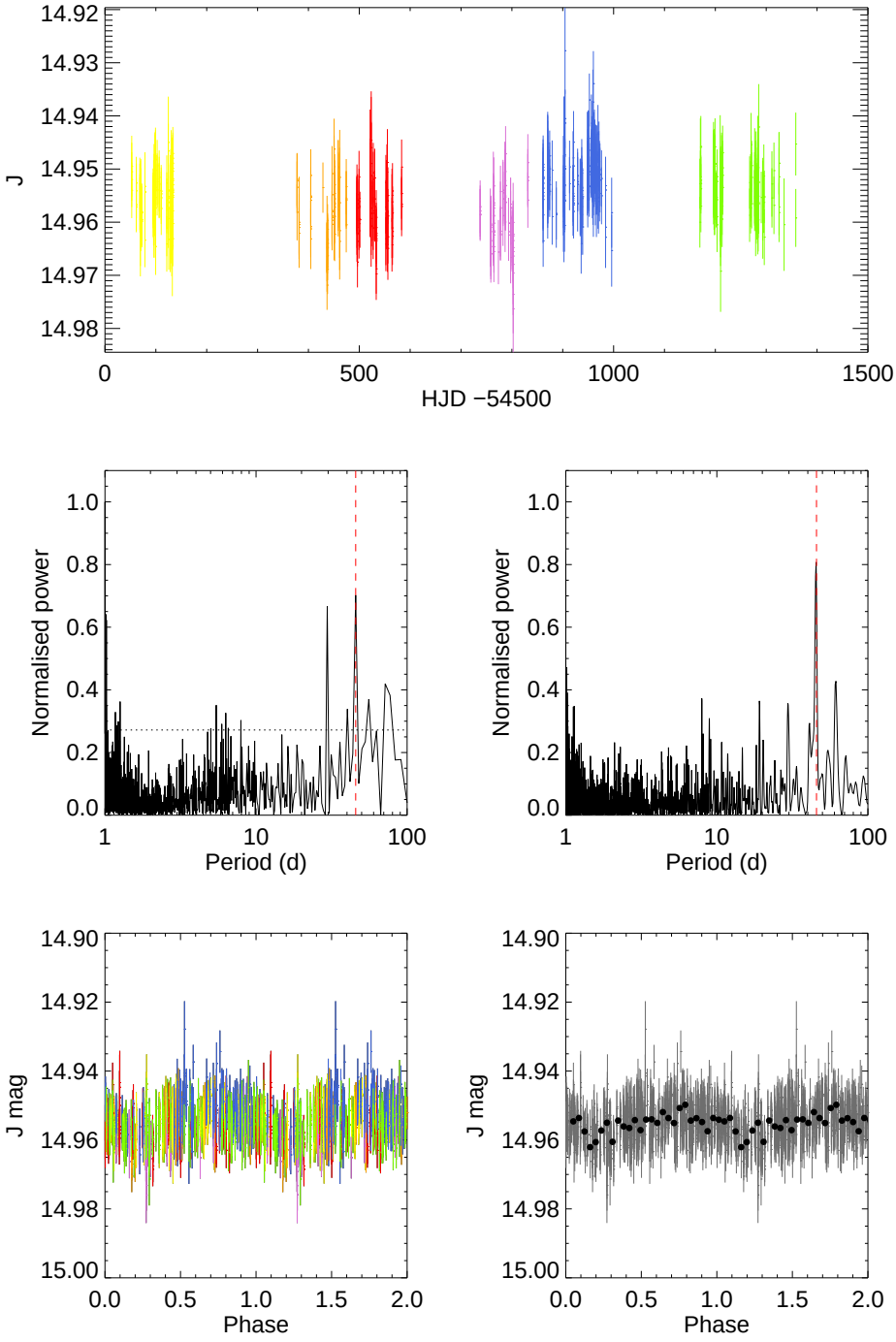

Period (d)	45.210
Amplitude (J)	0.068±0.005
Spectral Type	-±0.00

FIGURE A29: As in Figure A28 for the star 17a_3_03244. As seen in Figure A25 the periodic nature is not evident in the folded light curve, although is found by both periodograms throughout the observations.

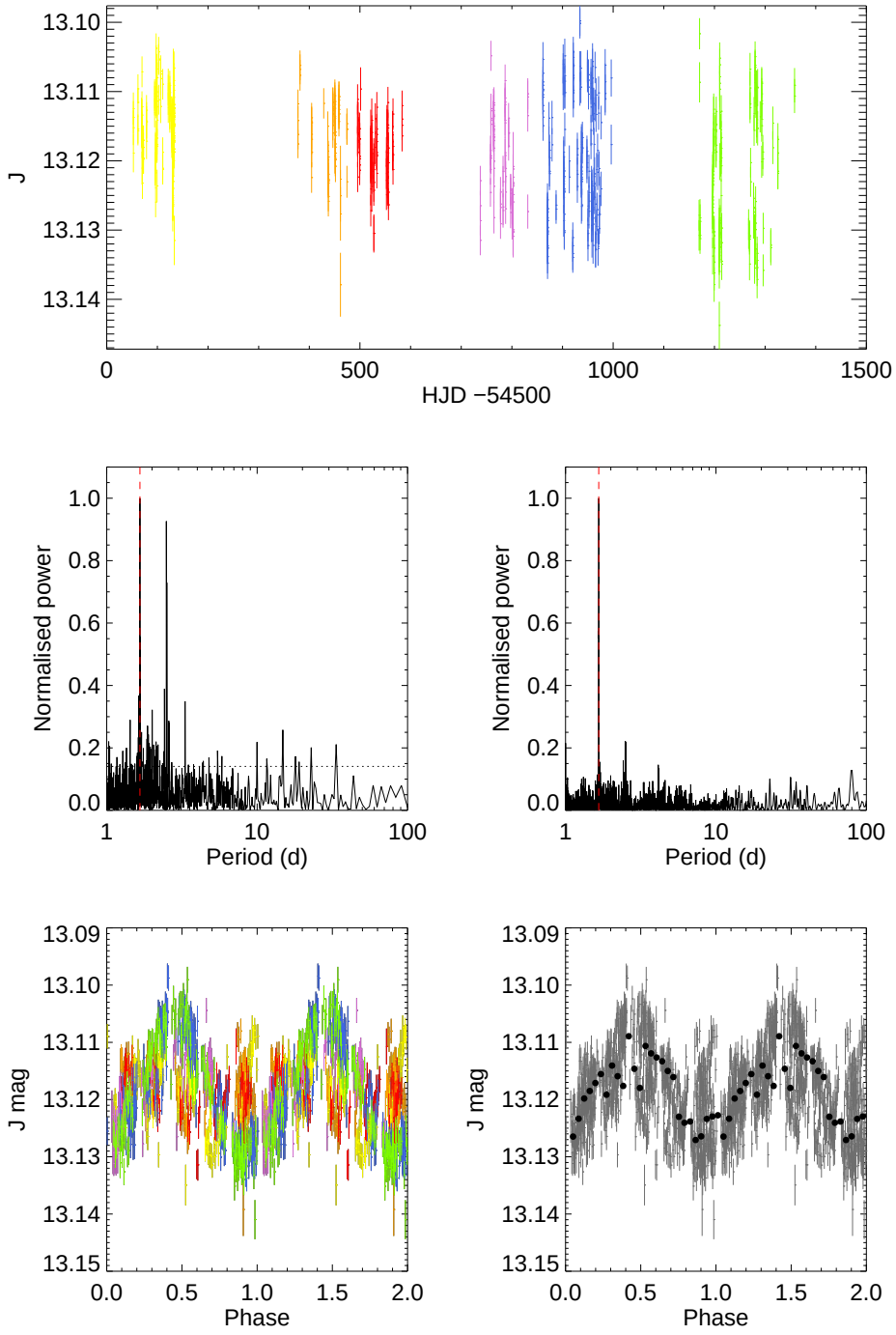

Period (d)	1.660
Amplitude (J)	0.022±0.006
Spectral Type	-±0.00

Figure A30: As in Figure A29 for the star 17d_1_06032.

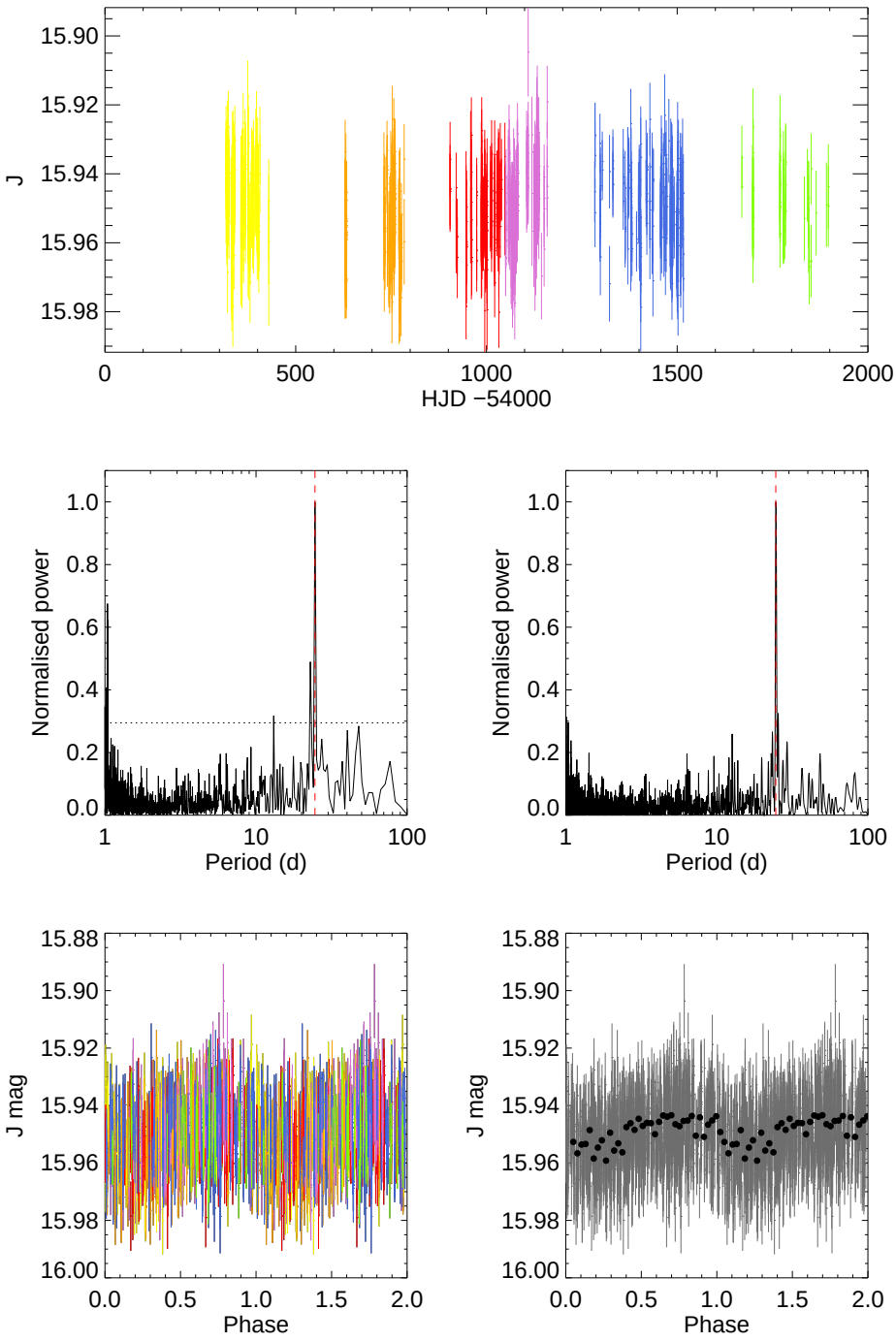

Period (d)	24.650
Amplitude (J)	0.025±0.011
Spectral Type	M0±1.61

FIGURE A31: As in Figure A30 for the star 19a_1_00838. As seen in Figure A25 and A29 the peridodic nature is not evident in the folded light curve, although is found by both periodograms throughout the observations.

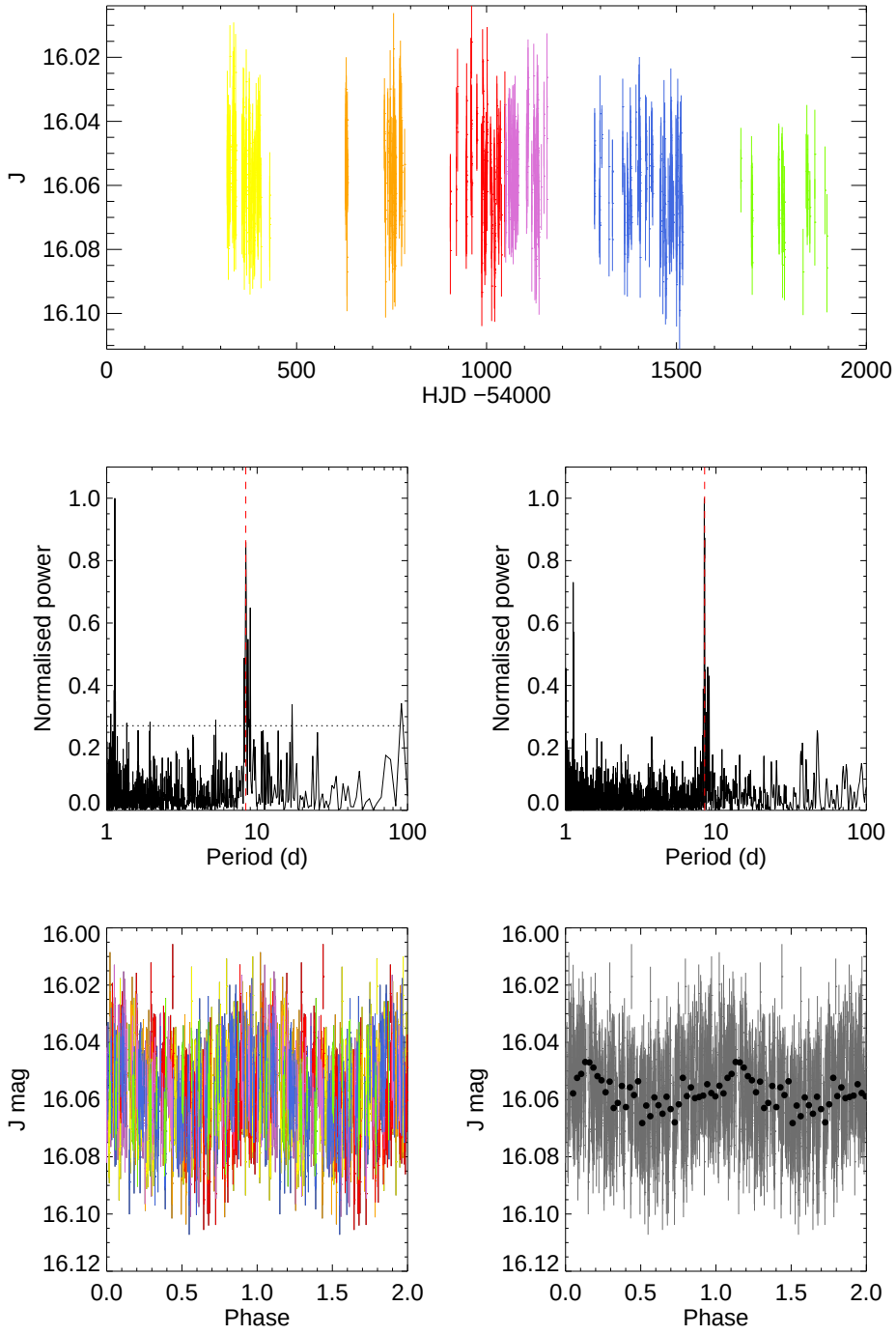

Period (d)	8.410
Amplitude (J)	0.030±0.011
Spectral Type	M0±1.02

Figure A32: As in Figure A31 for the star 19a_1_10932.

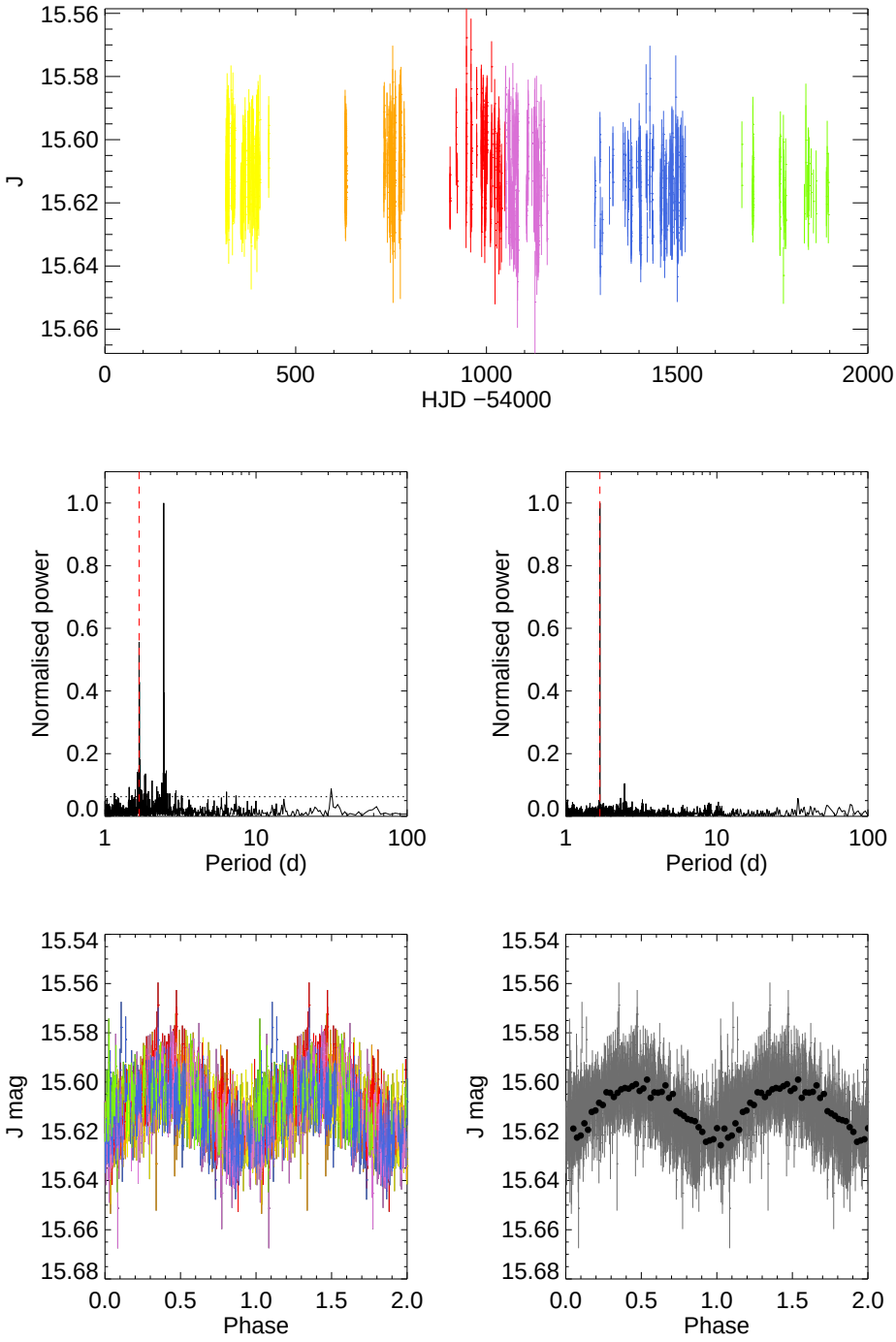

Period (d)	1.680
Amplitude (J)	0.027±0.008
Spectral Type	M4±1.00

FIGURE A33: As in Figure A32 for the star 19a_3_01981. The second most significant Lomb-Scargle peak was initially selected as the other significant peak did not result in a well-folded light curve and could have resulted from aliasing with the true period, which is clarified by the CLEAN periodogram.

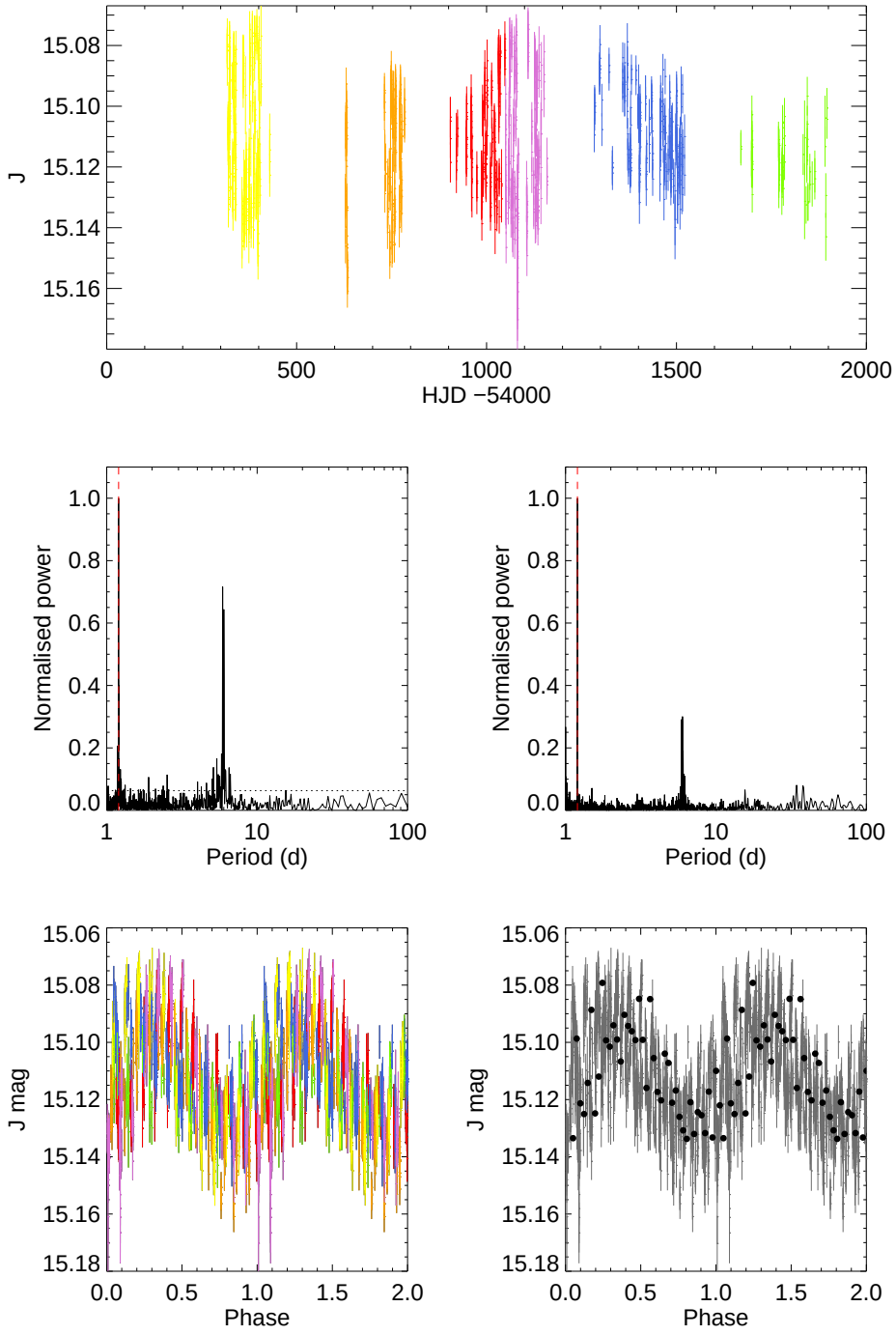

Period (d)	1.200
Amplitude (J)	0.059±0.006
Spectral Type	M0±1.21

Figure A34: As in Figure A33 for the star 19a_3_10735.

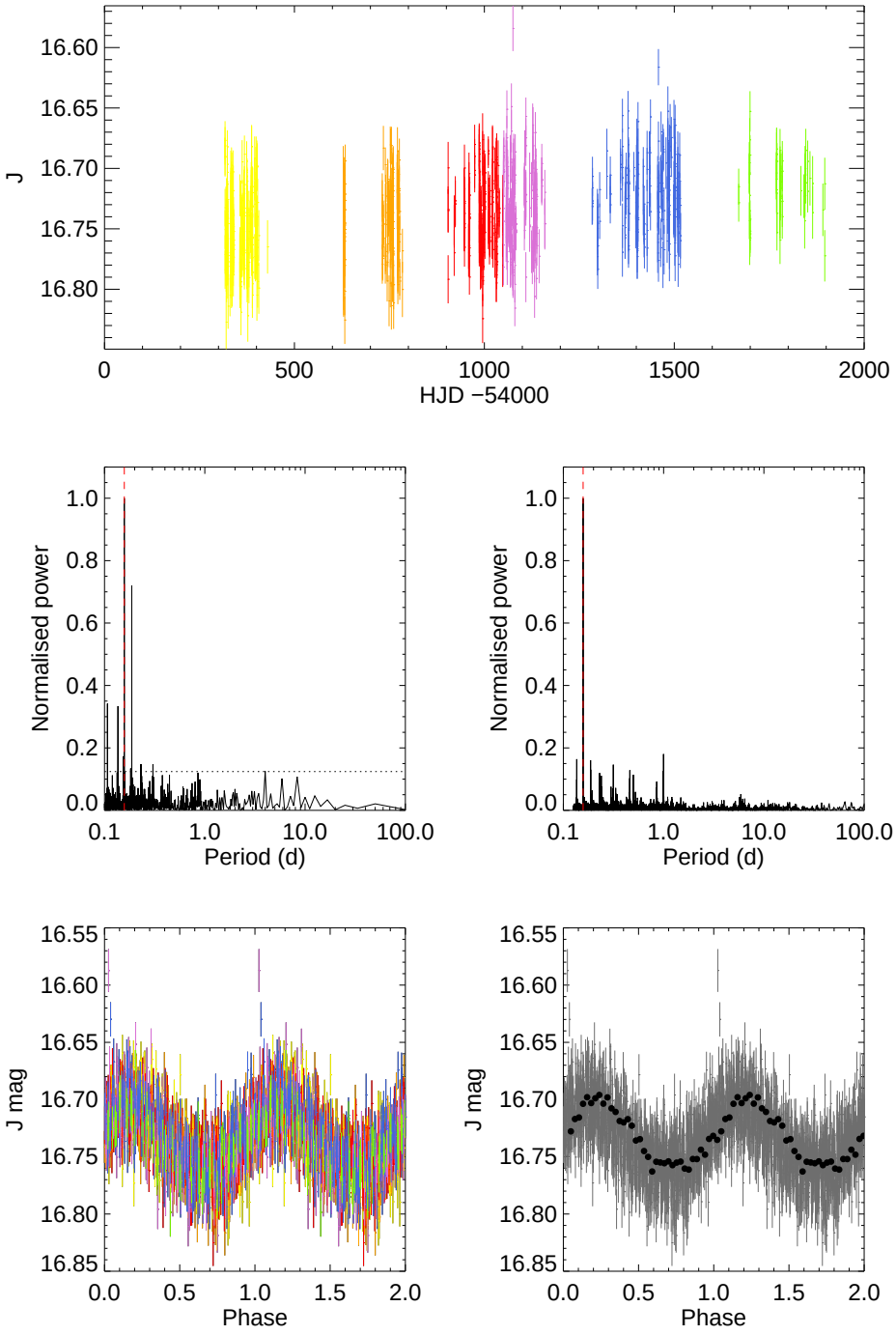

Period (d)	0.160
Amplitude (J)	0.081±0.017
Spectral Type	M0±1.00

FIGURE A35: As in Figure A34 for the star 19a_3_11735.

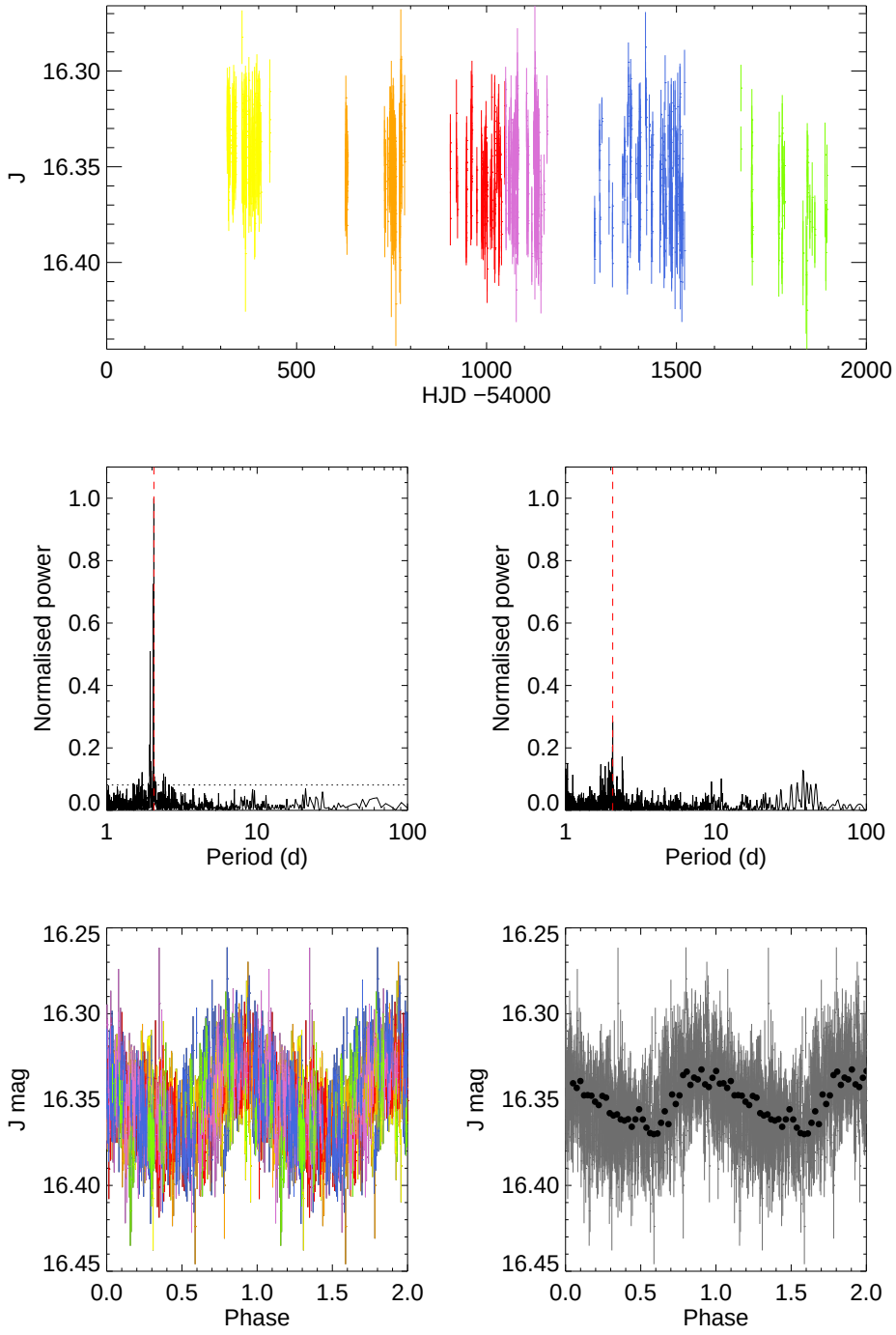

Period (d)	2.060
Amplitude (J)	0.038±0.014
Spectral Type	M1±1.19

Figure A36: As in Figure A35 for the star 19b_1_10542.

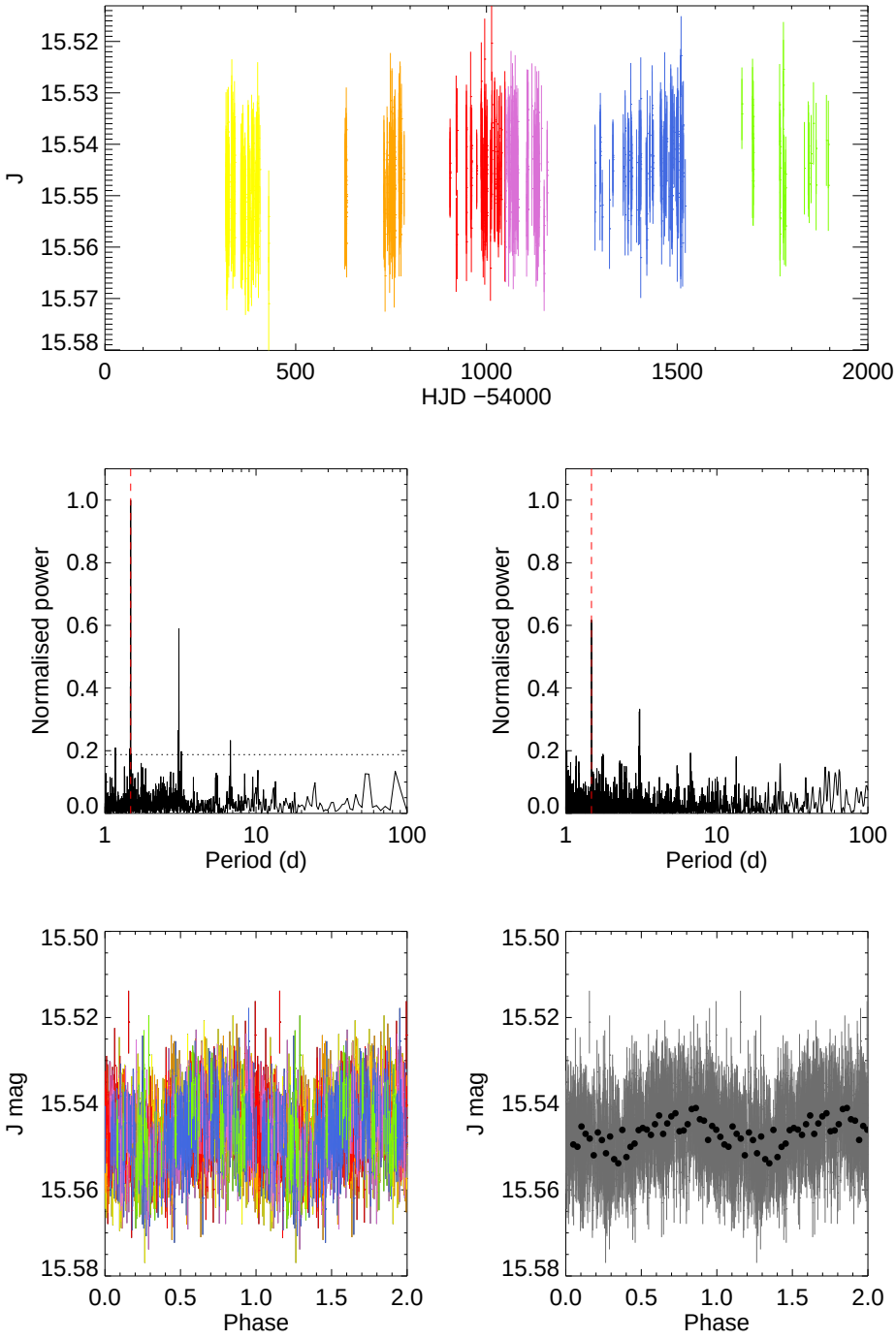

Period (d)	1.480
Amplitude (J)	0.015±0.008
Spectral Type	M4±1.00

FIGURE A37: As in Figure A36 for the star 19b_3_03003.

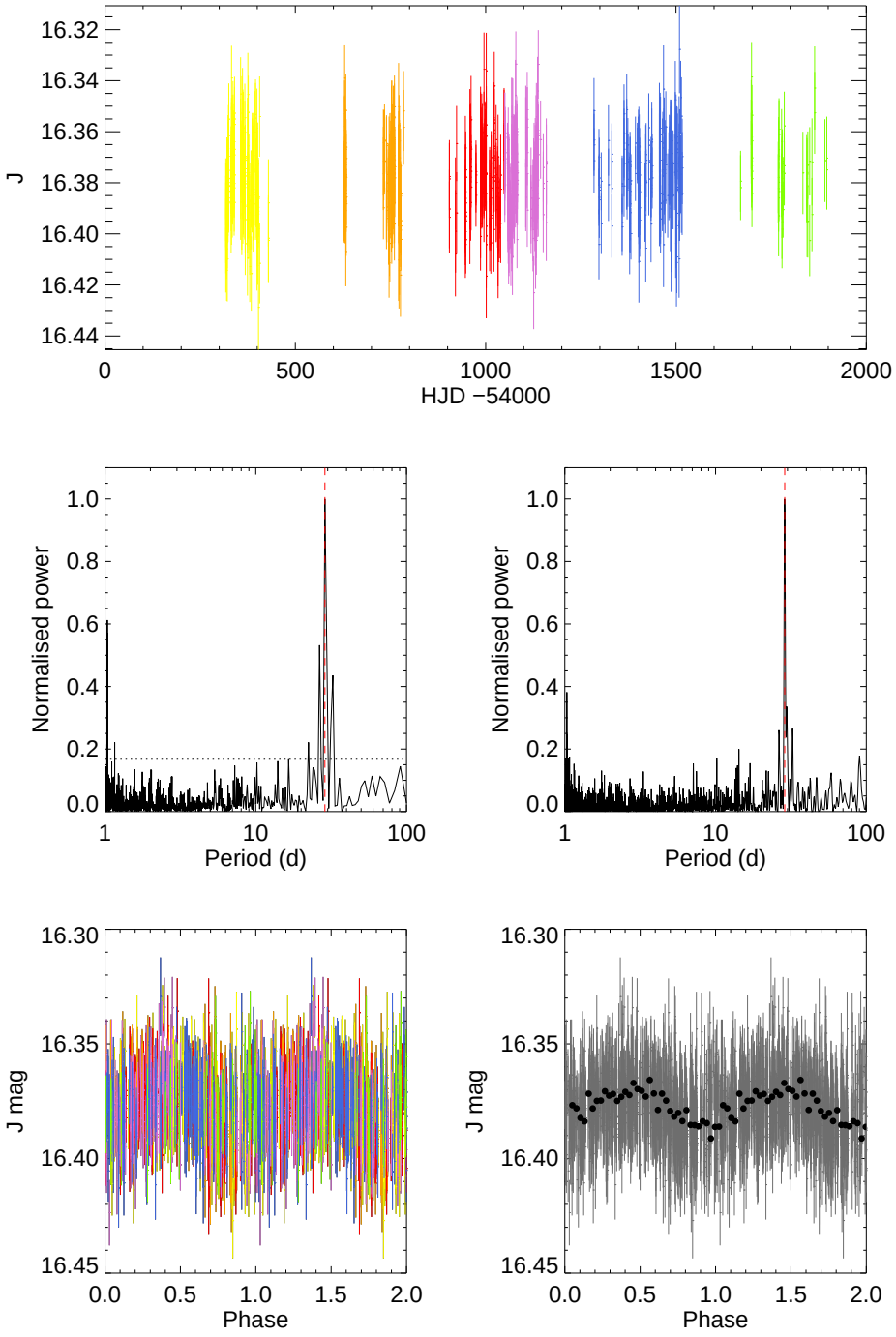

Period (d)	28.710
Amplitude (J)	0.028±0.013
Spectral Type	M0±1.05

Figure A38: As in Figure A37 for the star 19b_3_08292.

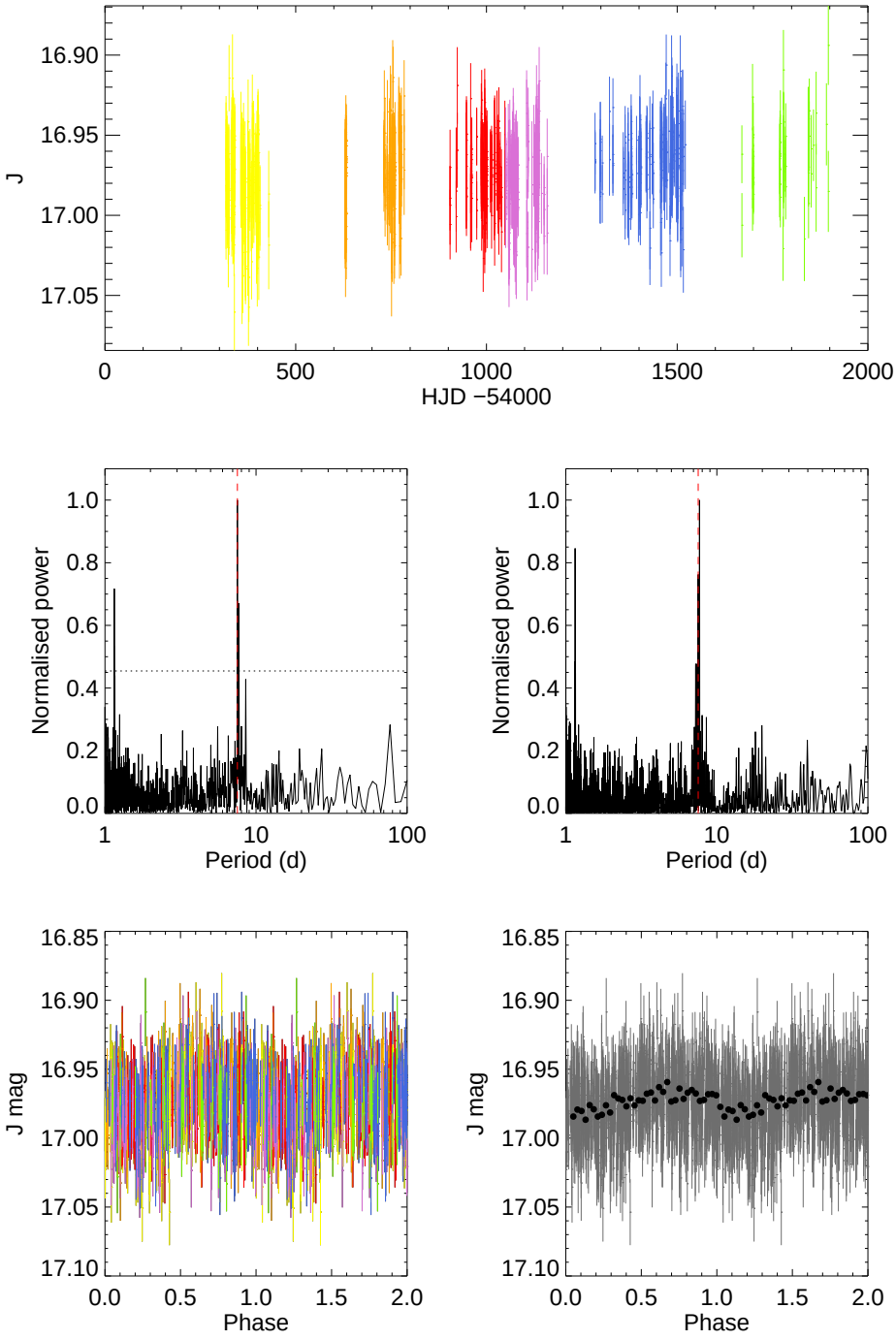

Period (d)	7.680
Amplitude (J)	0.028±0.020
Spectral Type	M1±1.06

FIGURE A39: As in Figure A38 for the star 19b_3_09282.

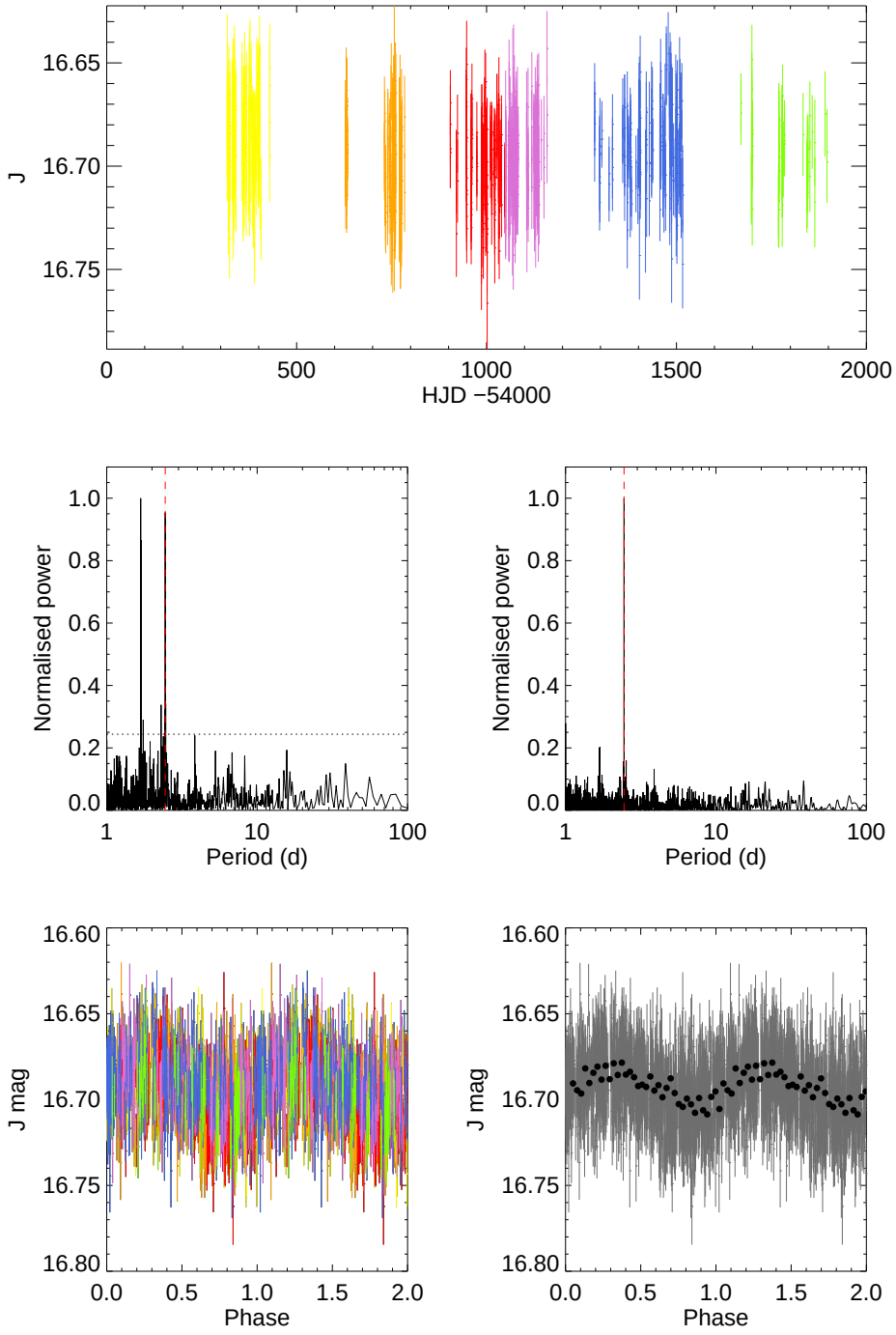

Period (d)	2.450
Amplitude (J)	0.037±0.016
Spectral Type	M3±1.01

Figure A40: As in Figure A39 for the star 19b_3_12753.

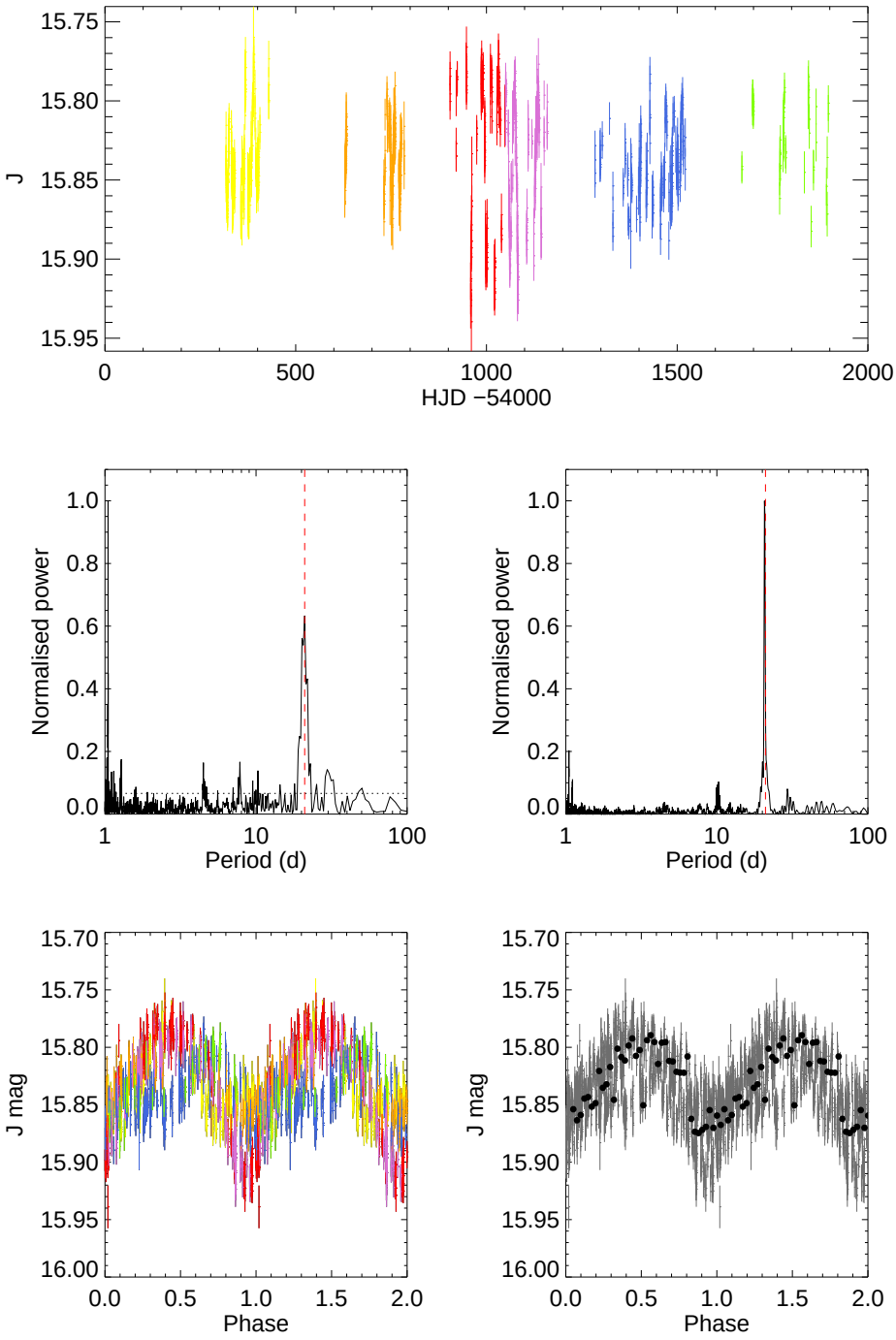

Period (d)	20.680
Amplitude (J)	0.115±0.010
Spectral Type	K7±1.00

FIGURE A41: As in Figure A40 for the star 19c_2_05428. As discussed in Section 3.5, this start sows obvious signs of spot evolution.

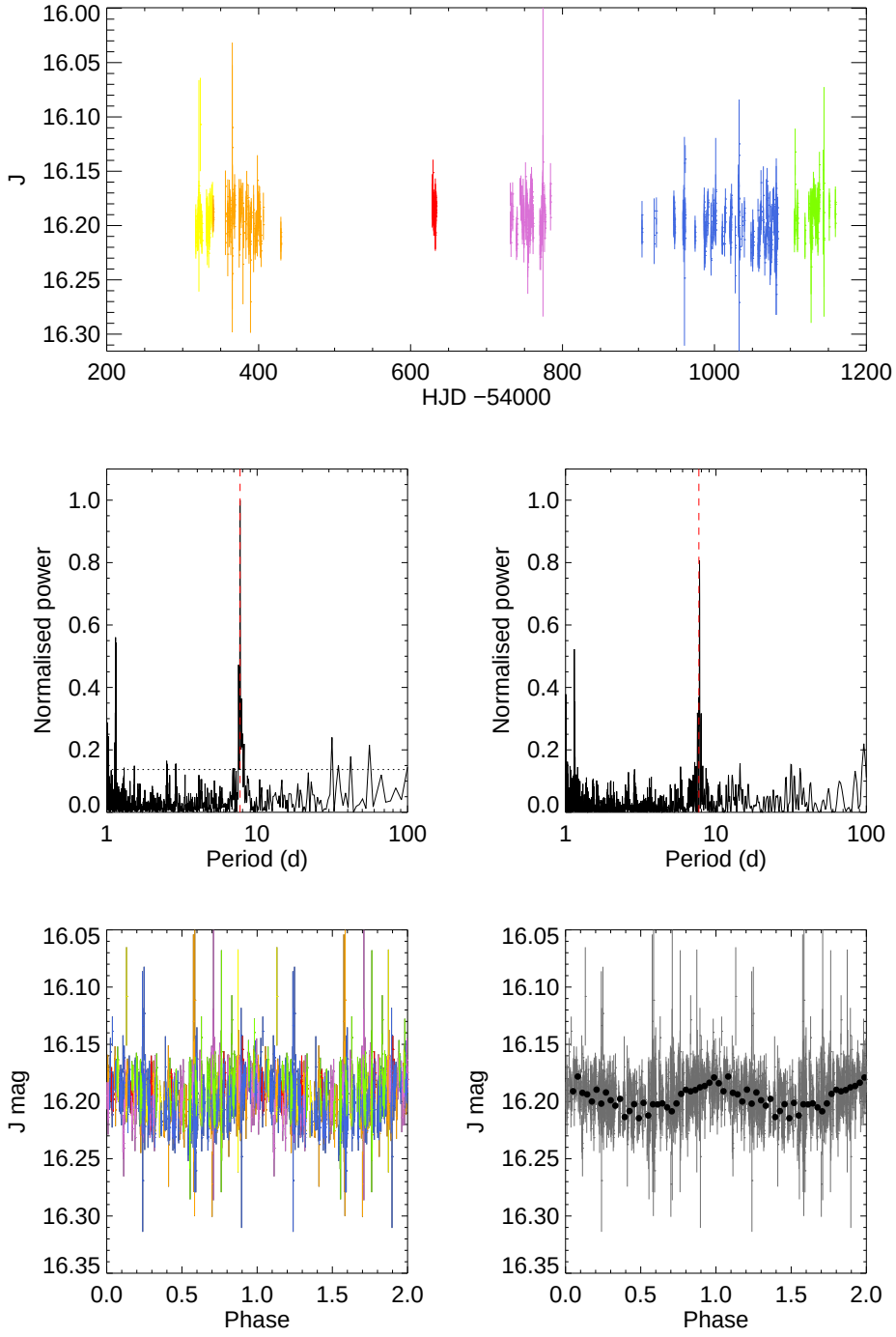

Period (d)	7.700
Amplitude (J)	0.036±0.012
Spectral Type	M3±1.00

Figure A42: As in Figure A41 for the star 19c_3_01804.

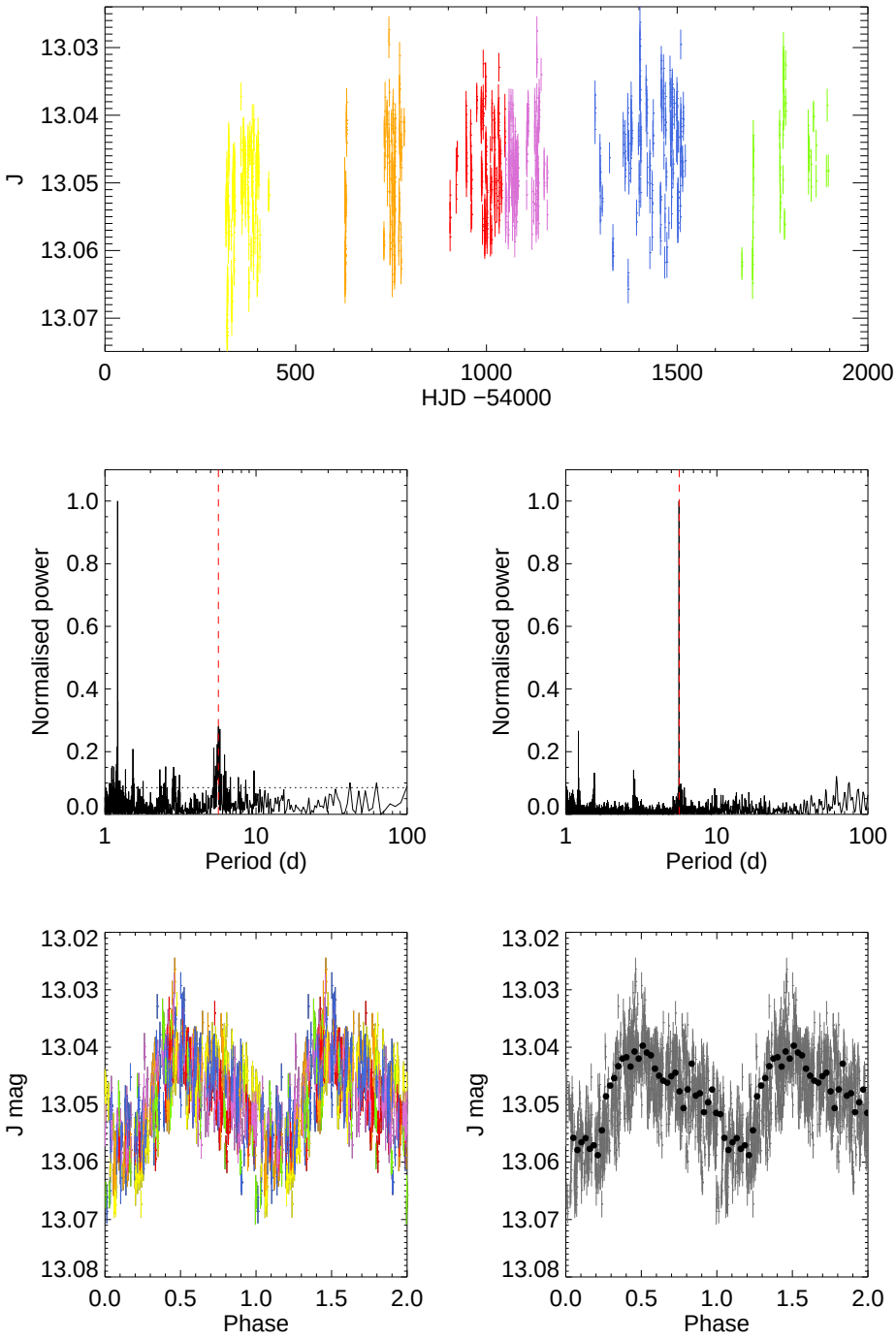

Period (d)	5.620
Amplitude (J)	0.016±0.002
Spectral Type	M0±1.00

FIGURE A43: As in Figure A42 for the star 19c_3_03299. In the Lomb-Scargle periodogram, the most significant peak is close to 1 day and does not fold to produce a varying light curve, so is not initially chose. The CLEAN periodogram reveals that the second most significant peak in the Lomb-Scargle periodogram is indeed the true period.

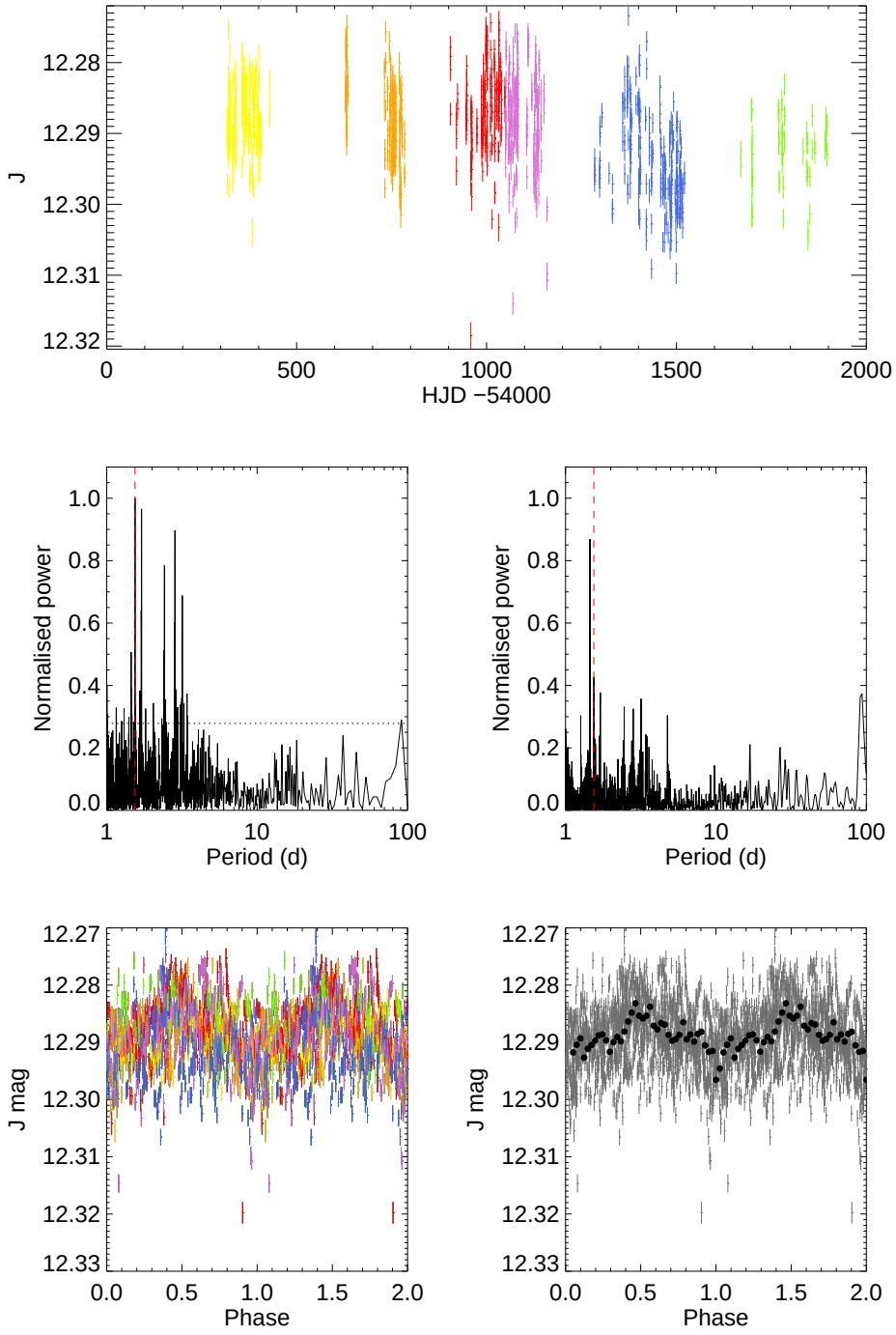

Period (d)	1.450
Amplitude (J)	0.010±0.002
Spectral Type	M2±1.64

Figure A44: As in Figure A43 for the star 19c_3_04974.

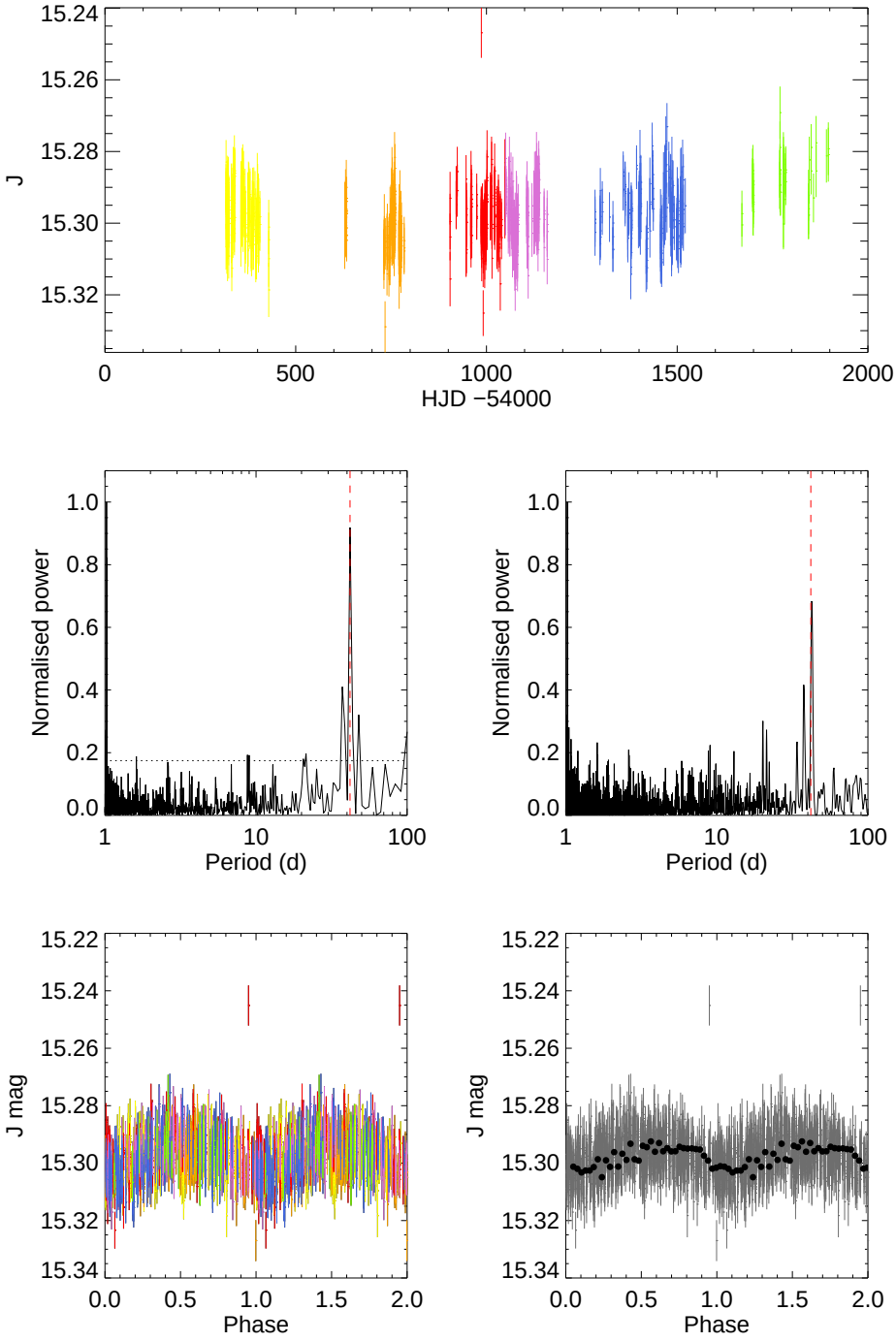

Period (d)	42.400
Amplitude (J)	0.016±0.006
Spectral Type	M4±1.05

FIGURE A45: As in Figure A44 for the star 19c_3_05921.

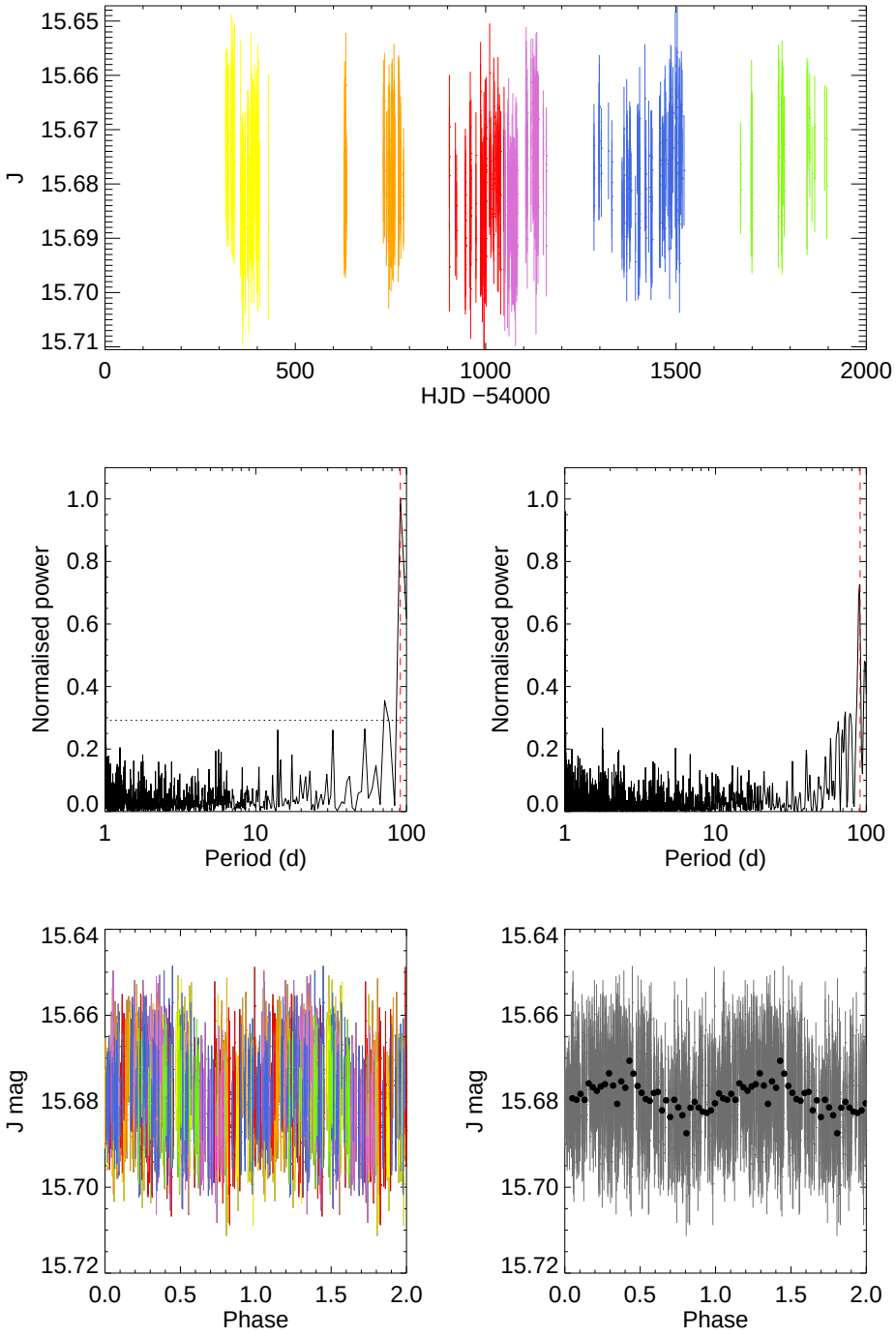

Period (d)	90.330
Amplitude (J)	0.016±0.008
Spectral Type	M3±1.06

Figure A46: As in Figure A45 for the star 19c_3_11273.

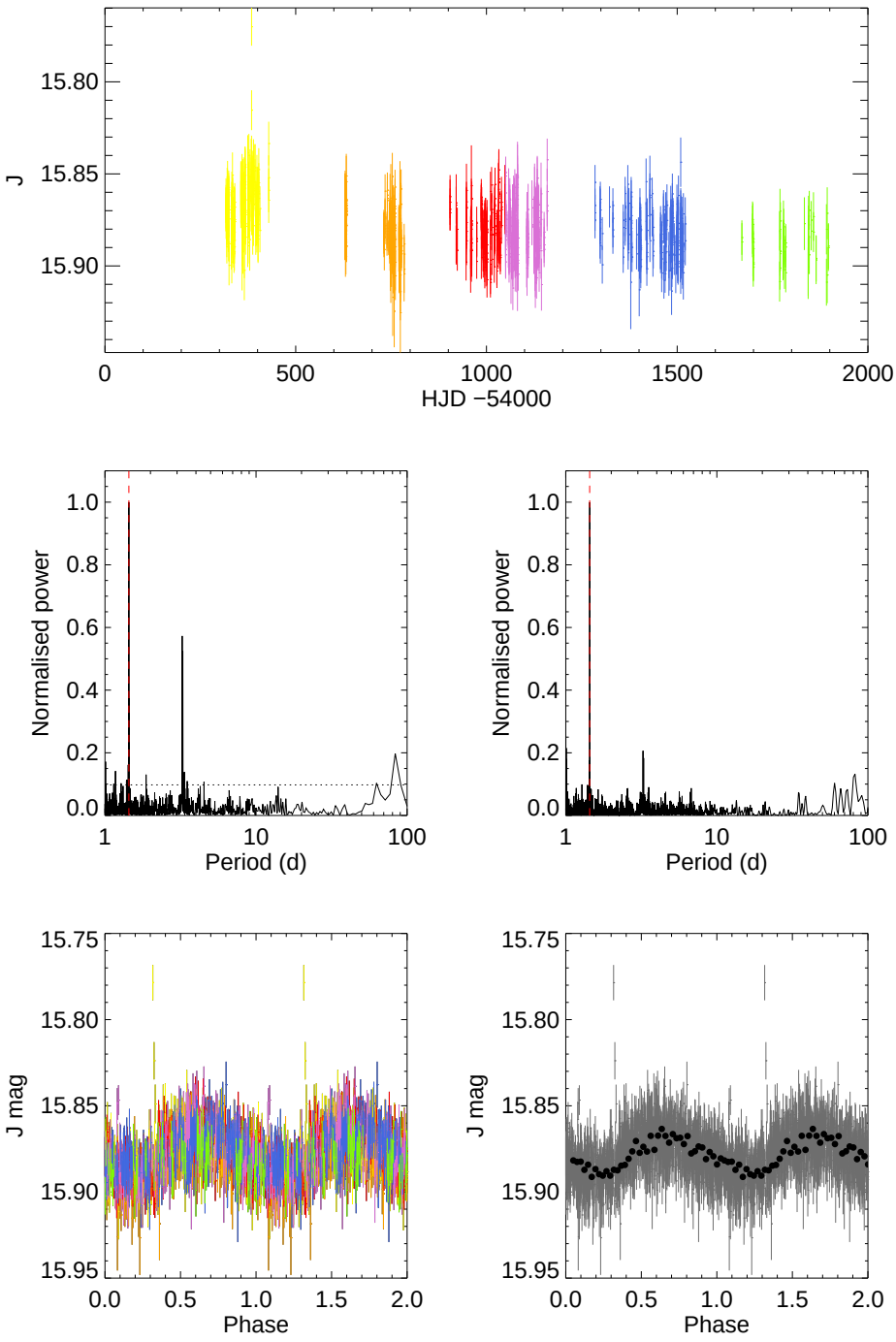

Period (d)	1.440
Amplitude (J)	0.032±0.011
Spectral Type	M4±1.02

FIGURE A47: As in Figure A46 for the star 19c_4_10571. Two sequentially brighter outliers in the earlier epochs (yellow) may be a flare.

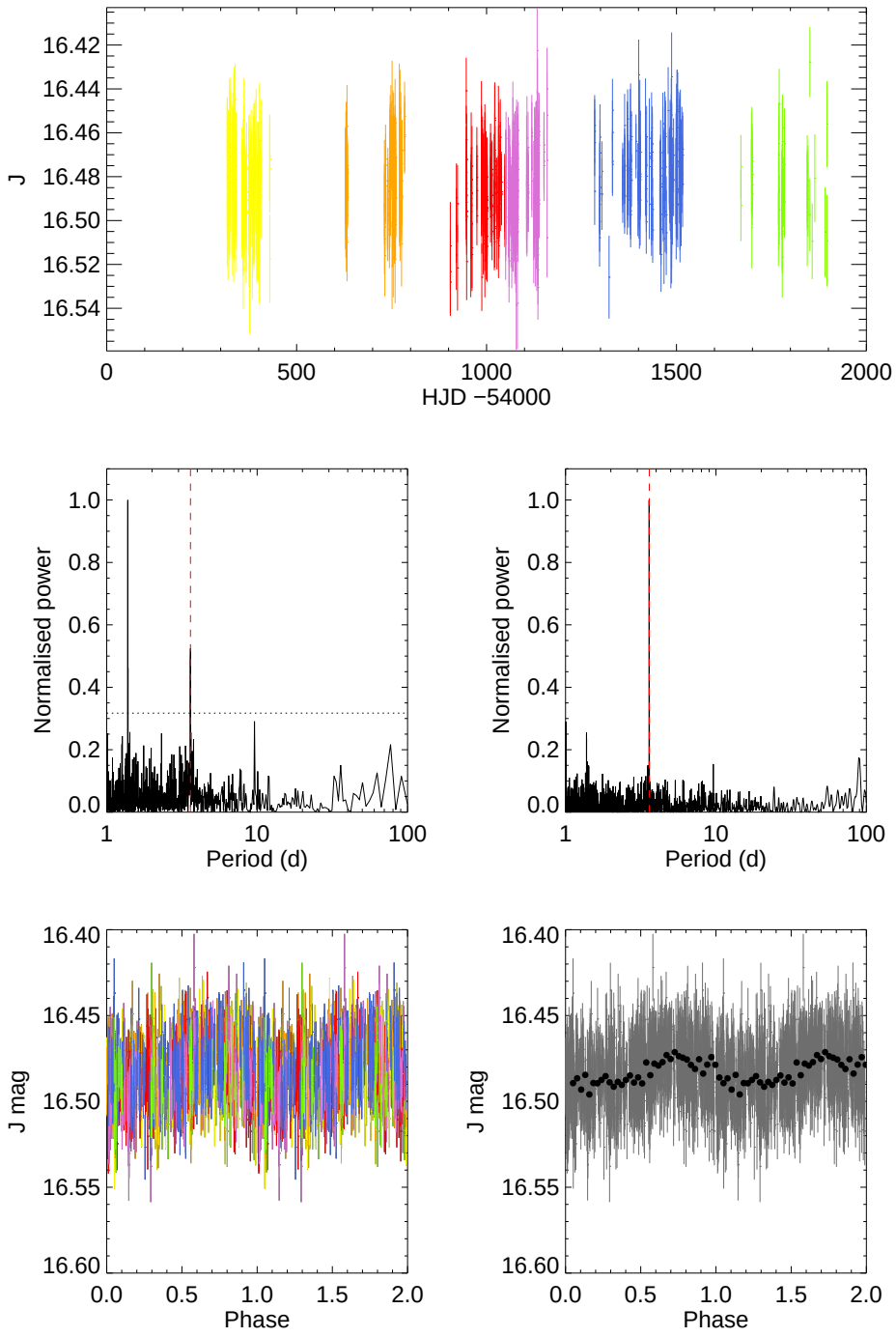

Period (d)	3.600
Amplitude (J)	0.034±0.016
Spectral Type	M3±1.10

Figure A48: As in Figure A47 for the star 19c_4_12623. As seen in Figure A43 the peak near to 1 day is spurious and ignored in the Lomb-Scargle periodogram, with the real peak conformed by the CLEAN periodogram.

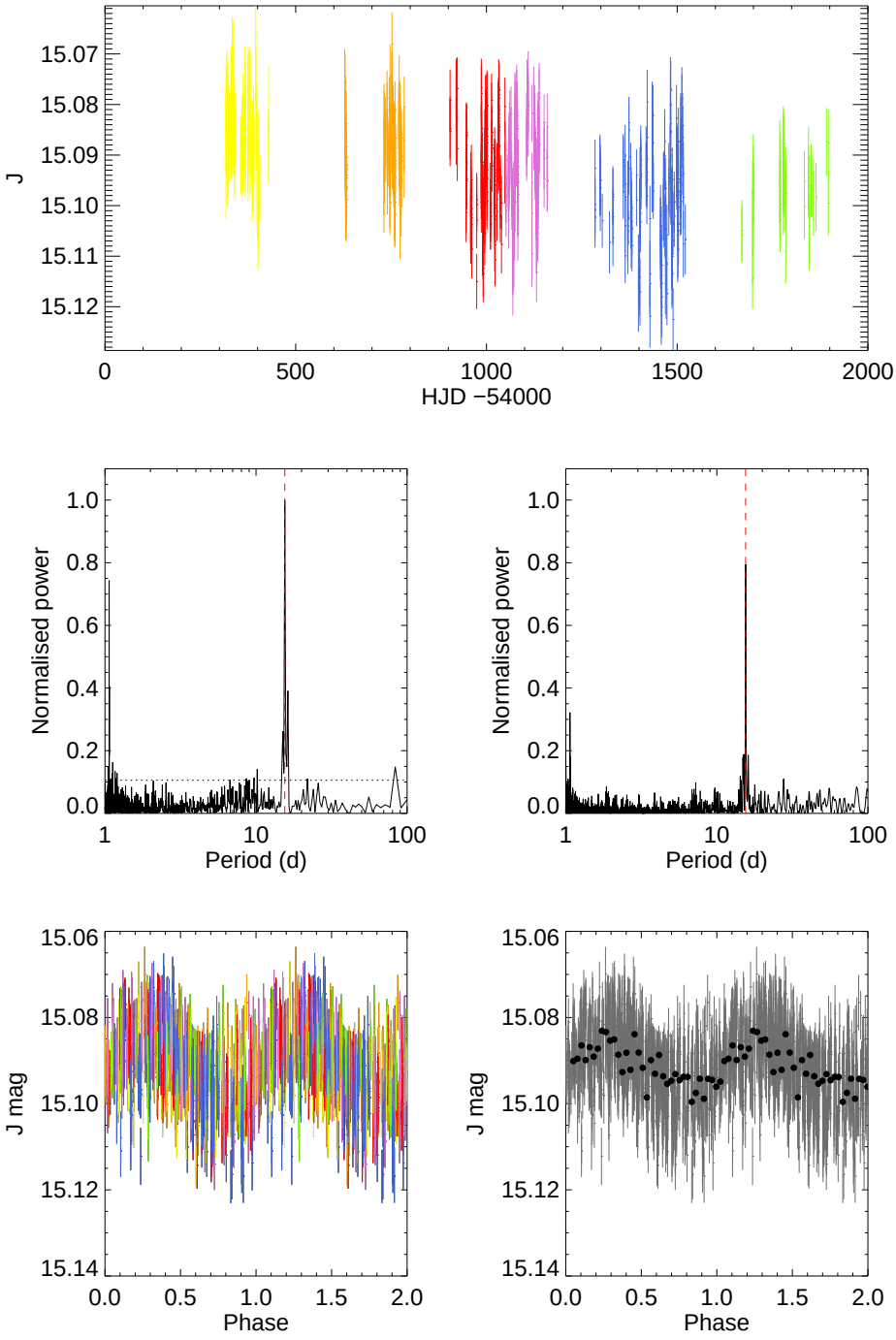

Period (d)	15.490
Amplitude (J)	0.023±0.006
Spectral Type	M1±1.00

FIGURE A49: As in Figure A48 for the star 19d_1_06078.

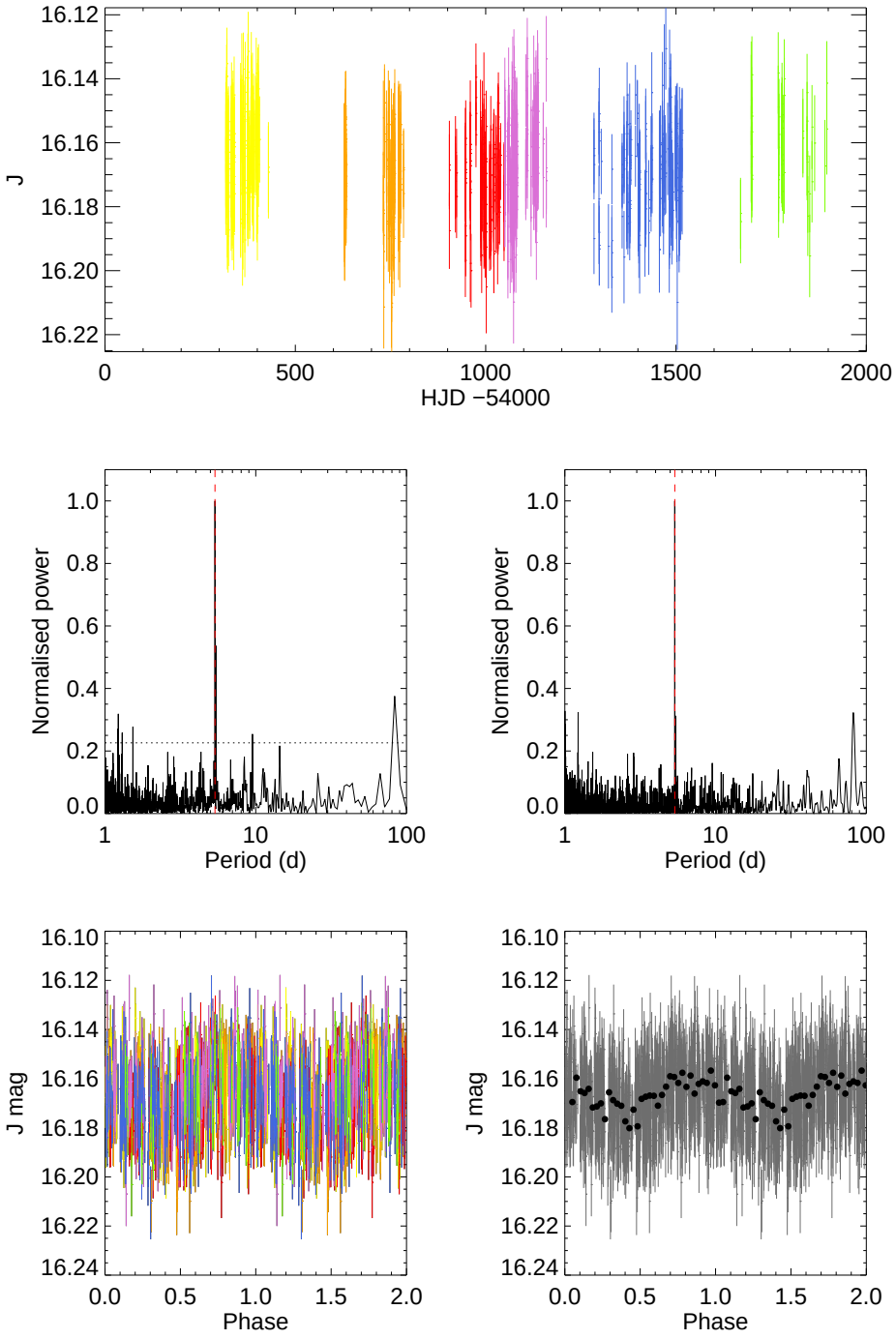

Period (d)	5.360
Amplitude (J)	0.027±0.012
Spectral Type	M2±1.10

Figure A50: As in Figure A49 for the star 19d_1_06603.

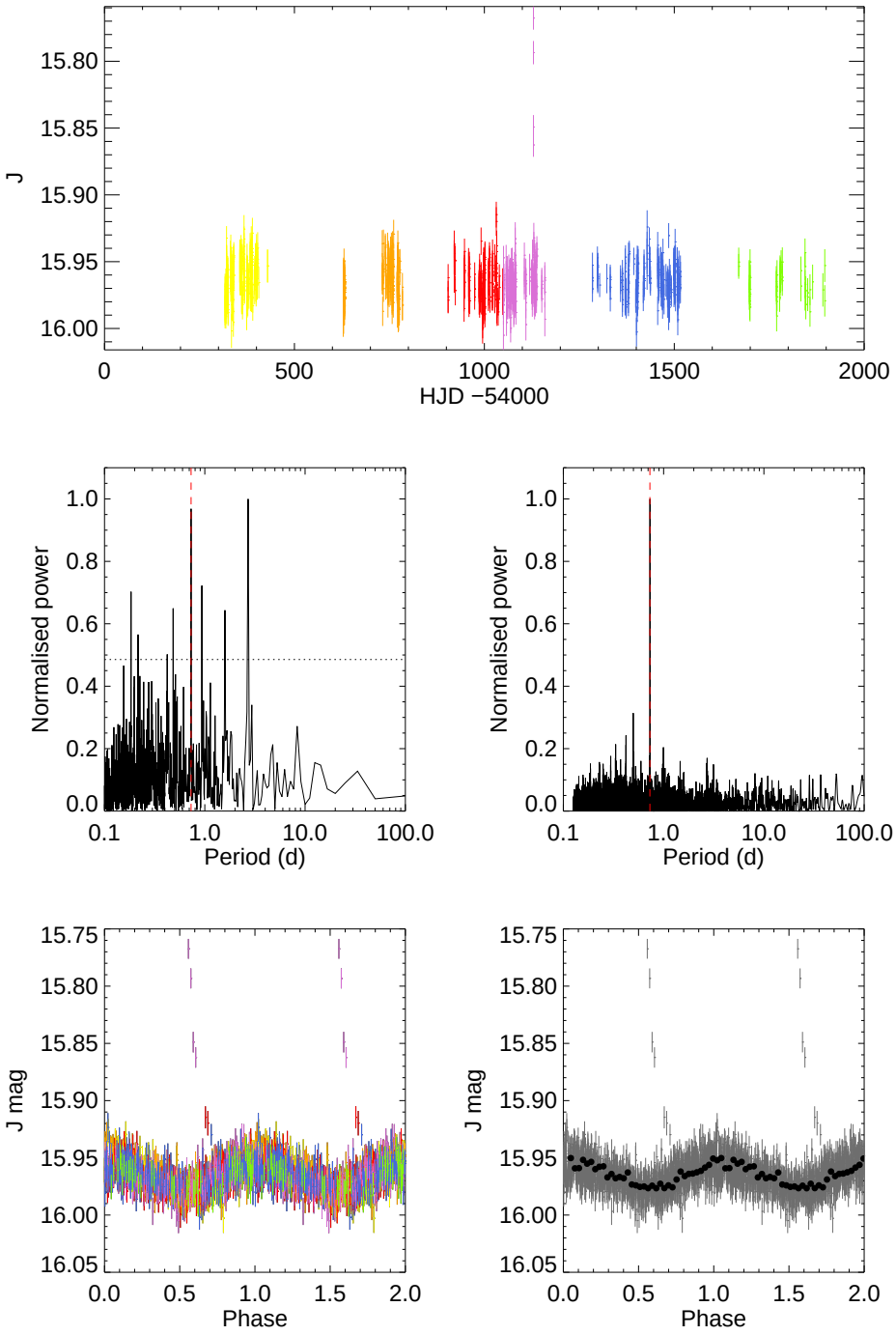

Period (d)	0.730
Amplitude (J)	0.033±0.010
Spectral Type	M4±1.03

FIGURE A51: As in Figure A50 for the star 19d_1_12693. The outliers in this light curve are likely a bright flare, as discussed in Section 3.6.

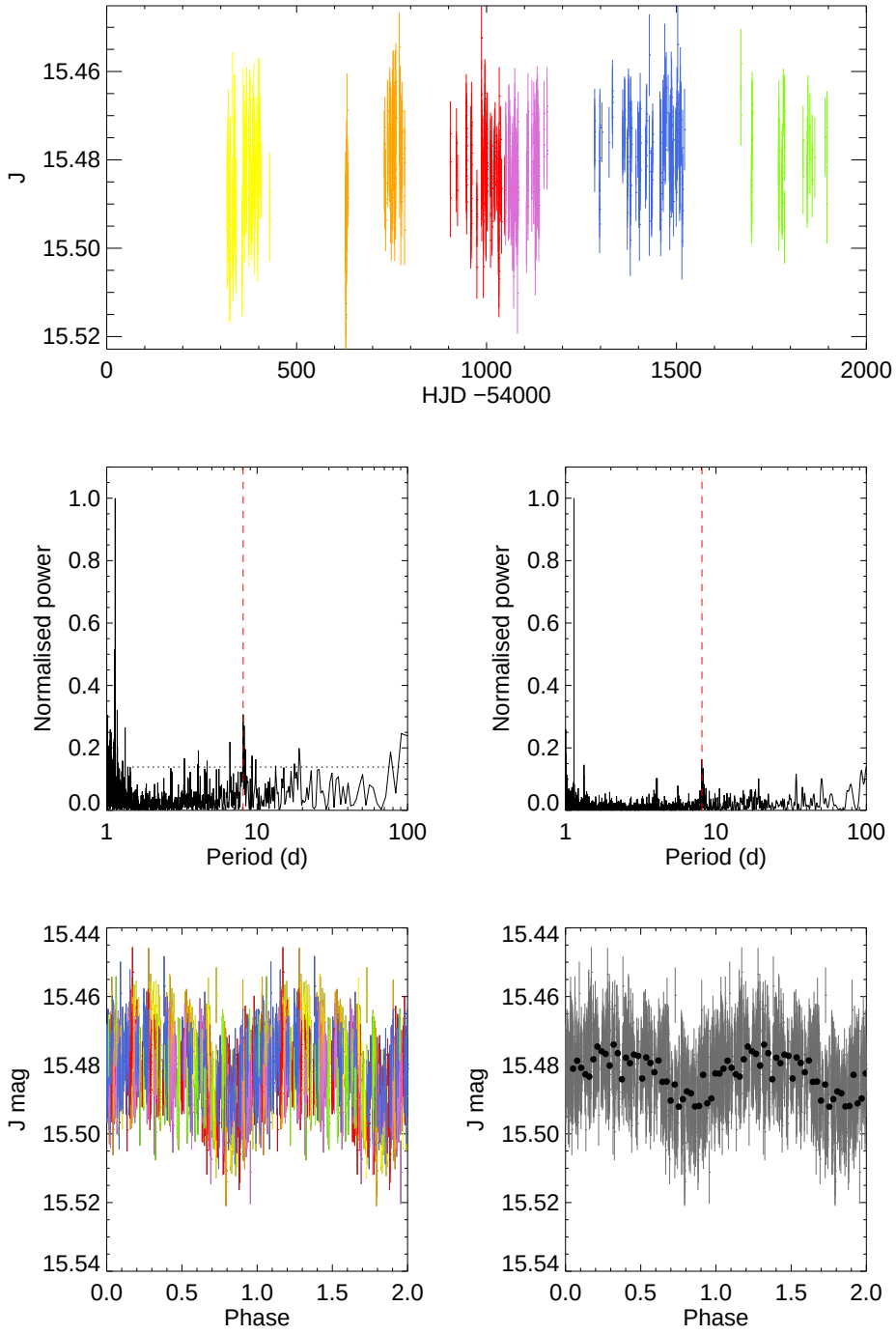

Period (d)	8.050
Amplitude (J)	0.025±0.008
Spectral Type	M3±1.00

Figure A52: As in Figure A51 for the star 19d_2_00740.

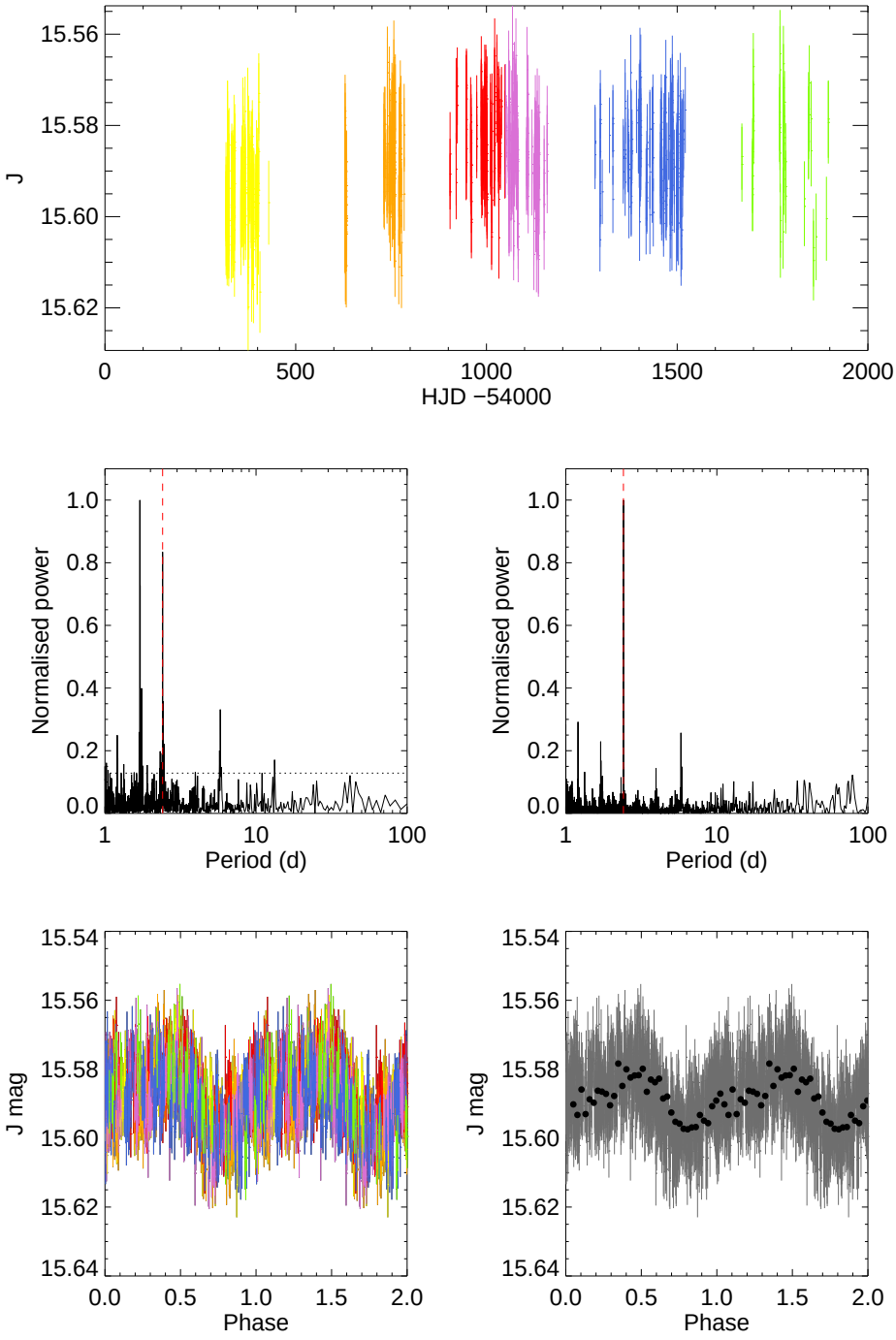

Period (d)	2.410
Amplitude (J)	0.019±0.008
Spectral Type	M4±1.01

FIGURE A53: As in Figure A52 for the star 19d_3_01140. The period near 1 day is ignored.

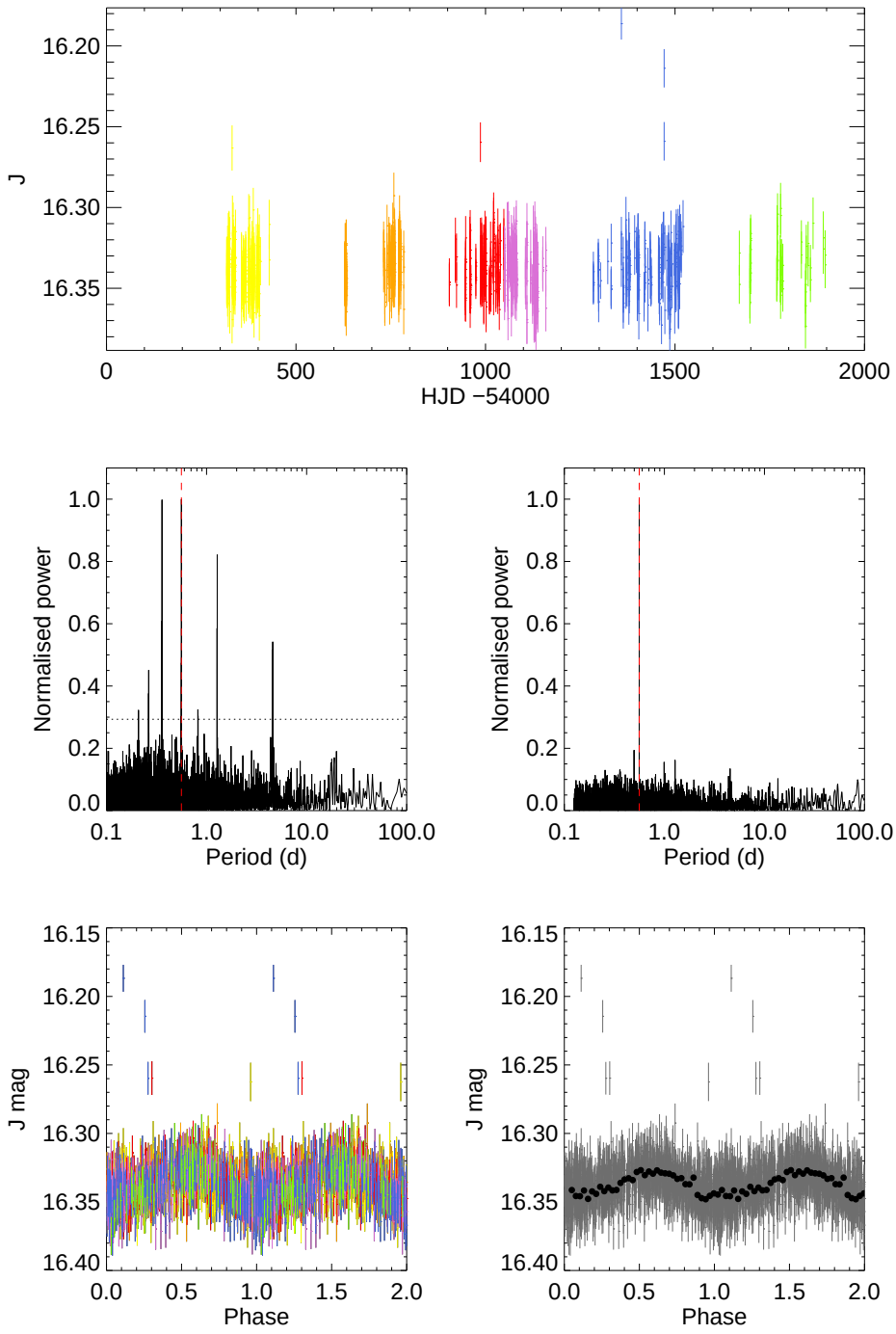

Period (d)	0.560
Amplitude (J)	0.026±0.013
Spectral Type	M4±1.00

Figure A54: As in Figure A53 for the star 19d_3_01271. Possible flares occur in the later (blue) observations.

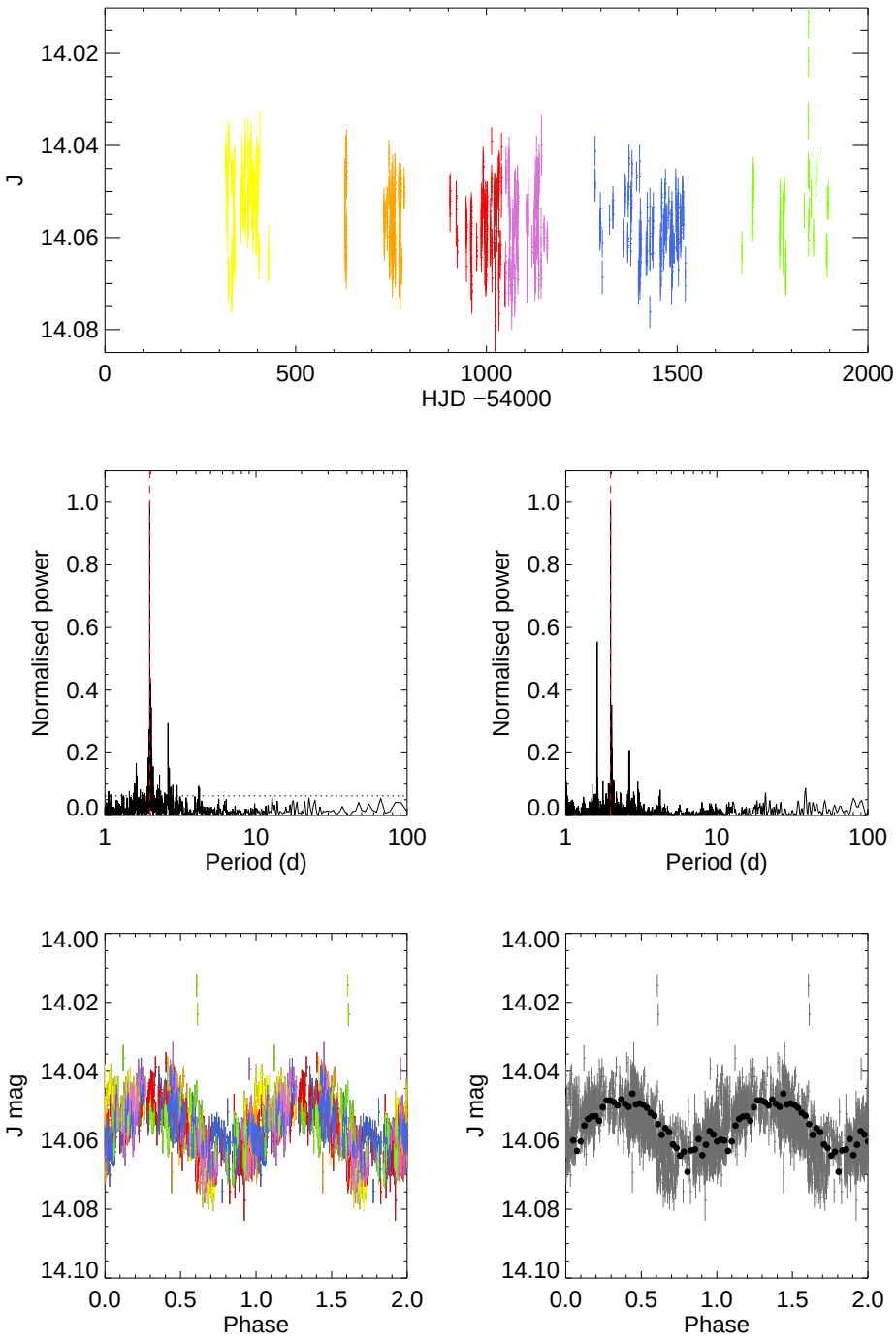

Period (d)	2.010
Amplitude (J)	0.023±0.003
Spectral Type	M4±1.00

FIGURE A55: As in Figure A54 for the star 19d_3_02216. A possible flare occurs in the lattermost (green) observations.

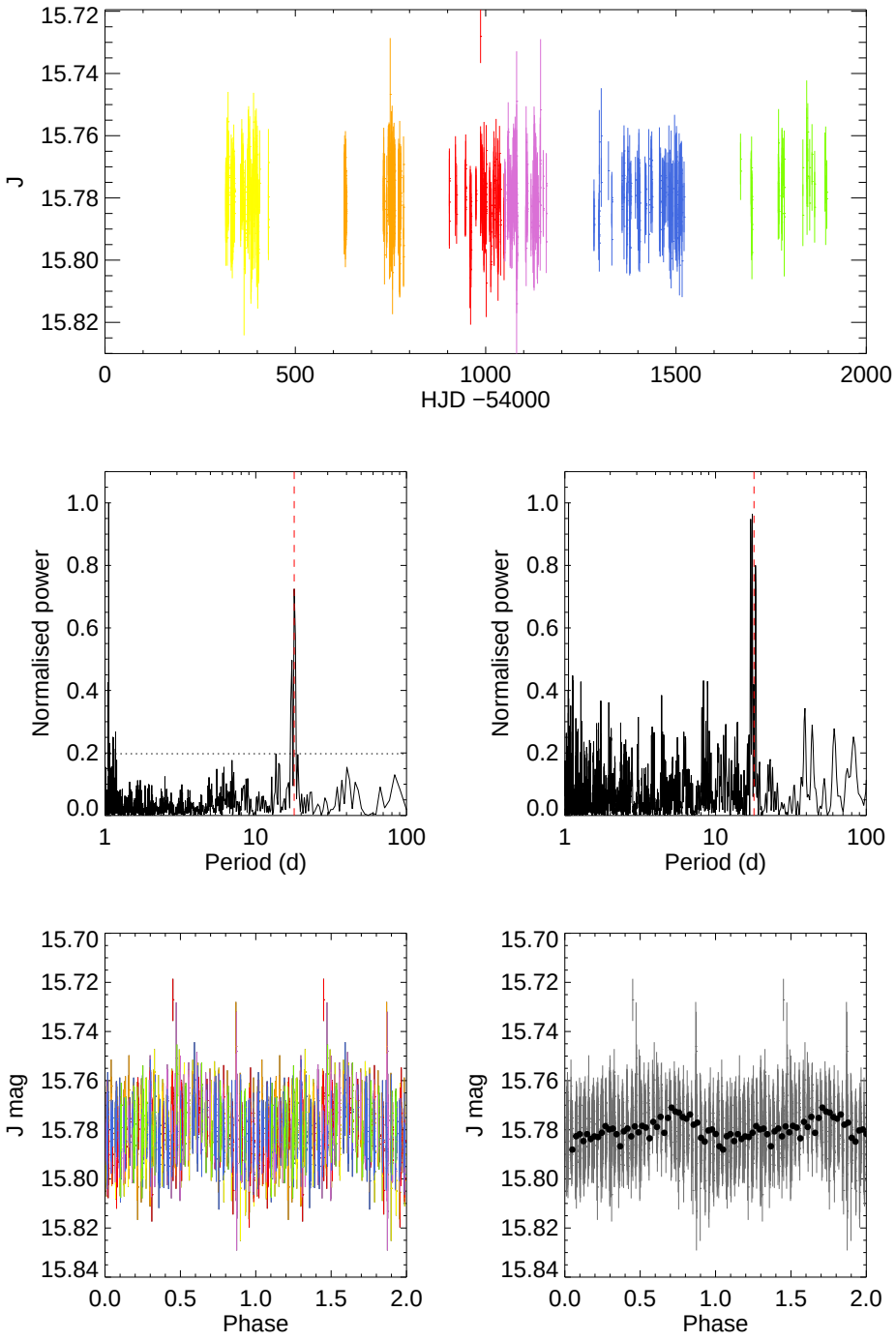

Period (d)	17.480
Amplitude (J)	0.019±0.009
Spectral Type	M0±1.00

Figure A56: As in Figure A55 for the star 19d_3_03681.

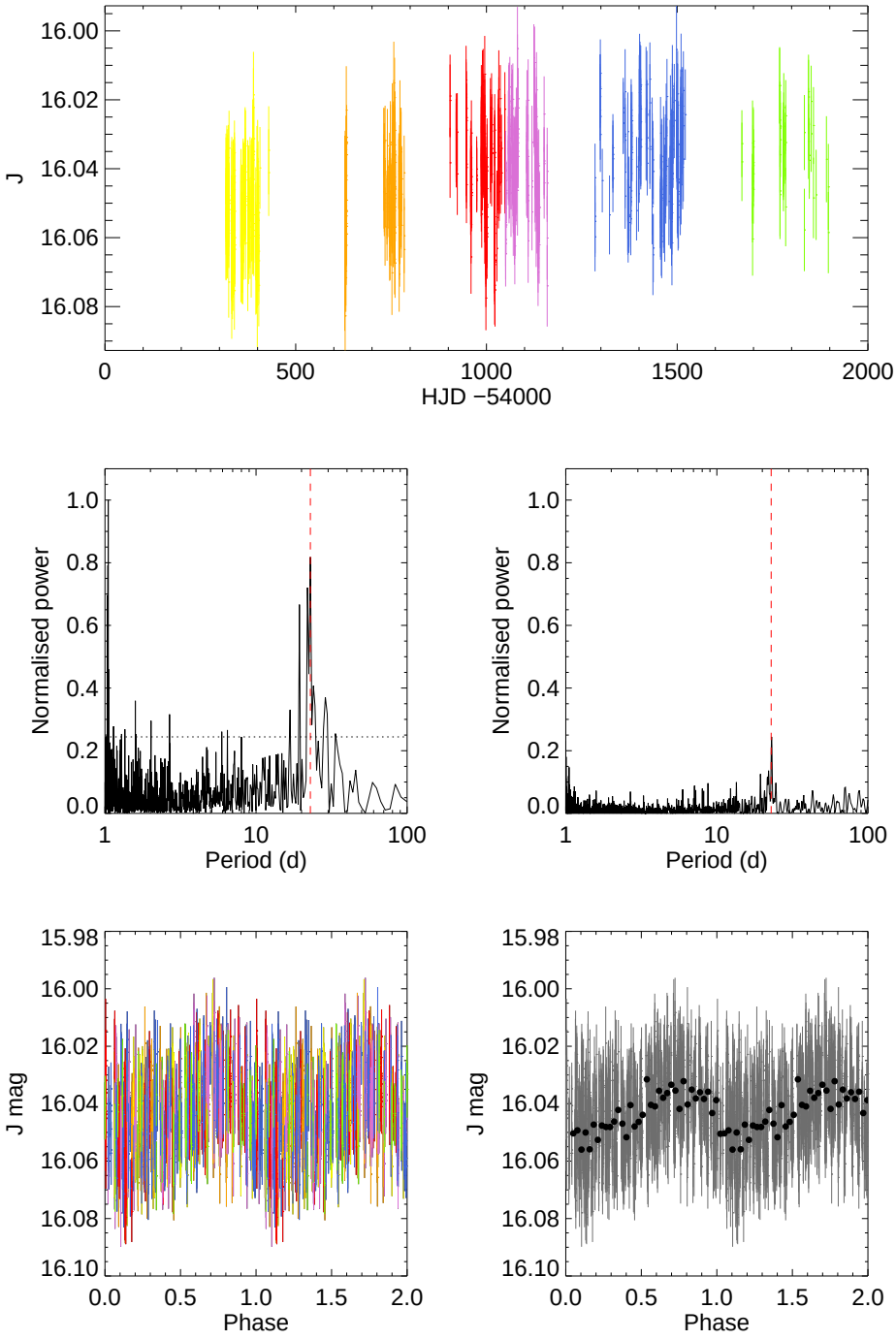

Period (d)	23.060
Amplitude (J)	0.029±0.010
Spectral Type	M2±1.12

FIGURE A57: As in Figure A56 for the star 19d_3_05922.

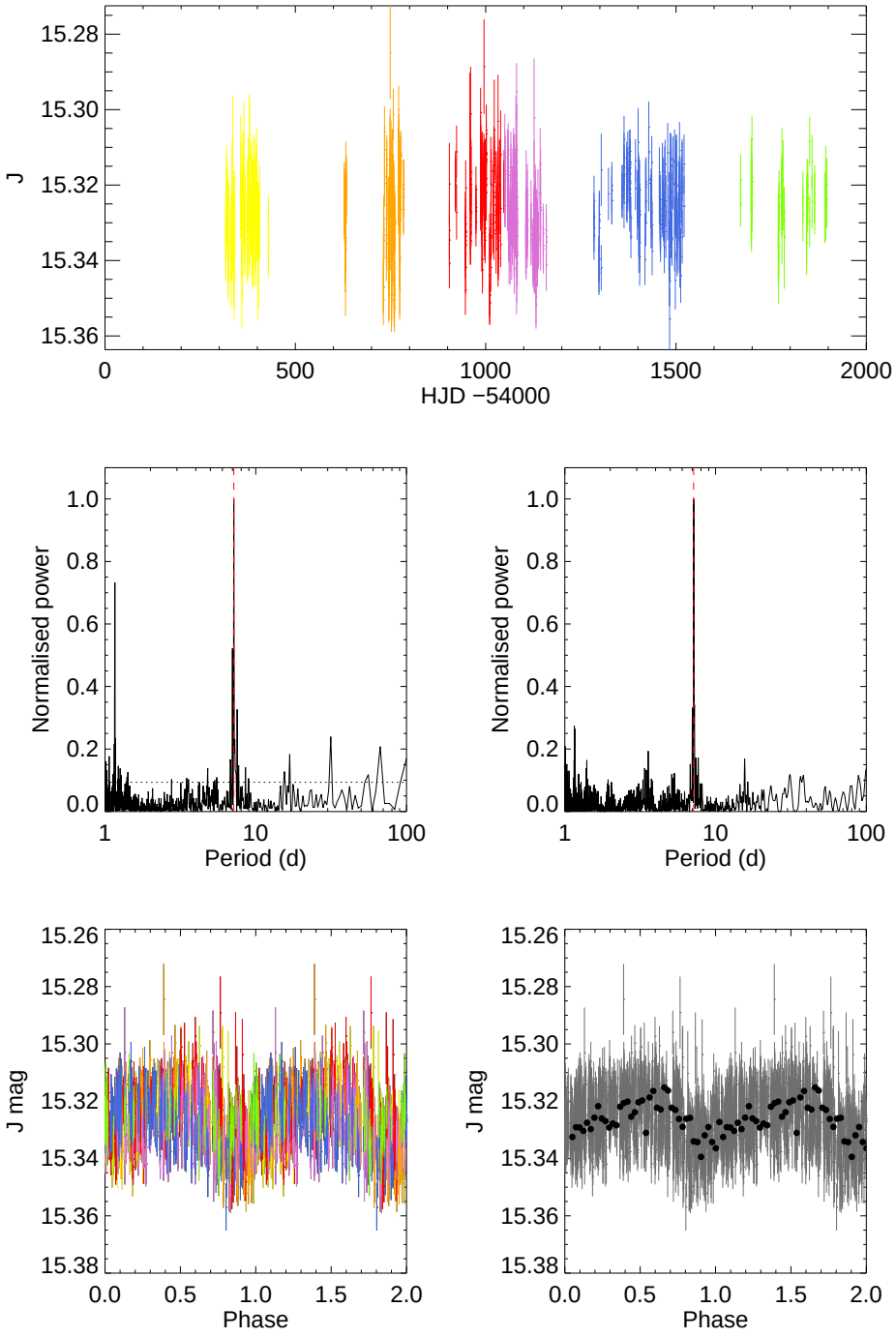

Period (d)	7.170
Amplitude (J)	0.026±0.007
Spectral Type	M0±1.00

Figure A58: As in Figure A57 for the star 19d_3_07286.

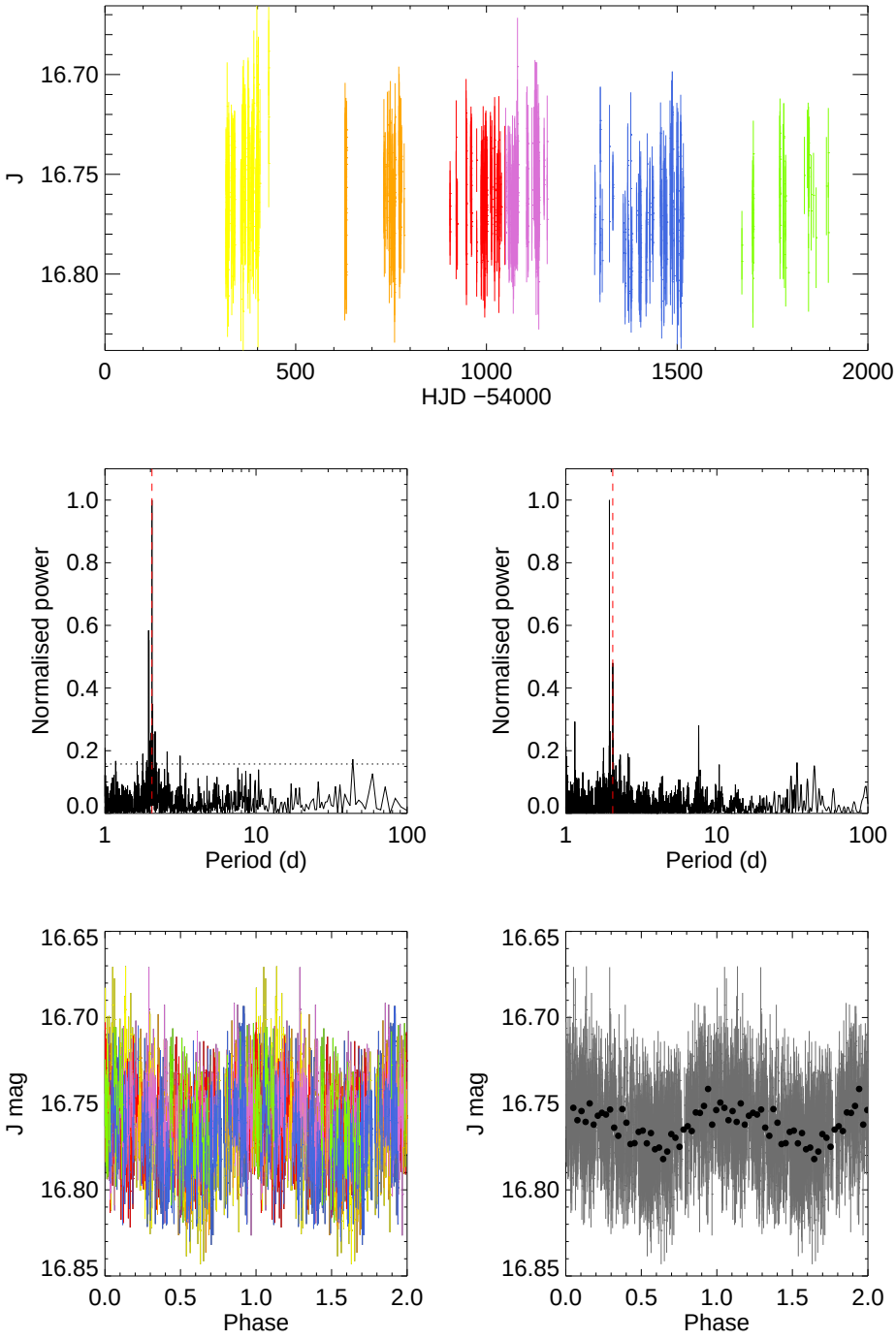

Period (d)	1.950
Amplitude (J)	0.042±0.018
Spectral Type	M1±1.19

FIGURE A59: As in Figure A58 for the star 19e_1_03204.

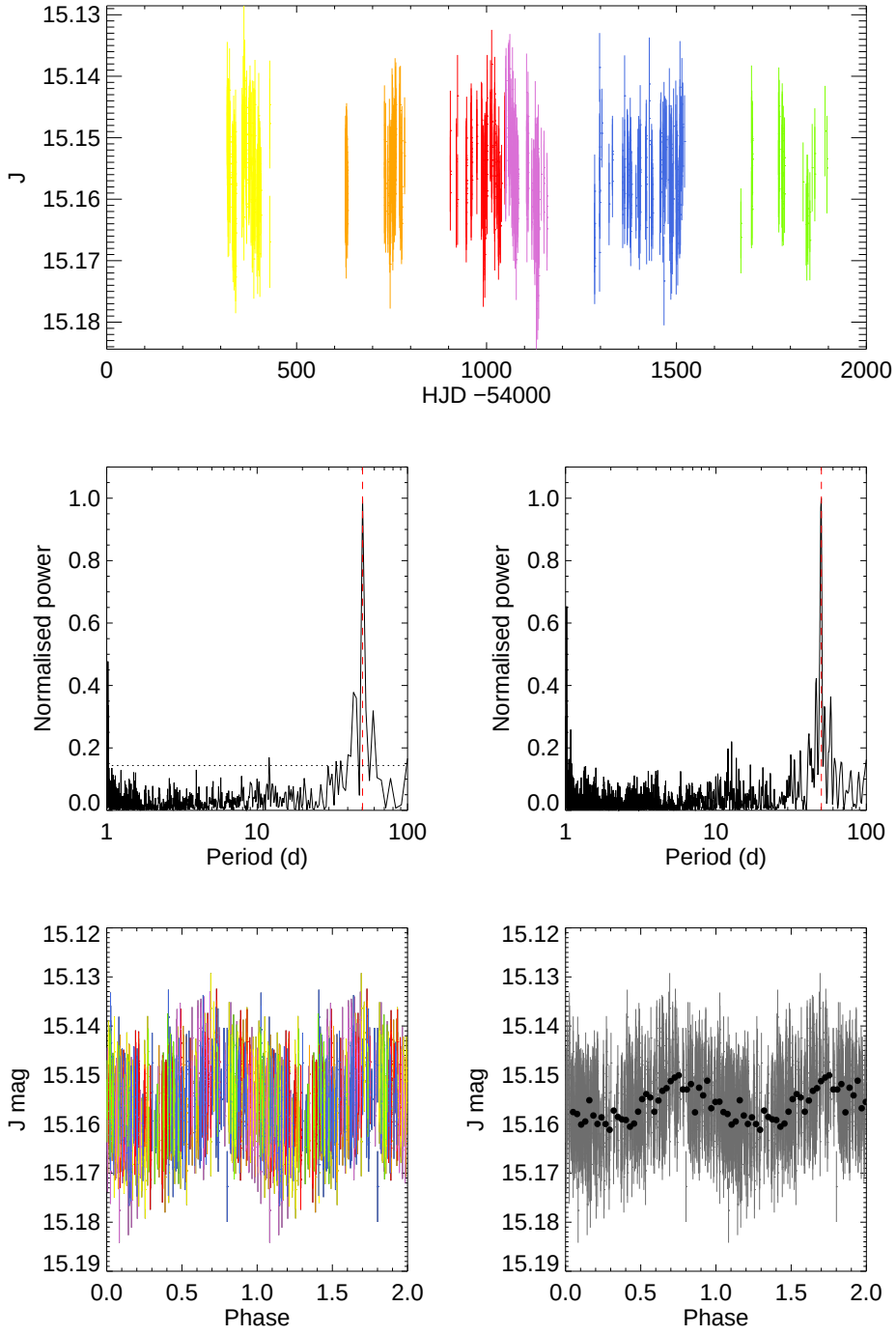

Period (d)	50.020
Amplitude (J)	0.013±0.006
Spectral Type	M4±1.00

Figure A60: As in Figure A59 for the star 19e_2_02880.

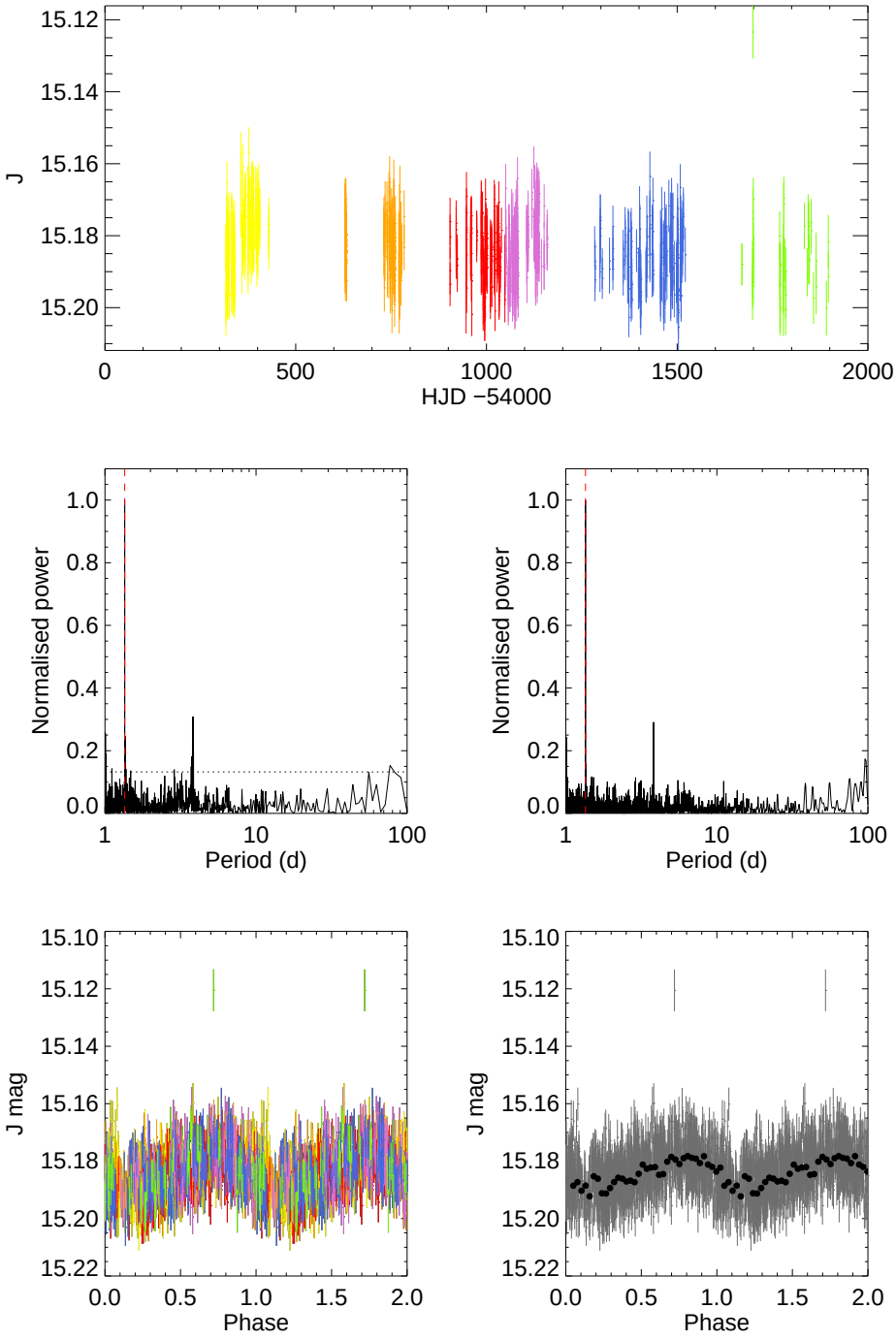

Period (d)	1.350
Amplitude (J)	0.018±0.006
Spectral Type	M4±1.00

FIGURE A61: As in Figure A60 for the star 19e_2_09200.

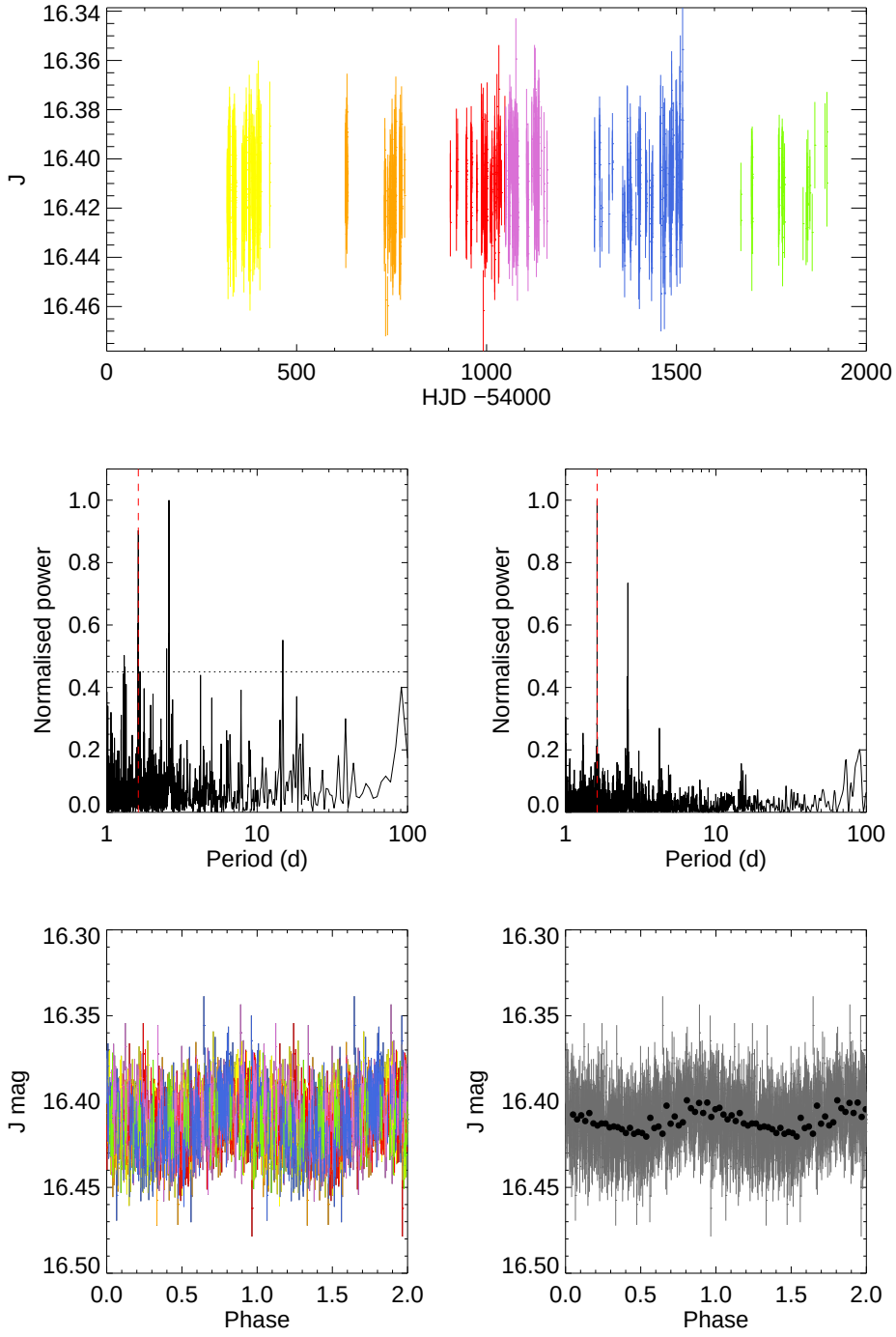

Period (d)	1.620
Amplitude (J)	0.025±0.014
Spectral Type	M4±1.00

Figure A62: As in Figure A61 for the star 19e_3_09622.

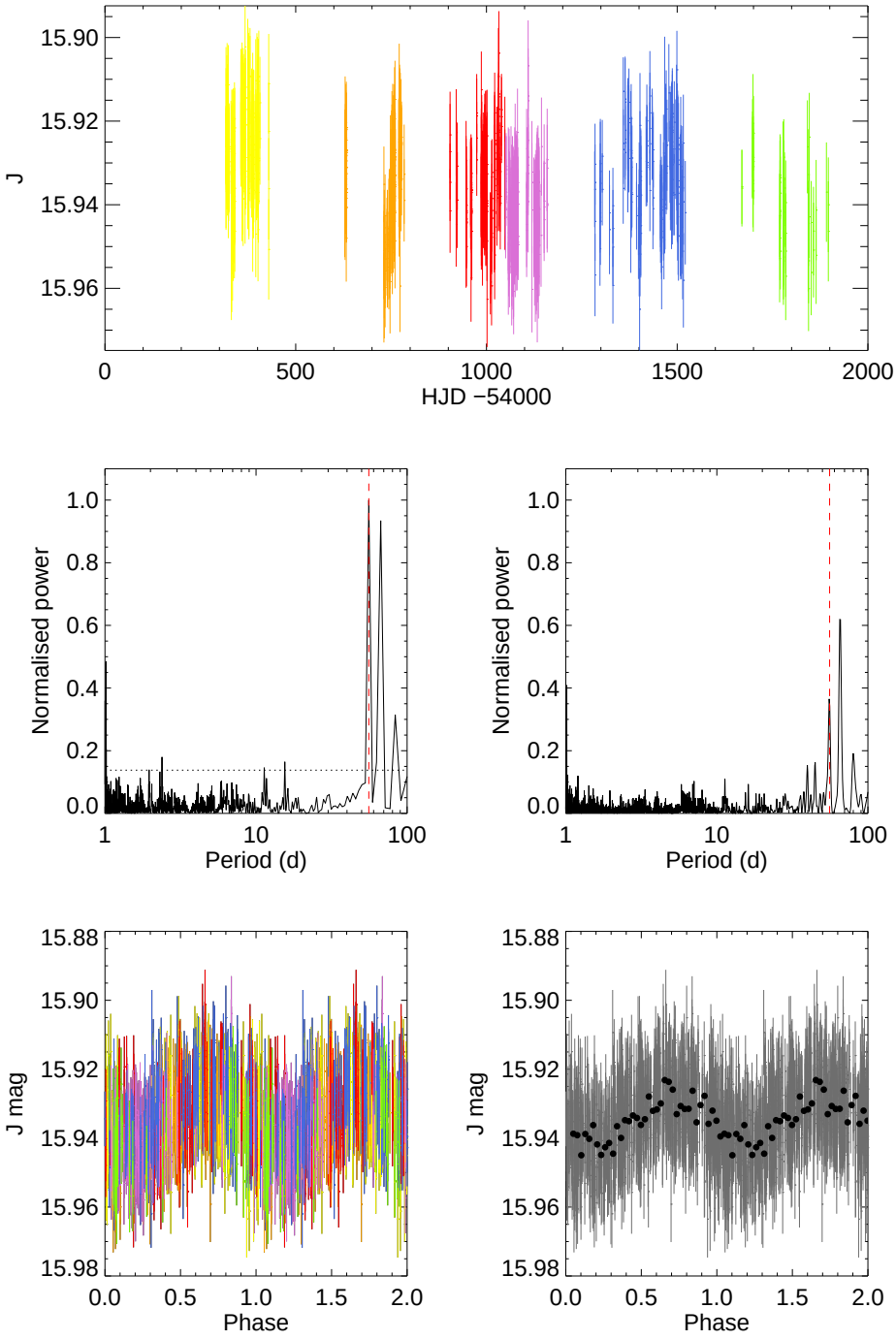

Period (d)	65.390
Amplitude (J)	0.026±0.010
Spectral Type	M4±1.00

FIGURE A63: As in Figure A62 for the star 19f_3_08798.

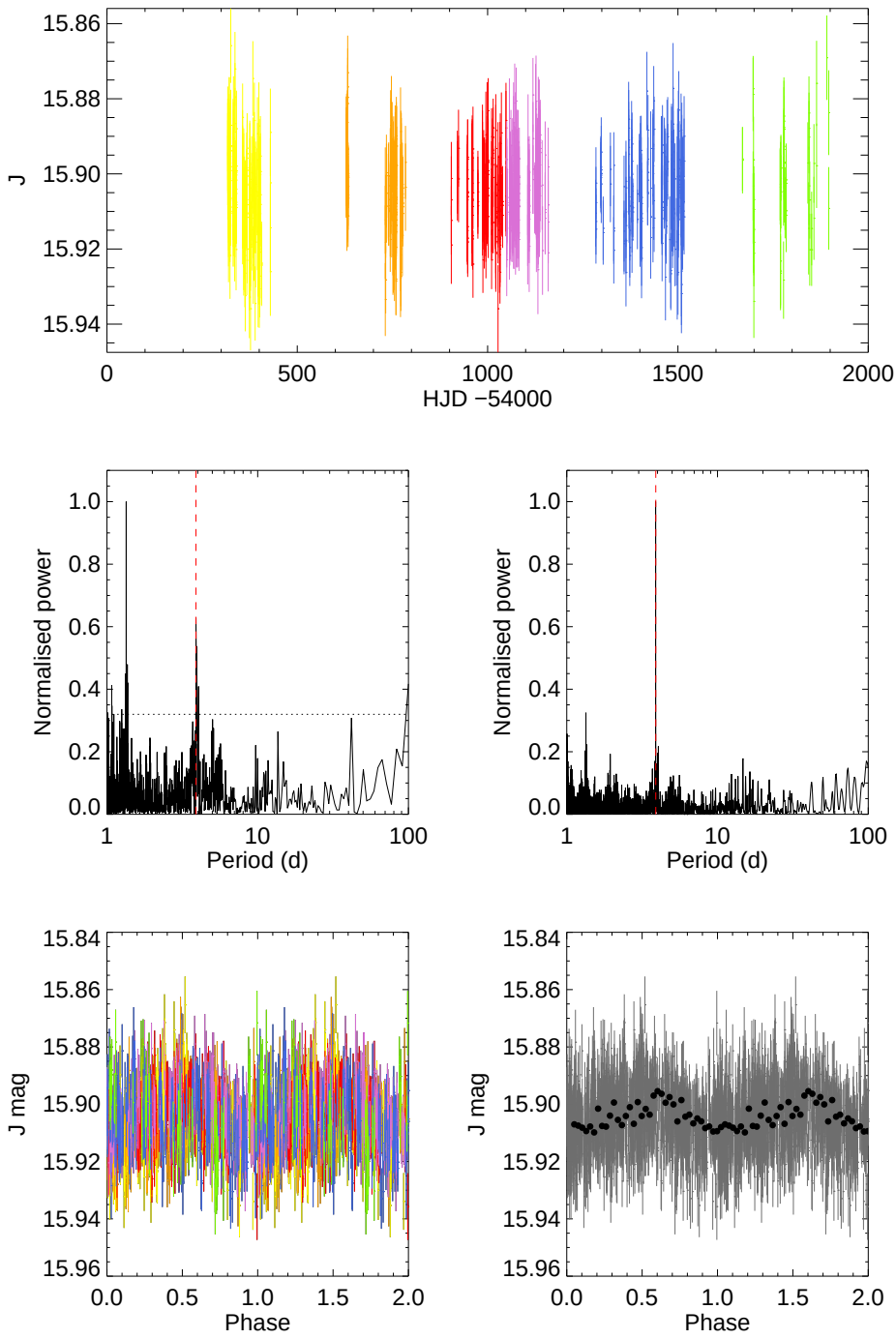

Period (d)	3.890
Amplitude (J)	0.018±0.009
Spectral Type	M3±1.18

Figure A64: As in Figure A63 for the star 19f_3_12800. The period near to 1 day is ignored.

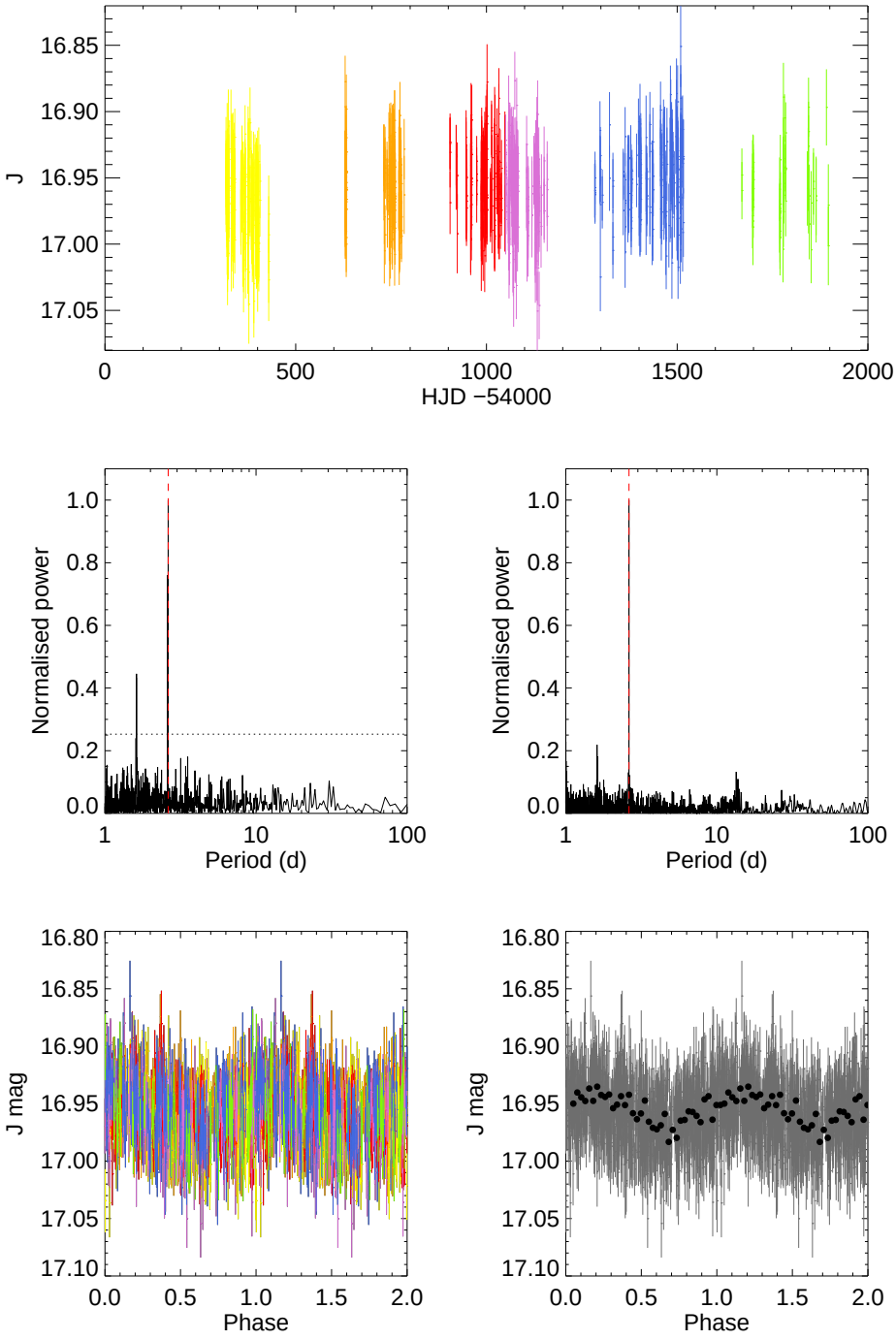

Period (d)	2.620
Amplitude (J)	0.048±0.022
Spectral Type	M0±1.76

FIGURE A65: As in Figure A64 for the star 19f_4_06780.

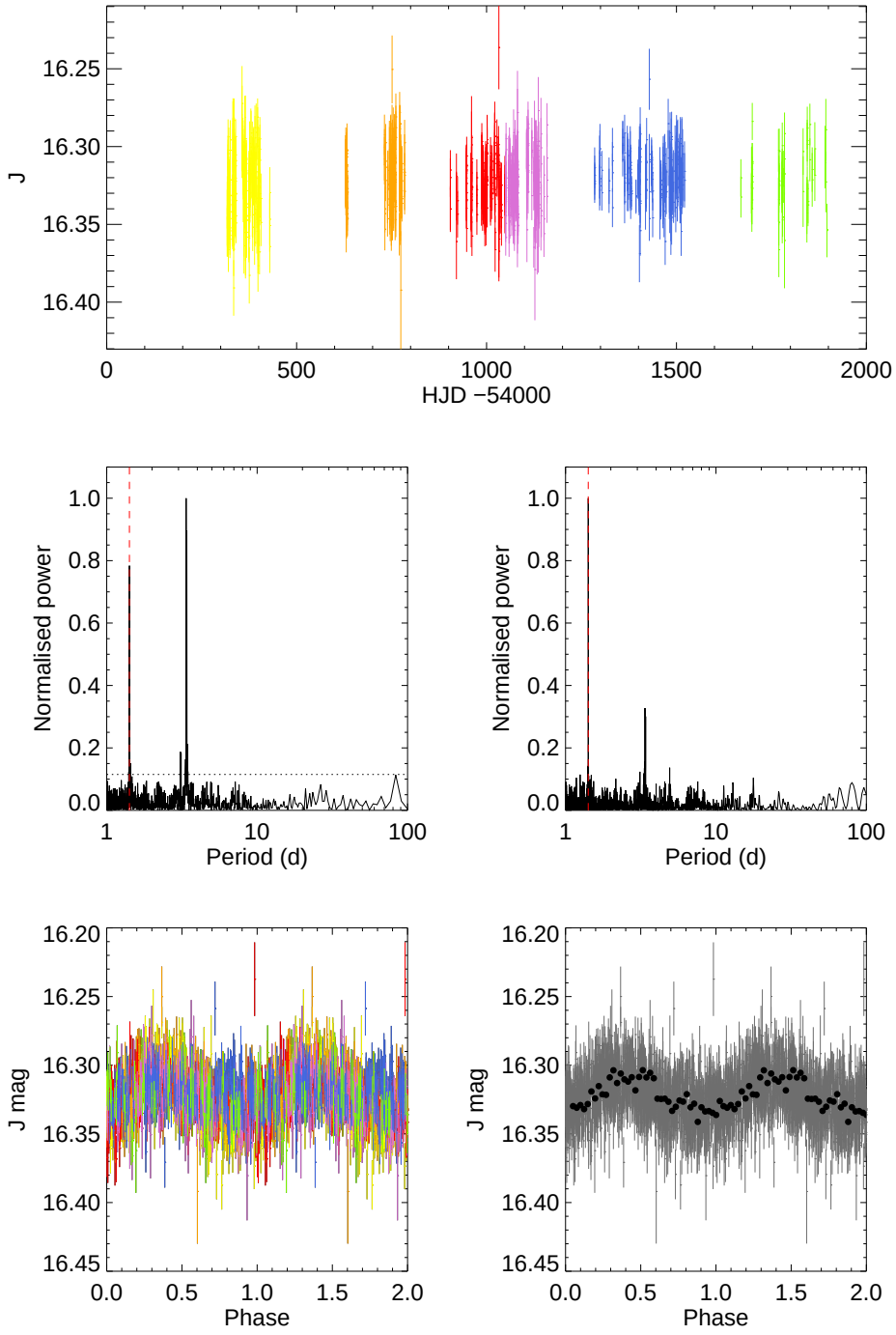

Period (d)	1.420
Amplitude (J)	0.042±0.014
Spectral Type	M0±1.06

Figure A66: As in Figure A65 for the star 19g_1_04348.

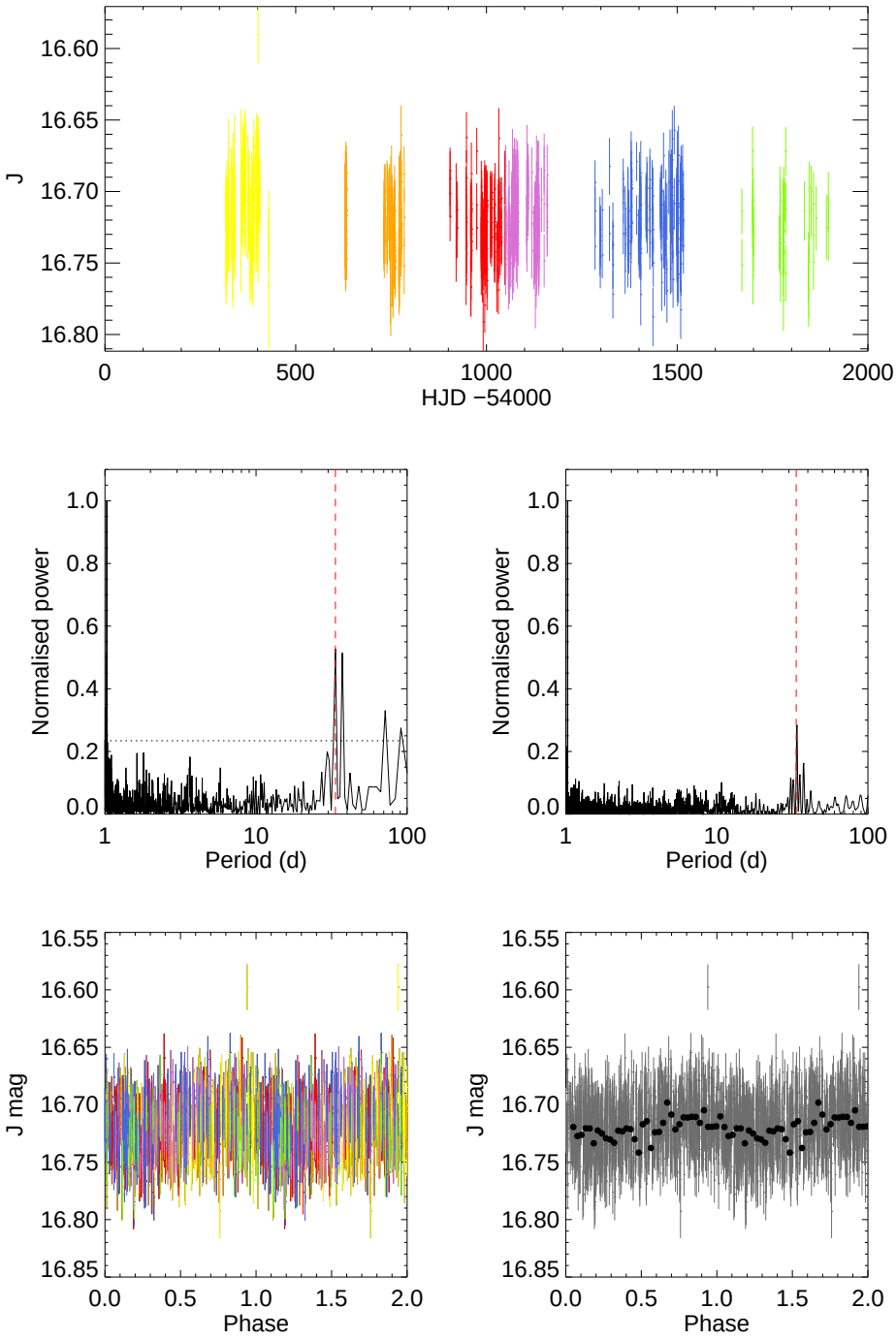

Period (d)	34.220
Amplitude (J)	0.041±0.017
Spectral Type	M4±1.00

FIGURE A67: As in Figure A66 for the star 19g_1_05313. The period near to 1 day is ignored.

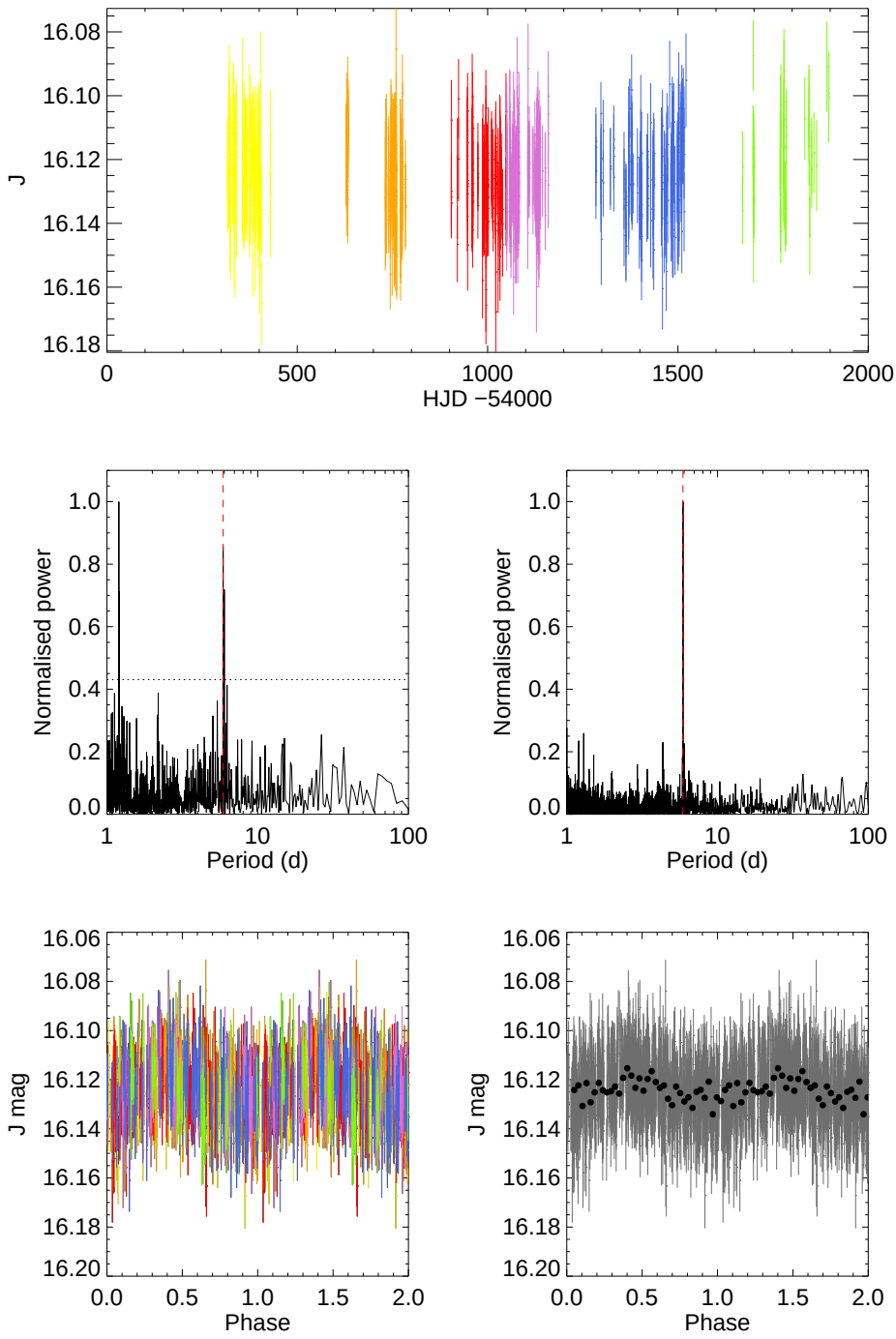

Period (d)	5.910
Amplitude (J)	0.023±0.011
Spectral Type	M4±1.08

Figure A68: As in Figure A67 for the star 19g_1_10773. The period near to 1 day is ignored.

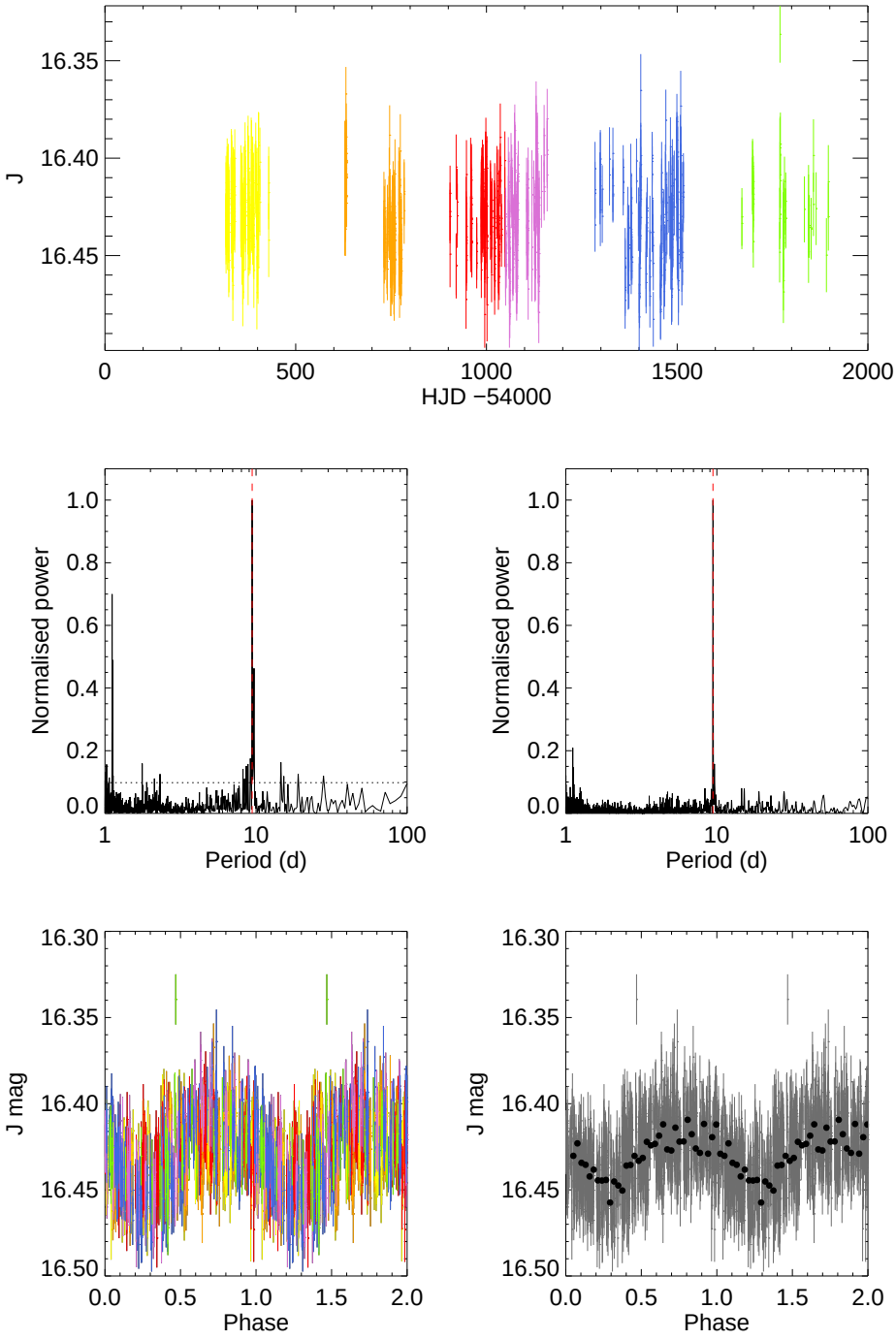

Period (d)	9.420
Amplitude (J)	0.053±0.015
Spectral Type	M3±1.00

FIGURE A69: As in Figure A68 for the star 19g_2_03649.

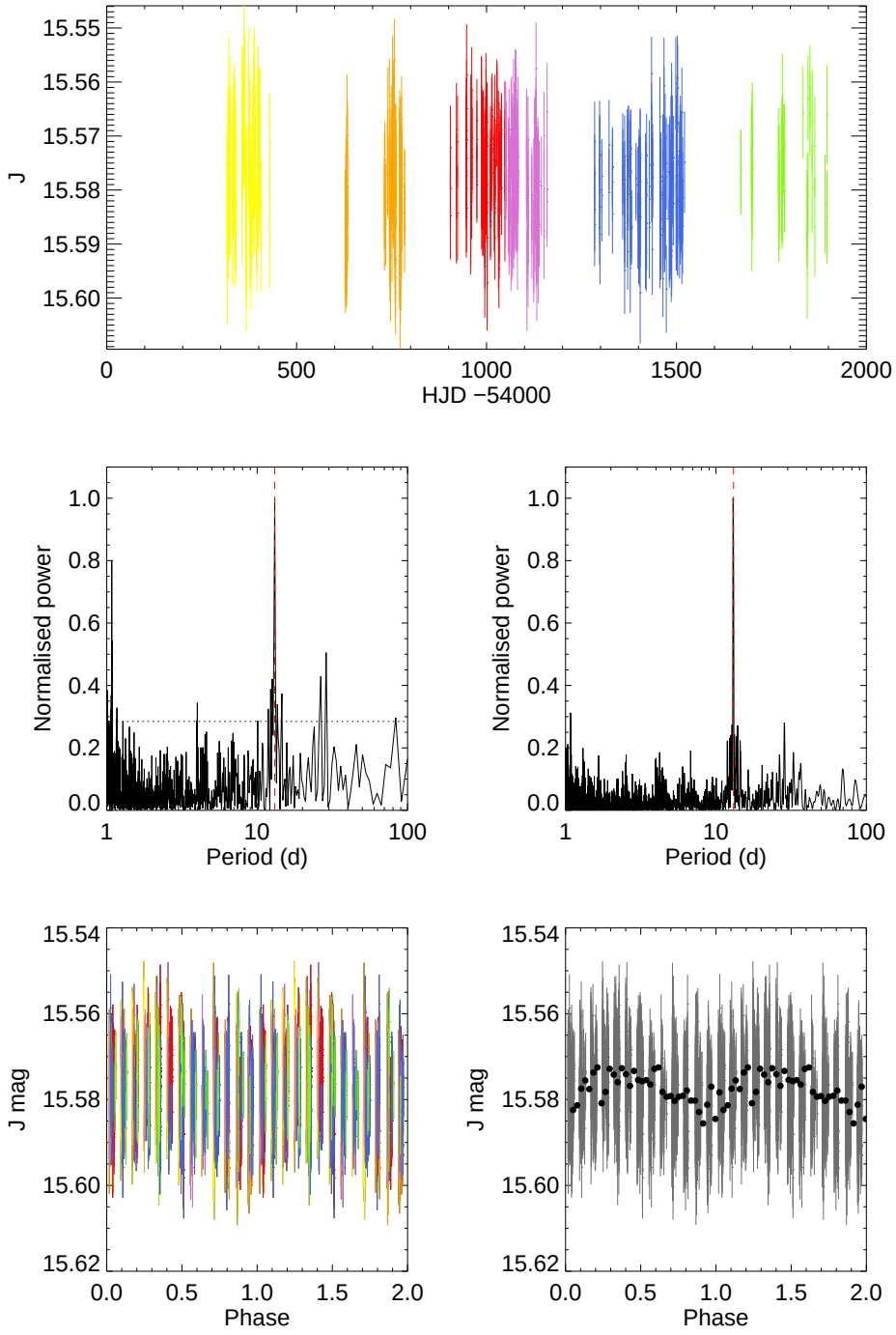

Period (d)	13.000
Amplitude (J)	0.014±0.008
Spectral Type	M4±1.06

Figure A70: As in Figure A69 for the star 19g_3_06870.

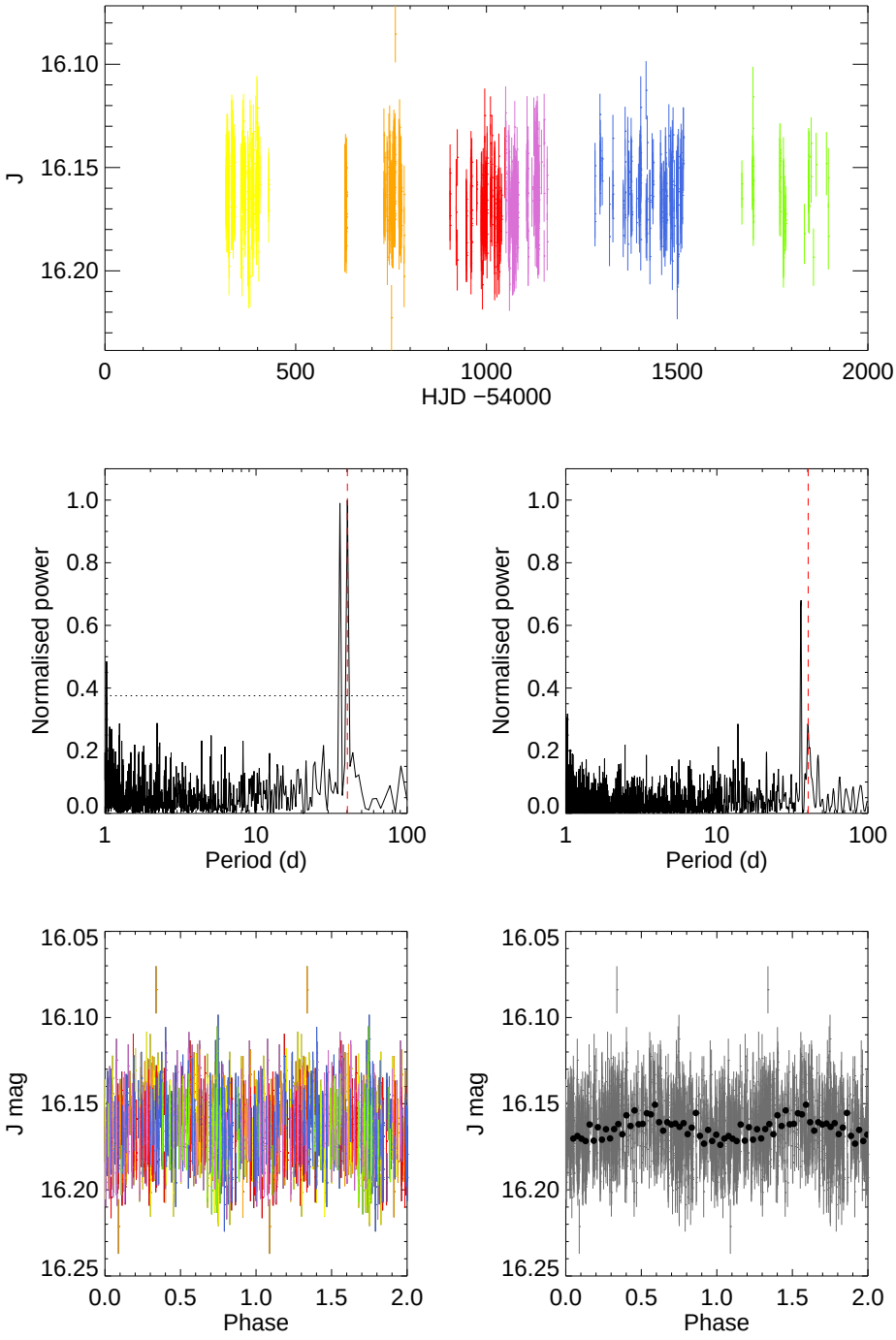

Period (d)	40.050
Amplitude (J)	0.025±0.012
Spectral Type	M4±1.20

FIGURE A71: As in Figure A70 for the star 19g_4_00989.

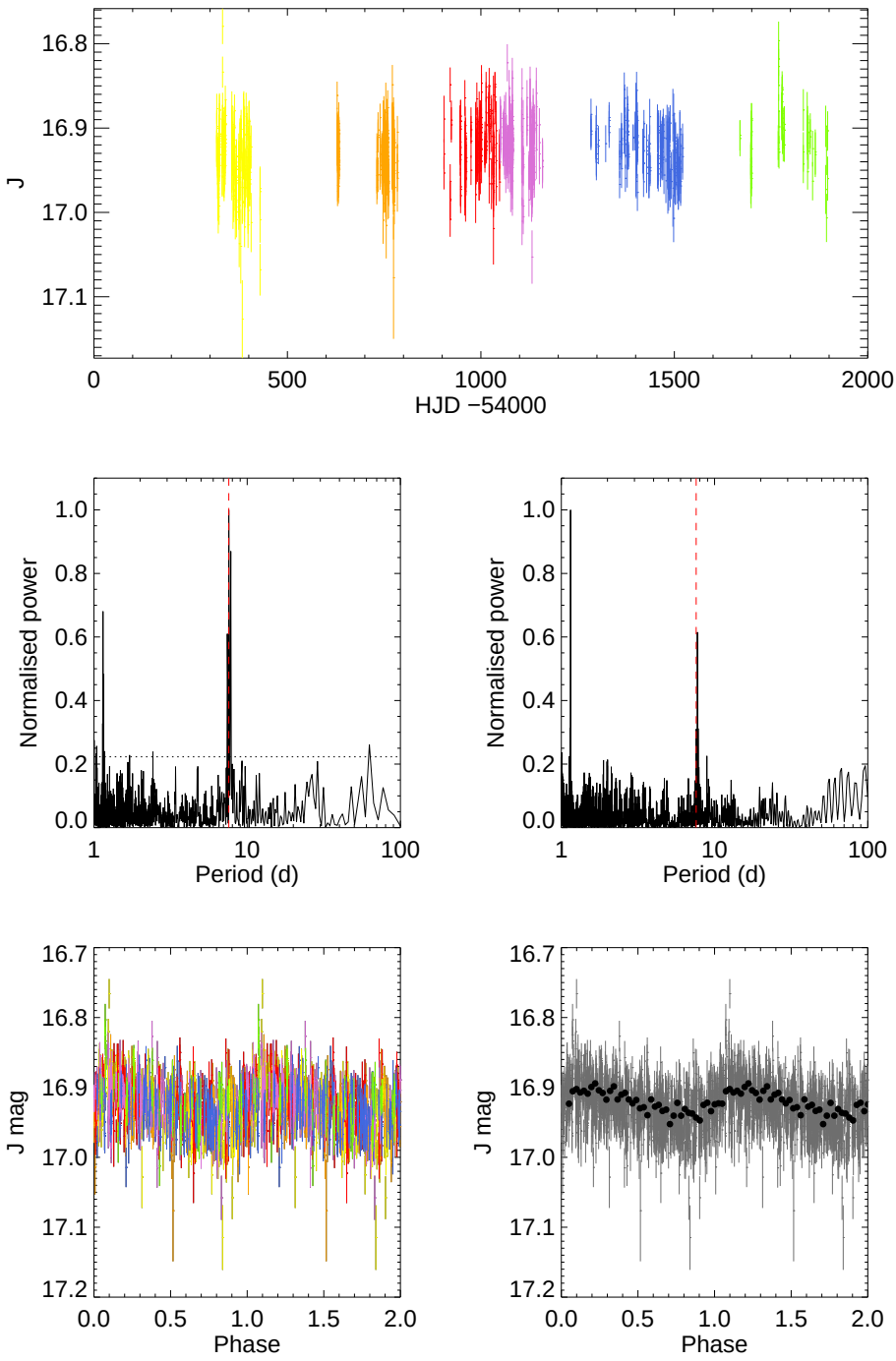

Period (d)	7.560
Amplitude (J)	0.052±0.018
Spectral Type	M0±1.31

Figure A72: As in Figure A71 for the star 19h_3_16170. The period near to 1 day is ignored.

A2 Eclipsing Binary Light Curves

In this section the phase folded light curves of the nine suspected eclipsing binaries incidentally found by the Lomb-Scargle periodogram are presented, folded over the periods as determined by the CLEAN algorithm.

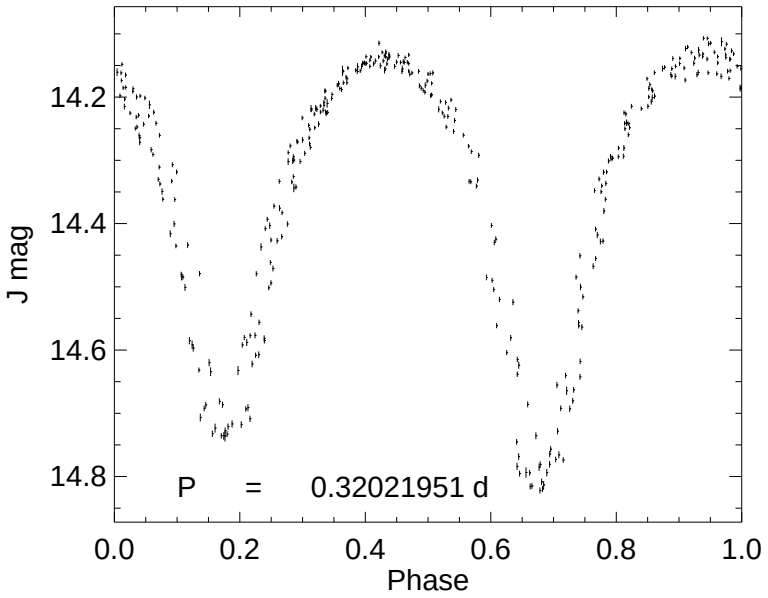

Figure A73: Light curve for 03g_4_00203, spectral type M1±1.1. The short period and non-flat maxima are indicatve of a very close binary system. The similar depths of the primary and secondary eclipse indicate the two components are of a similar luminosity.

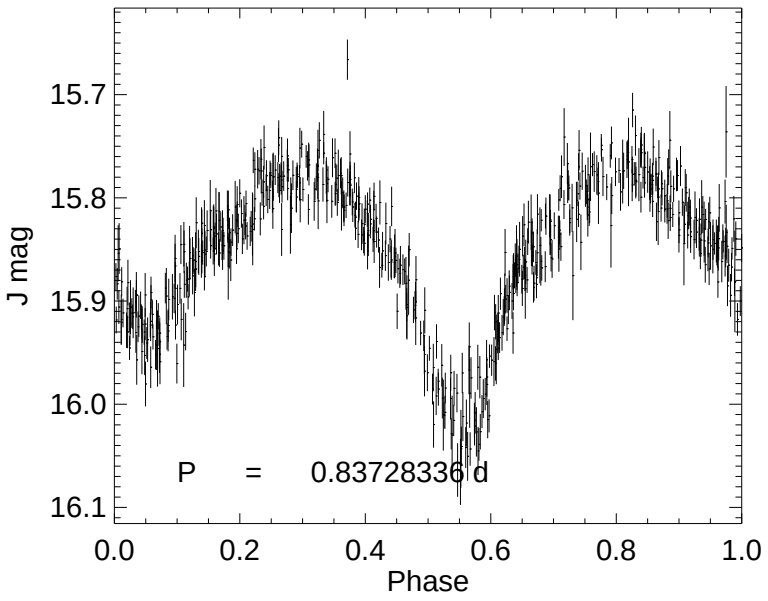

Figure A74: Light curve for 07e_4_01230, spectral type G4±3.4. As with 03g_4_00203, the period and morphology indicate a close binary. While the spectral typing procedure identified this star on average as a G4V type star, it was selected as $H - K = 0.26 \pm 0.02$, indicative of a M5V star.

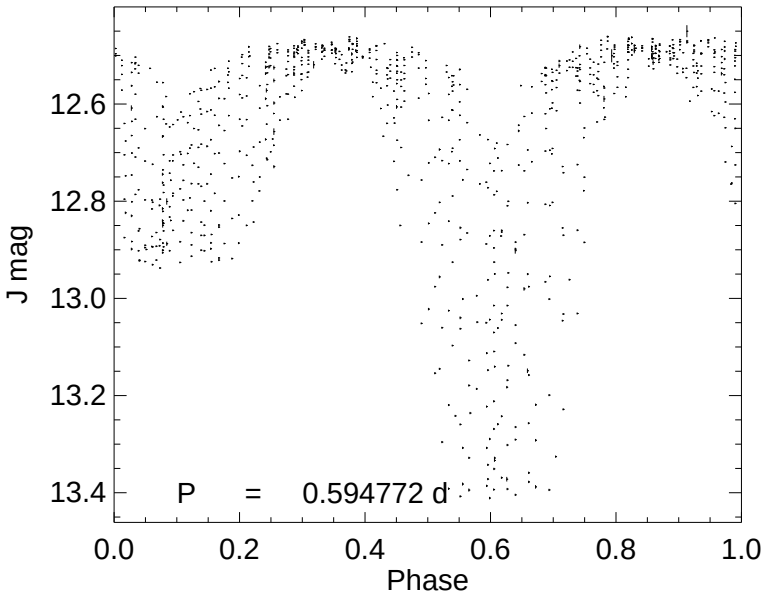

FIGURE A75: Light curve for 19a_3_05975, spectral type M2±1.8. While the light curve shows two peaks and troughs, neither the Lomb-Scargle peridoogram nor the CLEAN alogorithm could find a period for which the light curve appeared folded properly. This may be because the period evolved durin the observations, or because some other effect like spots or a third body modofied the light curve from the expected morphology.

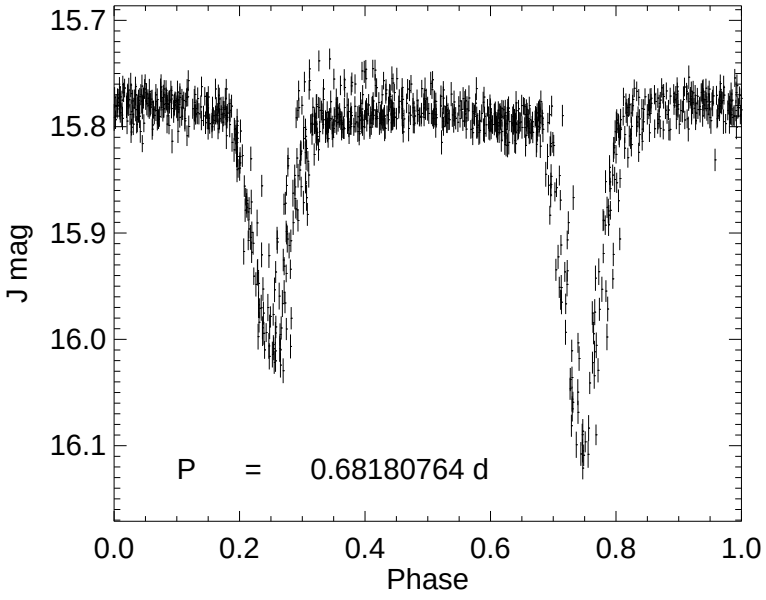

FIGURE A76: Light curve for 19c_4_11480, spectral type M1±1.6, a detached binary.

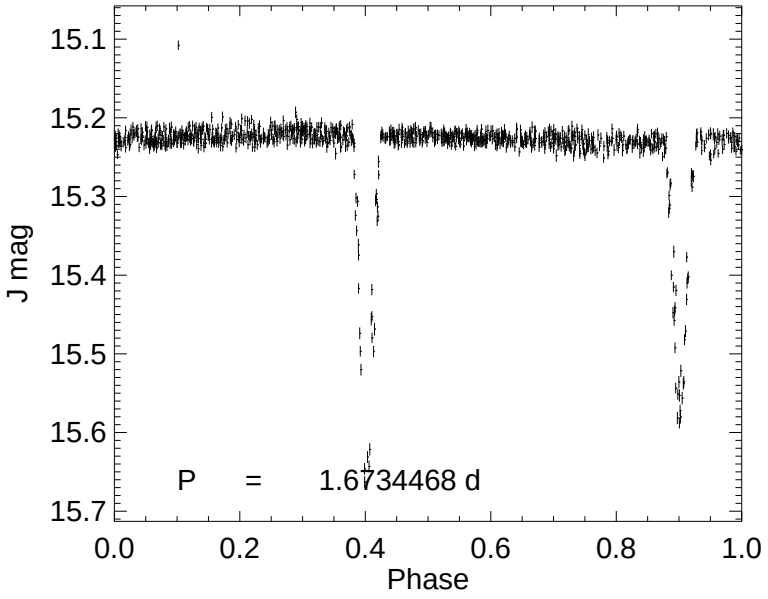

Figure A77: Light curve for 19e_3_08413, spectral type M3±1.01, a detached binary.

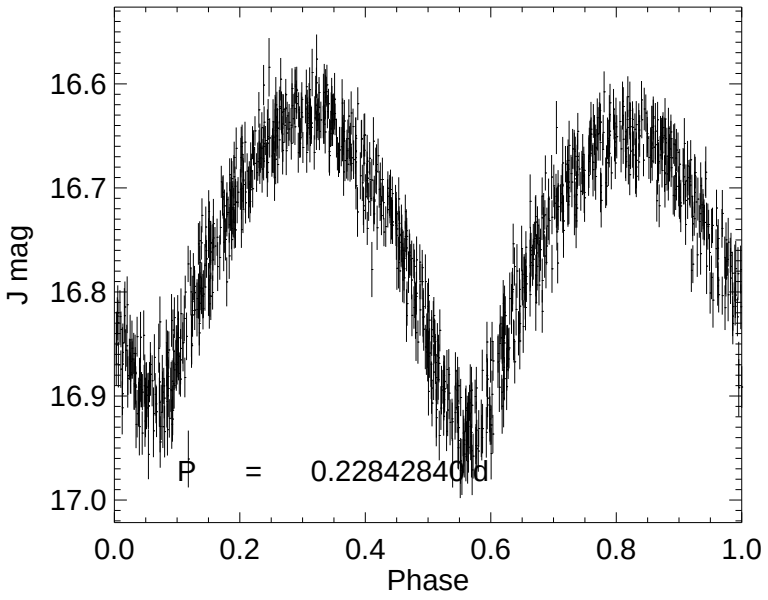

Figure A78: Light curve for 19e_4_00861, M0±1.31, a contact binary with components of similar luminosity as indicated by the nearly sinusoidal morphology. A period of 0.22842771 d and a T_{eff} of 4100K is reported by Nefs et al. (2012) for this system, in agreement with the period and spectral type found here.

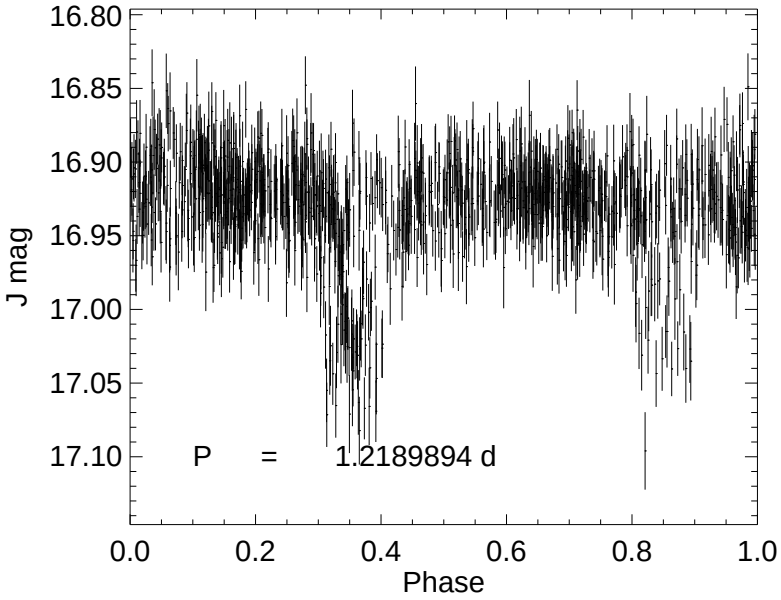

FIGURE A79: Light curve for 19g_1_05175, spectral type M1±1.54, a detached binary.

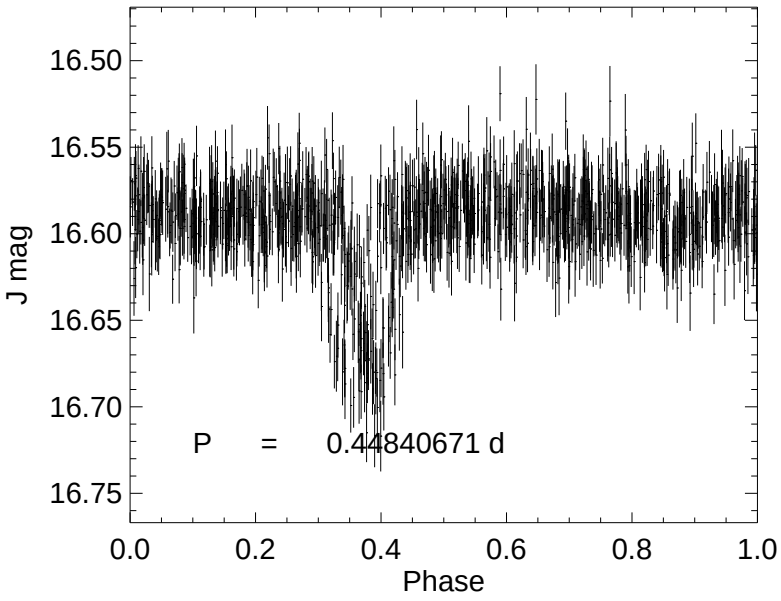

FIGURE A80: Light curve for 19g_2_05124, spectral type M3±1.00, a detached binary. The secondary eclipse for this system is particularly small.

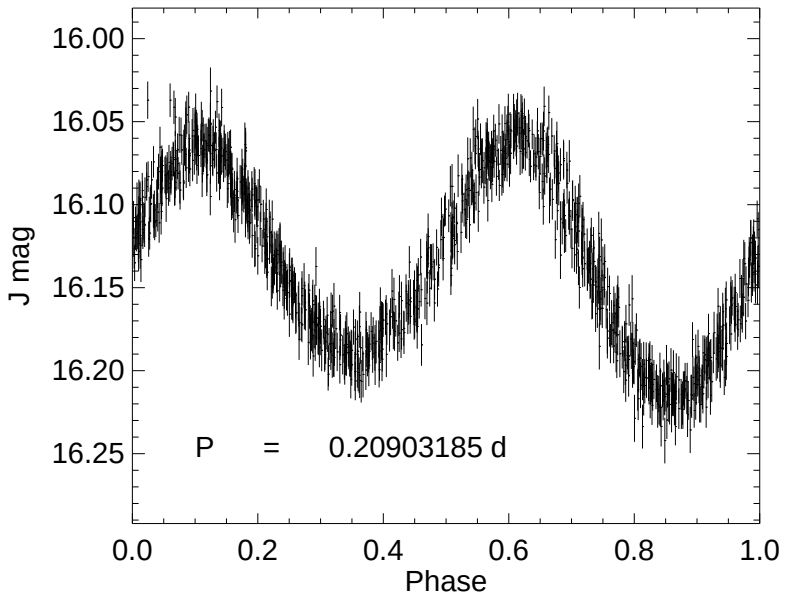

Figure A81: Light curve for 19g_3_06701, spectral type M2±1.06, a contact binary. A period of 0.2090313d and a T_{eff} of 3700K is reported by Nefs et al. (2012) for this system, in agreement with the period and spectral type found here.